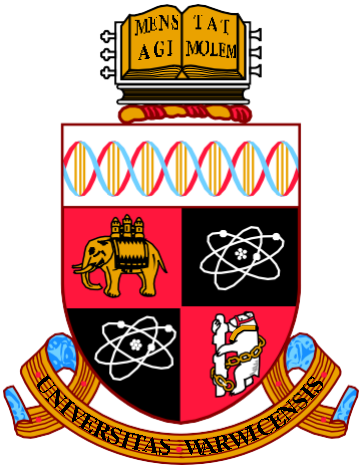

A multi technique characterisation approach to the analysis of polymers and biomaterials

by

Nicole Louise Kelly

Thesis

Submitted to The University of Warwick for the degree of **Doctor of Philosophy**

Department of Chemistry

September 2020

THE UNIVERSITY OF WARWICK

Contents

List of Tables

List of Figures

Acknowledgments

First, I would like to thank my supervisor Professor John V. Hanna, without his guidance this thesis would not have been possible.

I would also like to express my gratitude to Corbion Purac, EPSRC and the Molecular Analytical Science CDT for their financial support. I would like to also thank all my collaborators who have graciously provided me with samples, namely Corbion Purac and Dr Joshua Worch. I would also like to thank the spectroscopy RTP, especially Dr Ben Breeze and the X-ray RTP, in particular Dr David Walker and Dr Steven Hubband, who have provided valuable training and insight.

I would like to acknowledge everyone in the solid state NMR group and Warwick for the support throughout the last few years. I would especially like to thank Dr Samuel Page for his patience for all my questions and Dr Gregory Rees for his training in solid state NMR. I would also like to thank Professor Andrew P. Dove and everyone in the Dove group for their valuable insight into the world of polymers. I would like to thank everyone in the Molecular Analytical Science CDT for their support and friendship throughout my time at Warwick, in particular Emily Corlett and Georgina Charlton.

Finally, I would like to thank my parents for all the support they have given me throughout all of my academic studies.

Declarations

I hereby declare that A multi technique characterisation approach to the analysis of polymers and biomaterials is an original work and has not been submitted for a degree or diploma or other qualification at any other University.

For Chapter 4 all samples were provided by Corbion Purac.

For Chapter 5 all samples were injection moulded with the help of Gerald Schennink at Wageningen University & Research, University of Wageningen, Netherlands. Tensile measurements were also performed at Wageningen University & Research.

For Chapter 6 all samples were synthesised with the help of Dr Joshua Worch at the Department of Chemistry, University of Birmingham. The GPC and tensile testing were also performed by Dr Joshua Worch.

For Chapter 7 all samples were synthesised by Song-Yi Baek at the Division of Biomaterials and Tissue Engineering, Eastman Dental Institute, University College London. DSC measurements were also performed by Song-Yi Baek.

Abstract

A multi technique characterisation approach is vital for the full understanding of a material and its properties. Through combining predominantly solid state nuclear magnetic resonance (NMR), wide-angle (WAXS), small-angle X-ray scattering (SAXS), differential scanning calorimetry (DSC) and Raman spectroscopy, four different systems have been investigated.

The importance of the development of biopolymers cannot be understated, polylactide (PLA) is one such biopolymer that has a lot of focus due to its wide range of end uses through tailoring it's physical properties. The characteristics and behaviour of PLA pre and post processing has been investigated. The degradation of four PLA samples with different ratios of D- and L- polylactide (PDLA/PLLA) has been tracked over the course of a year using the aforementioned techniques. The long range order does not change over the course of a year for all of the samples. There is however a potential rearrangement of the PLA helix but without an overall change in mobility.

The end product PLA materials were injection moulded and underwent tensile and impact testing. Two different mould temperatures were applied to investigate the difference between amorphous and crystalline products of the same starting composition. Additionally, the effect of nucleating agents has been investigated by the incorporation of talc. The crystalline products resulted in strong materials, with the addition of talc resulting in the introduction of crystalline regions even at low mould temperatures increasing the strength of the materials.

The multi technique approach has also been applied to a series of polyester and polyamide elastomers with a range of *cis:trans* ratios. The Young's modulus is an important characteristic of any elastomer and is affected by crystallinity which in turn is influenced by the *cis:trans* ratio. The Young's modulus for the polyesters increases with a greater *cis* content directly matching the increase in $T_{1\rho}$ times. This confirmed that an increase in crystallinity and a consequent decrease in molecular mobility increases the Young's modulus. The effect of *cis:trans* ratio on polyamides is less pronounced than for the polyesters. The molecular weight has also been investigated and found to have little difference between 'oligomers' and 'polymers'.

Finally, an additional technique, electron paramagnetic resonance (EPR) has been implemented for the analysis of coper doped calcium phosphate bioactive glasses. Copper is incorporated into bioactive glass structures as Cu^{+} and Cu^{2+}. The combination of solid state

NMR, EPR and Raman spectroscopy allows for the determination of how each of the Cu species incorporates into the bioactive glass network. Increasing the copper doping, even up to ~ 20 % copper, results in a continuous incorporation of Cu ions without saturation. There is no net depolymerisation of the bioactive glass network due to two competing processes. These are Cu^{+} forming CuO chain ends and Cu^{2+} ions forming linear arrangements causing repolymerisation. The Cu^{2+} ions can also form tetragonally distorted octahedral coordination between phosphate chains.

Abbreviations

BABA Back to Back

CPMAS Cross Polarisation magic Angle Spinning

CSA Chemical Shift Anisotropy

CT Central Transitions

DAS Dynamic angle spinning

DBU 1,8-Diazabicycloundec-7-ene

DMTA Dynamic Mechanical Thermal Analysis

DOR Double orientation

DSC Differential Scanning Calorimetry

DTA Dynamic Thermal Analysis

EFG Electric Field Gradient

EPR Electron Paramagnetic Resonance

FID Free Induction Decay

FSL Spin-Lock Frequency

FSLG Frequency Switch Lee-Goldburg

GPC Gel Permeation Chromatography

HA Hydroxyapatite

hc homocrystalline

HDT Heat Deformation Temperature

HETCOR Heteronuclear Correlation

ICP Inductively Coupled Plasma

ID Interaction Distance

IG Industrial Grade

IM Injection Moulding

MAS Magic Angle Spinning

MG Medical Grade

NMR Nuclear Magnetic Resonance

NOESY Nuclear Overhauser Effect Spectroscopy

OLLA Oligo(lactic acid)

PA Polyamide

PAS Principle Axis System

PDDF Pair-distance Distribution Function

PDLA Poly(D-Lactic acid)

PDLLA Poly(DL-Lactic acid)

PE Polyester

PLA Polylactide

PLGA poly(lactide-co-glycolide)

PLLA Poly(L-Lactic acid)

PMMA Poly(methyl methacrylate)

P(q) Form factor

R_{av} Average Radius

RF Radiofrequency

R_g Radius of Gyration

ROP Ring Opening Polymerisation

SAE Spin Alignment Echo

SAXS Small Angle X-ray Scattering

sc stereocomplex

scPLA stereocomplex Poly(lactide)

S(q) Structure Factor

SSNMR Solid State Nuclear Magnetic Resonance

ST Satellite transitions

T_1 Spin-lattice relaxation

$T_{1\rho}$ Spin-lattice relaxation in the rotating frame

T_2 Spin-spin relaxation

T_c Crystallisation Temperature

T_{CH} Cross polarisation time constant

T_g Glass Transition Temperature

T_m Melting Temperature

T_p Polymorphic Rearrangement Temperature

TGA Thermogravimetric analysis

TPE Thermoplastic Elastomer

TPPM Two Pulse Phase Modulated

TSL Spin Lock Time

WAXS Wide-Angle X-ray Scattering

XRD X-ray Diffraction

XRF X-ray Fluorescence

1.0 Introduction

1.1 Analytical Techniques for Materials

In order to carry out a robust study of a material a multi technique approach is required, whilst this is logical it is only in recent years that this approach has been used. Historically only one or two techniques are used as each area feels that their technique can fully investigate a material. However, this is not the case as every analytical method has its own advantages and limitations. There can be times when specialising in one technique can be useful however to comprehensively understand a material and additionally to make progress in science, collaboration with others is required.

In this thesis a comprehensive methodology consisting of primarily solid state nuclear magnetic resonance (NMR), X-ray diffraction (XRD), small angle X-ray scattering (SAXS), differential scanning calorimetry (DSC) and Raman spectroscopy has been implemented to understand four different systems. These four systems are the degradation of poly(lactide), the effect of injection moulding temperature on poly(lactide), the properties of elastomers and the network formation of copper doped bioactive glasses. All of the techniques used in this work have all been used extensively for studying the systems here, however historically most studies only use one or two techniques. In recent years as a consequence of understanding the need for more robust studies more techniques have been used together.

The simplest use of solid state NMR is for determination of the functional groups present in a material which allows for confirmation of the material made. This routine analysis is usually carried out using solution state NMR especially for polymers, however in the case of a material being insoluble solid state NMR is particularly useful although it is significantly more time consuming. Structural determination is accomplished using both 1D and 2D NMR, experiments on multiple nuclei showing the correlations between different nuclei, such as in this thesis carbon and protons, either through bond or through space. Whilst the chemical shift gives a good indication of what chemical species is inducing a resonance for more complex cases caused by multiple occurrences of a species, *e.g.* in a long hydrocarbon chain, 2D NMR allows for the definitive assignment of each individual group involved.

X-ray diffraction is an important tool for the characterisation of materials and is used for determining a vast amount of structural information. The most important of these include determination of the crystal structure of a material, measuring the spacings between atoms; consequently acquiring the lattice parameters and space groups for a material, determining

the orientation of a single crystal and measuring the size and shape of crystalline regions in a material. The limiting factor for X-ray diffraction is that a material must be crystalline or semi-crystalline in order to produce the diffraction pattern for analysis. In the case of biopolymers and elastomers there are no limitations as they are comprised of both crystalline and amorphous domains whereas for bioactive glasses which are commonly amorphous X-ray diffraction serves purely as a confirmation of this amorphous nature and other techniques need to be implemented instead.

The thermal properties of a material are equally important to understand and relate to the long and short range order probed by XRD and NMR, respectively. The main thermal analysis technique used in this thesis is differential scanning calorimetry, which allows for the determination of several transition temperatures. The most important of these for materials presented in this thesis, are the glass transition temperature, (T_g), melting temperature, (T_m), crystallisation temperature, (T_c) and polymorphic rearrangement temperature (T_p). In biopolymers knowledge and control of the T_g and T_m are important for tailoring the uses of the material, especially for use in high heat applications such as automotive parts. In elastomers the T_g is important to control as one of the key fundamentals of an elastomer is to exist above this transition point. T_g is also important parameter for characterising bioactive glasses as an indirect measure of network connectivity. Furthermore, it is related to glass solubility and degradation, crystallisation, and the mechanical properties. In addition to DSC, dynamic mechanical thermal analysis (DMTA) and thermogravimetric analysis (TGA) can provide further information about phases changes and thermal stability of a polymer. TGA is a vital technique to perform before injection moulding a material to be able to identify the correct temperatures used for the injection moulding process.

Raman spectroscopy is another useful diagnostic tool for understanding the chemical composition and structure of a material. Similar to NMR it benefits from little to no sample preparation and no contact with or destruction of the material. It is particularly useful for analysis of the polymer backbone configuration, microstructures and in the case of polylactide (PLA) the helical arrangement. Raman is also used in bioactive glasses for looking at the PO_2 and POP species along the phosphate chains and how these are perturbed by the addition of dopants.

The multi-technique methodology is applied to three different materials systems, two polymer systems, poly(lactide) and poly(amide)/poly(ester) elastomers and bioactive glasses. The importance of the development of biopolymers such as PLA cannot be

understated. PLA is made from the by-products of other industries such as the agricultural industry and from bacterial reactions, lactic acid, the starting material, is therefore easily available. PLA can be tailored to an immense range of products from take away coffee cups to aeronautical parts and even medical devices. The mechanical properties and the control of the degradation process of PLA are important towards determining the potential end uses. There are several ways in which the properties of PLA can be controlled, including controlling the ratio of L/D isomers which affects the crystallinity, the use of additives such as talc which enhance the strength of the PLA end product or using PLA as a copolymer such as with poly caprolactone or polyethylene glycol.

Whilst PLA is a versatile material it cannot be used in situations where elasticity is required, in these scenarios such as rubbers elastomers must be used. Elastomers have many requirements such as the existence above the glass transition temperature, possession of long flexible chains and the presence of amorphous components. The Young's modulus is the most important mechanical property for elastomers as it is the measure of elasticity. There are many factors that can affect the Young's modulus, predominantly the crystallinity of the material. The presence of crystalline domains hinders the free movement of the chains by increasing the interaction strength between adjacent chains.

Polymers have many uses including in the field of medical devices however there are many occasions where other materials are favourable, one such case is the use of bioactive glasses. Calcium phosphate bioactive glasses are able to mimic natural materials found in the body and have many therapeutic effects such antimicrobial and antibacterial properties. The application for these within the body ranges from cell transportation to muscular scaffolds and nerve conduits. Doping of bioactive glasses can help to improve the therapeutic effects, copper is a common dopant. The incorporation of copper occurs as both Cu^{+} and Cu^{2+} and can take many different arrangements. It is important to understand the arrangements that copper can take, especially Cu^{2+}, in order to develop bioactive glasses with enhanced properties.

1.2 Motivations

The motivation of this thesis is to demonstrate that a multi technique approach is required for the comprehensive analysis of materials. Whilst each individual analytical technique can provide useful information about a material this thesis aims to show that with more analytical techniques and a wider range of information on long and short range order and physical properties can provide the best analysis of a material. Each chapter has a sub aim to

show that the same techniques can be used in tandem for different materials and investigations. These sub aims are to understand the physical ageing of high-heat polylactide, correlating the molecular motion and long and short range order of injection moulded polylactide and elastomers to the thermal and mechanical properties, and to show conclusively how copper doping affects calcium phosphate bioactive glasses.

1.3 Thesis Overview

To understand some concepts in this thesis the background theory of NMR is given in Chapter 2. It covers the main NMR interactions present in the systems under investigation in this thesis.

In Chapter 3, the main methods used in this thesis are detailed. This covers the solid state NMR techniques, as well X-ray diffraction, differential scanning calorimetry, raman Spectroscopy and Electron Paramagnetic Resonance used in this thesis.

Chapter 4 details the study into the analysis of polylactide powders and the degradation of industrial grade and medical grade polylactide powders and crystals using solid state NMR, WAXS/SAXS and DSC under three storage conditions over the course of a year.

Chapter 5 continues the study of polylactide and investigates how the mechanical properties, *i.e.* tensile properties, impact resistance and HDT-B, of injection moulded polylactides are affected by the mould temperature and how this relates to the molecular mobility and structure. Neat industrial grade and medical grade polylactide and talc blended polylactide materials are compared using solid state NMR, SAXS/WAXS, DSC and Raman.

Chapter 6 is an investigation into two different novel elastomers, polyester and polyamide based, and the effect that *cis/trans* content and molecular weight play on the Young's modulus. This is related to the molecular mobility and crystallinity of the elastomers using solid state NMR, SAXS/WAXS and DSC.

Chapter 7 details the study of copper doped bioactive glasses and how copper affects the phosphate network. This is accomplished using many techniques to look at the long and short range order of the bioactive glass materials and the effect that paramagnetic Cu^{2+} has on the systems.

2. Solid State NMR Theory

Solid-state nuclear magnetic resonance is the technique that underpins all the studies undertaken within this thesis. The theory in this chapter has been based on a number of sources to provide a background into NMR theory for each section[1-6].

2.1 Spin Angular Momentum

One of the fundamental properties of the nucleus that is exploited during nuclear magnetic resonance is the spin angular momentum quantum number, *I*, this can be a positive integer or half integer.

$$I = 0, \frac{1}{2}, 1, \frac{3}{2}, 2, \ldots \tag{2.1}$$

A nucleus must have $I > 0$ in order to be NMR active, this is due to the dependency of nuclear magnetism on the magnetic moment, μ. Where $I > 0$, μ will be proportional to the angular momentum.

$$\hat{\boldsymbol{\mu}} = \gamma \hat{\boldsymbol{I}} \tag{2.2}$$

where γ is the gyromagnetic ratio, an intrinsic frequency of each isotope. The magnetic moment interacts with an external applied magnetic field and allows for the NMR experiment to be performed.

2.2 Bulk Magnetisation

Most experiments are not performed on a single isolated spin and are instead performed on a bulk amount of spins in a system. The net magnetisation (M) is considered as the sum of the vectors of the individual magnetic moments.

$$M = \sum_i \mu_i \tag{2.3}$$

In the absence of a magnetic field, all magnetic moments are randomly aligned and cancel out leading to M = 0. When a uniform static field *B*, is applied the magnetic moments in a system experience a net alignment parallel to this field. This alignment is generally small and can be given as:

$$M = \frac{N\gamma^2 BI(I+1)\hbar^2}{3kT} \tag{2.4}$$

Where N is the number of spins, ħ is the reduced Plank's constant (h/2π), k is the Boltzmann constant and T is the temperature. When I = 0 there is no net magnetisation, consequently

the nucleus is considered to be NMR inactive. The optimal conditions to acquire the strongest signal are; low temperatures, high applied magnetic field, large number of spins and a high gyromagnetic ratio.

NMR is an inherently insensitive technique, even for a high γ nucleus, such as ^{1}H an excess of only 3.2×10^{-3} % of the nuclei align with *B* and this percentage is even less for nuclei with low γ. The second limiting factor is the natural abundance of the nuclei, for example ^{13}C which is a commonly used nucleus has a natural abundance of 1.1 % resulting in a low proportion of contributing nuclei. To overcome this problem several methods to enhance μ can be employed including isotope enrichment, which is expensive, cross polarisation, which will be explained later and dynamic nuclear polarisation which is not a subject of this thesis.

2.3 External Interactions

2.3.1 Zeeman Interaction

A nucleus with a spin I has 2I+1 degenerate spin states, for example a spin half nucleus has spin quantum number, m_s = +1/2 or -1/2, when an external magnetic field is applied, $\mathbf{B}_0$, the degeneracy is broken. This is called the Zeeman interaction and is a result of the interaction of the applied magnetic field and the intrinsic magnetic moment, μ, possessed by the spin, Figure 2-2.

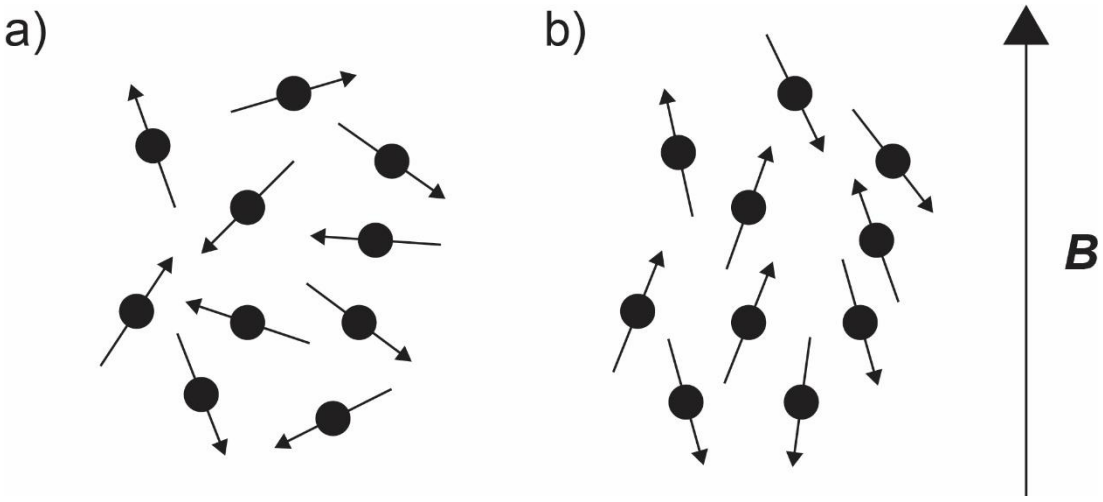

Figure 2-1. Net magnetisation for a spin system where (a) no B is applied with no net magnetisation and (b) where net magnetisation is present along B.

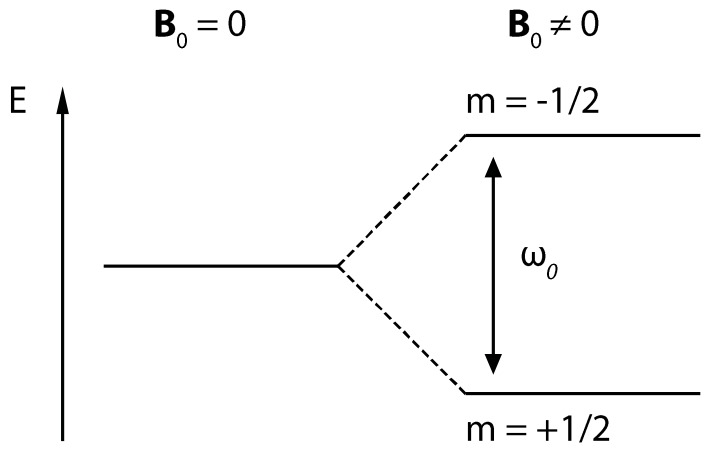

Figure 2-2. Representation of the Zeeman splitting for a nucleus with spin I = 1/2.

The Zeeman Hamiltonian, when the applied to the magnetic field is defined in the z-axis, B = (0, 0, B_0), is given by,

$$\hat{H}_Z = -\hat{\mu} \cdot \hat{B} = -\hat{\mu}_z B_0 = -\gamma \hbar \hat{I}_z B_0 \tag{2.5}$$

The energy difference between the states is equivalent to the Larmor frequency, ω_0, of the nucleus in the presence of an applied magnetic field.

$$\omega_0 = -\gamma B_0 \tag{2.6}$$

2.3.2 Frame Rotations

In order to fully understand the interactions felt by the nuclear spins in three-dimensional space, the principle axis system (PAS), the laboratory frame and the rotating frame must be introduced.

The principle axis system is where the spatial information for the interactions is diagonalized along the PAS axis,

$$A^{PAS} = \begin{pmatrix} A_{xx} & 0 & 0 \\ 0 & A_{yy} & 0 \\ 0 & 0 & A_{zz} \end{pmatrix} \tag{2.7}$$

The PAS frame is different for each interaction; therefore it is useful to rotate them into a common frame, the lab frame. When a Hamiltonian is described in spherical tensor form the spatial information can be represented as.

$$\hat{H} = C \sum_{l=0,2} \sum_{m=-l}^{l} A_{lm} \hat{T}_{l-m} \tag{2.8}$$

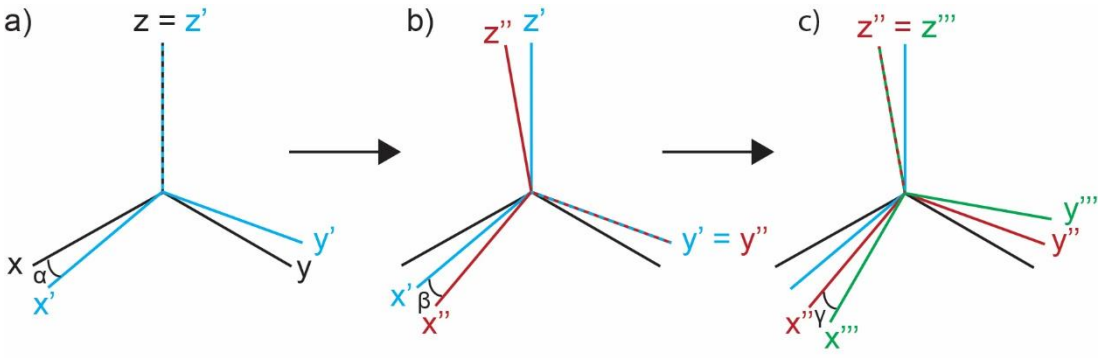

Figure 2-3. Representation of frame rotations using Euler angles (α,β,γ), from (a) the original frame (x,y,z) to (c) the final frame (x''',y''',z''').

where C is a constant based on the interaction, A is the spatial component and T is the spin tensor, A and T are represented with the limits l and m where l is the rank and m is the order of the tensors. Only the spatial term is affected under rotations.

The rotation operator $\hat{R}$ uses the Euler angles (α,β,γ) to describe the rotation between the frames.

$$\hat{R}(\alpha,\beta,\gamma) = \hat{R}_z(\alpha)\hat{R}_y(\beta)\hat{R}_z(\gamma) \tag{2.9}$$

The original frame (x, y, z) is transformed to the final frame (x''', y''', z'''). The rotation is first applied parallel to the z axis about the angle α, then along the y axis by β and the finally around the z axis by γ, a representation of this rotation is given in Figure 2-3.

The rotating frame rotates around the z axis at the frequency of the radiofrequency pulse and will be introduced further in 2.3.3.

The rotation operator can be applied to the spatial information to transform the original orientation (***A****(x,y,z)*) to the new orientation (***A****(X,Y,Z)*).

$$\boldsymbol{A}(X,Y,Z) = \boldsymbol{R}(\alpha,\beta,\gamma)\cdot\boldsymbol{A}(x,y,z)\cdot\boldsymbol{R}^{-1}(\alpha,\beta,\gamma) \tag{2.10}$$

2.3.3 Radiofrequency Pulse

Observation of NMR signal requires the application of a radiofrequency pulse to introduce an oscillating magnetic field, $B_1(t)$ and cause perturbation of equilibrium. The oscillating rf pulse has a frequency ω_{rf} and if this frequency is close to the Larmor frequency there will be a strong effect on the nuclear magnetisation. The oscillation of the rf pulse introduces a time dependence,

$$B(t) = 2B_1\cos\left(\omega_{rf}t + \phi\right) \tag{2.11}$$

where ϕ is the phase of the rf pulse. The interaction between the rf magnetic field and the nuclear spin is analogous to the Zeeman interaction with the addition of time dependence. The rf pulse is generally applied along x, the Hamiltonian for this, $\hat{H}_{rf}$, becomes:

$$\hat{H}_{rf} = -2\gamma\hbar\hat{I}_x B_1 \cos(\omega_{rf} + \phi) \tag{2.12}$$

The external spin Hamiltonian, $\hat{H}_{ext}$, is a combination of $\hat{H}_z$ and $\hat{H}_{rf}$ when the oscillating field is introduced in the presence of an applied magnetic field B_0

$$\hat{H}_{ext} = \hat{H}_z + \hat{H}_{rf} = \hbar\omega_0\hat{I}_z + 2\hbar\omega_1\hat{I}_x \cos(\omega_{rf}t + \phi) \tag{2.13}$$

Where ω_1 is the nutation frequency of the applied rf pulse.

It is convenient to transform this interaction into the rotating frame which offers a classical viewpoint to the applied rf system. The resonant part of the rf field is rotating at ω_{rf} with respect to the lab frame. In the rotating frame ω_{rf} is around B_0 and the rf field B_1 appears static and the x-y plane rotates around it.

This transformation removes the time dependence of $\hat{H}_{ext}$, consequently the Hamiltonian becomes

$$\hat{H}_{ext}^{rot} = -\hbar\left((\omega_o - \omega_{rf})\hat{I}_z + 2\omega_1\hat{I}_x\right) \tag{2.14}$$

The term $-\hbar(\omega_0-\omega_{rf})$ represents the magnetisation in the z direction and when $\omega_{rf} \approx \omega_0$ the Hamiltonian becomes

$$\hat{H}_{ext}^{rot} = -2\hbar\omega_1\hat{I}_x \tag{2.15}$$

resulting in the magnetisation precessing around the x-axis. This precession is called nutation with the frequency of nutation ω_{nut} given by

$$\omega_{nut} = -\gamma B_1 \tag{2.16}$$

The magnetisation is nutated by the angle θ_{nut}, the flip angle during the time τ_1

$$\theta_{nut} = \omega_1\tau_1 \tag{2.17}$$

A flip angle of 90° ($\pi/2$) transfers magnetisation so that it becomes aligned in the $-\hat{i}_y$ direction. When the B_1 field is removed, the magnetisation will return to equilibrium via relaxation processes (see Section 3.1.1). The precession back to equilibrium around B_0 can be measured and forms the basis of the NMR experiment and is called free induction decay (FID).

2.4 Internal Interactions

External interactions, *i.e.* the Zeeman interaction and the rf pulse are not the only interactions to consider in an NMR experiment. There are multiple internal interactions which allow for elucidation of the nuclear environment. These interactions are contained in the nuclear spin Hamiltonian.

$$\widehat{H} = \widehat{H}_Z + \widehat{H}_{CS} + \widehat{H}_J + \widehat{H}_D + \widehat{H}_Q + \widehat{H}_k + \cdots \tag{2.18}$$

The above interactions include the Zeeman interaction ($\hat{H}_Z$, Chapter 2.3.1), the chemical shielding interaction ($\hat{H}_{CS}$, Chapter 2.5.1), the indirect dipole interaction ($\hat{H}_J$, Chapter 2.5.3), the dipolar interaction ($\hat{H}_D$, Chapter 2.5.2), the quadrupolar interaction ($\hat{H}_Q$, Chapter 2.3.5), and the Knight shift ($\hat{H}_K$) which will not be discussed due to their limited relevance. The paramagnetic interaction will also be discussed ($\hat{H}_P$,Chapter 2.3.4). The relative strength of the internal interactions to the Zeeman interaction allow them to be treated as perturbations to the Zeeman Hamiltonian. In solids the strength of the interactions generally follows a hierarchy

$$\widehat{H}_Z > \widehat{H}_Q > \widehat{H}_K > \widehat{H}_{CS} > \widehat{H}_D > \widehat{H}_J \tag{2.19}$$

2.5.1 Chemical Shielding

Chemical shift goes hand in hand with chemical shielding. The electrons in a molecule magnetically shield the nuclei in a molecule when placed in a magnetic field. This shielding leads to the chemical shift which is different for each electronic environment allowing for the determination of the structure of a molecule. The chemical shift is comprised of the diamagnetic contribution and the paramagnetic contribution. When the external magnetic field, $\mathbf{B}_0$ is applied the electrons circulate and induce a secondary magnetic field, the induced field, this is the diamagnetic contribution. The electron distribution is distorted by the applied magnetic field, this distortion can be explained by the mixing of excited and ground state electrons. Paramagnetism can be induced by the excited electron states, this in turn creates a field which supports the applied field consequently deshielding the nucleus and is further explained in Chapter 2.5.4. The chemical shielding Hamiltonian is described using the chemical shielding tensor σ as:

$$\widehat{H}_{CS} = \gamma\hbar\hat{\boldsymbol{I}} \cdot \boldsymbol{\sigma} \cdot \boldsymbol{B}_0 \tag{2.20}$$

Chemical shielding is a second rank tensor and can be defined in the PAS frame by

$$\sigma^{PAS} = \begin{pmatrix} \sigma_{xx} & 0 & 0 \\ 0 & \sigma_{yy} & 0 \\ 0 & 0 & \sigma_{zz} \end{pmatrix} \tag{2.21}$$

where

$$|\sigma_{ZZ} - \sigma_{iso}| \geq |\sigma_{XX} - \sigma_{iso}| \geq |\sigma_{YY} - \sigma_{iso}| \tag{2.22}$$

and

$$\sigma_{iso} = \frac{\sigma_{XX} + \sigma_{YY} + \sigma_{ZZ}}{3} \tag{2.23}$$

The chemical shielding tensor in the PAS frame can be rotated using equation 2.10 to the lab frame

$$\sigma^{PAS} = \begin{pmatrix} \sigma_{XX} & \sigma_{XY} & \sigma_{XZ} \\ \sigma_{YX} & \sigma_{YY} & \sigma_{YZ} \\ \sigma_{ZX} & \sigma_{ZY} & \sigma_{ZZ} \end{pmatrix} \tag{2.24}$$

Capital subscripts are used in the lab frame to distinguish them from the PAS frame.

When the main field and shielding are included the induced magnetic field (B^{ind} can be represented by

$$B^{ind} = (1 - \sigma) \cdot B_0 = \begin{pmatrix} 1 - \sigma_{XX} & -\sigma_{XY} & -\sigma_{XZ} \\ -\sigma_{YX} & 1 - \sigma_{YY} & -\sigma_{YZ} \\ -\sigma_{ZX} & -\sigma_{ZY} & 1 - \sigma_{ZZ} \end{pmatrix} \begin{pmatrix} 0 \\ 0 \\ B_0 \end{pmatrix} = \begin{pmatrix} -\sigma_{XZ} B_0 \\ -\sigma_{YZ} B_0 \\ (1 - \sigma_{ZZ}) B_0 \end{pmatrix} \tag{2.25}$$

Only the zz component is of interest, which is aligned with B_o. The terms σ_{xz} and σ_{yz} are second order contributions and can be neglected. The chemical shielding Hamiltonian becomes

$$\hat{H}_{CS} = \gamma \hbar \hat{I} \cdot \sigma_{ZZ} \cdot B_0 \tag{2.26}$$

The tensor element for σ_{ZZ} is obtained by applying the rotations from the PAS to the LAB frame

$$\sigma_{ZZ} = \sigma_{iso} + \frac{\Delta\sigma}{2}[(3cos^2\theta - 1) + \eta(sin^2\theta cos2\phi)] \tag{2.27}$$

Where

$$\Delta\sigma = \sigma_{ZZ} - \sigma_{iso} \tag{2.28}$$

And

$$\eta = \frac{\sigma_{XX} - \sigma_{YY}}{\Delta\sigma} \tag{2.29}$$

where θ and ϕ are the polar angles of the LAB frame in the PAS of the tensor. Δσ is called the shielding anisotropy and η is the asymmetry. The three components of the shielding tensor; isotropic shielding value, σ_{iso} (equation 2.23), shielding anisotropy (equation 2.28) and asymmetry (equation 2.29), reflect the local symmetry in the nuclear environment. The Haeberlen convention uses these terms to describe the chemical shielding interactions.

For a single crystal placed in a magnetic field, all identical nuclei will have the same orientation with respect to B_0. This will produce a single peak in the NMR spectrum, the shift will be dependent on θ and ϕ relative to B_0. In a powder sample all possible orientations of θ and ϕ, in this case a broad line will be formed of the different overlapping crystallite orientations, Figure 2-4. The line shape will be dependent on Δσ and η.

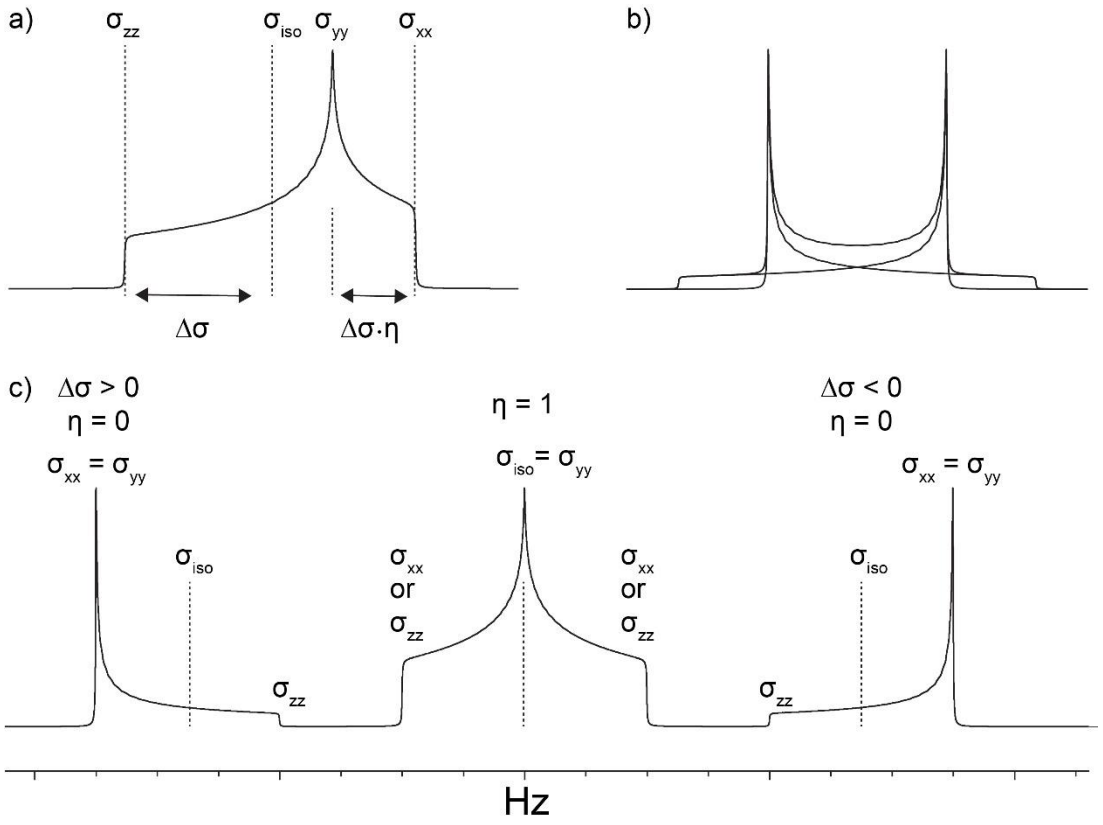

Figure 2-4. The a) typical chemical shift anisotropy (CSA) line shape with shielding parameters, b) Pake doublet for a powder pattern under dipolar coupling and c) the CSA line shapes for various symmetries with respect to B_0.

The isotropic chemical shift, δ_{iso} is used instead of σ_{iso} experimentally to measure shift, this normalises the shielding of a sample to that of a known reference sample

$$\delta_{iso} = \frac{\omega - \omega_{ref}}{\omega_{ref}} \times 10^6 = \frac{\sigma_{ref} - \sigma_{iso}}{1 - \sigma_{ref}} \tag{2.30}$$

where, ω is the spectral frequency, ω_{ref} is the reference frequency, σ is the shielding tensor and σ_{ref} is the standard resonance. The isotropic chemical shift is given in parts per million (ppm) and is field independent which allows for easy comparisons.

2.5.2 The Dipolar Interaction

The dipolar interaction is a through space interaction between the magnetic moments of two nuclear spins. Classically the interaction of the magnetic dipoles, μ_1 and μ_2 is given by,

$$E_D = \frac{\mu_0}{4\pi}\left(\frac{\mu_1 \cdot \mu_2}{r^3} - 3\frac{(\mu_1 \cdot r)(\mu_2 \cdot r)}{r^4}\right) \tag{2.31}$$

where r is the distance between the two spins.

The Hamiltonian is generated by substituting the magnetic moment operator $\hat{\boldsymbol{\mu}}$ into equation 2.31, for two spins I and S the Hamiltonian becomes

$$\begin{aligned} \hat{H}_D &= -\frac{\mu_0}{4\pi}\frac{\gamma_I \gamma_S \hbar}{r^3}\left(I \cdot S - 3\left(\frac{(I \cdot r)(S \cdot r)}{r^2}\right)\right) \\ &= -\frac{\mu_0}{4\pi}\frac{\gamma_I \gamma_S \hbar}{r^3} f\left(\hat{I}_z, \hat{S}_z\right)\frac{(3\cos^2\beta - 1)}{2} \end{aligned} \tag{2.32}$$

where β is the angle between the vector joining the two spins and B_0. The strength of the dipolar interaction is dependent upon the distance between spins, r and their gyromagnetic ratios, γ.

The dipolar interaction alters the resonance frequency of both spins and is orientation dependent. In an isolated system the distribution results in a pair of characteristic powder patterns which overlap to form a Pake doublet (Figure 2-4 (c)) however in a complex system the pattern is broadened into a Gaussian/Lorentzian peak.

2.5.3 Indirect Dipole-Dipole Interaction

The indirect dipole-dipole interaction is also called spin-spin, scalar or J-coupling. This is an indirect interaction between two nuclei that is influenced by the electrons in the chemical bonds between nuclei, as such it is a through bond interaction. The electrons surrounding

the first nucleus are perturbed by the nucleus, this results in an additional magnetic field at the second nucleus.

For the coupling of two spins $\hat{I}_j$ and $\hat{I}_k$ the indirect dipole-dipole Hamiltonian is

$$\hat{H}_J = 2\pi J_{jk} \hat{I}_j \cdot \hat{I}_k \tag{2.33}$$

The second rank j-coupling tensor (J_{jk}) is given in Hz which results in the factor of 2π, additionally there is no dependence upon B_0. In liquids J_{jk} is an isotropic interaction consequently it is equal to the average of the diagonal tensor elements

$$J_{jk} = \frac{1}{3}\left(J_{xx}^{jk} + J_{yy}^{jk} + J_{zz}^{jk}\right) \tag{2.34}$$

In solids the indirect dipole-dipole interaction is not isotropic, there are three contributing sources, spin-orbital, spin-dipolar and Fermi contact interactions. The main contribution is from the Fermi contact interaction, in diamagnetic solids this interaction is small and is obscured by larger interactions. The contribution from the Fermi contact interaction is larger for paramagnetic materials and will be discussed in Section 2.5.4.

2.5.4 Paramagnetic Interaction

The presence of unpaired electrons in a material results in additional magnetic field at the nucleus. A material with unpaired electrons is paramagnetic and has a positive magnetic susceptibility (χ).

The Hamiltonian for the interaction between the nucleus and electron is described by two interactions, the through bond or Fermi contact interaction, $\hat{H}^C$, and the through space or electron-nuclear dipolar interaction, $\hat{H}^D$.

$$\hat{H}_p = \hat{H}^C + \hat{H}^D \tag{2.35}$$

The isotropic chemical shift is a combination of the diamagnetic shift, $\delta^{diamagnetic}$, and the hyperfine shift, $\delta^{hyperfine}$.

$$\delta^{measured} = \delta^{diamagnetic} + \delta^{hyperfine} \tag{2.36}$$

where

$$\delta^{hyperfine} = \delta^{contact} + \delta^{dipolar} \tag{2.37}$$

Where $\delta^{contact}$ is the Fermi contact contribution and $\delta^{dipolar}$ is the electron-nuclear dipole interaction.

The diamagnetic shift is the shift if there were no unpaired electrons in the material. The hyperfine shift derives from the interaction between the unpaired electron and nuclear spin. To understand this relationship the contribution from the magnetic susceptibility must be understood. The magnetisation per unit volume M of a group of spins in an external magnetic field is given by:

$$M = \frac{\mu_{ind}}{V} = \frac{1}{\mu_0}\chi v B_0 \tag{2.38}$$

where χv is the magnetic susceptibility per unit volume and μ_0 is the magnetic constant. The magnetic susceptibility can be calculated per mole χM

$$\chi M = V_M \chi v = V_M \frac{\mu_0 M}{B_0} \tag{2.39}$$

where V_M is the molar volume. Using Avogadro's constant, the magnetic susceptibility per molecule χ is determined by

$$\chi = \frac{\chi M}{N_A} \tag{2.40}$$

From equation 2.38 μ_{ind} can be defined as:

$$\mu_{ind} = \frac{N_A \langle \mu \rangle V}{V_M} \tag{2.41}$$

Combining equation 2.38 and 2.41, χ can be expressed as:

$$\chi = \frac{\mu_0 \langle \mu \rangle}{B_0} \tag{2.42}$$

Where $<\mu>$ is the average induced magnetic moment per particle.

The dynamics of the electron spin are several orders of magnitude faster than the NMR timescale. The electron spin is consequently averaged over several Zeeman states resulting in the Curie spin $<S_z>$

$$\langle S_z \rangle = \frac{\sum_{M_S} M_S \left\{ \frac{-g_e \mu_B M_S B_0}{k_B T} \right\}}{\sum_{M_S} \left\{ \frac{-g_e \mu_B M_S B_0}{k_B T} \right\}}$$
$$\langle S_{\pm} \rangle = 0 \tag{2.43}$$

With the high temperature approximation this simplifies to

$$\langle S_z \rangle = -\frac{g_e \mu_B B_0}{3k_B T} S(S+1) \tag{2.44}$$

The induced magnetic moment per particle is proportional to the Curie spin

$$\langle \mu \rangle = -\mu g_e \langle S_z \rangle \tag{2.45}$$

The Curie moment can consequently be determined

$$\langle \mu_S \rangle = \frac{g_e^2 \mu_B^2 S(S+1)}{3k_B T} B_0 \tag{2.46}$$

Combining equation 2.42 for the magnetic susceptibility and 2.46 the Curie moment can be expressed in terms of isotropic magnetic susceptibility

$$\chi_{iso} = \mu_0 \frac{g_e^2 \mu_B^2 S(S+1)}{3k_B T} \tag{2.47}$$

and in terms of the Curie spin

$$\langle S \rangle = \langle S_z \rangle = -\frac{\chi_{iso}}{\mu_0 \mu_B g_e} B_0 \,. \tag{2.48}$$

The Hamiltonian for the through bond coupling between the nucleus I and the electron S is proportional to the s orbital for the atom containing the spin I

$$\hat{H}^C = A\chi \cdot \hat{I} \tag{2.49}$$

where the through bond coupling of the nucleus to the average electron spin is defined by the hyperfine Fermi constant A is

$$A = \frac{\mu_0}{3S} \hbar g_e \mu_B \gamma_I \rho_s \tag{2.50}$$

Where γ_I is the nuclear gyromagnetic ratio and g_e the electron g-value represents the gyromagnetic ratio and magnetic moment of the electron and ρ_s is the spin density at the nucleus, described by the sum of *i* of the spin density for the *i*th nuclear orbitals

$$\rho_s = \sum_i [|\psi_i^-(0)|^2 - |\psi_i^+(0)|^2] \tag{2.51}$$

with the positive $|\Psi_i^-(0)|^2$ and negative $|\Psi_i^+(0)|^2$ spin densities.

The energy of the contact interaction needs to be related to the size and strength of the magnetic field to determine the shift contribution of the Fermi contact δ^{contact} to the hyperfine shift $\delta^{\text{hyperfine}}$.

$$\delta^{contact} = \frac{E_{contact}}{\gamma_I \hbar I_z B_0} \tag{2.52}$$

Where $E_{contact}$ is the energy for this isotropic hyperfine coupling

$$E_{contact} = A I_z \langle S_z \rangle \tag{2.53}$$

Substituting the Curie spin, equation 2.48, and the isotropic magnetic susceptibility, equation 2.47, the Fermi contact interaction becomes

$$\delta^{contact} = A \frac{g_e \mu_B S(S+1)}{3\gamma_I \hbar k_B T} \tag{2.54}$$

The inverse relationship to temperature comes from the Fermi contact interaction. In the case where the electronic field at the paramagnetic nucleus is anisotropic, the g factor is represented by the components, parallel, $g_{\parallel}$ and perpendicular, $g_{\perp}$. The g factor now becomes,

$$g = \frac{1}{3}(g_{\parallel} + 2g_{\perp})\,. \tag{2.55}$$

The magnetic susceptibility will now have an orientation dependence, the average induced magnetic field becomes,

$$\langle \hat{\mu} \rangle = \frac{\hat{\chi}\hat{B}_0}{\mu_0}\,. \tag{2.56}$$

The electron nuclear interaction Hamiltonian ($\hat{H}^D$) can be described as analogous to the dipolar interaction. There are however a few differences between the nuclear-nuclear and electron nuclear interaction. An approximation must be made for the distance between the electron and nucleus by taking the distance between the nucleus and the metal centre, r. The approximation allows for the fractional electron density covered by the Fermi contact shift to be ignored. The dipolar Hamiltonian $\hat{H}_d$ can be expressed in terms of the electron nuclear interaction by taking the magnetic moment of the electron $\hat{\mu}$ as the averaged induced electron magnetic moment $\langle \hat{\mu} \rangle$ in the magnetic field.

$$\widehat{H}^D = -\frac{\mu_0}{4\pi}\left[\frac{3\left(\hbar\gamma \hat{I}\cdot r\right)(\langle \hat{\mu} \rangle \cdot r)}{r^5} - \frac{\hbar\gamma \hat{I}\langle \hat{\mu} \rangle}{r^3}\right] \tag{2.57}$$

The Hamiltonian can be rewritten using equation 2.39 and 2.55 and $\hat{I} = \hat{I}_{\kappa}\kappa$, where κ is the external magnetic field along which direction the nucleus is quantized.

$$\widehat{H}^D = -\frac{\hbar\gamma I B_0}{4\pi r^5}\hat{I}_{\kappa}\kappa \cdot [3r(r\cdot\chi) - r^2\chi]\cdot\kappa \tag{2.58}$$

A second rank magnetic susceptibility tensor σ_p can be defined as,

$$\sigma_p = 3r(r \cdot \chi) - r^2\chi \tag{2.59}$$

The electron nuclear Hamiltonian becomes,

$$\hat{H}^D = -\frac{\hbar\gamma I}{4\pi r^5}\hat{\boldsymbol{I}} \cdot \boldsymbol{\sigma}_p \cdot \boldsymbol{B} \tag{2.60}$$

which has a similarity to the chemical shielding Hamiltonian

$$\hat{H}_{CS} = \gamma\hat{\boldsymbol{I}} \cdot \boldsymbol{\sigma} \cdot \boldsymbol{B} \tag{2.61}$$

As with CSA the paramagnetic interaction scales linearly with magnetic field.

2.5.5 Quadrupolar Interaction

The majority of NMR active nuclei have a spin I > ½, these nuclei are considered as quadrupolar nuclei. For these nuclei, a non-spherical charge distribution is observed around the nucleus, this gives rise to the electric quadrupole moment (eQ), a fundamental property of each quadrupolar nuclei. The quadrupolar interaction describes the coupling of the electric quadrupole moment with the electric field gradient (EFG) around the nucleus.

The strength of the quadrupolar interaction is proportional to the size of the EFG which is dependent upon the environment around the nucleus, therefore the interaction can vary from zero to several MHz in size. The size of the electric quadrupole moment in many cases results in the quadrupolar interaction dominating the other internal interactions. In solid state NMR where anisotropy is not averaged out by motional averaging, as is the case in solution NMR, the quadrupolar interaction results in large anisotropic components of the interaction.

The electric field gradient is described by a second-rank diagonal tensor $\boldsymbol{V}$, in the principle axis system,

$$\boldsymbol{V} = \begin{bmatrix} V_{XX} & 0 & 0 \\ 0 & V_{YY} & 0 \\ 0 & 0 & V_{ZZ} \end{bmatrix} \tag{2.62}$$

Where $V_{XX} + V_{YY} + V_{ZZ} = 0$ and by convention $|V_{XX}| \geq |V_{YY}| \geq |V_{ZZ}|$. The EFG can be described by two independent parameters,

$$eq = V_{ZZ} \tag{2.63}$$

And

$$\eta_Q = \frac{V_{XX} - V_{YY}}{V_{ZZ}} \tag{2.64}$$

The Hamiltonian in the PAS arising from the EFG tensor is,

$$\hat{H}_Q = \frac{eQ}{2I(2I-1)\hbar}\hat{\boldsymbol{I}}\cdot\boldsymbol{V}\cdot\hat{\boldsymbol{I}} = \frac{e^2qQ}{4I(2I-1)\hbar}\left[3\hat{I}_z^2 - I(I+1) + \eta\left(\hat{I}_x^2 - \hat{I}_y^2\right)\right] \tag{2.65}$$

Assuming the system is in a high field regime, $\hat{H}_Q$ can be treated as first $\hat{H}_Q^1$ and second $\hat{H}_Q^2$ order perturbations of the Zeeman interaction. The derivation is described in full in the literature, the theory in this chapter is taken from the report by Man[7] and can be used for further embellishment. The first and second order quadrupolar Hamiltonians are given by,

$$\hat{H}_Q^1 = \frac{e^2qQ}{4I(2I-1)\hbar}\left[3\hat{I}_z^2 - I(I+1)\right]\left[\frac{(3\cos^2\beta - 1) + \eta_Q\sin^2\beta\cos 2\alpha}{2}\right] \tag{2.66}$$

And

$$\hat{H}_Q^2 = -\frac{1}{\omega_0}\left[\frac{eQ}{4I(2I-1)\hbar}\right]^2\begin{Bmatrix} f(\alpha,\beta,\eta_Q)\hat{I}_z\left[4I(I+1) - 8\hat{I}_z^2 - 1\right] + \\ 2f'(\alpha,\beta,\eta_Q)\hat{I}_z\left[2I(I+1) - 2\hat{I}_z^2 - 1\right]\end{Bmatrix} \tag{2.67}$$

Where

$$f(\alpha,\beta,\eta_Q) = -\frac{3}{2}e^2q^2\begin{bmatrix} \left(-\frac{1}{3}{\eta_Q}^2\cos^2 2\alpha + 2\eta_Q\cos 2\alpha - 3\right)\cos^4\beta + \\ \left(\frac{2}{3}{\eta_Q}^2\cos^2 2\alpha + 2\eta_Q\cos 2\alpha - \frac{1}{3}{\eta_Q}^2 + 3\right)\cos^2\beta \\ +\frac{1}{3}{\eta_Q}^2(1-\cos^2 2\alpha)\end{bmatrix} \tag{2.68}$$

And

$$f'^{(\alpha,\beta,\eta_Q)} = -\frac{3}{2}e^2q^2\begin{bmatrix} \left(\frac{1}{24}{\eta_Q}^2\cos^2 2\alpha - \frac{1}{4}\eta_Q\cos 2\alpha + \frac{3}{8}\right)\cos^4\beta + \\ \left(-\frac{1}{12}{\eta_Q}^2\cos^2 2\alpha + \frac{1}{6}{\eta_Q}^2 - \frac{3}{4}\right)\cos^2\beta \\ +\left(\frac{1}{24}{\eta_Q}^2\cos^2 2\alpha - \frac{1}{4}\eta_Q\cos 2\alpha + \frac{3}{8}\right)\end{bmatrix} \tag{2.69}$$

The first and second order quadrupolar interactions shift the spin energy levels which results in a change in the resonance frequency. For the single transitions the shift for the first order interaction is given by,

$$\omega_{m-1,m}^1 = \langle m-1|\hat{H}_Q^1|m-1\rangle - \langle m|\hat{H}_Q^1|m\rangle =$$

$$\frac{3e^2qQ}{4I(2I-1)\hbar}\left[\frac{\left((3\cos^2\beta - 1) + \eta\sin^2\beta\cos 2\alpha\right)^*}{2}\right](1-2m) \tag{2.70}$$

And for the second order interaction,

$$\omega_{m-1,m}^{2} = \langle m-1|\hat{H}_Q^2|m-1\rangle - \langle m|\hat{H}_Q^2|m\rangle =$$

$$-\frac{1}{\omega_0}\left[\frac{eQ}{4I(2I-1)\hbar}\right]^2 \begin{pmatrix} f(\alpha,\beta,\eta_q)[24m(m-1)-4I(I+1)+9]+ \\ f'^{(\alpha,\beta,\eta_q)[12m(m-1)-4I(I+1)+6]} \end{pmatrix} \tag{2.71}$$

For simplicity, the quadrupole coupling constant, C_Q, and the quadrupolar frequency, ω_Q, are often used, where

$$C_Q = \frac{e^2qQ}{\hbar} \tag{2.72}$$

And

$$\omega_Q = \frac{3C_Q}{4I(2I-1)} \tag{2.73}$$

The effect that C_Q, η_Q and *I* have on the static lineshape are demonstrated in Figure 2-5 The first order interaction creates 2I+1 energy levels with 2I transitions which results in a multiplet from the central transition (CT) (m=1/2) and the satellite transitions (ST). The first order transition frequencies are dependent on the Euler angles α and β, therefore the first quadrupolar interaction produces a powder pattern. The number of peaks is dependent upon the nuclear spin I and the shape depend on the asymmetry parameter η_Q.

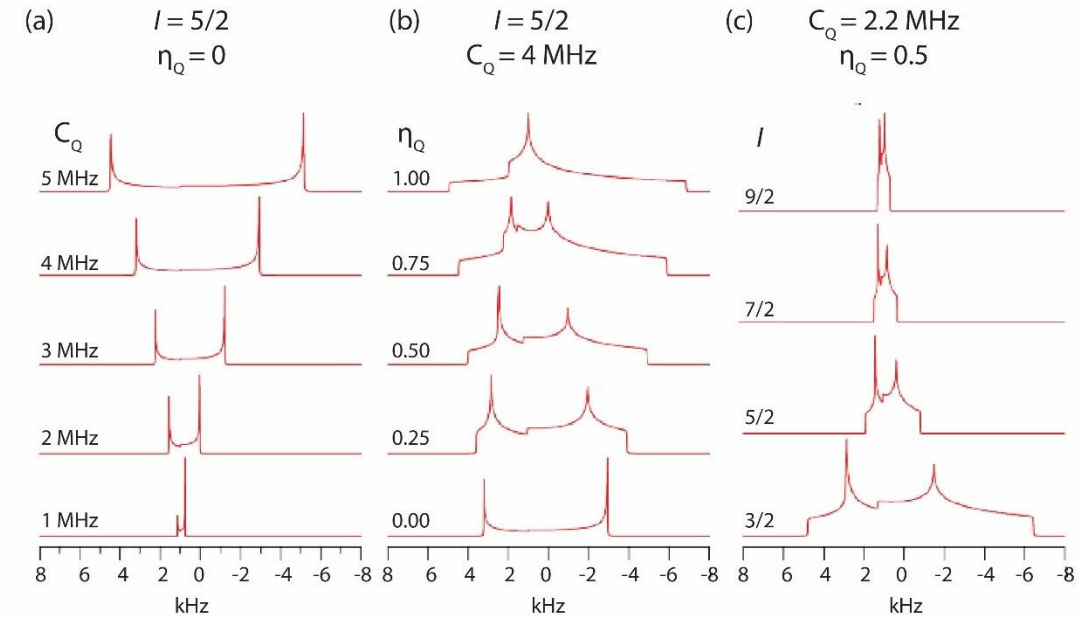

Figure 2-5. A representation of the quadrupolar lineshape when (a) C_q, (b) η_Q and (c) *I*, are varied.

The central transition is unaffected by the first order shift, whereas the second order quadrupolar interaction affects all the transitions, due to this most quadrupolar NMR focuses on the central transition. The wide frequency range of the first order quadrupole pattern makes it difficult to completely observe. The second order quadrupole shift at the CT is given be m=1/2 in equation 2.69,

$$\omega^2_{-\frac{1}{2},\frac{1}{2}} = -\frac{1}{6\omega_0}\left[\frac{3C_q}{2I(2I-1)}\right]^2\left[I(I+1)-\frac{3}{4}\right]\begin{bmatrix} A(\alpha,\eta_Q)\cos^4\beta \\ +B(\alpha,\eta_Q)\cos^2\beta + C(\alpha,\eta_Q)\end{bmatrix} \qquad (2.74)$$

$$A(\alpha,\eta) = -\frac{27}{8}+\frac{9}{4}\eta_Q\cos 2\alpha - \frac{3}{8}{\eta_Q}^2\cos^2 2\alpha$$

$$B(\alpha,\eta) = \frac{30}{8}-\frac{1}{2}{\eta_Q}^2 - 2\eta_Q\cos 2\alpha + \frac{3}{4}{\eta_Q}^2\cos^2 2\alpha$$

$$C(\alpha,\eta) = -\frac{3}{8}+\frac{1}{3}{\eta_Q}^2 - \frac{1}{4}\eta_Q\cos 2\alpha - \frac{3}{8}{\eta_Q}^2\cos^2 2\alpha$$

The second order shift at the central transition is orientation dependent, the breadth of the CT, determined from equation 2.72, is given by,

$$\Delta\left(\omega^2_{-\frac{1}{2},\frac{1}{2}}\right) = \frac{25+22\eta_Q+{\eta_Q}^2}{144}\left(\frac{{\omega_Q}^2}{\omega_0}\right)\left[I(I+1)-\frac{3}{4}\right] \qquad (2.75)$$

2.5 Magic Angle Spinning

Solid state NMR suffers from the lack of isotropic tumbling of molecules which, in solution state NMR averages out the molecular orientations. The averaging of the molecular orientations narrows the resonances therefore the line shapes do not present as a powder pattern (Figure 2-4 (b)). In simple systems it is possible to analyse the broadened line shapes and powder patterns however in a system with many chemically inequivalent sites it will not be possible to distinguish any spectral features and determine information about the system. Magic angle spinning (MAS), developed by Andrew, Bradbury and Eaves[8] and separately by Lowe,[9] is used in solid state NMR to average the molecular orientations and reduce the effect of CSA. This is achieved by rapid mechanical rotation of the sample, with speeds of up to 110 kHz now being achievable.

To describe the interaction under MAS frame rotation from the PAS frame to the Lab frame via the rotor frame, this is described in full by Mackenzie and Smith.[2] The Hamiltonian becomes time-dependent due to the rotation and is consequently split into time-dependent and time-independent parts. The time-dependent component is averaged by MAS and the time-independent component is a version of the static Hamiltonian. When described by a

rank two tensor the anisotropic component acquires a modulation factor. The modulation factor is equal to the second order Legendre polynomial,

$$P_1(cos\theta) = 3cos^2\theta - 1 \tag{2.76}$$

Under MAS applied at an angle θ_r the average of the orientation dependence becomes:

$$\langle\frac{1}{2}(3cos^2\theta - 1)\rangle = \frac{1}{2}3 = (3cos^2\theta_r - 1) \times \frac{1}{2}(3cos^2\beta - 1) \tag{2.77}$$

Where θ is the angle between the applied field and the principal z-axis, β is the angle between the principal z-axis and the spinning axis and θ_r is the magic angle. If θ_r is set to 54.74°,the Legendre polynomial ($3\cos^2\theta_r - 1$)=0, this reduces the anisotropic first order components to zero. For this to hold true the MAS speed (ω_r) must be greater than the anisotropy in Hz. When the anisotropy is equal to or greater than the ω_r the time dependent component will not be completely averaged out. The time modulation produces spinning sidebands at integer values of ω_r away from the isotropic shift. A greater ω_r will shift the sidebands further from the isotropic shift and they will become weaker.

Magic angle spinning only removes the first order components of the interactions, higher order effects have a dependence on the fourth order Legendre polynomial

$$P_4(cos\theta) = 35cos^4\theta - 30cos^2\theta + 3 \tag{2.78}$$

There are two solutions to $P_4(\cos\theta) = 0$, these are 30.6° and 70.1°, spinning at one of these angles will remove a large proportion of the second order quadrupolar interaction. In order to simultaneously remove the 2nd and 4th order Legendre polynomials, techniques such as double rotation (DOR) and dynamic angle spinning (DAS) are employed to spin at both the magic angle and one of the second order quadrupolar angles. These experiments will not be covered in this work as the quadrupolar interaction is not observed in the systems studied here.

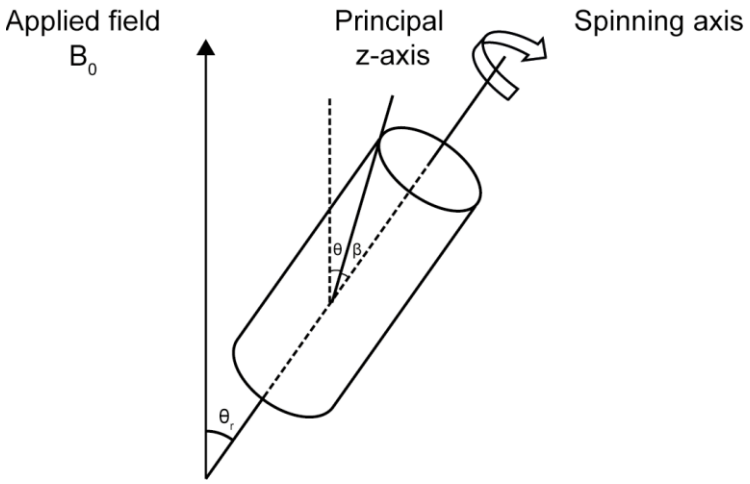

Figure 2-6. A representation of the rotation of a sample relative to B_0 in a MAS experiment, θ is the original rotation between the PAS and LAB frames, θ_r is the rotation between the LAB and MAS frames and β is the rotation from the PAS to the MAS.

3. Experimental Methods

3.1 NMR Spectroscopy

3.1.1 Relaxation

After the application of the rf pulse (section 2.3.3) the bulk magnetisation reverts to thermodynamic equilibrium via relaxation processes. There are two key relaxation processes, spin-lattice relaxation also called longitudinal relaxation, T_1, (section 3.1.1.1) and spin-spin relaxation also called transverse relaxation, T_2 (section 3.1.1.2). An additional relaxation process will be discussed, Spin-lattice relaxation in the rotating frame, $T_{1\rho}$ (section 3.1.1.3). The different relaxation processes occur on different timescales and therefore can provide different information on a system. In this thesis $T_{1\rho}$ relaxation is used to probe the molecular mobility of polymer chains at the kHz time scale.

3.1.1.1 Longitudinal Relaxation

The spin-lattice relaxation is governed by the interaction between the spin and the lattice, it is the time required for the bulk magnetisation to return to equilibrium along the z-axis. The time dependence of the z magnetisation (M_z) is described in the Bloch-equations

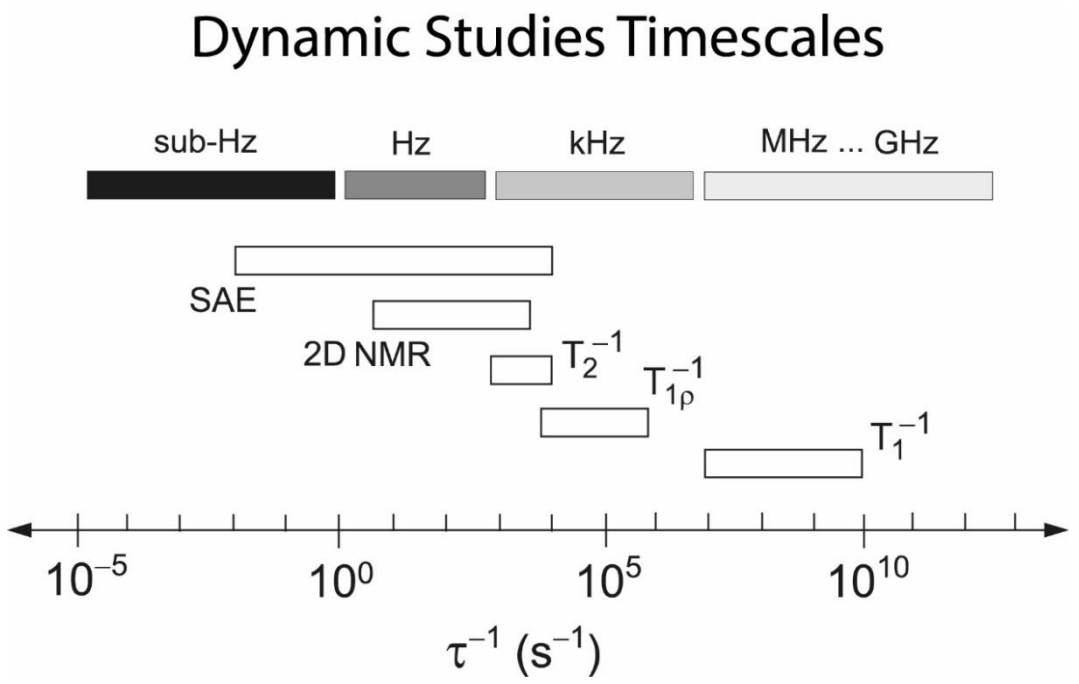

Figure 3-1. The relaxation timescales adapted from Wilkengin and Heitjans [10] where SAE is the spin alignment echo

$$\frac{dM_z}{dt} = \frac{M_0 - M_z}{T_1} \tag{3.1}$$

Where M_0 is the magnetisation at thermal equilibrium. For a sample in a magnetic field with no initial magnetisation, the magnetisation aligned with the magnetic field has an exponential build up

$$M_z(t) = M_0\left(1 - e^{\frac{-t}{T_1}}\right) \tag{3.2}$$

where T_1 is the rate constant. The length of T_1 depends on the nuclei and system studied due to the difference in local interaction strengths around the nucleus of interest. This causes transitions between the Zeeman energy levels and a change in the bulk magnetisation, the frequency of these transitions is dependent upon the strength of the interactions and amount of fluctuations at ω_0. The spin-lattice relaxation time is also dependent upon temperature, heating a sample increases the frequency of the fluctuations and reduce the T_1. There is also a field-dependence of the T_1 time as the Larmor frequency, ω_0 is proportional to the field B_0. For spin ½ systems the dipolar interaction is most prominent relaxation mechanism this is also the case where the quadrupolar interaction is small. For many quadrupolar systems the quadrupolar interaction will be the dominant relaxation mechanism and tends to reduce the T_1. The paramagnetic interaction also has a significant contribution towards the relaxation process brought on by the rapid electron spin flipping of an unpaired electron causing a great decrease in T_1.

3.1.1.2 Transverse Relaxation

The transverse relaxation relates to the magnetisation in the x-y plane, this is orthogonal to the z plane and follows the same mechanism as spin-lattice relaxation however is distinct from it, consequently T_2 is also governed by the Bloch equations.

$$\frac{dM_x}{dt} = \frac{-M_x}{T_2}, \frac{dM_y}{dt} = \frac{-M_y}{T_2} \tag{3.3}$$

This can be rewritten in the rotating frame as

$$M_x(T) = M_x(0)e^{\frac{-t}{T_2}}, M_y(T) = M_y(0)e^{\frac{-t}{T_2}}. \tag{3.4}$$

However, this is for the ideal transverse relaxation. Inhomogeneities in the static magnetic field sum with the ideal magnetic field resulting in T_2^* which is related to the transverse relaxation by

$$\frac{1}{T_2^*} = \frac{1}{T_2} + \frac{1}{T_{2(\Delta B_0)}} \tag{3.5}$$

where $T_{2(\Delta B_0)} = 1/R_{inhom}$ is the size of the magnetic field inhomogeneities and T_2^* is the total transverse magnetisation. T_2* is proportional to line width,

$$\Delta\nu_{\frac{1}{2}} = \frac{1}{\pi T_2^*} . \tag{3.6}$$

A larger interaction results in a smaller T_2* and a larger linewidth. This can be used to determine the homogeneity of the magnetic field and adjust it so that R_{inhom} is reduced resulting in as narrow linewidth as possible, this process is called shimming.

3.1.1.3 Relaxation in the Rotating Frame

Spin lattice relaxation in the rotating frame is the return of magnetisation to equilibrium in the presence of an RF field B_1. The magnetisation is described as spin-locked as the rate constant $T_{1\rho}$ is significantly longer than transverse relaxation and is more sensitive to slower fluctuations, this is particularly useful for the study of polymers where most motion is in the kHz regime. The spin-lock pulse supresses the free evolution of transverse magnetisation "locking" it in a particular direction in the rotating frame.

$T_{1\rho}$ relaxation is sensitive to motion on the nanoscale-millisecond timescale, making it ideal for the study of mobility in polymers. In theory spin-lock magnetisation decays mono-exponentially with regard to spin lock time at a rate of $1/T_{1\rho}$ however inhomogeneities in the B_0 and B_1 field can obscure the actual spin-lock direction and strength. B_1 inhomogeneities lead to deviation of the true spin-lock frequency (FSL), while B_0 inhomogeneities lead to a deviation of the magnetisation nutation about the spin-lock field direction from the Z direction with an angle of

$$\theta = \tan^{-1}\left(\frac{\Delta\omega_1}{\Delta\omega_0}\right) = \tan^{-1}\left(\frac{FSL}{\gamma\Delta B_0}\right) \tag{3.7}$$

The effective spin-lock pulse is calculated by,

$$\Delta\omega_{eff} = (\Delta\omega_0^2 + \Delta\omega_1^2)^{1/2} \tag{3.8}$$

A simple solution used to overcome the B_0 homogeneities is to use a spin-lock pulse with strong spin-lock strength and large FSL so that θ approaches 90° and $\Delta\omega_{eff} \approx \Delta\omega_1$. In practice this is restricted by limitations of the instrumentation.

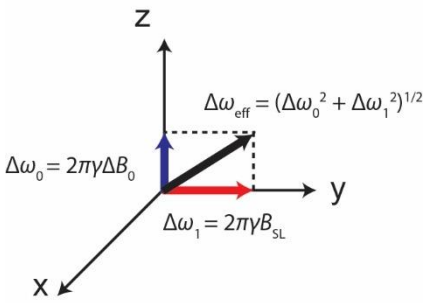

Figure 3-2. The effective spin-lock strength and direction in the rotating frame under the influence of B_0 inhomogeneity.

To simplify the full Bloch analysis while maintain acceptable accuracy the transient relaxation effect is usually neglected. The magnetisation evolution can be traced as the multiplication of a series of rotation and relaxation matrices to present each RF component. Starting from an instantaneous RF pulse, $R_\varphi(\phi)$, where R is a rotation matrix, φ is the pulse field orientation and ϕ is the pulse flip angle. The magnetisation evolution under the RF pulse is generally expressed by,

$$M_{t1} = R_\varphi(\phi) M_{t0} \tag{3.9}$$

Where M_{t0} and M_{t1} are the magnetisation before and after the pulse excitation, respectively. The basic rotation matrices rotate about x, y and z by the angle ϕ,

$$R_x(\phi) = \begin{bmatrix} 1 & 0 & 0 \\ 0 & \cos\phi & \sin\phi \\ 0 & -\sin\phi & \cos\phi \end{bmatrix}; \; R_y(\phi) = \begin{bmatrix} \cos\phi & 0 & -\sin\phi \\ 0 & 1 & 0 \\ \sin\phi & 0 & \cos\phi \end{bmatrix}; \; R_z(\phi) = \begin{bmatrix} \cos\phi & \sin\phi & 0 \\ -\sin\phi & \cos\phi & 0 \\ 0 & 0 & 1 \end{bmatrix} \tag{3.10}$$

The spin-lock relaxation matrix under a spin-lock pulse of duration T is assuming the spin-lock pulse is along y is given by,

$$E_\rho(T) = \begin{bmatrix} e^{-T/T_{2\rho}} & 0 & 0 \\ 0 & e^{-T/T_{1\rho}} & 0 \\ 0 & 0 & e^{-T/T_{2\rho}} \end{bmatrix} = \begin{bmatrix} E_{2\rho}(T) & 0 & 0 \\ 0 & E_{1\rho}(T) & 0 \\ 0 & 0 & E_{2\rho}(T) \end{bmatrix} \tag{3.11}$$

Where $T_{2\rho}$ is the decay rate of magnetisation perpendicular to the spin lock pulse.

Assuming a flip angle of β for the tip-down pulse, P_1 and tip-up pulse P_2 plus α. The spin lock component SL, α = 2π·FSL·TSL, where TSL is the spin-lock time, the magnetisation for a given FSL is expressed as,

$$M(TSL) = R_{-x}(\beta) \cdot R_y(\alpha) \cdot E_\rho(TSL) \cdot R_x(\beta).M(t_0); \tag{3.12}$$

$$Where\ M(t_0) = \begin{bmatrix} 0 & 0 & M_0 \end{bmatrix}^T$$

P_1 and P_2 have much shorter duration than SL, therefore the relaxation during P_1 and P_2 is negligible. Substituting eq. 3.10 and eq. 3.11 into eq. 3.12 the final M_z is given by,

$$M_z = \left(\sin^2\beta \cdot e^{-TSL/T_{1\rho}} + \cos^2\beta \cdot \cos\alpha \cdot e^{-TSL/T_{2\rho}}\right)M_0 \qquad (3.13)$$

M_z will follow and exponential decay so long as β equals 90° or π/2, when this is not the case M_z will be composite of $T_{1\rho}$, $T_{2\rho}$ and α.

3.1.2 Cross Polarisation

The cross polarisation technique is used to enhance the signal and assist in the observation of dilute spins, *eg*. ^{13}C. The low natural abundance of dilute spins results in a poor signal to noise ratio, additionally the relaxation times for dilute spins tend to be very long as strong homonuclear dipolar interactions are largely absent so do not aid relaxation. These two considerations both lead to longer collection times for a spectrum.

In order to explain the cross polarisation, process the doubly rotating frame must be used. The abundant ^1H spins are considered in a frame where all magnetic fields due to ^1H pulses appear static, the dilute X spins are considered in a frame in which all pulses due to X pulses appear static. The ^1H spins and X spins rotate about B_0 at the respective frequency of ^1H and X rf irradiation, all pulses are assumed to be on resonance.

A ^1H π/2 pulse creates ^1H magnetisation along -y, an on resonance -y ^1H contact pulse is then applied, this field is known as the spin lock field, $B_1(^1H)$, this maintains ^1H magnetisation along -y. The spin lock pulse on the ^1H channel is matched to a contact pulse on the X channel. The Hartmann-Hahn matching condition must be met:

$$\gamma H B_1(^1H) = \gamma X B_1(X) \qquad (3.14)$$

when the amplitude of both pulses is the same, the energy gaps between the two spins are equal allowing for the redistribution of spin states, with a net gain in the X spins. After the contact pulse ^1H decoupling is applied to remove dipolar coupling during acquisition of the X channel.

The amplitude of the contact pulse or the spin lock pulse are varied over the contact time to compensate for imperfections in the setting of the Hartmann-Hahn match condition. At MAS frequencies higher than 12 kHz, where the rotor period is a fraction of the length of the

contact time, the net cross polarisation averages to zero reducing the effectiveness of the Hartmann-Hahn match condition. An additional match condition can be found where

$$\gamma H B_1(^1H) - \gamma X B_1(X) = \pm n\omega_r \quad (3.15)$$

Is true, resulting in the sideband match condition. In this thesis all CP experiments have been performed at ω_r = 12 kHz, where the match condition still holds.

3.1.5 Heteronuclear Decoupling

MAS removes most of the heteronuclear dipolar coupling however some anisotropy remains. Decoupling sequences are used to remove any broadening remaining due to dipolar coupling. This is most commonly applied to the ^{1}H channel during the acquisition of FIDs on the X channel.

In an initial system, *i.e.* CH, where the heteronuclear dipolar interaction is proportional to $S_z(C)/I_z(H)$, the proton magnetisation initially lies parallel to the z-axis (I_z)The application of an rf pulse on the proton channel rotates the ^{1}H magnetisation to the xy plane then to the –z-axis. The proton spin will vary between I_Z and $-I_Z$, if this is rapid compared to the experiment timescale I_z tends to zero. The heteronuclear dipolar Hamiltonian oscillates between $\pm I_zS_z$ so that the average is zero. In order to work the rf field strength has to be greater than the strength of the dipolar interaction. Typically, a nutation frequency (ω_1) of 100 kHz is used however it can cause undesired heating to the sample if the strength is too great. This problem has resulted in the development of more efficient sequences such as SPINAL-64 and two pulse phase modulated (TPPM).[11-12]

3.1.6 The Hahn -Echo Experiment

The first spin echo experiments was performed by Erwin Hahn.[13] It was discovered that using successive π/2 pulses which are separated by a short time period (τ) will result in an echo like appearance evolved in the signal. The π/2 – τ – π/2 sequence is called the solid echo or quadrupolar-echo.

The original sequence was modified by Carr and Purcell,[14] they changed the second π/2 pulse into a π pulse. This substitution promotes coherence refocusing and effectively rotates the spins around the π axis. The spins are flipped and start to undo any dephasing, this results in the faster precessing spins being effectively behind the slower spins. All coherences are refocused after a time τ after the π pulse, at which point the FID is collected.

The Hahn Echo technique is particularly useful for systems with broad resonances and low T_2^*. During the dead time after the final pulse no FID is collected, by collecting the signal from

the top of the FID the potential loss of crucial information is removed. When used with MAS, the pulses are timed so that $\tau = n\omega_r$, where n is an integer and ω_r represents a full rotor cycle.

The theory for the following sections comes predominantly from 'Principles of Instrumental Analysis',[15] 'Fundamentals of Analytical Chemistry'[16] and 'The SAXS Guide'.[17]

3.2 Differential scanning calorimetry

Differential scanning calorimetry (DSC) is one of the most commonly used thermal analysis methods for investigating phase transitions and temperatures, primarily due to its speed and simplicity. In DSC a sample undergoes cycles of heating and cooling while the difference in heat flow between the sample and a reference pan is measured. When the sample undergoes a thermal transition there will be either and exothermic or endothermic event occurring, through measuring the heat flow these events can be detected and measured. Thermogravimetric analysis is a complementary technique to DSC and measures the loss of mass of a material as it is heated, this allows for the determination of phase transitions. TGA is particularly useful when determining the processing conditions of a material to avoid causing degradation from too high temperatures. A third thermal technique used is dynamic mechanical thermal analysis, this technique can be used to test the mechanical properties and behaviour of polymers. DMTA is the most sensitive technique for measuring glass transition temperatures.

Typical transitions measured are the glass transition temperature, this especially important for polymers. This is when the material goes from a glassy state to a rubbery state as polymers will undergo changes in volume and expansion, heat flow and heat capacity. Above the glass transition temperature crystallisation can occur if a polymer has enough energy to form ordered crystalline arrangements. The third important transition occurring during heating is the melting temperature, T_m, which will occur last, as the chains become disordered. There are other events that can occur during heat such as evaporation of solvents, consequently usually more than one cycle is undertaken so that the second heating cycle will show only transitions related to the sample and not any residual solvents. In theory on cooling the sample reverts to the same state as before the transitions and therefore a sample can be measured as many times as desired. However this will not be the case is the sample solidifies to a glassy amorphous state at a fast cooling rate resulting in no melting peak occurring on a second heating.

The shape of the transition peak can provide additional information about the sample. The melting peak can show any impurities, partial crystallinity and decomposition with melting; the crystallisation peak can also indicate impurities and indicate the process of crystallisation, Figure 3-3.

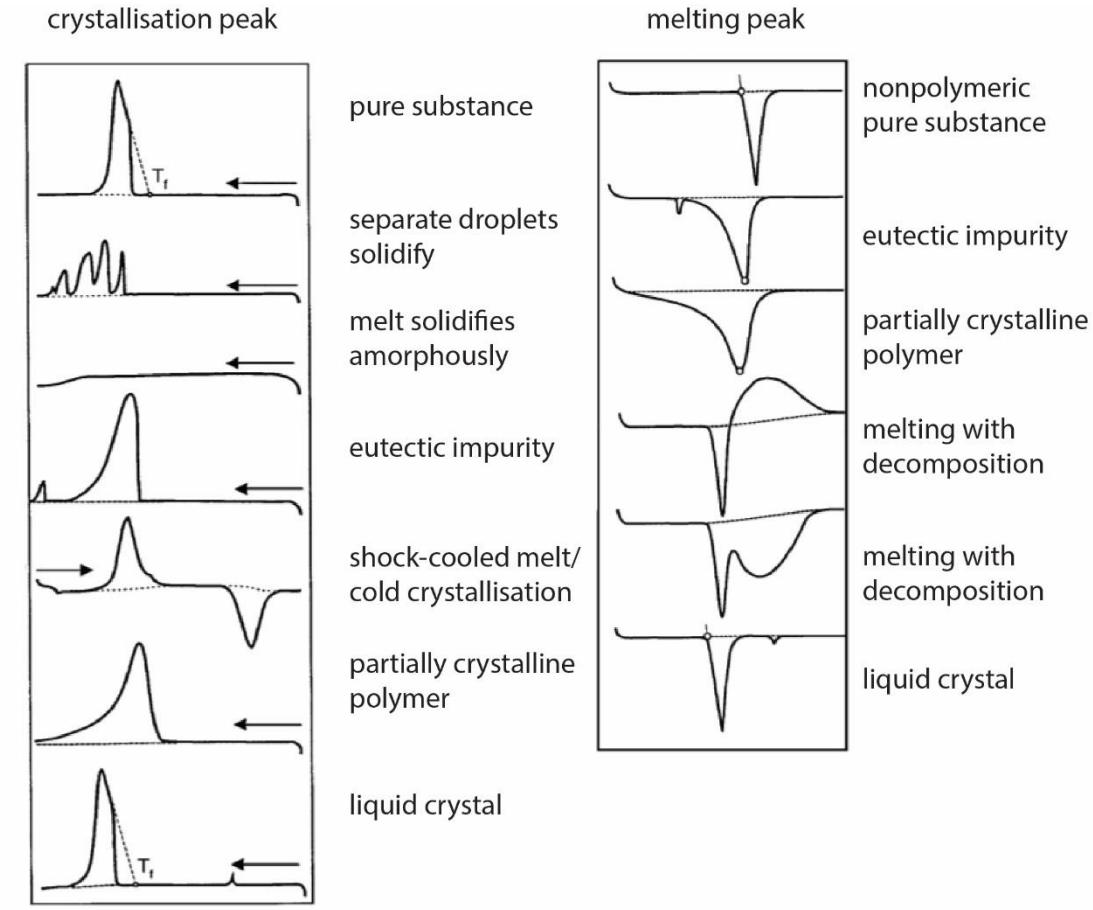

Figure 3-3. The DSC transition shapes for the crystallisation peak (left) and the melting peak (right) under the influence of impurities, partial crystallisation and decomposition.[18]

3.3 Electron Paramagnetic Resonance

The main theory behind electron paramagnetic resonance (EPR) is analogous to the NMR theory, the main difference is that EPR probes the electron spins and focuses on the interaction between unpaired electrons in a system and the external magnetic field. EPR is performed using microwaves in the 3 – 400 GHz range compared to a range of 100 – 1200 MHz utilised in NMR. One of the limiting factors for EPR is the short relaxation times of electron spins which lead to broadening of the spectra; therefore, experiments are often performed below 10 K to reduce the motions. EPR is around 1000 times more sensitive than NMR which greatly reduces the length of experiments due to the Boltzmann distribution.

In EPR there are two magnetic moments, the orbital magnetic moment is induced by an electron spinning around the nucleus, while the spin magnetic moment is caused by the electron "spinning" around its own axis. The unpaired electron's spin magnetic moment primarily contributes to the magnetic moment

$$M_S = \hbar\sqrt{S(S+1)} \tag{3.16}$$

where M_S is the total spin angular momentum and S is the spin quantum number. In the z direction M_s becomes

$$M_{SZ} = m_s\hbar \tag{3.17}$$

where m_s can have 2S+1 values, for a single unpaired electron m_s can be ±1/2. The magnetic moment μ_e is directly proportional to the spin angular momentum,

$$\mu_e = -g_e\mu_B M_S \tag{3.18}$$

where g_e is the free electron g-factor and the term $g_e\mu_B$ is the gyromagnetic ratio. The magnetic moment of an electron is antiparallel to the spin resulting in the negative sign. The Bohr magneton μ_B is given by

$$\mu_B = \hbar\frac{e}{2\pi m_e}\ . \tag{3.19}$$

For a single unpaired electron, the two possible energy states will be,

$$E_{\pm\frac{1}{2}} = \pm\frac{1}{2}g\mu_B B \tag{3.20}$$

In the presence of an external magnetic field the difference between the two states will be,

$$\Delta E = h\nu = g\mu_B B \tag{3.21}$$

As the intensity of the applied magnetic field increases the energy levels widen until they match the microwave radiation which results in absorption of photons.

Systems studied by EPR often have both orbital and spin angular momentum. A scaling factor is used to account for the coupling of the two, this is the g-factor. The g-factor is given by,

$$g_J = \frac{J(J+1)(g_L+g_S) + \big(L(L+1) - S(S+1)\big)(g_L - g_S)}{2J(J+1)} \tag{3.22}$$

where g_L is the orbital g value and g_S is the spin g value, it can be approximated in most systems that g_L is exactly 1 and g_S is exactly 2 and the quantum number J = L+S. This can be reduced to the Landé formula,

$$g_J = \frac{3}{2} - \frac{L(L+1) - S(S+1)}{2J(J+1)} \tag{3.23}$$

The electronic magnetic dipole now becomes,

$$\mu_J = -g_J \mu_B J \tag{3.24}$$

These approximations are not always true as there are systems where J-coupling does not occur. The g-factor takes into consideration the local environment of the spin system as well as the magnetic dipole moment. Other local magnetic fields, such as those arising from other paramagnetic species, magnetic nuclei, electric quadrupoles and ligand fields can all influence the effective magnetic field,

$$B_{eff} = B_0 + B_{local} \tag{3.25}$$

The local fields can be both induced by the applied field, having a dependence on B_0 or permanent and independent of B_0. Where the local field is induced by the applied field B_{eff} becomes,

$$B_{eff} = B_0(1 - \sigma) \tag{3.26}$$

where σ is the shielding factor, this can be replaced by the g-factor resulting in

$$B_{eff} = B_0 \cdot \frac{g}{g_{eff}} \, . \tag{3.27}$$

In cases where L is near zero J becomes approximately S, the g-values are therefore typically close to 2, such as in organic radicals and radical ions. Unpaired electron spins in transition metal ions and complexes have large L and S values and therefore the g value diverges from 2. The energy levels of the spins in an applied magnetic field can now be written as

$$E_{ms} = m_s g_e \mu_B B \tag{3.28}$$

thus the energy difference becomes,

$$\Delta E_{ms} = \Delta m_s g_e \mu_B B \tag{3.29}$$

EPR is performed in perpendicular mode where the magnetic field component of the microwave radiation is perpendicular to the magnetic field. The selection rules for the allowed EPR transitions is $\Delta m_s = \pm 1$, the energy difference becomes,

$$\Delta E_{ms} = g_e \mu_B B \tag{3.30}$$

Parallel mode EPR can be performed in which case $\Delta m_s = \pm 2$.

In theory in a paramagnetic molecule one spectral line should be observed, this is not the case in practice due to the hyperfine interaction. The hyperfine interaction arises from the interaction of the magnetic moment of the unpaired electron and the magnetic nuclei. The hyperfine pattern allows for elucidation of the spatial structure and identity of a paramagnetic species.

3.4 Raman

Raman spectroscopy is used to investigate the vibrational modes of bonds, a sample is irradiated with a monochromatic beam of energy, $h\nu_{ex}$, of visible or near infrared wavelength. When a molecule absorbs a photon of energy, ground state electrons are excited to the excited virtual state, Figure 3-4(b). There are three methods of scattering by which a photon is reemitted, Stokes, anti-Stokes and Rayleigh scattering. When the scattered energy is lower than the excitation radiation stokes scattering occurs, when the reverse is true and the scattered energy is higher than the excitation radiation anti-Stokes scattering occurs, this is inelastic scattering. Rayleigh scattering is an elastic scattering that occurs when the scattered energy and the excitation energy are the same frequency.

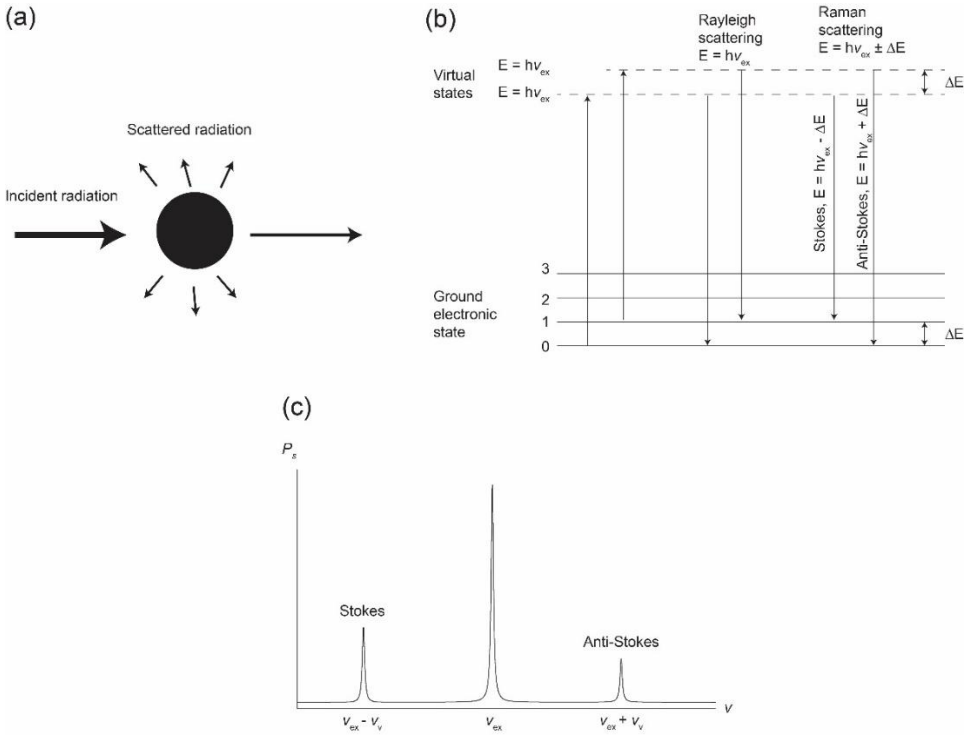

Figure 3-4. (a) A representation of incident radiation being scattered, (b) the Rayleigh and Raman scattering and the transitions between the ground electronic state and virtual states and (c) the Raman spectra consisting of low-frequency Stokes emissions and higher frequency anti-Stokes emissions.

Stokes emission is favoured over anti-Stokes due to the relative populations of the two upper energy state, additionally Rayleigh scattering has a higher occurrence due to the higher probability of energy transfer to molecules in the ground state and reemission by return of these molecules to the same ground state. The energy changes from Stokes and anti-Stokes radiation differ from the Rayleigh radiation by frequency of ±ΔE, the energy of the first ground state vibrational level.

Raman and Rayleigh scattering can be described using a wave model. A beam of radiation with a frequency ν_{es} incident to an analyte has an electric field *E*,

$$E = E_0 \cos(2\pi\nu_{es}t) \tag{3.31}$$

where E_0 is the amplitude of the wave. When the electric field interacts with the electron cloud of a bond in the analyte a dipole moment is induced,

$$m = \alpha E = \alpha E_0 \cos(2\pi\nu_{ex}t) \tag{3.32}$$

where α is the polarizability of the bond, a measure of the deformability of a bond in an electric field. The polarizability is dependent upon the distance between the nuclei.

$$\alpha = \alpha_0 + (r - r_{eq})\left(\frac{d\alpha}{dr}\right) \tag{3.33}$$

where α_0 is the polarizability of the bond at the equilibrium internuclear distance r_{eq} and r is the internuclear separation at any instant. The change in separation varies with vibration frequency ν_v.

$$r - r_{eq} = r_m \cos(2\pi\nu_v t) \tag{3.34}$$

where r_m is the maximum internuclear separation relative to the equilibrium position.

Substituting eq. 2.44 into eq. 2.43 gives

$$\alpha = \alpha_0 + (r_m \cos(2\pi\nu_v t))\left(\frac{d\alpha}{dr}\right) \tag{3.35}$$

An expression for the induced dipole moment, m, can then be obtained by combining eq. 2.45 and eq. 2.42.

$$m = \alpha_0 E_0 \cos(2\pi\nu_{ex}t) + E_0 r_m \left(\frac{d\alpha}{dr}\right) \cos(2\pi\nu_v t)\cos(2\pi\nu_{ex}t) \tag{3.36}$$

Using the trigonometric identity for the product of two cosines,

$$\cos x \cos y = [\cos(x+y) + \cos(x-y)]/2 \tag{3.37}$$

The equation for the induced dipole moment becomes

$$m = \alpha_0 E_0 \cos(2\pi\nu_{ex}t) + \frac{E_0}{2} r_m \left(\frac{d\alpha}{dr}\right) \cos[2\pi(\nu_{ex} - \nu_v)t] + \frac{E_0}{2} r_m \left(\frac{d\alpha}{dr}\right) \cos[2\pi(\nu_{ex} + \nu_v)t] \tag{3.38}$$

The first term represents the Rayleigh scattering occurring at excitation frequency ν_{ex}, the second and third terms represent the Stokes and anti-Stokes scattering respectively with

corresponding frequencies of $\nu_{ex} \pm \nu_v$. The excitation frequency is modified by the vibrational frequency of the bond. The selection rules for Raman scattering require a change in polarizability during vibration, $\frac{d\alpha}{dr}$ is greater than zero.

3.5 SAXS/WAXS

The initial principle of SAXS and Wide-angle X-ray scattering (WAXS) measurements is the same as those discussed for Raman spectroscopy, see chapter 3.4, where X-rays are scattered by a sample and the scattered radiation is detected, however Thompson scattering is used rather than Raman scattering. In SAXS/ WAXS experiments the scattered radiation is detected across a range of angles 2θ to the incident light.

Outgoing light waves from Thompson scattering processes are synchronised with the incoming plane waves, consequently they produce interference at the detector. Depending on the observation angle, orientation and distance, r, between the light emitting atoms the waves can be constructive in phase, destructive out of phase or in between. Constructive waves result in a light spot at the detector whereas destructive waves result in a dark spot, a 2D interference pattern is produced which is characteristic of the internal structure of the material providing information about the orientation and distance of atoms relative to each other.

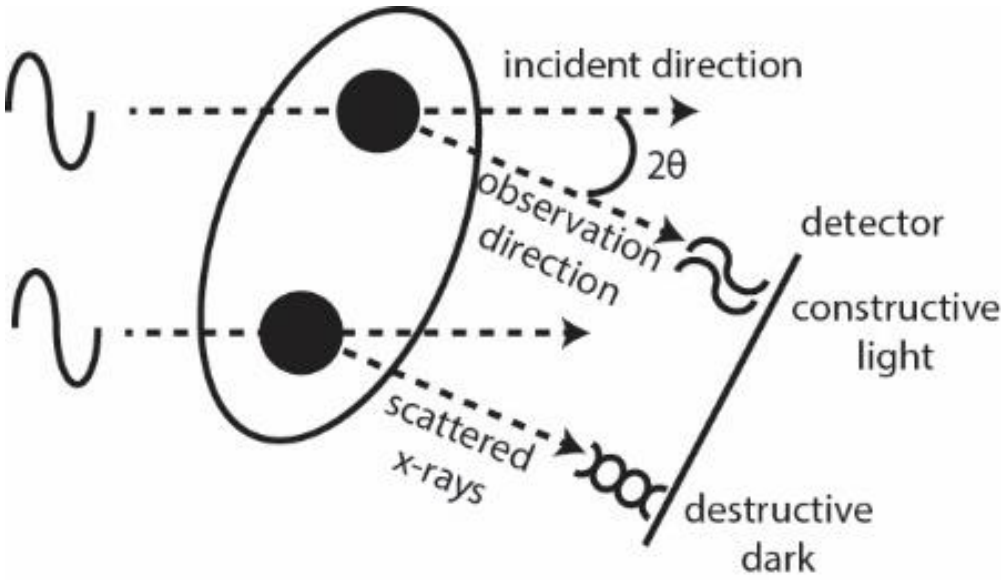

Figure 3-5. A representation of the scattering of X-rays by a material. The scattered X-rays are observed at an angle of 2θ to the detector. Constructive waves form light spots and deconstructive waves form dark spots.

In SAXS every distance is relative to the wavelength, in order to become independent of the wavelength scattering patterns are presented as a function of q.

$$q = \frac{4\pi}{\lambda} \sin \phi \tag{3.39}$$

Where ϕ is the azimuthal angle or 2θ/2, conversion to 2θ values is therefore possible where useful for the analysis of WAXS patterns which are often collected simultaneously with SAXS measurements.

The interference pattern oscillates in a characteristic fashion depending on the shape of the particle, this is referred to as the form factor. The observed pattern corresponds to the form factor of one particle rather than all of the illuminated particles if it meets two conditions; firstly, the particles must be identical in shape and size and secondly the particles are far away from each other, i.e. the system is dilute. In a dilute system the form factors of all particles can be summed, if the particles have different sizes then the form factor is an average scattering pattern of the whole sample.

If the particle system is densely packed and the distance between the particles is the same magnitude as the distance within particles, then the pattern will have interference from neighbouring particles. This interference pattern multiplies with the form factor and is referred to as the structure factor. This is can also be referred to as the lattice factor as it contains information about the position of the particles with respect to each other. The intensity at small angles can indicate the interaction between the particles, if there is a decrease in the intensity there will be a repulsive interaction whereas an increase indicates attractive attraction. The wave can develop into a pronounced peak when particles are aligned and form highly ordered and periodic arrangements. These peaks are called Bragg peaks, the position of the maximum q_{max} indicates the distance between aligned particles using Bragg's law,

$$d_{Bragg} = \frac{2\pi}{q_{peak}} \tag{3.40}$$

The ratio of the peak positions on the q scale have typical values that indicate the crystal symmetry. These are for lamellar symmetry, 1, 2, 3, 4, 5…, cubic symmetry, $1, \sqrt{2}, \sqrt{3}, 2, \sqrt{5}$ …, and hexagonal symmetry, $1, \sqrt{3}, 2, \sqrt{7}, 3, \ldots$ In addition to the positional order, particles can have a preferential orientation to each other especially for a non-spherical particle. This orientation can be visualised in a 2D scattering pattern by the amplitude of intensity modulation measured in a circle around the primary beam, Figure 3-6. A disperse system or

crystal powder will have equal intensities throughout the concentric circles. When the system is partially oriented there will be modulations and in a single crystal there will be intensive spots.

To extract useful information from a SAXS pattern a modelling procedure of the data is required, from the model the form factor and structure factor can be used to determine parameters such as the radius of gyration (R_g), average particle radius and information on the particle-particle interaction. There are three important components involved in the extraction of information from the intensity of the scattering pattern, I(q), a constant, K, representing the particle volume, contrast, concentration etc. The form factor, P(q), from which the shape and internal density distribution of the particles can be determined and the structure factor, S(q), which carries information relating to particle-particle interactions.

$$\Delta I(q) = K \cdot P(q) \cdot S(q) \tag{3.41}$$

The form factor can be approximated at small angles using a Gaussian curve, the curvature of the Gaussian is due to the overall size of the particles.

$$P(q) = a_0 \cdot e^{-\left(\frac{R_G^2 q^2}{3}\right)} \tag{3.42}$$

Where a_0 is the extrapolated zero-angle intensity and the size parameter R_g is model independent. If the structure of the particles can be assumed, then the average particle size can be determined.

$$R = \sqrt{3/5\, R_G} \tag{3.43}$$

The parameters R_G and a_0 can be determined by straight-line fitting of the Guinier plot where the logarithm of the intensity is plotted versus q^2.

$$\ln\left[\Delta I_q\right] = \ln[a_0]^{-\left(\frac{R_G^2 q^2}{3}\right)} \tag{3.44}$$

Model calculations are needed to determine the relative positions and orientation of the subunits and consequently S(q), these consist of calculations of the pair-distance distribution function (PDDF) or form factor, refined to the experimental data, the modelling software Irena is used in this thesis. The inter-particle forces contribute towards $S_{(q)}$, these include the hard-spheres interaction, where particles can move freely but cannot penetrate each other, allowing for the determination of hard spheres radius, inter-particle distance and

concentration. The other two interactions are the coulomb interaction and Van-der-Waals interaction, in this thesis the hard-spheres model is used to fit the data. There are two ways of treating the data for modelling $S_{(q)}$, the first is by removing the small angles and interpret only the large angles. The second way which is now considered as the better method is to simultaneously fit the $P_{(Q)}$ at small angles and the $S_{(Q)}$ at larger angles allowing for both the inter-particle and single-particle terms to be taken into account.

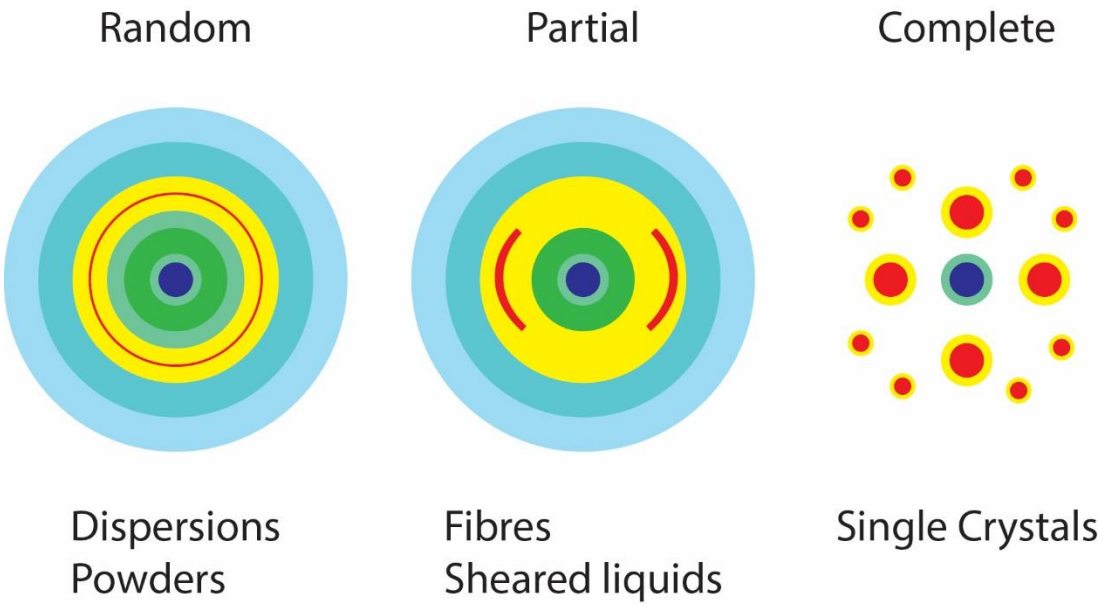

Figure 3-6. The 2D scattering patterns of randomly, partial and completely oriented samples, such as dispersions and powders, fibres and shear liquids and single crystals respectively.

4. Understanding the physical ageing of high-heat polylactide

4.1 Introduction

Biodegradable and bioresorbable polymers can be used in a wide range of applications, from industrial applications such as packaging container and films, bottles and drink cups to medical applications including drug delivery systems,[19-20] protein encapsulation and delivery,[21-22] and scaffold materials.[23] Aliphatic polyesters are of great interest and form important biodegradable polymers, one of these is Poly(lactide).[24] With the development of high heat PLA produced from stereo complexes of PLA with melting temperatures of 180-200 °C, PLA can now be used as a high-performance material for automotive and aeronautical applications.

PLA was first synthesised by polycondensation of lactic acid in 1845, in recent years ring-opening polymerisation (ROP) of lactide, a cyclic dimer of lactic acid has been used as an alternative synthesis route.[25-28] ROP is preferable to polycondensation as high-molecular weight PLA with narrow distribution can be achieved at lower temperature with shorter reaction times; for the production of poly(l-lactic acid) (PLLA) it has become the industry standard.[29-30] Industrial production methods utilising poly(d-lactic acid) (PDLA) to form stereo-complexes are more challenging, current synthesis methods involve synthesis of stereo-block polymers of PLLA and PDLA chains.[31-35] PLA is often co-polymerised to tailor the properties of the end materials, an example of this is poly(lactide-co-glycolide) (PLGA) which can be effectively used as a drug delivery system. Synthetic polymers such as PLGA are attractive as they can be engineered from monomers to suit the target use. The properties of both copolymers are retained and by customising the ratio of the copolymers the properties can be further varied, for example increasing the glycolic to lactic acid ratio increases hydrophilicity and leads to faster degradation.[36-38] The synthesis method for PLGA will also affect the properties such as stability and particle size.[39]

Bacterial reactions result in lactic acid fermentation; the bacteria are divided into categories based on their cell morphology, these are *Aerococcus, Coryne, Lactobacillus, Leuconostoc, Pediococcus,* and *Streptococcus*.[40-41] Most bacteria produce L-lactic acid while some produce D- or DL- lactic acid, in ordinary lactic acid fermentation yields for L- and D-lactic acid are 85-90 % and 70-80 % respectively.[32] The fermentation liquor acquired will contain impurities such as raw materials, amino acids, carboxylic acids, inorganic salts, proteins and saccharides. In the fermentation process lactic acid is neutralised *in situ* with either calcium oxide or ammonia, use of ammonia results in higher purity than calcium salt.[42]

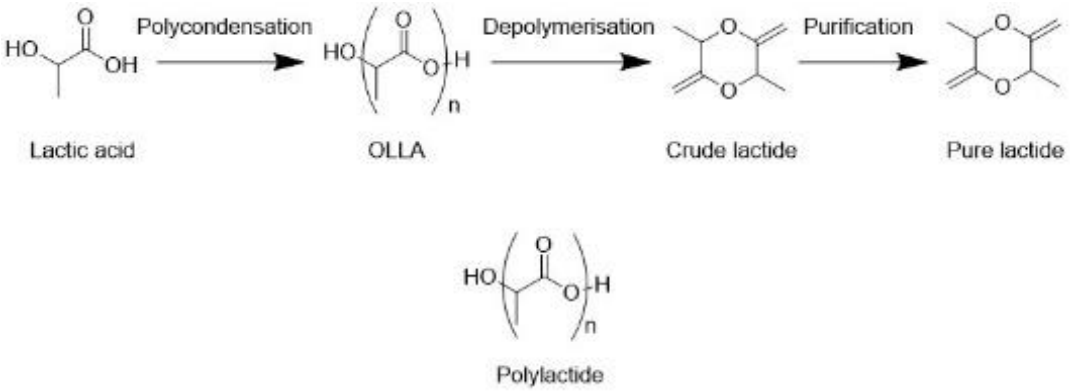

Figure 4-1. The three step synthesis of a pure lactide monomer from lactic acid, via polycondensation, depolymerisation and finally purification (top) and the structure of polylactide (bottom).

Pure lactides are synthesised through three stages from lactic acid, the first is polycondensation of lactic acid into oligo(lactic acid) (OLLA).[42] OLLA is then depolymerised to form crude lactide through back-biting mechanism using the -OH terminals as the active site.[43] Once the crude lactide is obtained it is the purified by either melt crystallisation or recrystallisation from solution.

As stated previously ROP is the preferred method of synthesis of optically pure PLA resulting in isotactic homopolymers of PLLA and PDLA. Stereocomplex PLA (scPLA) can be synthesised between PLLA and PDLA in several different ways, in solution, in solid state from the melt, during polymerisation or during hydrolytic degradation. Stereocomplexation can take place in enantiomeric polymer blends and in non-blended stereoblock PLA.[44]

Three types of crystallites can be formed in the presence of both L and D PLA chains. The first, where there is a strong interaction between chains of opposite configuration, L and D chains will be packed side by side. The second configuration is where the interaction between identical chains prevails resulting in the formation of two different homo-crystallites.[44-45] The properties of PLA are highly dependent upon their crystallinity, PLLA crystallises slowly allowing for a high tunability of the degree of crystallinity, this is also achieved by changing the thermal history. Crystallinity influences the degradation and mechanical properties of PLA and is therefore an important factor for the potential applications. Additionally, to the crystallinity, the amorphous region has an impact on the properties. The changes of the physical properties over time can be linked to the structural relaxation of PLA.[46]

The understanding of how PLA degrades, and the control of these processes is important for tailoring the properties of the final materials. There are several pathways and causes of

degradation which all have different mechanisms but mainly work on the principle of main chain or side chain scission. The main mechanisms are hydrolysis, thermal degradation and photodegradation; other methods are microbial and enzymatic degradation however they will not be discussed here.

Chemical hydrolysis is the most likely degradation pathway for this study due to the prevalence of moisture in air. The ester groups on the main chain of the polymer are cleaved which causes a reduction in molecular weight and the production of soluble oligomers and monomers. The hydrolysis process commences with the diffusion of water molecules into amorphous regions initiating the cleavage of ester bonds, the degradation then continues into the crystalline domains.[47-48] Depending on the intended use, hydrolysis can pose more of a problem, this is mainly where PLA is used as packaging for fresh produce or a beverage container. Not just the transference of moisture but also the pH of any liquid can increase the rate of hydrolysis.[49] Hydrolysis is catalysed by hydroxide and hydronium ions, H_3O^+, therefore under strong acidic and basic conditions the chains will be more easily degraded. PLA bottles used for storing alcohol, have their own set of complications especially once the ethanol content exceeds 50 % and at temperatures exceeding 40 °C. Ethanol additionally causes the PLA matrix to swell which increases the chain mobility and results in solvent induced crystallisation. Another factor that contributes to accelerated hydrolysis is the temperature which induces faster chain scission at higher temperatures. In addition to moisture other contributing factors towards the reactivity of the hydrolysis process are molecular weight, residual lactic acid, particle size and shape, crystallinity and catalyst impurities.[50-53]

Thermal degradation, which can be measured suing thermal techniques such as differential thermal analysis (DTA) and DSC, occurs during processing which leads to inferior final products. Hydrolysis initiated by residual water contributes to thermal degradation as well as unzipping depolymerisation reactions, random main-chain scission, and transesterification. It is of high importance to fully dry PLA resins before processing. The thermal degradation process is highly complex and results in many different low molecular weight compounds and linear and cyclic oligomers; additionally, CO, CO_2, acetaldehyde, and methyl ketones have been detected. Many factors influence thermal degradation including molecular weight, moisture and residual catalysts and metals; the extrusion time is an external factor that will also change the effect of thermal degradation. Countermeasures to improve thermal stability include end-protection or chain extenders, protection of the hydroxyl group inhibits depolymerisation from the hydroxyls. The acetylation process not

only achieves end-protection but also removes residual metals, chain extenders increase the onset temperature for degradation by extending the polymer chains and reducing the number of active sites on the chain end.[54-57]

Photodegradation is where plastic degradation is induced by low wavelength and high-energy UV radiation. The COO group in PLA absorbs UV radiation at 280 nm which increases the susceptibility to photodegradation. The mechanism by which PLA undergoes photodegradation is the Norrish II mechanism; this is where chain end scission of the main chain occurs and C=C bonds are formed with carboxyl end groups; this is triggered by C=O electron transition.[58] Main-chain scission occurs randomly however there is a higher probability of it occurring in amorphous regions. Other mechanisms have also been proposed; one is the breakage of main-chain C-O by photolysis and the other is formation of hydroperoxides and degradation into carboxylic acid and diketone end groups by photooxidation. Other than UV light, γ-irradiation causes a γ-sterilisation where radicals are formed due to scission of the ester bonds and hydrogen abstraction from methane groups, this occurs mainly in the amorphous region.[59-61]

Several techniques have been used to study PLA, in this particular study solid state NMR, powder XRD and DSC will be combined to develop a greater understanding of the physical ageing process of PLA. Powder XRD provides information on the structural arrangement of crystalline polymers. The crystalline regions in PLA cause diffraction of the X-ray beam, the homo-crystallites and stereocomplex crystallites diffract differently so have distinct patterns allowing for the detection of each in the XRD powder pattern. XRD is used in this study to confirm the absence or presence of the two crystalline components before and after annealing and over time.[62-64]

Differential scanning calorimetry can also be used to indicate the presence of crystalline regions in PLA. The strength of the interactions between identical chains is weaker than those of chains with opposite arrangement. The melting point of homo-crystallites is consequently lower than that of the stereocomplex crystallites as less energy is required to overcome the interactions. Where both crystalline sites are present there will be two melting peaks in the DSC.[65-66]

Solid state NMR measurements are commonly performed on PLA, standard 1D ^{13}C CPMAS measurements are often used for studying the crystallinity and morphology of PLA. The different amorphous and crystalline components can be observed, the disordered amorphous regions will result in broad resonances whereas the crystalline regions will have

narrower line widths.[67-68] In addition to basic determination of crystalline regions, solid state NMR has been used to probe helical jump motion using 2D exchange NMR showing large scale chain diffusion in crystalline regions.[69-70] Measurements of the relaxation times also allow for investigation of the differences between amorphous and crystalline regions.[71-72] The crystalline regions will be tightly packed and therefore have restricted molecular mobility comparative to the amorphous regions, consequently their relaxation times will be longer.

In this chapter solid state NMR, XRD and DSC measurements will be used to highlight the different information provided by each technique for the analysis of PLA and track the degradation of different PLLA/PDLA blends. This will be achieved by observing how the molecular mobility changes over the course of a year from solid state NMR $T_{1\rho}$ relaxation and cross polarisation, T_{CH}, times. This is the related to the WAXS and SAXS patterns as well as the average particle size and hard spheres radius. Finally, this will then be compared to the changes in the T_m from DSC measurements.

4. 2 Materials and Methods

4.2.1 Materials

The PLA samples were synthesised and supplied by Total Corbion PLA, Netherlands. These samples were low quality stereocomplex poly(D,L-lactide powder (scPLA) used in the heat treatment study and high quality stereocomplex poly(D,L-lactide powder (scPLA) used in the heat treatment and aging studies; pure PLLA (L105) powder, medical grade (MG) PLA pellets and industrial grade (IG) PLLA (PL38) pellets also used in the aging study with. The quality of scPLA is defined by the number of homocrystalline regions deconvoluted in the ^{13}C CPMAS NMR measurements, whereby low quality has two components and high quality has one component.

In the long term aging study samples were measured over the course of a year, being stored in three distinct regimes, named ‘room’ where the samples were kept in the laboratory under conditions of ambient temperature and humidity; ‘glovebox’ where the samples were stored under nitrogen at ambient temperature; ‘freezer’ stored at -18 °C. In the heat treatment studies the samples were heated for 12 hours at 200 °C. All samples were measured as supplied after heating at 200 °C for 12 hours for all measurements described in 4.2.2.

4.2.2 Methods

All ^{13}C Solid State Nuclear Magnetic Resonance measurements were performed at 9.4 T using a Bruker Avance 400 MHz spectrometer operating at ^{13}C Larmor frequency (ν_o) of 100.59 MHz. These experiments were performed using a Bruker 4 mm HX probe which enabled a MAS frequency of 12 KHz to be implemented. Pulse length calibration was performed on alanine$_{(s)}$ from which a π/2 pulse time of 2.5 μs was measured. All measurements were undertaken with a π/2 nutation angle along with a delay between subsequent pulses of 10 s. A cross polarisation contact time of 1500 ms was used with a 70-100 % ramp[73] for ^{13}C cross polarisation magic angle spinning (CPMAS) experiments. The $T_{1\rho}$ relaxation experiments used spin lock delays from 0.3 to 50 ms, the T_{CH} experiments used contact times of 0.1 to 10 ms. $T_{1\rho}$ times were calculated using $I = I_0 exp\left(\frac{-\tau}{T_{1\rho}}\right)$, where τ is the spin-lock pulse length, T_{CH} build up times were calculated using a single component exponential fit. For the determination of the integration of the deconvoluted components and the fitting of the subsequent curves were performed using Dynamics Center, Bruker. All data was processed using Bruker TopSpin and the initial deconvolutions were performed using OriginPro 2016.

All ^{13}C chemical shifts were externally referenced against the IUPAC recommended primary reference of $Me_4Si_{(l)}$ (1 % in $CDCl_3$, δ_{iso} = 0.0 ppm), via the secondary solid alanine$_{(s)}$ reference (δ_{iso} = 20.5 ppm)[74].

Thermal analysis data were measured by differential scanning calorimetry (DSC, Mettler Toledo, Leicester, UK). All measurements were performed under nitrogen, heating from 25°C to 250 °C at a rate of 10°C/min. Powder X-ray diffraction was performed on a Panalytical X-Pert Pro MPD Kα1 over a 2θ range of 8-40° under Cu Kα (1.54).

Small angle X-ray scattering (SAXS) measurements were performed on a Xenocs Xeuss 2.0 equipped with a micro-focus Cu Kα (1.54) Å source under vacuum. Scattering was measured by a Pilatus 300k hybrid photon counting detector with a pixel size of 0.172 mm x 0.172 mm. The distance between the detector and the sample was calibrated by using silver behenate ($AgC_{22}H_{43}O_2$). Measurements were taken over a q range of 0.004 to 0.16 $Å^{-1}$. Wide angle X-ray scattering (WAXS) was performed simultaneously with a q range of 1.31 to 3.26 $Å^{-1}$, q values were converted to 2θ angles using the equation $q = 4\pi\sin(\theta)/2$, where λ is the wavelength of Cu, 1.54 Å. SAXS and WAXS data was acquired and processed using Foxtrot 3.3.4 software. All SAXS parameters were extracted as described in Chapter 3 section 3.5.

4.3. Results

4.3.1 Initial studies of stereocomplex PLA

Powder XRD produces a pattern of diffraction peaks which can be attributed to different crystalline domains. The initial powder pattern of the stereocomplex samples showed many peaks that can be attributed to the homocrystalline and stereocomplex domains, Figure 4-2 (left). After the heat treatment, the number of diffraction peaks are reduced, the peaks that have been removed are those produced by homocrystalline domains.

Differential scanning calorimetry measures the heat output as the temperature increases, this allows for determination of the melting points among other thermal characteristics. In scPLA as provided there are two melting points for the homocrystalline and stereocomplex domains at approximately 180 °C and 230 °C respectively, Figure 4-2 (right). After the heat treatment only one melting point is present, at the higher temperature for the stereocomplex domain, the DSC results show successful removal of the homocrystalline domains, Figure 4-2 (right).

There are three carbons present in the PLA monomer; COO, CH and methyl functional groups, the resonance peaks in the ^{13}C spectrum are at 171, 69 and 16 ppm respectively.

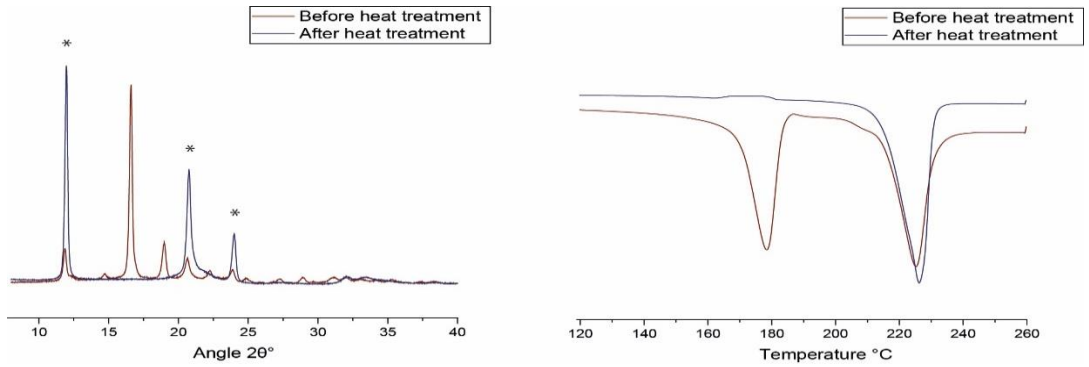

Figure 4-2. The powder X-ray diffraction pattern (left) and differential scanning calorimetry (right) results for low quality stereocomplex poly(d,l-lactide) before and after heat treatment at 200°C for 24 hours. The starred diffraction peaks are attributed to the stereocomplex crystalline component.

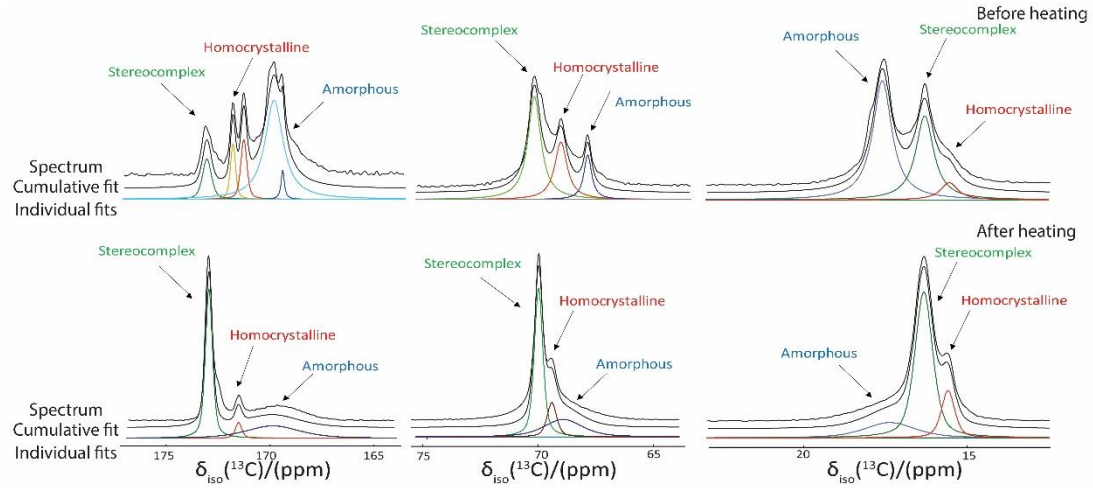

Figure 4-3. The ^{13}C CPMAS spectra for low quality stereocomplex poly(d,l-lactide) before (top) and after (bottom) a heat treatment at 200°C for 24 hours with the individual fitted peaks, the cumulative fitted spectrum and the acquired spectrum.

The resonance peaks can be deconvoluted into three gaussian-lorentzian components, each of these can be attributed to the stereocomplex, homocrystalline and amorphous domains, Figure 4-3. The fitting procedure was performed on the ^{13}C spectra acquired before and after heat treatment, with three components fitted in each. The three components have different intensities before and after heat treatment with the amorphous component broadening, the homocrystalline component being reduced and the stereocomplex component increasing.

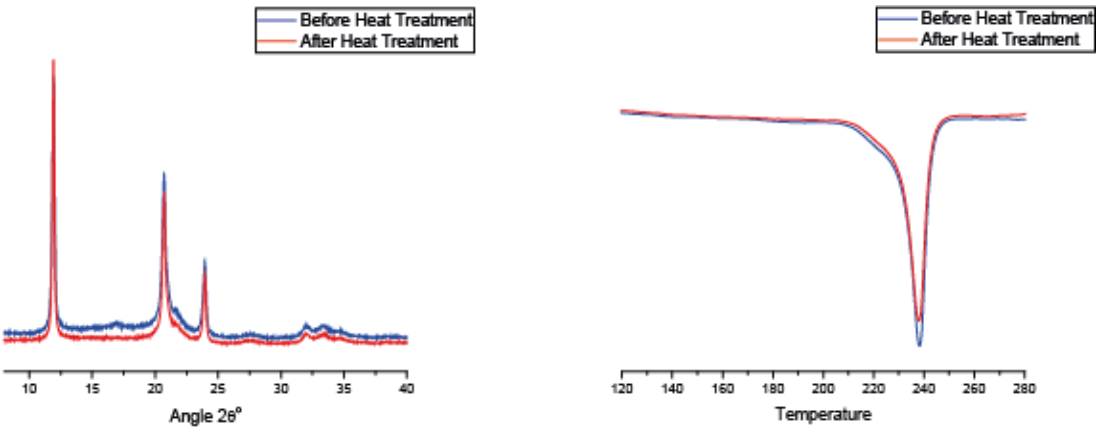

Figure 4-4. The powder X-ray diffraction pattern (left) and differential scanning calorimetry (right) results for high quality stereocomplex poly(d,l-lactide) before and after a heat treatment at 200°C for 24 hours.

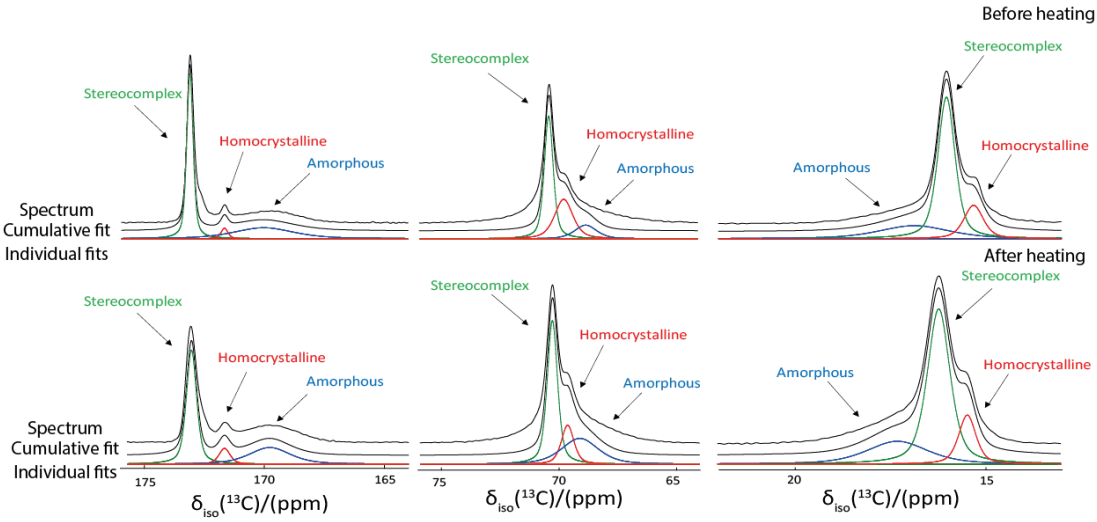

Figure 4-5. The ^{13}C CPMAS spectra for high quality stereocomplex poly(d,l-lactide) before and after a heat treatment at 200°C for 24 hours with the individual fitted peaks, the cumulative fitted spectrum and the acquired spectrum.

The experiments from the initial study of PLA were repeated on a second sample of higher quality scPLA. The initial XRD showed only diffraction peaks from the sc component and the DSC curve showed one melting point at the temperature for the sc component, Figure 4-4. The CPMAS NMR spectrum however for high quality scPLA both before and after heating showed three components, again attributed to the sc, hc and amorphous components, Figure 4-5.

4.3.3 Long term studies

After the methodology of combining solid state NMR, XRD and DSC was developed, these three techniques with the addition of small-angle X-ray scattering have been implemented on four PLA samples. Measurements have been acquired every month over the course of a year, the four samples are split into two powders, scPLA and L105 which is pure PLLA, and two pellets, medical grade (MG) PLA and industrial grade (IG) PL38 PLLA. The NMR spectra of the four samples, whilst all having the same three main resonances, have very different splitting's, Figure 4-6.

For L105 which is a PLLA powder there is a single component within each resonance, these are at the shifts correlating to the amorphous component, as determined from the initial studies of scPLA. The two pellets, MG and PL38 both have pronounced splitting's from the different crystalline regions. Unlike scPLA they do not have a broad amorphous component and have greater crystallinity and more crystalline regions. None of the crystalline regions

will be attributed to stereocomplex sites especially for PL38 as it is pure PLLA. The splittings are more pronounced for PL38 showing that it has greater crystallinity than MG PLA.

The four samples were initial stored in a room under ambient conditions, the $T_{1\rho}$ and T_{CH} times have been tracked. The amorphous region in scPLA has the greatest stability in terms of molecular mobility over the course of a year, the two crystalline regions fluctuate between each month however there is no overall increase or decrease in $T_{1\rho}$ times, Figure 4-7. The T_{CH} times, which can be used as an indication of how the interaction strength and distance between adjacent PLA chains changes, are stable for the methyl group and have little overall change for the COO group. For the CH group there is an increase in T_{CH} over time which would suggest that the distance between the PLA chains is increasing, this change is also consistent across all three regions, suggesting that the potential rearrangement of the polymer chains has no relation to crystallinity and is affecting the entire polymer matrix.

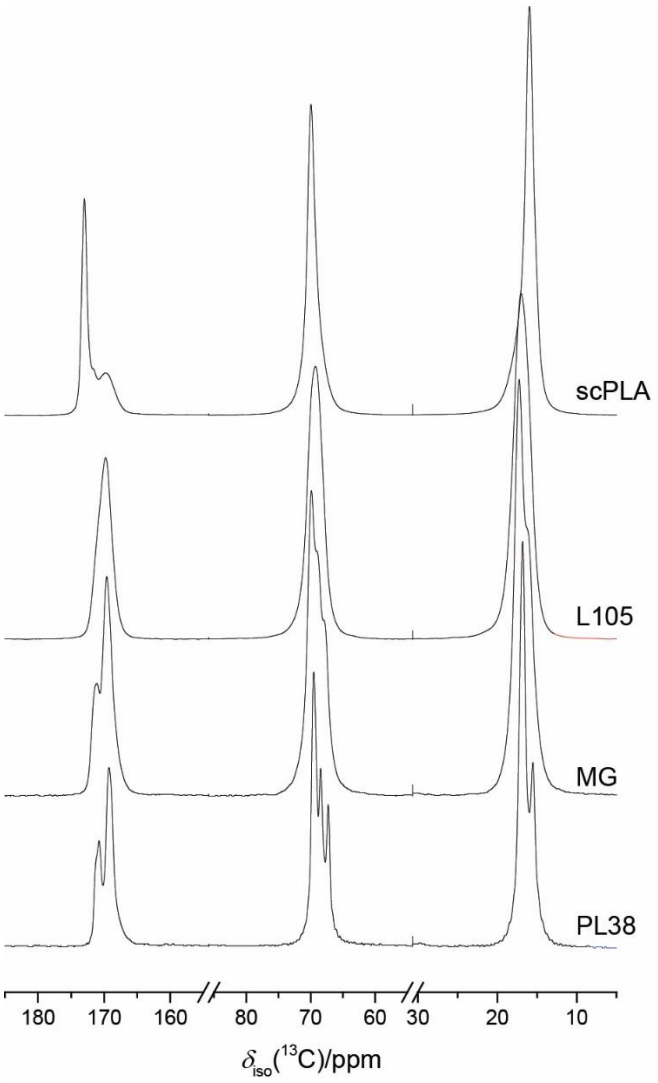

Figure 4-6. The ^{13}C CPMAS spectra for stereocomplex scPLA, industrial grade PLLA, L105 and medical grade PLLA, MG and PL38.

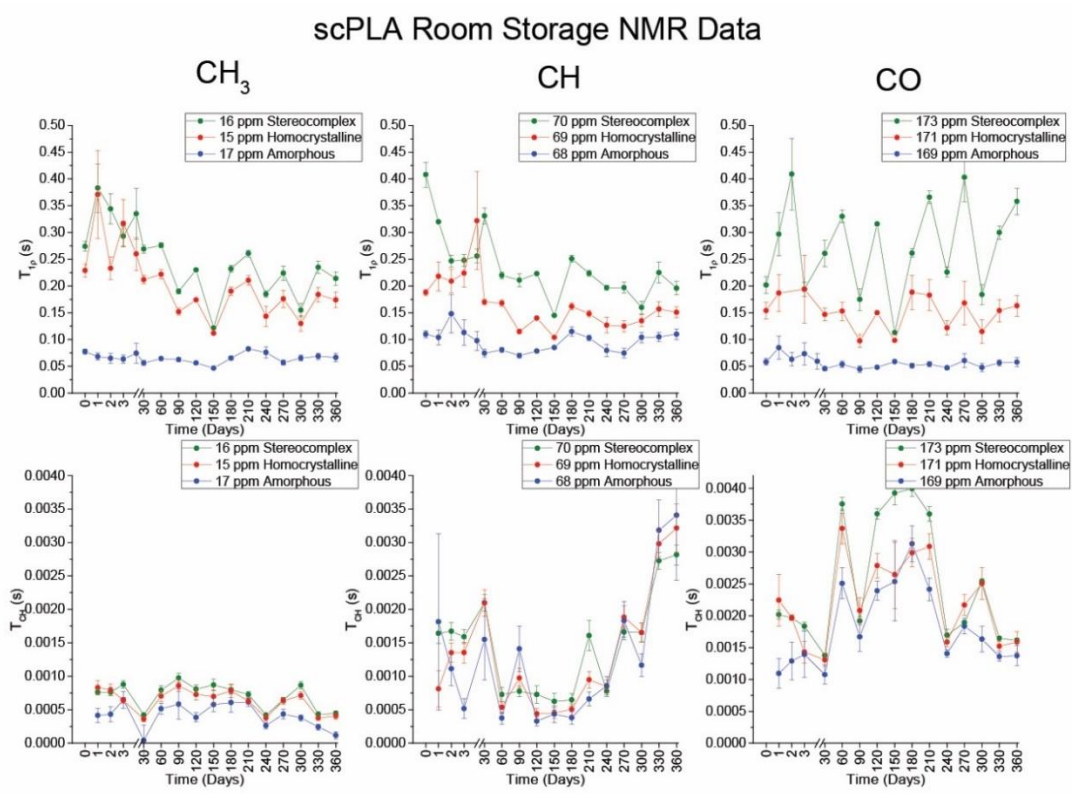

Figure 4-7. The change in $T_{1\rho}$ (top) and T_{CH} (bottom) times for scPLA stored in room conditions for the two crystalline and one amorphous region for CH_3 (left), CH (middle) and COO (right).

L105 is a fully amorphous PLLA material and has similar behaviour to the amorphous component in scPLA, the T_{CH} times for the methyl group also have the same behaviour as in scPLA. The T_{CH} times for CH and COO have a more consistent behaviour than in scPLA with a contrasting change of an increase in time for CH and decrease in time for COO, Figure 4-8. This converse relationship suggests that there could be a rearrangement of the PLA helix resulting in COO having greater proximity to H species, namely from the methyl groups. The MG PLA, Figure 4-9 and IG PL38 PLLA, Figure 4-10 have both amorphous and crystalline components, across all functional groups all of the components were motionally stable and had the same T_{CH} activity as scPLA and L105. This shows that the form the PLA is in, powder or chunk, does not affect the ability for helical rearrangement and change of chain distance and interaction strength.

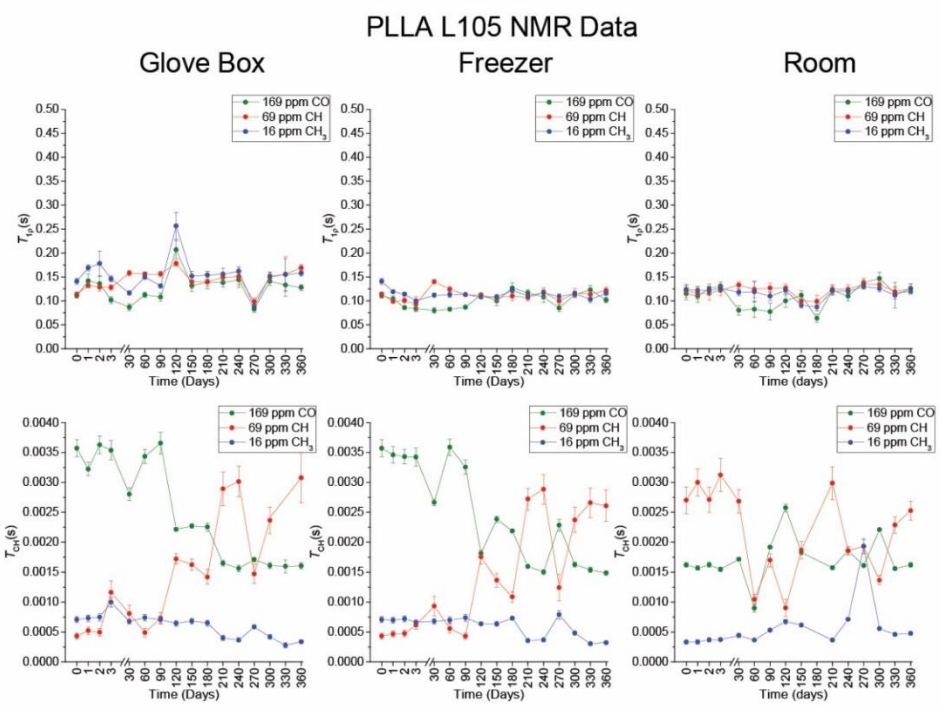

Figure 4-8. The change in $T_{1\rho}$ and T_{CH} for L105 stored in a glove box (left), freezer (middle) and under room conditions (right). All three functional groups are plotted together for the single amorphous region.

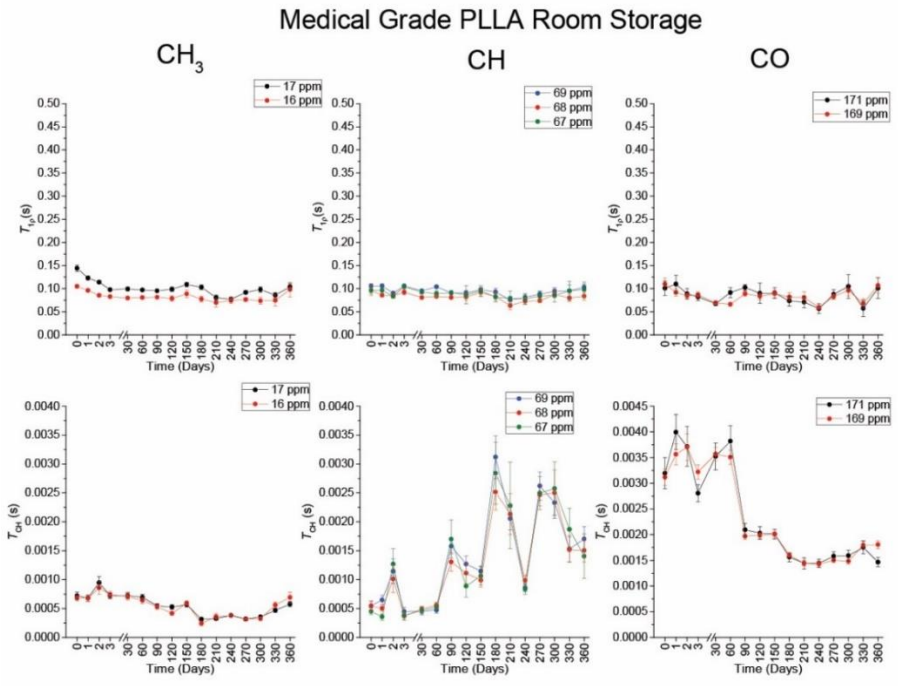

Figure 4-9. The change in $T_{1\rho}$ (top) and T_{CH} (bottom) times for medical grade PLA stored in room conditions for the two crystalline and one amorphous region for CH_3 (left), CH (middle) and COO (right).

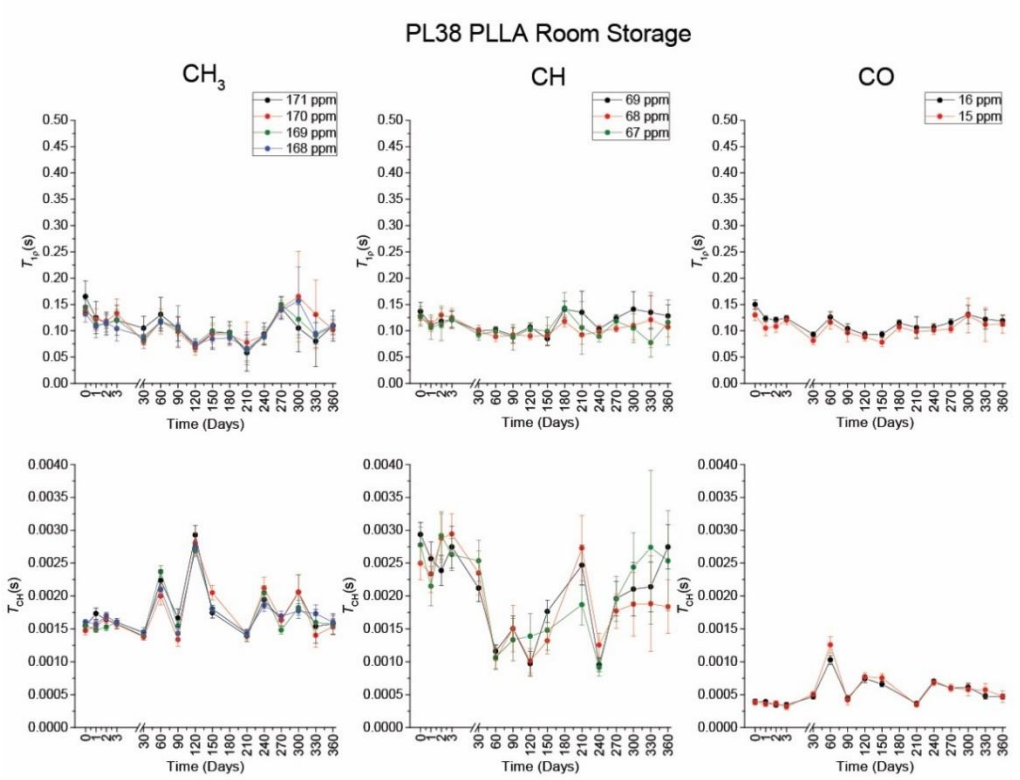

Figure 4-10. The change in $T_{1\rho}$ (top) and T_{CH} (bottom) times for industrial grade PLLA stored in room conditions for the two crystalline and one amorphous region for CH_3 (left), CH (middle) and COO (right)

SAXS measurements have been performed over the course of a year for all four different PLA materials, Figure 4-11 (right). The SAXS scattering pattern for the MG and PL38 show interaction between particles and can be fit using a hard spheres model to determine the hard spheres interaction distance. The two powders scPLA and L105 do not show any interaction between particles, therefore only an average particle size was able to be determined. Along with the particle size distribution, the particle form factor can be determined which relates to the structure of the particle, all four PLA samples have a spherical shape as determined by the form factor. The structure factor is also determined from the SAXS data, this is related to the interparticle forces and the strength of the interactions, the structure factor for the powders is dilute and for the pellets is concentrated. In a dilute system the particle densities do not have any alternating arrangements of particle density suggesting a lack of short range order. It is not possible to determine the degree of crystallinity for these samples as an amorphous reference sample is needed. Visually the scattering pattern does not change over the course of a year for all of the samples; the only

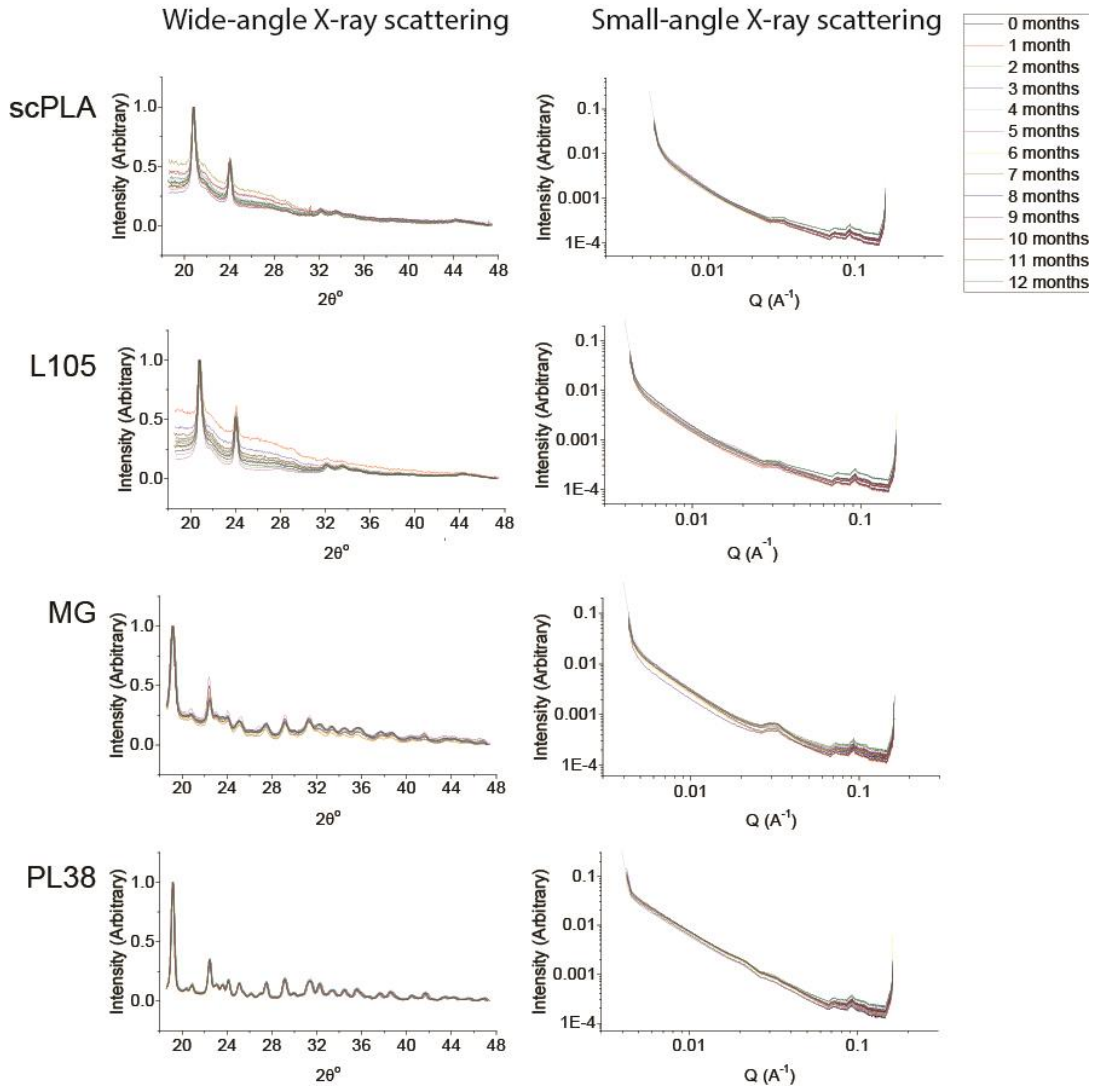

Figure 4-11. The WAXS (left) and SAXS (right) patterns for the four PLA samples stored under room conditions over the course of a year.

changes are in intensity, which are attributed to instrumental fluctuation and inhomogeneity in the sample.

The mean particle size has been determined and tracked over the course of a year, . The two powders both have similar particle sizes and regardless of the storage condition the size does not change significantly, the slight fluctuations are expected as the powders are not homogenous. The particle sizes for MG and PL38 are completely different to each other and are either side of the powders. As with the powders the mean particle size fluctuates slightly but not significantly enough to be a sign of degradation. Whilst the same chunk of MG and PL38 was used each month slight variations in crystal orientation during measurement caused this variation. Comparing these measurements there does not appear to be much effect from degradation.

The only exception is for MG stored under room conditions, where in the last two months the mean particle size increased, this results from preferred orientation which would cause changes in the particle size distribution and consequently

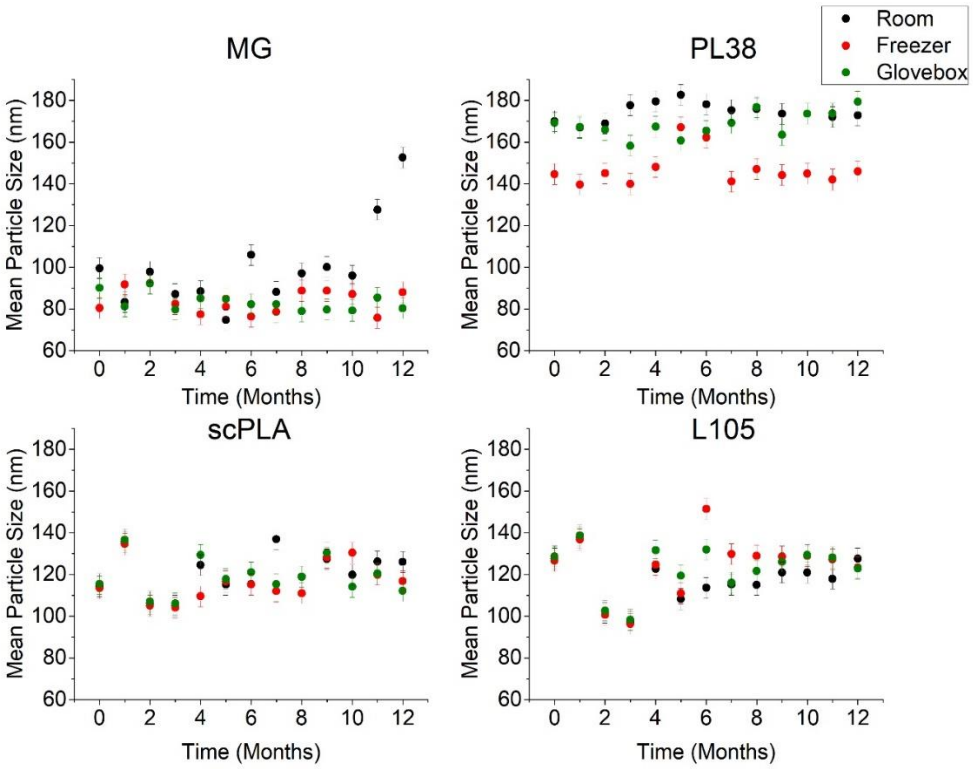

Figure 4-12. The mean particle size measured from small-angle X-ray scattering experiments tracked over the course of a year for all four samples stored under room conditions, in a freezer and in a glovebox.

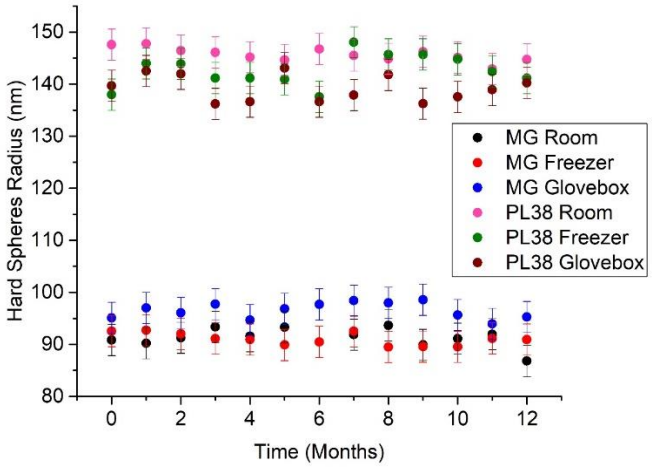

Figure 4-13. The hard sphere radius measured from small-angle X-ray scattering experiments tracked over the course of a year for all MG PLA and IG PLLA pellets stored under room conditions, in a freezer and in a glovebox.

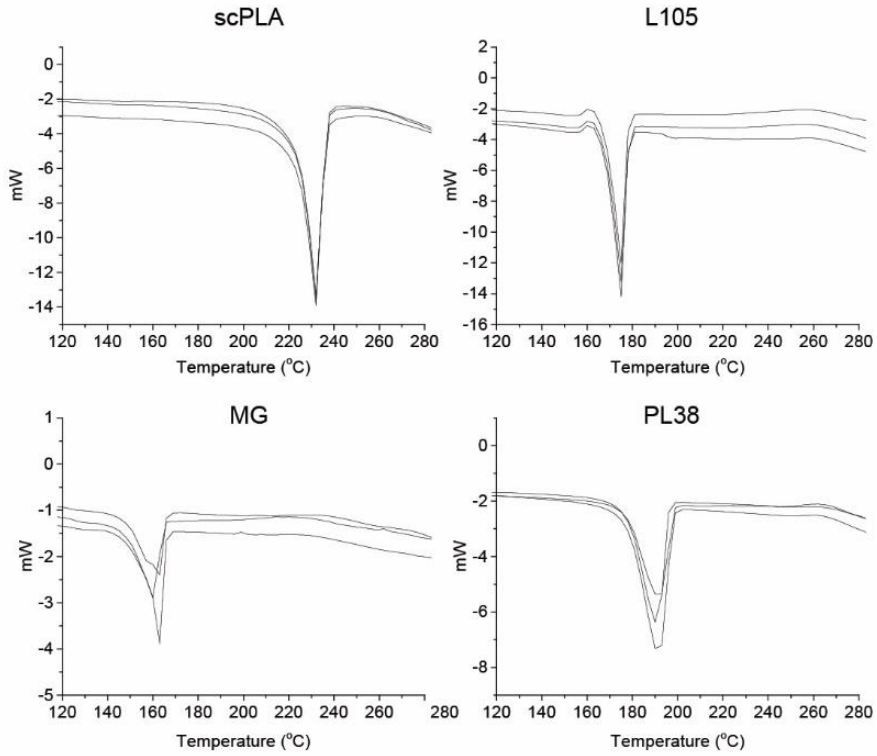

Figure 4-14. The differential scanning calorimetry first heating scans showing the melting temperature for three repeats from the same batch of scPLA, L105, MG and PL38 undertaken in one session.

mean particle size. The difference in hard spheres radius for MG and PL38 mirrors the difference between the average particle size. Changes in hard spheres radius is even less pronounced than for the mean particle size showing that over time the size of the particles is stable regardless of the storage conditions.

The WAXS patterns have been collected simultaneously with the SAXS patterns, similarly to these there is no change in the scattering pattern over the course of the year for the MG and PL38 pellets, Figure 4-11 (left). There are however changes in the intensity and baseline for the two powders but not 2θ's. This will be because the samples each month come from the same batch but are not the exact same grains each time and will therefore have different surface morphology at each timepoint. This along with the SAXS patterns show that over the course of a year there is minimal change in the long range order.

In order to determine whether any changes observed in the DSC will be due to degradation or due to the inhomogeneity of the powders or pellets three samples from a single batch were measured, Figure 4-14.

For the two powders the line shape and melting temperatures were consistent across the batch, the two pellets however, especially MG PLA, had different line shapes, this suggests that whilst degradation could have an impact on the T_m it cannot conclusively be said for the

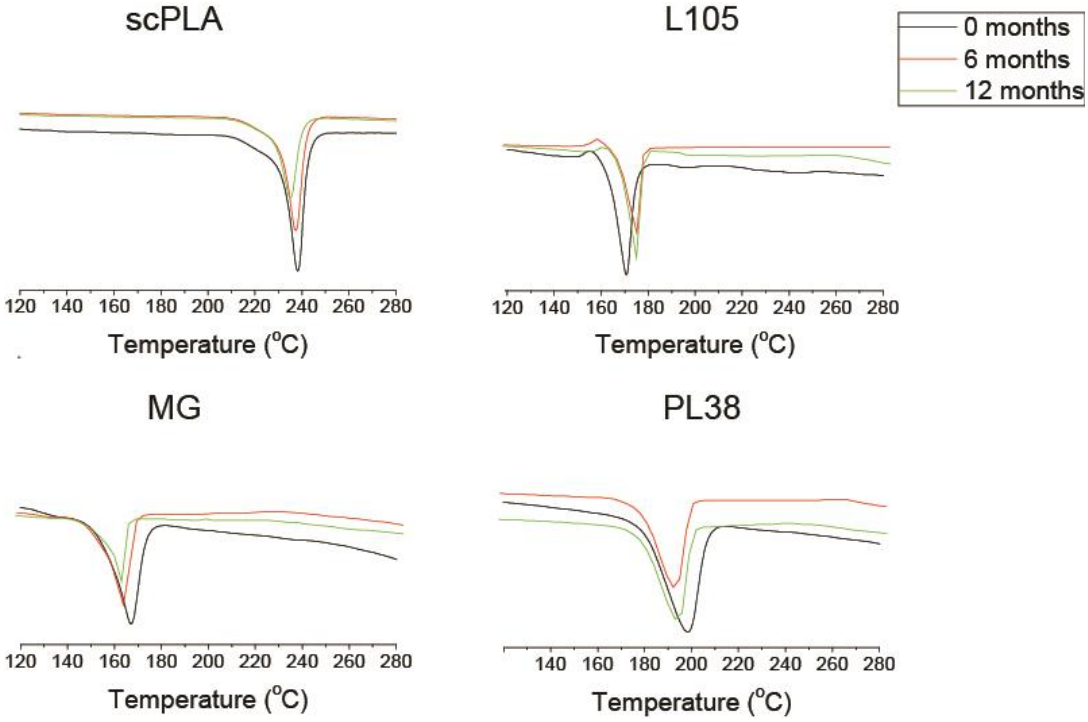

Figure 4-15. DSC for stereocomplex scPLA, industrial grade PLLA, L105 and medical grade PLLA, MG and PL38, stored under room conditions at 0, 6 and 12 months.

pellets to be so. The lack of change in the $T_{1\rho}$ times and SAXS/WAXS data, especially for MG PLA, all suggest that changes will be due to batch inhomogeneities.

The melting temperature has been shown at 0, 6 and 12 months, whilst there are differences between the melting temperature there is no systematic change This can be confidently attributed to some batch variation but not to conclusively to degradation therefore for this study the DSC is also unreliable for tracking degradation of unprocessed PLA.

Two main contributors to degradation are temperature and humidity, to investigate the effect of these two factors the same measurements were performed on samples stored in a freezer and in a glovebox. The $T_{1\rho}$ and T_{CH} times had the same trend as the samples stored under room conditions, Figure 4-8, Appendix, Figure A-1, Figure A-2, Figure A-3. The SAXS, WAXS and DSC patterns also had no change regardless of the condition in which the sample was stored, Appendix, Figure A-4, Figure A-5 and Figure A-6.

The initial interesting finding from the first studies undertaken on the low quality scPLA sample was the contrasting results between XRD, DSC and solid state NMR. The three techniques each provide information on different ranges, *i.e.* XRD shows long range periodicity whereas NMR provides information on short range chemical environments. It is reasonable to expect scPLA to be comprised of an amorphous component and stereocomplex (sc) sites, as is seen in the XRD and DSC results however, as is shown by NMR, there is a third component present, the homocrystalline (hc) site.

The initial studies of low quality scPLA suggest a transition from scPLA with two types of crystalline site, sc and hc to a highly stereocomplex PLA after heat treatment. When the measurements were performed on an scPLA sample of higher quality the initial XRD and DSC experiments showed only sc sites both before and after annealing. The NMR however showed the presence of three sites both before and after heating. Annealing scPLA results in phase transitions, recently there have been many studies looking at the presence of mesophase PLA.[75] The mesophase has intermediate ordering between amorphous and crystalline phases and limited mobility.[76] The assignments of the three different sites was based on both the position of the components and the relaxation times. Tsuji *et al* performed ^{13}C CPMAS experiments on stereocomplex PLA, the COO resonance was deconvoluted for component analysis and the three components then attributed to sc, hc and amorphous components.[77] The NMR measurements show that there is no mesophase present as a fourth component would be present at a $T_{1\rho}$ time between the amorphous and crystalline components. This method was used to determine the components for the samples in this

study, the component assignment was confirmed using $T_{1\rho}$ relaxation times. Each of the three components has a different range of mobility, naturally the amorphous component will have the greatest mobility and therefore have the shortest relaxation time. The crystalline components have order to them due to the interactions between the chains, the homocrystalline component has greater mobility due to weaker interactions between chains of the same configuration therefore, the hc component will have a slightly shorter relaxation time[78-79]. Due to the confirmation of the component assignments by $T_{1\rho}$ relaxation it is safe to conclude that mesophase PLA is not present in our systems, however a way to further confirm this would be to perform Fourier transform infrared studies.[80]

During the first long term studies under room conditions, the amorphous component in scPLA was stable over the course of a year whereas the two crystalline components $T_{1\rho}$ relaxation times fluctuate significantly over time. This shows that the mobility of the crystalline chains changes significantly. The mobility is related to the strength of the interactions between the chains in the two crystalline sites, the change in mobility therefore indicates that the interactions are becoming weaker or stronger between months[81]. The changes in T_{CH} times were also investigated and fluctuated for all three components for both the high and low quality scPLA. If changes are approached from the perspective of changes in interaction strength and distance then it appears that the interaction strength is constantly changing both on a long and short term basis, and overall after 4 months the helical arrangement of PLA becomes distorted affecting the CH and COO regions differently.

To better understand the cause of the changes in mobility and interaction strength both temperature and humidity were investigated. Even though the effect of either temperature or humidity were removed the only change over time was the T_{CH} times under both conditions for the CH and COO groups, as previously suggested this will be due to changes in distance between PLA chains and strength of interaction, the two main contributors to the CP process. Based on the different response for the two functional groups there is clearly no movement of the chain as a whole rather it is the groups individually, this is why it is suggested that there is polymorphic rearrangement or rearrangement of the PLA helix. The $T_{1\rho}$ times were unaffected by the storage condition for the three samples other than scPLA, the only difference between the samples was the presence of stereocomplex crystalline regions, the presence of D-lactide forming stereocomplex regions appears to decrease the stability of the molecular motion over time.

Several groups have researched the effect of moisture exposure on the degradation of PLA, the studies took a gravimetric analysis approach to the measurement of degradation[82]. One of the major pathways of degradation for PLA is hydrolysis of the ester linkages resulting in the production of carboxylic acid end groups. The CPMAS spectra of the samples in this study do not change over time suggesting that there is no alteration in the structure of the samples, which would be seen if the end groups were changing due to hydrolysis.

The PLLA powder, L105, was fully amorphous, the amorphous component had the same nature as the amorphous component in scPLA, whereby there was no change in the $T_{1\rho}$ times over the course of the year for all three storage conditions. Although the trend is the same as scPLA the actual times are different, 0.05 - 0.1 s for scPLA and 0.1 - 0.15 s for L105; This will be caused by the crystalline regions introducing more order overall and restricting the amorphous components.

The SAXS data shows a great difference between the powders and pellets, the form factor shows the greatest difference. The two powders have a dilute form factor whereas the two pellets have a concentrated form factor. Concentrated samples have greater order than dilute systems, this suggests that the pellets have greater order than the powders, this is also reflected in the solid state NMR measurements, in particular the ^{13}C CPMAS spectra. There is no change in the SAXS and WAXS patterns for the concentrated systems showing that the long range order does not change over time regardless of the storage conditions. The two dilute systems also have no change that can be attributed to changes in order but rather is caused by inhomogeneities of the powders. The DSC additionally shows that there is no trend in the change in T_m over time and that there is batch variation again highlighting the inhomogeneity of both the powders and pellets. There is also no change in the average particle size for all four systems and hard sphere radius for the two pellets, which combined with the rest of the long term data again shows there is no change in the systems over time other than the change in T_{CH} times.

4.4. Conclusion

The combination of XRD, DSC and solid state NMR has been successful in highlighting the advantages and limitations of each of the techniques as well as being able to track motional changes and the changes in interaction strength in four different poly(lactide) samples. Stereocomplex PLA has been used to highlight the different information that can be elucidated from the three techniques and that a multi technique approach is best for this

study. The integration of solid state NMR into this study allowed for the identification of homocrystalline components in scPLA which were not detected by XRD and DSC.

Combining all three techniques has not been able to show changes in the mobility of the different regions, long range order and particle size and hard spheres radius. The only change that occurred was the change in T_{CH} time for two of the functional groups present in PLA, CH and COO, which suggests that there could be a rearrangement of the PLA helix which does not however effect the overall mobility of any of the functional groups especially or the PLLA samples.

5. Injection Moulding of Polylactide

5.1 Introduction

Injection moulding is a common way of forming end products of poly(lactide), there are several stages to the injection moulding process. First, the starting material is fed into the injection moulding machine via the hopper. The material is melted in the heated barrel which contains the reciprocating screw which provides additional heating via shearing of the material. The molten material is then injected under high pressures into the mould. The temperature of the mould will affect the crystallinity of the end product. In this study a mould temperature of 30 °C produces amorphous PLA bars and a mould temperature of 130 °C produces crystalline PLA bars. Following the injection of the molten material a holding phase is implemented. When the material cools in the mould it starts to shrink, in the holding phase additional material is injected to fill the mould and remove any voids. The holding time and pressure is dependent on the material used. The material is then cooled and released from the mould.[83]

Polymer additives take on the role of tailoring the macromolecular properties to improve the processability and end-use properties.[84] Additives can take many different forms and is influenced by the production method, these include powders, beads, emulsions and spheres. The ideal form is highly homogenous spheres that possess suitable mechanical resistance and will not segregate in the polymer mixture.[85] The properties of PLA end products can be modified by adding nucleating agents, plasticisers, fillers, impact modifiers and stabilisers.

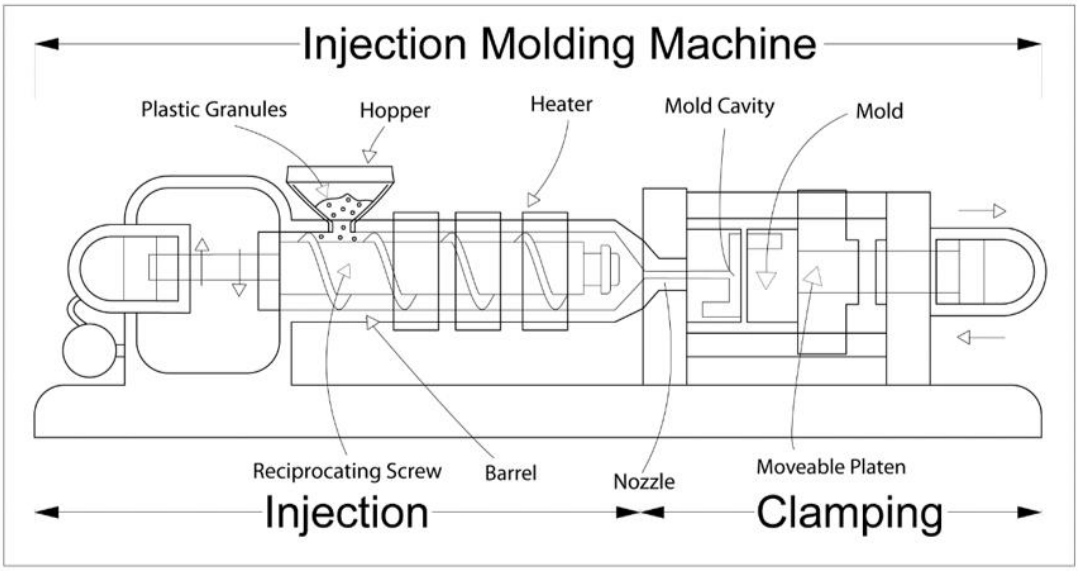

Figure 5-1. A schematic of the injection moulding machine, showing the hopper, heated barrel with reciprocating screw, mould cavity and mould.[86]

Controlling polymer crystallinity can also help to improve the properties of PLA end products. The degree of crystallinity and presence of additives affects the mechanical, thermal, and molecular properties of the PLA end product.[87] The Young´s modulus is an important measure of stiffness of a material, it is mostly affected by additives however below a critical particle size the size will start to influence the stiffness.[88] The size of the particles in the material can also affect the brittleness of the material.[89-90] A smaller particle size can result in brittleness, the addition of interfacial crystallites on the other hand can strengthen the material and increase the toughness. There has been recent work into controlling properties using homocomposites of PLA instead of introducing additives.

Plasticisers are used to increase the flexibility and toughness of a plastic and will reduce the Young's modulus, density, glass transition temperature and melt viscosity of the polymer.[91-92] During the plasticisation process secondary bonds are formed between the plasticiser and polymer chains which increases the distance between neighbouring chains consequently reducing the interaction and increasing the mobility. Impact modifiers are used to overcome the inherent brittleness of most plastics. Impact modifiers tend to be elastomeric and have a lower Young's modulus and low glass transition temperature relative to the polymer matrix. Impact modifiers are incorporated either during polymerisation or in processing in the form as particles. Nucleating agents are used to shorten the processing time in injection moulding, reduce average particle size and improve mechanical properties. Nucleating agents can be in many chemical structures, for example minerals such as talc, organics and organic salts.[93] Fillers will have a range of effects depending on the shape and size, for example fibres increase both the tensile and flex strength whereas spheres or cubes have no effect on these properties. The size mostly effects the tensile and impact strength, a larger size creates greater stress in the polymer matrix. In order to better strengthen the properties a uniform particle size is required. Closely related to the particle size another consideration for fillers is the surface area which will affect the processibility of the polymer. This is due to the degree of wetting, a well-wetted filler will flow more easily, when the surface area is too large three will be poor dispersions and no-uniform properties. Unlike the other additives which enhance the physical properties, stabilisers are used to prevent degradation.[94] Stabilisers are often used so that they undergo sacrificial reactions to protect the polymer matrix. Stabilisers are rejected from crystals during processing as they are soluble in the melt consequently they have no effect on the end product.[95]

Talc ($Mg_3Si_4O_{10}(OH)_2$) can be used as both a nucleating agent at < 3 wt% or as a reinforcing filler at 10-40 wt%. The effect of talc compared to other nucleating agents has been

investigated in PLA and has also been found to increase crystallinity of PLA from 2% up to 25% with significant improvement to the Young's modulus.[96-97] Talc has Its plate-like structure is held together by weak Van der Waal's forces which allows for delamination at low sheer stresses and easy dispersion.[97-98] When used as a filler talc increases the tensile modulus and stiffness and conversely reduces the strain-to-break and impact strength.[87, 99] When used as a nucleating agent talc, in addition to shortening processing time, increases crystallinity and decreases crystallisation times.[93]

For semicrystalline polymers the effect of injection moulding on the interfacial crystalline arrangements has been investigated. Arias *et al.* used DSC, XRD and tensile testing amongst other techniques to see how homocomposites of PLA are affected by the induction of interfacial stereocomplex crystallites.[100] Their method was successful in showing that the formation of interfacial stereocomplex crystallites enhanced the mechanical properties of the materials, as such a similar method will be implemented in this study.

During the injection moulding process many defects can occur, understanding what these are and how they arise is important for overcoming them.[101] Wavy patterns called flow lines appear on narrow sections and have slight discolouration to them. They may also occur at the entrance of the mould and present as rings. These are caused by nonuniformity of material cooling; the way to overcome this is to increase injection speed pressure and temperature so that the mould is filled before cooling starts. Other lines can appear when the initial injection of the molten material solidifies before the mould is filled caused by excessive injection pressure.

When the injection speed is too fast air can be trapped in the mould this can lead to burn marks, these marks can also be formed if overheating occurs either at the melt or in the mould. If the cooling speed is too rapid the plastic will not cool uniformly and will lead to warping. As well as causing burn marks trapped air can form vacuum voids, these can also be formed when the material closer to the mould walls cools more quickly than the inside which pulls the hot material towards the wall. As well as inadequate injection pressure, the viscosity of the material effects the formation of air bubbles. Sink marks have the opposite formation process to vacuum voids whereby the material cools quickly in the middle and pulls the hot material near the walls inwards.

The mishandling of the unprocessed material can also cause defects that will be apparent after moulding. Discolouration occurs when there are leftover pellets in the hopper, or resin in the nozzle or mould from previous use. Delamination is where thin layers of the plastic

peel or flake due to inefficient bonding of materials. This is usually caused by contamination of the starting material, excess release agents in the mould and moisture due to insufficient drying. The mould design and maintenance are also contributing factors to defect formation.

This study will investigate the relationship of the mechanical and thermal properties of 9 injection moulded PLA samples with different crystallinities and additives, to the presence of crystalline domains from wide angle X-ray scattering and the average particle size and interaction distance as measured by small angle X-ray scattering. In the injection moulded materials, the “particles” are referring to an individual crystallite within a crystallite domain. The molecular mobility of the crystalline domains as determined by solid state NMR measurements will also be compared.

5.2 Materials and Methods

5.2.1 Materials

Tensile bars and impact bars were produced by injection moulding at Wangeningen University and research, University of Wangeningen, Netherlands. The injection moulding samples and parameters are given in Table 5-1. The starting form of LX175, L130 were powders, the starting form of PL38, 120318-VI and 120318-VII were pellets.

5.2.2 Methods

Tensile tests were performed using a Zwick Z010 all-round line 10 kN mechanical testing machine according to ISO 527-1. The Young’s modulus, maximum stress and strain at break for each of the injection moulded samples were determined Impact tests were performed using a Ceast impact tester according to ISO 179. Impact tests were performed on notched and unnotched injection moulded impact bars of each of the samples. Notched tests are used to simulate the effect of faults in a sample. Heat Deformation Temperature-B tests were performed using a RAY-RAN HDT-VICAT softening point apparatus according to ISO 075 at a heating rate of 2 °C/min. The impact bars were submerged in an oil bath and heated and placed under a constant pressure until deformation occurred.

Thermal analysis data was measured by differential scanning calorimetry (DSC, Mettler Toledo, Leicester, UK). All measurements were performed under nitrogen, heating from 25°C to 250°C at a rate of 10 °C/min. The tensile bars were cut into small pellets to fit into 40 µm aluminium pans.

Small angle X-ray scattering (SAXS) measurements were performed on a Xenocs Xeuss 2.0 equipped with a micro-focus Cu Kα (1.54) Å source under vacuum. The tensile bars were

mounted whole onto the sample holders attached with double sided tape. Scattering was measured by a Pilatus 300k hybrid photon counting detector with a pixel size of 0.172 mm x 0.172 mm. The distance between the detector and the sample was calibrated by using silver behenate ($AgC_{22}H_{43}O_2$). Measurements were taken over a q range of 0.004 to 0.16 $Å^{-1}$. Wide angle X-ray scattering (WAXS) was performed simultaneously with a q range of 1.31 to 3.26 $Å^{-1}$, q values were converted to 2θ angles using the equation $q = 4\pi\sin(\theta)/2$, where λ is the wavelength of Cu, 1.54 Å. SAXS and WAXS data was acquired and processed using Foxtrot 3.3.4 software. The average crystallite size and hard spheres radius were obtained from the experimental data as described in chapter 3 section 3.5.

All Raman measurements were performed on a Renishaw inVia Raman microscope using a 785 nm DPSS laser over a wavenumber range of 300-2000 cm^{-1}, Renishaw CCD detector and a grating of 1800 lines/mm. A ×20 Olympus objective lens was used to focus the beam into the sample. Calibration was performed on diamond and 3 static scans of 3 s at 50 % laser power were used for the measurements. Measurements were performed on the as prepared tensile bars with no further preparation required.

All ^{13}C Solid State Nuclear Magnetic Resonance measurements were performed at 9.4 T using a Bruker Avance 400 MHz spectrometer operating at ^{13}C Larmor frequency (ν_o) of 100.59 MHz. These experiments were performed using a Bruker 4 mm HX probe which enabled a MAS frequency of 12 KHz to be implemented. Pulse length calibration was performed on alanine$_{(s)}$ from which a π/2 pulse time of 2.5 μs was measured. All measurements were undertaken with a π/2 nutation angle along with a delay between subsequent pulses of 10 s. A cross polarisation contact time of 1500 ms was used with a 70-100 % ramp[73] for ^{13}C cross polarisation magic angle spinning (CPMAS) experiments. The $T_{1\rho}$ relaxation experiments used spin lock delays from 0.3 to 50 ms. The $T_{1\rho}$ values were obtained from the experimental data as described in chapter 4 section 4.2.1. All ^{13}C chemical shifts were externally referenced against the IUPAC recommended primary reference of $Me_4Si_{(l)}$ (1 % in $CDCl_3$, δ_{iso} = 0.0 ppm), via the secondary solid alanine$_{(s)}$ reference (δ_{iso} = 20.5 ppm)[74].

Table 5-1. The injection moulding parameters for the PLA dogbones and impact bars.

Dogbones

sample code	Description	Mould temperature (°C)	Machine temp (°C)	Cooling time (S)	Processing
L130 30C	PLLA L130 (Batchnr 7K002006321/20130908)	30 °C	195/195/195/160/40	15/35	Automatically
L130 103C	PLLA L130 (Batchnr 7K002006321/20130908)	103 °C	195/195/195/160/40	15/120	Automatically
LX175 30C	PLLA LX175 (Batchnr 1712003519)	30 °C	195/195/195/160/40	15/35	Automatically
Purasorb PL38 30C	Purasorb PL38 (Batchnr 1707001317)	30 °C	230/225/220/190/40	15/35	Automatically
Purasorb PL38 103C	Purasorb PL38 (Batchnr 1707001317)	103 °C	230/225/220/190/40	15/90	Automatically
120318-VI 30C	Total-Corbion Reference B Talc	30 °C	195/195/195/160/40	15/35	Automatically
120318-VI 103C	Total-Corbion Reference B Talc	103 °C	195/195/195/160/40	15/35	Automatically
120318-VII 103C	Total-Corbion Reference C Talc	103 °C	195/195/195/160/40	15/35	Automatically

Impact samples

	Description	Mould temperature (°C)	Machine temp (°C)	Cooling time (S)	Processing
L130 30C	PLLA L130 (Batchnr 7K002006321/20130908)	30 °C	195/195/195/160/40	15/35	Not automatically
L130 103C	PLLA L130 (Batchnr 7K002006321/20130908)	103 °C	195/195/195/160/40	15/120	Automatically
LX175 30C	PLLA LX175 (Batchnr 1712003519)	30 °C	195/195/195/160/40	15/35	Automatically
Purasorb PL38 30C	Purasorb PL38 (Batchnr 1707001317)	30 °C	230/225/220/190/40	15/35	Automatically
Purasorb PL38 103C	Purasorb PL38 (Batchnr 1707001317)	103 °C	230/225/220/190/40	15/90	Automatically
120318-VI 30C	Total-Corbion Reference B Talc	30 °C	195/195/195/160/40	15/35	Automatically
120318-VI 103C	Total-Corbion Reference B Talc	103 °C	195/195/195/160/40	15/35	Automatically
120318-VII 103C	Total-Corbion Reference C Talc	103 °C	195/195/195/160/40	15/35	Automatically

5.3 Results and Discussion

5.3.1 Visual Differences

The Raman microscope images allow for the investigation of the homogeneity of the injection moulding process, Figure 5-2. The three pellets all have a rough texture, upon injection moulding the resulting dog bones are smooth, however there are some striations in the direction of the injection and in some cases small indentations.

The appearance of the L130 materials shows the difference that the mould temperature has upon the final dog bones. A mould temperature of 30 °C for the amorphous dog bone

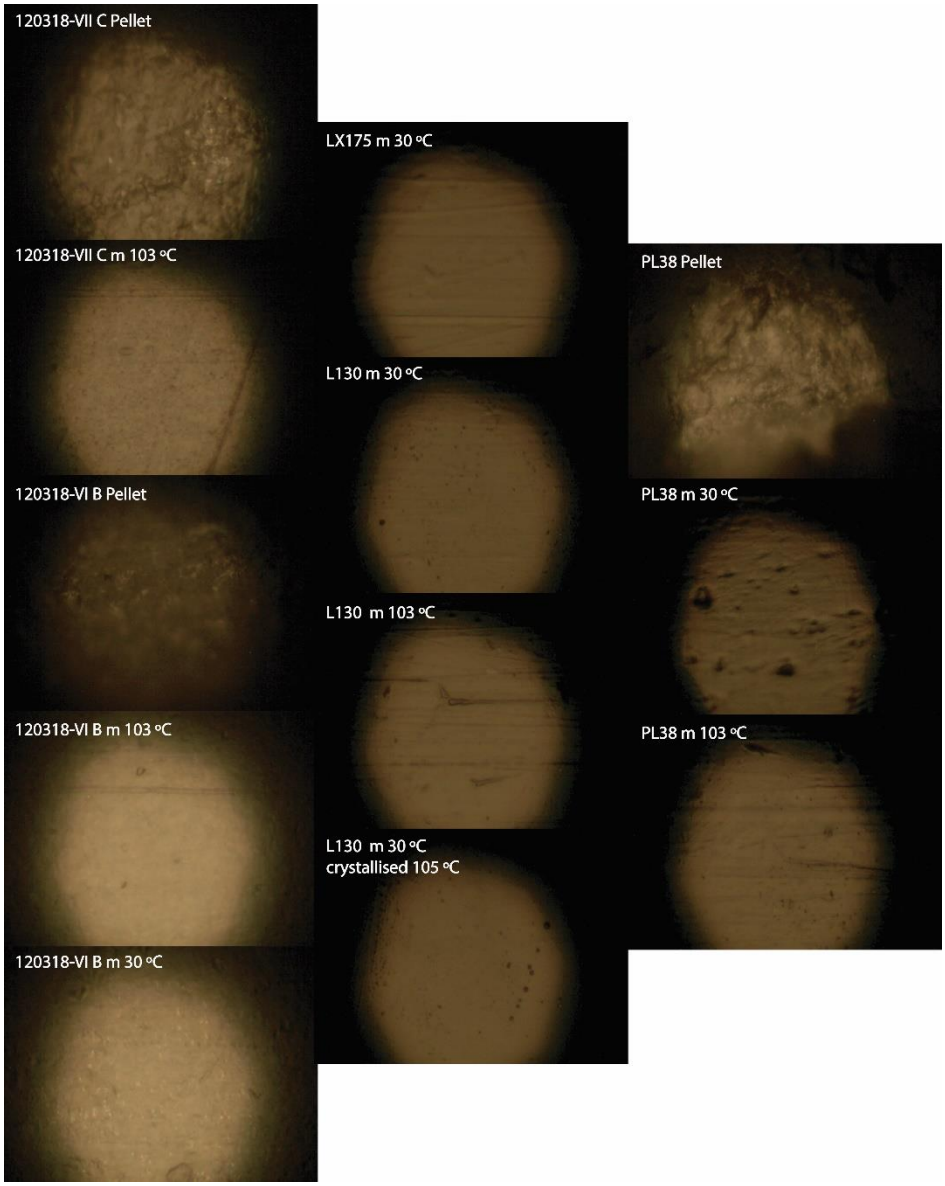

Figure 5-2. The Raman microscope images of the injection moulded materials and starting pellets, for the blends (left), L130/LX175 (middle) and PL38 (right). The Raman images show imperfections in the injection moulded materials.

resulted in a smooth dog bone with no striations, contrary to this the final dog bone at a mould temperature of 103 °C which has several striations in the direction of moulding. The final sample where the mould temperature was 30 °C and crystallisation was induced by annealing, also has no striations showing that for L130 a lower mould temperature results in a smoother end product. The annealed material has some indentations which could be the result of the crystallisation process. The mould temperature for LX175 is also 30 °C however compared to L130 at this temperature there are light striations, this would be caused by the difference in the materials.

The two mould temperatures for PL38 also produce materials with different appearances, a mould temperature of 103 °C produced striations on the surface as with L130. Contrary to L130 a mould temperature of 30 °C resulted in a material with some striations and many indentations. This difference is due to the starting materials composition and form, PL38 starts as a pellet where as L130 starts as a powder.

Continuing with a comparison of 30 °C mould temperature, blend B has no striations as with L130, similarly there are striations present at 103 °C. However not to the same extent, which could be due to the effect of talc as a nucleating agent resulting in a smoother less flawed end product. Blend C with a mould temperature of 103 °C also has no striations in the direction of injection however there is a perpendicular striation; again, the effect of talc as a nucleating agent has been shown to produce a less flawed material. The dog bones have been photographed and shown in Figure 5-3. The melt temperature affects the appearance of the injection moulded material, looking at the pure PLA materials

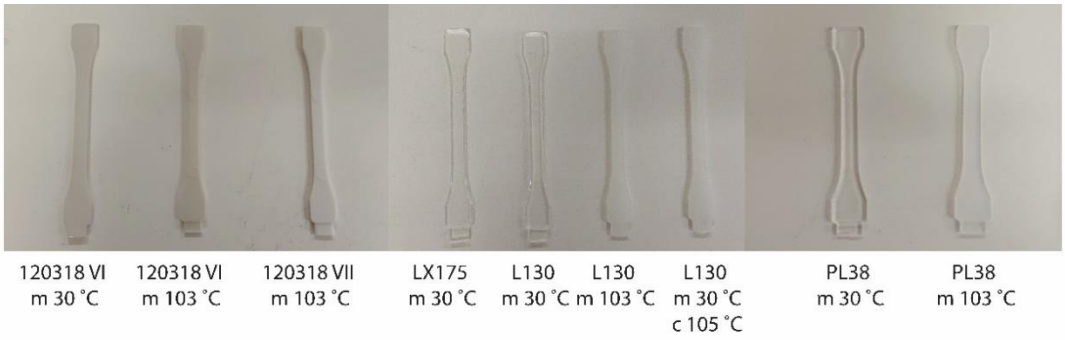

Figure 5-3. The injection moulded Poly(lactide) dog bones for the blends (left), L130/LX175 (middle) and PL38 (right). The materials are opaque, translucent, and transparent for the blends, crystalline materials and amorphous materials respectively.

the amorphous materials, mould temperature 30 °C, are clear whereas the crystalline materials, mould temperature 103 °C and annealed 105 °C, are white and opaque.

All three of the blended materials are white and opaque, this is expected for the crystalline materials and is caused by the nucleating agent talc for the amorphous material.

5.3.2 Mechanical Properties

The results of the mechanical tests are shown in Table 5-2, the Young's modulus, stress-max and strain at break were determined from the tensile tests. Impact tests were performed on notched and unnotched injection moulded impact bars of each of the samples. Notched tests are used to simulate the effect of faults in a sample. The heat deformation temperature was determined for each of the injection moulded samples on impact bars. The Young's modulus is a measure of the elasticity of a material, the stress-strain relationship before deformation occurs, a more amorphous material will have a lower Young's modulus. This is seen with L130 30 °C which has a smaller Young's modulus than the 105 °C annealed and L130 103 °C, both of which are crystalline, similarly PL38 moulded at 30 °C has a smaller Young's modulus than 103 °C. With blend VI at 30 °C the Young's modulus is higher than 103 °C, this is due to the addition of talc, a nucleating agent.

Comparing the maximum stress a material can take before breaking, the amorphous materials have a greater stress-max than the crystalline materials meaning they can be stretched further before breaking. The exception to this general statement is the L130 annealed material which has a higher stress-max than its amorphous counterpart. The blend samples have a lower stress-max than all the other PLA materials indicating greater rigidity of the materials.

The strain at break is another characteristic related to the ability of a material to stretch and how much strain it can undergo before breaking. As was the case with the stress-max the strain at break is greater for the amorphous materials; however, for the blend materials the strain at break is greater than the unblended materials. The addition of talc into the blend materials results in a greater resistance to strain but lower stress tolerance.

The unnotched impact tests show that the crystalline materials are more resistant to to impact, as with the previous mechanical tests this result is expected. Unlike the other measurements there is a significant difference in the impact resistance between amorphous L130 and annealed L130. Out of the two blends crystalline blend C shows greater resistance to impact than all other materials whereas blend B resulted in a weaker material with regards

Table 5-2, The Young's Modulus, Stress-Max, strain at break, the notched and unnotched impact resistance and the heat deformation temperature B (HDT-B) for the injection moulded polylactide samples.

Sample	Young's Modulus (MPa)	Stress-max (MPa)	Strain at break (%)	Impact resistance (kJ/m^2) Unnotched	Impact resistance (kJ/m^2) Notched	HDT-B (°C)
L130 30C	3442 [47]	68.1 [0.4]	4 [1.3]	19.3 [1.3]	2.9 [0.1]	55.8
L130 30C annealed	4005 [98]	68.8 [0.5]	3.5 [0.6]	41.6 [11.3]	11 [0.6]	116.7
L130 103C	3939 [179]	66.6 [0.6]	2.7 [0.8]	44.9 [10.7]	4.9 [0.7]	126.1
LX175 30C	3420 [26]	67.6 [0.5]	38.3 [51.9]	18.2 [2]	2.9 [0.2]	54.5
Purasorb PL38 30C	3470 [30]	71.1 [0.3]	3.7 [0.6]	20.1 [1.3]	3.5 [0.1]	54.5
Purasorb PL38 103C	3587 [235]	69 [0.4]	3.3 [0.3]	37.7 [8.4]	5.3 [1.4]	69.5
120318-VI 30C	4724 [53]	52.7 [0.7]	96.6 [17.2]	35.7 [6.6]	3.6 [0.1]	51.6
120318-VI 103C	4555 [250]	47.8 [0.7]	12.2 [2.4]	38.5 [3.8]	4.2 [0.4]	105.2
120318-VII 103C	4111 [40]	42.1 [0.3]	51.6 [7.5]	74.6 [11.5]	13.4 [0.5]	93.1

to impact resistance than the unblended materials. When a flaw is introduced to the impact bars blend C is still the most resistant material to impact, annealed L130 again has a much greater resistance to amorphous L130 and indeed the other materials both amorphous and crystalline.

The heat deformation temperature-B (HDT-B) is an indication of a materials resistance to heat and is an important factor to consider for the uses of a material. The crystalline materials have a higher HDT-B temperature than the amorphous materials, which is anticipated as a greater amount of heat is required to break crystalline domains than amorphous ones. Blend B has a higher HDT-B than blend C however the differences is not as dissimilar as the other mechanical properties suggesting that in this case the filler, talc, has more of an effect on the stress-strain relationship and impact resistance than the HDT-B. Neither of the blends however are as resistant to heat as both crystalline L130 materials.

The differences in the mechanical properties shows the importance of the formulation to achieve the desired properties of a material and in some cases the use of a pure PLA powder is more useful than adding fillers such as talc.

5.3.3 Thermal Properties

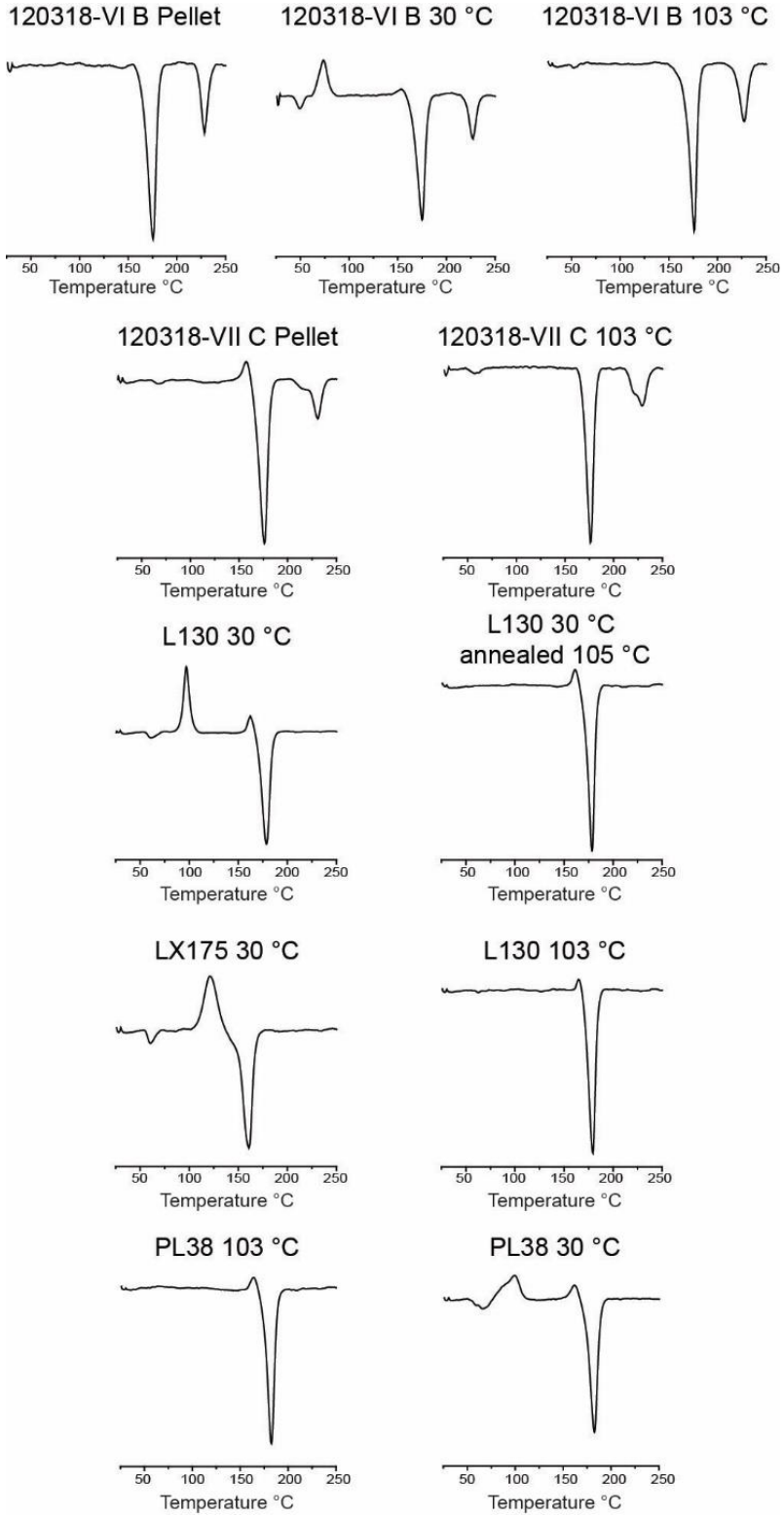

Figure 5-4. The DSC first heating scans for the injection moulded samples and the blend starting pellets, to investigate changes caused by processing, for the blends (top), L130/LX175 (middle) and PL38 (bottom). The glass transition temperature and melting temperature of PLA and talc can be extracted from the scans.

The thermal properties are an important characteristic of a material to understand, especially when considering the potential applications. The melting temperature (T_m) is very restrictive for the uses of materials; therefore, it is necessary to identify how the crystallinity and formulation of a material affect this property. The T_m is not the only transition observed in the DSC. For the amorphous materials, in addition to the melting temperature the glass transition temperature is observed in the amorphous materials and blended materials, a crystallisation temperature for the amorphous materials and potential polymorphic rearrangement all L130 materials and crystalline PL38. The melting temperatures for the materials has been extracted from the first heating scans, Figure 5-4, and are shown in Table 5-3, for the blended samples there are two melting temperatures due to the presence of an additional crystalline site induced by the nucleating effect of talc. The T_m for the three L130 materials is between 181-183 °C with the melt crystallised material at the higher end. The T_m of LX175 is 20 °C lower than L130 30 °C showing that it is a more amorphous material. The T_m and the heat output are lower showing that the intermolecular forces are easier to overcome.

Table 5-3. The melting point for the injection moulded polylactide samples.

	Melting Point		
Sample	Onset °C	Peak °C	Jg^{-1}
L130 30 °C	172.49	181.63	-60.42
L130 30 °C annealed 105 °C	173.72	181.56	-62.42
L130 103 °C	173.89	182.61	-55.99
LX175 30 °C	152.79	163.42	-37.67
PL38 30 °C	176.2	186.14	-61
PL38 103 °C	177.56	185.95	-58.5
120318-VI Pellet	167.15	178.65	-40.41
120318-VI B 30 °C	166.95	178.02	-38.92
123018-VI B 103 °C	169.43	179.25	-37.93
120318-VII Pellet	167.95	178.81	-37.44
120318-VII C 103 °C	170.67	179.15	-30.23
	Talc		
120318-VI Pellet	225.36	232.03	-12.08
120318-VI B 30 °C	223.68	231.41	-10.6
123018-VI B 103 °C	222.5	231.32	-11.83
120318-VII Pellet	227.8	235.01	-5.24
120318-VII C 103 °C	217.65	233.4	-10.61

The T_m for PL38 is 5 °C higher than for L130 indicating that it is slightly more crystalline. The first T_m for the blends, arising from the same crystalline sites as seen in the non blended material is between 177-180 °C, which is lower than the other materials additionally, the heat output is also lower. The addition of talc into the blend has reduced the first T_m and has also resulted in a second T_m at 230 – 235 °C with a much lower heat output. As with the mechanical testing, the differences in T_m also highlight the need for careful formulation to result in the desired properties.

The SAXS data for each of the injection moulded samples provided different information for each sample. The radius of gyration, R_g, was determined for materials with no interaction between neighbouring crystallites, this is a measure of the spread of the mass of a crystallite and is estimated from the lowest scattering angles. From this the average radius, R_{av}, was determined using the equation, $R_g = \sqrt{3/5\, R_{av}}$. Samples with interacting crystallites were fit using a hard sphere interacting model which enabled a particle radius distribution and interaction distance (ID) to be determined. Samples with weak scattering did not allow for the determination of any information. The information extracted is shown in Table 5-4. A porod slope was fitted for the samples where the scattering was strong enough, Figure 5-5.

An initial comparison of the R_g for the different materials showed that the two amorphous materials had a R_g twice the size of the crystalline materials. Since a smaller R_g allows for tighter packing of the particles and a more ordered packing structure, this is to be expected of a crystalline material.

Table 5-4. The radius of gyration, average particle radius and interaction distance for the injection moulded samples as determined from small angle X-ray scattering data.

Sample	Radius of Gyration R_g (nm)	Average particle radius (nm)
L130 30 °C		
L130 30 °C annealed 105 °C		
L130 103 °C		4
LX175 30 °C	12.6	2.75
PL38 Pellet		160
PL38 30 °C		
PL38 103 °C		6.2
120318-VI Pellet	6.4	1.96
120318-VI B 30 °C	12.0	2.68
123018-VI B 103 °C	7.3	2.09
120318-VII C Pellet	6.3	1.94
120318-VII C 103 °C	7.9	2.18

The blended materials were measured in a pre and post processing state, the R_g increased after injection moulding the materials for both blends by approx. 1 nm.

5.3.4 Small-Angle X-ray Scattering/Wide-Angle X-ray Scattering

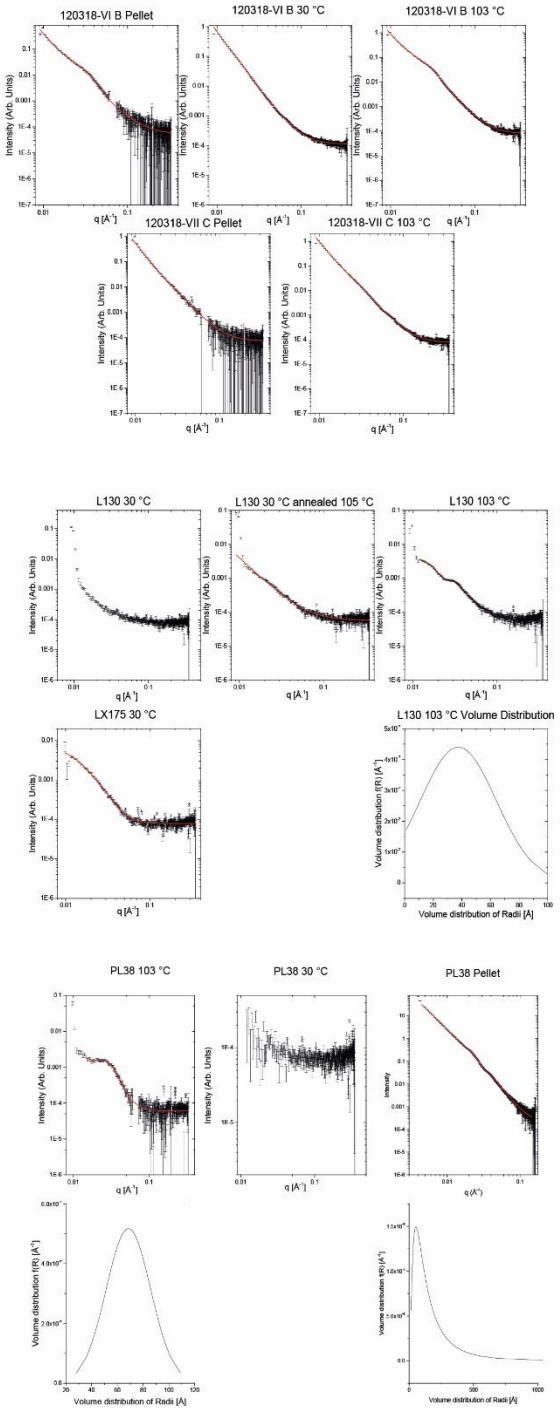

Figure 5-5. The SAXS patterns for the injection moulded polylactide sample for the blended samples (top), L130/LX175 (middle) and PL38 (bottom). The volume distribution is shown for L130 103 °C, PL38 pellet and PL38 103 °C.

Crystalline PL38 and melt crystallised L130 scattered strongly enough to be able to see interactions between individual crystallites of PLLA, as such a confident R_{av} and ID were determined 17 and 20 nm respectively. PL38 has a greater R_{av} than L130 however has a shorter ID. The limitations of the molybdenum X-ray source for the SAXS measurements mean that the upper limit of particle size detection is 20 nm, which is the ID measured for L130. It is not possible to conclusively state that there are therefore no particles of this size present in the sample. It is unfortunate that only two samples showed interaction between particles and therefore it is not possible to relate ID to the material properties.

WAXS measurements were taken of all the PLA materials, Figure 5-6, the most notable difference across the samples is the presence of sharp scattering peaks in the blends which are attributable to talc.[102] The best place to start is with the three L130 samples, by having the pattern of the amorphous sample it is then possible to detect the crystalline peaks. The only clear diffraction peak in both crystalline samples is at ~20˚. This diffraction peak is also seen in PL38 103 ˚C and not in PL38 30 ˚C.

The second set of WAXS patterns to look at are the blends B and C, 120318-VI B 30 ˚C is an amorphous material therefore the crystalline peaks will only be attributable to talc. In 120318-VI B 103 ˚C there are an additional three diffraction peaks at ~20, 21 and 22 ˚. There are an additional two crystalline peaks in the blend samples than in the pure PLLA sample showing that talc has increased the crystallinity of the material. 120318-VII C 103 ˚C has fewer crystalline diffraction peaks than 120318-VI B 103 ˚C suggesting that blend B results in a material with greater crystallinity and that talc has a greater nucleating effect on blend B than blend C, this is corroborated by the difference in mechanical properties of the materials.

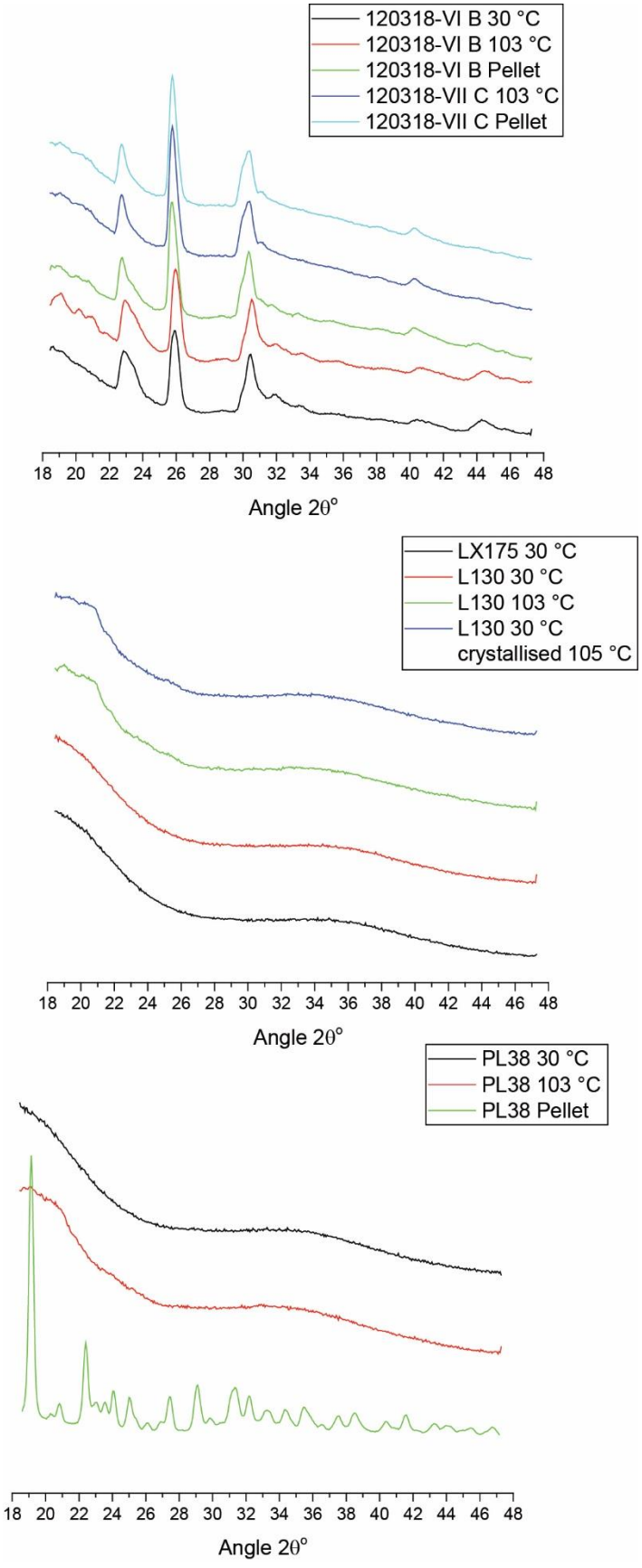

Figure 5-6. The WAXS patterns for the injection moulded polylactide samples for the blended samples (top), L130/LX175 (middle) and PL38 (bottom).

5.3.5 Solid state NMR

Three solid state NMR experiments were performed on each of the injection moulded samples and the starting materials, the ^{13}C CPMAS spectra have been compared, Figure 5-7. All the ^{13}C spectra have three resonance peaks at 169, 68 and 17 ppm for the carbonyl, methane, and methyl carbons, respectively. The crystallinity of a material affects the nmr spectra by causing splitting in the resonance peaks. It is known that for polylactide the amorphous component will be present at 169, 68 and 17 ppm, depending on the amount of each isomer present two crystalline components can arise, for the materials measured here only a homocrystalline component will be present at 171, 69 and 15 ppm.

L130 and LX175 are PLLA's, all four materials have a single resonance peak for amorphous PLA. L130 has been crystallised via two different methods, crystallisation in the mould and annealed post injection moulding, however the ^{13}C CPMAS spectra do not show the crystalline component expected. The only PLLA that showed a homocrystalline region was PL38. In the blended materials an amorphous component was observed across all materials, additionally a homocrystalline component was observed in the crystalline materials and starting pellets. An additional splitting was observed in the blended materials at 172 ppm, this is potentially attributable to the nucleating effect of talc inducing an additional crystalline domain.

The mobility of polymer chains is related to the crystallinity of the materials, the $T_{1\rho}$ relaxation times are a measure of mobility in the kHz regime which is perfect for polymers. A shorter $T_{1\rho}$ time means that the chemical environment is more mobile and is therefore more amorphous. The $T_{1\rho}$ times for each of the amorphous and crystalline components have been determined, Table 5-5.

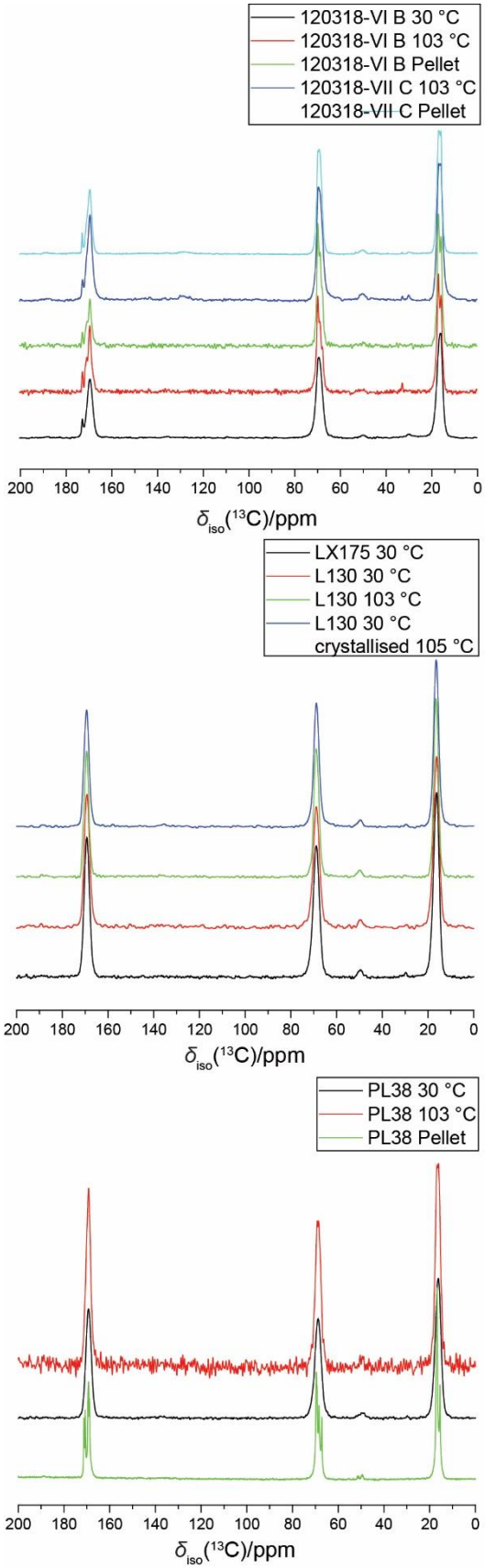

Figure 5-7. The ^{13}C CPMAS NMR data for the injection moulded polylactide samples for the blended samples (top), L130/LX175 (middle) and PL38 (bottom)

Table 5-5. The $T_{1\rho}$ relaxation times for the injection moulded materials and the blend starting materials.

Sample	$T_{1\rho}$ (s) relaxation times						
	Amorphous			Crystalline			Talc
	169 ppm	68 ppm	17 ppm	171 ppm	69 ppm	15 ppm	172 ppm
L130 30 °C	0.038± 0.006	0.062± 0.005	0.051± 0.006				
L130 30 °C annealed 105 °C	0.088± 0.008	0.091± 0.007	0.087± 0.005				
L130 103 °C	0.091± 0.007	0.091± 0.008	0.088± 0.006				
LX175 30 °C	0.066± 0.01	0.061± 0.009	0.055± 0.008				
PL38 30 °C	0.050± 0.006	0.051± 0.006	0.054± 0.006				
PL38 103 °C	0.062± 0.01	0.082± 0.03	0.07±0 .01	0.062± 0.02	0.075± 0.02	0.082± 0.02	
120318-VI B Pellet	0.079± 0.014	0.071± 0.008	0.074± 0.006	0.073± 0.01	0.087± 0.007	0.079± 0.008	0.14±0.1
120318-VI B 30 °C	0.027± 0.004	0.045± 0.006	0.044± 0.005				0.11±0.05
123018-VI B 103 °C	0.050± 0.01	0.053± 0.02	0.063± 0.006	0.050± 0.02	0.068± 0.01	0.060± 0.009	0.20±0.03
120318-VII C Pellet	0.080± 0.02	0.125± 0.02	0.11±0 .01		0.136± 0.02	0.11±0 .01	0.15±0.1
120318-VII C 103 °C	0.053± 0.02	0.072± 0.04	0.077± 0.03	0.047± 0.05	0.072± 0.04	0.10±0 .04	0.074±0.0 8

Overall, the amorphous materials have shorter $T_{1\rho}$ times; the greatest differences are seen in the carbonyl region showing that L130 is more mobile than LX175 and PL38, however the presence of talc in blend B has resulted in shorter $T_{1\rho}$ times across all environments. Turning to the crystalline PLLA materials, crystallising in the melt rather than post processing annealing has resulted in longer $T_{1\rho}$ times for the carbonyl region and therefore a slightly more rigid amorphous domain. Crystallised PL38 is less mobile across all environments, this along with the amorphous PL38 suggest that on the whole the amorphous region of PL38 is a more mobile than L130 or LX175.

Comparing the blended materials showed that blend B had greater mobility in the amorphous domains than blend C both pre and post processing. The $T_{1\rho}$ times for the homocrystalline component also show that blend B has greater mobility across all environments. The talc induced crystalline site is the least mobile for all the materials out of

all three components. The starting pellets for both blend B and C have similar $T_{1\rho}$ times however crystalline blend C has greater mobility.

5.3.6 Raman Spectroscopy

The Raman assignments for the polylactide materials are shown in Figure 5-8. The most important raman vibrations are the C-CO vibration at 395 and 410 cm^{-1} for the amorphous E mode and crystalline A mode backbone vibrations respectively. Using the percentage of the E mode vibrations a comparison of the amorphicity of the backbone can be performed,

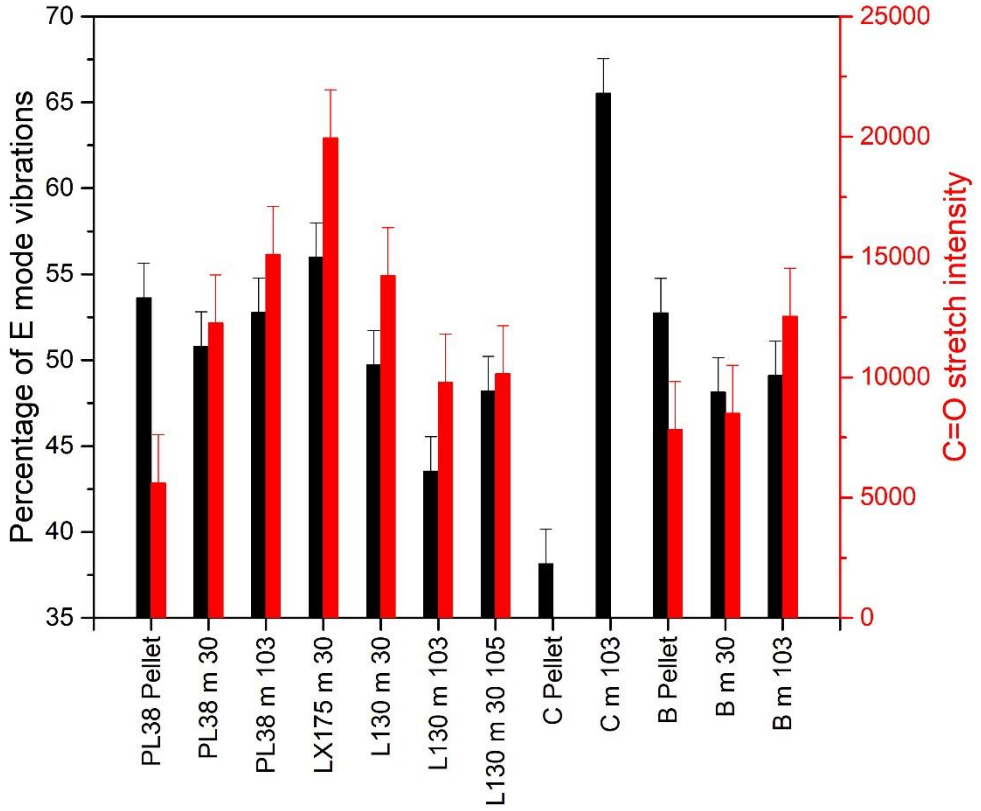

Figure *5-9* (black).

The higher the percentage of E-mode vibrations the more amorphous the PLA backbone. This is confirmed by the IM materials with higher mould temperature having both a lower percentage of E mode vibrations and also have less than 50 % E mode showing that there are more crystalline A mode vibrations than E mode. The effect of talc on the nucleation of PLA is highlighted by 120318-VI B 30 ˚C which has a smaller percentage of E mode vibrations lower than 50 % showing that talc has induced crystalline regions even at low mould temperatures.

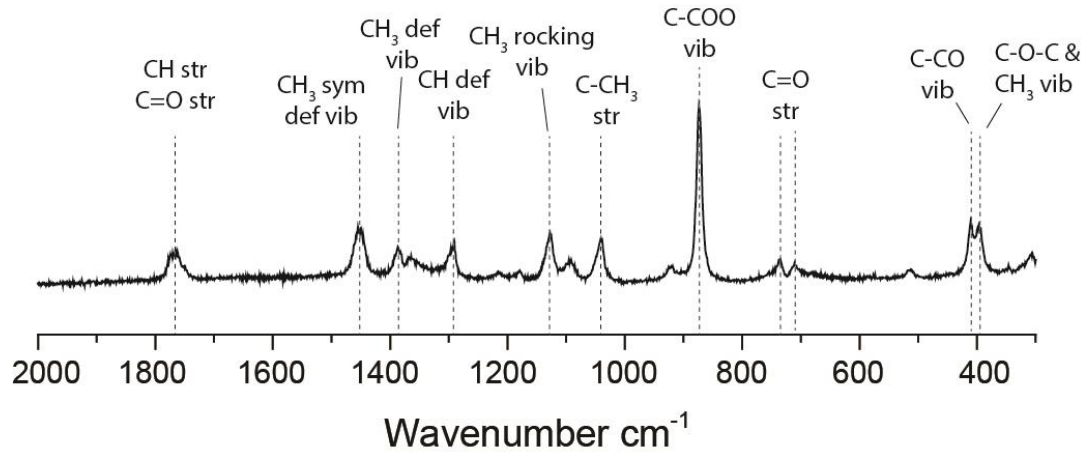

Figure 5-8. The Raman assignments for polylactide.

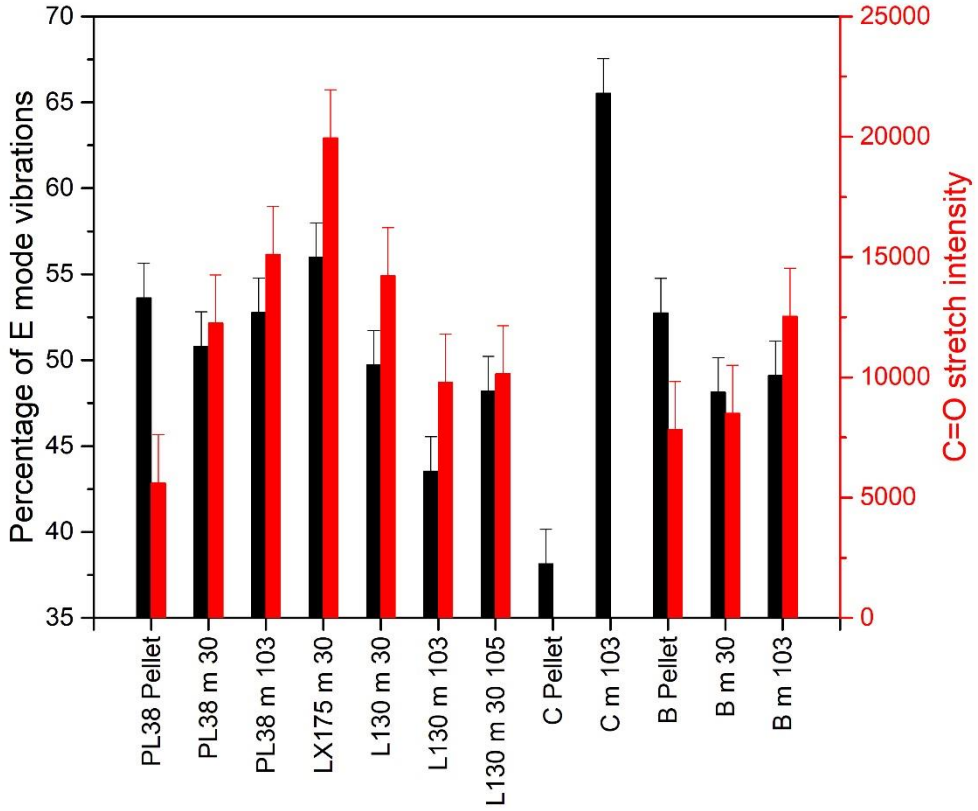

Figure 5-9. The percentage of C-O E mode vibrations (black) and the intensity of the C=O stretch (red).

The C=O stretch at 736 cm^{-1} allows for investigation into the restriction of the stretching of the C=O species, in densely packed regions the C=O stretch will be inhibited to an extent which is indicated by a decrease in the intensity of this wavenumber. Whilst there are only two pellets to investigate both of them have a lower intensity than the IM materials at each mould temperature. During the moulding procedure the PLA chains will be become aligned

which will allow for more freedom of stretching than in an entangled system. The MG and IG materials have opposite responses to the mould temperatures. For the MG PLA there is a greater intensity for the higher mould temperature whereas the converse is true for the IG PLA. This difference could be attributed to the presence of small amounts of d-isomer in the MG PLA resulting in both stereocrystalline and homocrystalline regions being formed.

A secondary observation is that the two crystalline samples for L130 have the same intensity of C=O stretch, suggesting that annealing the materials or using a higher mould temperature makes no difference to the restriction on the C=O stretch when forming the crystalline

material. The effect of talc is the same as the MG PLA, talc creates additional crystalline regions similar to the D-isomer forming additional crystalline sites.

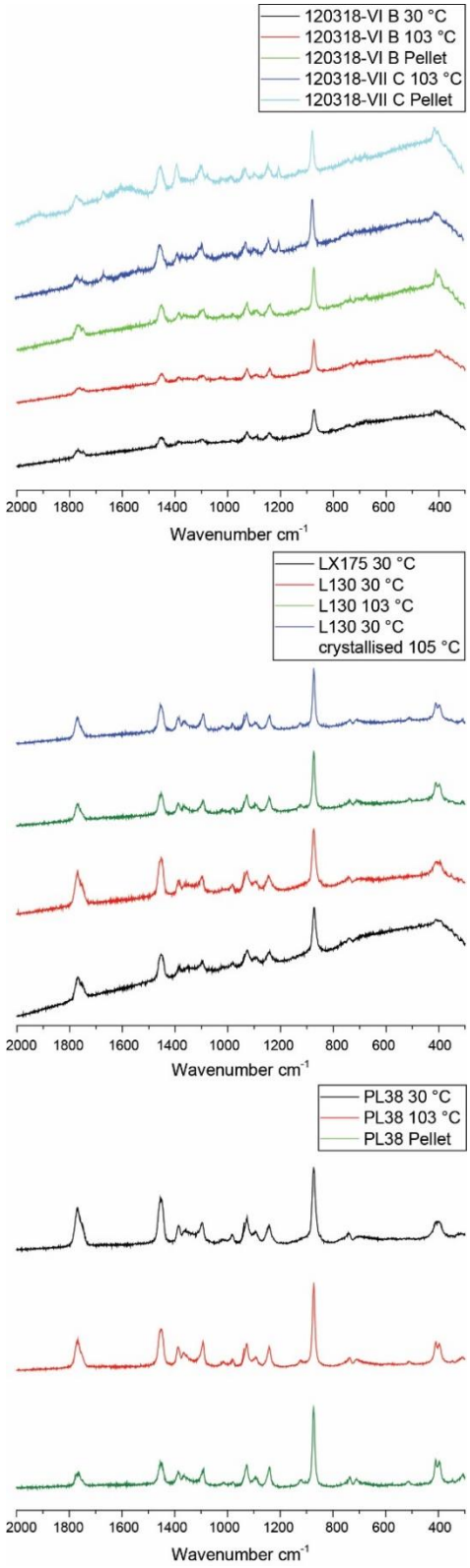

Figure 5-10. The Raman spectra for the injection moulded polylactide samples and starting pellets for, the blends (top), L130/LX175 (middle) and PL38 (bottom).

The 1044 and 1128 cm^{-1} vibrations are also important and are attributed to C_α-C stretching/$C_\beta H_3$ rocking and O-C_α stretching/$C_\alpha H_\alpha$ bending, these are sensitive to conformational changes. The three skeletal backbones in PLA are C-O, O-C_α and C_α-C. There are four conformations that these can take, tt't, tg't, tt'g and tgg'. The dihedral angles are 160°, -160°, -73° and 48° for t, t', g and g' respectively. The relative populations are 5, 72-81, 5 and 9-18 % respectively, tt't and tg't are straight conformers and tt'g and tg'g are bent conformers. The raman spectra in the region of 900-1200 cm^{-1} are different depending on the confirmation of the backbone in the amorphous region, therefore can be used to look at conformational changes. In the case of the PLA materials here, the region does not match for any of the individual regions entirely and therefore more than one conformer exists among the PLA helices present. The 300 – 1000 cm^{-1} region can be indicative of the PLA helix arrangement, 2_1, 3_1, 4_1 or 5_1, for the injection moulded materials, the raman spectra is indicative of a 3_1 helical arrangement, this is common when poly(l-lactic acid) is co-crystallized with poly(d-lactic acid). There are four possible 3_1 helices depending on the conformational angles, the presence of raman shifts at ~730 and ~410 cm^{-1} indicate that model I is the best fit except for 120318-VII C where both the pellet and the IM material do not have a shift at ~730 cm^{-1}.

5.3.7 Amorphous materials

There are 4 amorphous materials that can be compared to see how fillers and grade effect the properties. There are two industrial grade PLLA samples, one medical grade PLLA and one blend (blend B), the second blend is not processable at low enough temperatures to produce an amorphous material.

The mechanical properties of the materials show that the two IG PLLA samples have similar Young's modulus, stress-max, strain at break and therefore elasticities, additionally they both have poor resistance to impact and deform at around 55 °C. The MG PLLA material also has a similar Young's modulus however can undergo greater stress before necking. The unblended PLLA's have similar resistance to impact with the MG PLLA retaining greater strength when flaws are introduced. The PLLA blend has the greatest resistance to impact despite having the highest strain at break, while it is expected that stronger materials should be more resistant to stress and break at lower elongations, it is suggested that the talc nucleating agent is resulting in the unusual combination of properties. All four amorphous materials have similar HDT-Bs.

The DSC first heating scans show the presence of the second T_m in the blended material. This additional crystalline site goes towards explaining the enhancement in properties. The crystalline domains result in stronger intermolecular bonding which enhances the strength, however the material is predominantly amorphous which accounts for the increased elongation. Comparing the melting temperatures for the for the lower T_m, LX175 has a lower melting temperature and has a lower heat output, however this does not appear to affect the mechanical properties of the material.

The results of the SAXS and WAXS measurements are similar across all four materials as is the ^{13}C CPMAS data. The WAXS and CPMAS data shows that the materials are fully amorphous under ambient conditions, the only difference being the presence of additional scattering peaks/resonances caused by talc. The SAXS measurements showed that the R_g is also similar, due to this no parallels can be drawn between the WAXS/SAXS/CPMAS data and the mechanical properties. The $T_{1\rho}$ relaxation measurements however do go towards explaining the differences.

The carbonyl region is the most indicative of changes in the mobility of the PLLA chains, the stronger blend material has greater mobility than the IG and MG PLLA materials, indeed the blend material has greater mobility across all groups. A greater mobility means that the polymer chains are packed less tightly and are more amorphous in nature. The max stress is caused by the ability of the chains to resist the forces applied, if the chains are packed less tightly, they will yield sooner as the intermolecular forces are weaker. A more amorphous material will additionally be able to elongate further. The blend material has a crystalline component as is seen in the DSC, this has much less mobility than the amorphous component and will contribute to the enhanced impact resistance when unnotched. Whilst there is a difference in the $T_{1\rho}$ relaxation times for the carbonyl region between the two IG PLLA materials, the times for the other regions is similar. The mechanical properties are very similar and therefore the carbonyl region potentially does not contribute as much to these properties. The difference in the melting temperature and the heat output is approx. 20 °C, the greater mobility and weaker bonding in the carbonyl region does appear to affect the energy required to overcome the intermolecular forces.

Comparing the C=O shift intensity and the A mode percentage for the amorphous materials the amorphicity and restriction of the backbone can be examined. First comparing the two IG PLA materials, LX175 and L130, the LX175 has a much greater intensity of C=O stretch and E mode percentage indicating that it is more amorphous than L130, the difference between

the two IG PLLA's is different to the results seen in the carbonyl region of the NMR. In the NMR the whole carbonyl region is being investigated whereas in the Raman it is just the stretching of the C=O, considering that the mobility of the carbonyl region is greater and therefore more amorphous for L130 than LX175 it could be suggested that the C=O stretch does not contribute in this case to the relaxation processes. The E mode is for the backbone, therefore comparisons should be made to the methyl and methine relaxation times, for this case the relaxation times are similar, showing that Raman can probe the backbone as a whole and provide information that NMR cannot as it probes the individual functional groups rather than the whole unit. Continuing on this comparison to the difference between MG and IG PLLA two separate comparisons would need to be made for the intensity of the C=O stretch MG PLLA is lower than both IG materials whereas there is a greater E mode percentage than L130 and less than LX175. Neither of these trends align with the NMR relaxation times, Since the addition of talc to the material has reduced the intensity of the C=O stretch and the percentage of amorphous E mode is less than 50 %. This is to be expected as previously mentioned as talc introduces additional crystalline sites even at lower mould temperatures where an amorphous material is expected.

Comparing the Raman and $T_{1\rho}$ data with the DSC and mechanical data we can see that when the molecular mobility is different across all regions we see a change in the mechanical properties however when there is only one region that is different only the thermal properties are affected. The effect of adding talc as a nucleating agent is very evident across the mechanical properties and $T_{1\rho}$ data, in its ability to strengthen the final material through the introduction of additional crystalline regions.

5.3.8 Crystalline

There are 5 crystalline materials that can be compared to investigate the effect of crystallisation method, IG vs MG PLLA and the effect of two different blends. IG PLLA has been crystallised in the melt whilst processing and also by post processing annealing. Annealing post processing has resulted in greater impact resistance when flaws are introduced and a lower resistance to heat, all other mechanical properties are very similar. Crystalline MG PLLA has similar mechanical properties to both IG materials within experimental error except for the HDT-B temperature which is 50 °C lower.

The two blends show much greater differences in the mechanical properties, blend VI results in a stiffer material that is more resistant to stress and has lower elongation however is less resistant to impact. Blend VII resulted in a material that more greatly differed from the

unblended materials in terms of elongation and impact resistance. The differences in the properties go to show the differences the two formulations have on the materials.

The DSC of the blended PLLA materials is 3 °C lower than the IG PLLA materials and 7 °C lower than the MG PLLA materials, the heat output is additionally lower, this suggests they are more amorphous materials; however, the enhanced strength is provided by the second crystalline site induced by talc. The SAXS measurements showed that the different blends did not affect the radius of gyration, however the MG PLLA had a larger average particle size, narrower distribution, and shorter interaction distance. In the case of the SAXS the grade of the PLLA material has more affect than blends. The WAXS patterns of both IG PLLA materials and MG PLLA showed a single scattering peak at 20 °, the blends added in the extra scattering peaks from talc in addition to two extra peaks at 21 and 22 ° showing that the talc caused two additional crystalline domains to form, this is also seen by the presence of the additional resonances in the CPMAS data.

The two forms of crystallisation for L130 resulted in similar levels of mobility, which correlates with the similarities in mechanical and thermal properties. The mobility of all C regions in MG PLLA is greater than IG PLLA in the amorphous region, the large particle sizes could contribute to this. There is however an additional crystalline region present indicating that the material overall is more crystalline which is seen in the DSC data by the higher T_m. Both the blends have greater mobility than the other materials, VI is more mobile than VII except for the talc induced crystalline site which is much less mobile. The overall increased mobility results in the weaker resistance to impact however the stiffness and resistance to stress is improved by the talc induced crystalline site.

The same comparison can be performed on the crystalline materials as on the amorphous ones between the C=O intensity and E mode percentage with the $T_{1\rho}$ relaxation data. The intensity of the C=O stretch is greatest for PL38, adding talc increases the intensity compared to the IG PLLA materials and in situ or annealing crystallisation results in little difference. The E mode percentage has the same differences between the materials, blend C is comparable in this situation and has a much greater percentage of E mode being at 65 %. Comparing to the $T_{1\rho}$ data the changes match more closely in trend for the C=O intensity than the E mode %, these differences again show that the Raman and NMR data provide different information and are therefore useful to use in conjunction.

5.4 Conclusion

The properties of polymeric materials can be changed by controlling the crystallinity of the material and using blends. Stress-strain testing to determine the Young's modulus, maximum stress point and the strain at break are useful for investigating the elasticity and stiffness of a material. Impact testing is important to determine the impact resistance of a material, unnotched and notched tests are useful to understand the impact resistance for a pristine material and in the presence of flaws. It is also important to determine the HDT-B point of a material to investigate the heat resistance. Understanding the thermal properties of materials is also useful for determining the potential applications of the final material. Combining Raman and NMR allows for an investigation into both the individual functional groups and backbone as a whole which provides more information to compare the structure and mobility to the thermal and mechanical properties.

The effect of adding talc as a nucleating agent is evident in the enhancement of the mechanical properties in terms of strength. Talc induces additional crystalline regions as demonstrated by the NMR data which contributes to the increase in strength of the IM material. The difference between industrial grade and medical grade PLLA has also been demonstrated for both crystalline and amorphous materials, there is a difference in mechanical properties however whether the properties achieved are advantageous is based on the desired use as these two materials have vastly different applications.

The limitation in this study mainly comes from the SAXS measurements, especially with regards to the amorphous samples which have weak scattering where crystallite sizes are unobtainable and where there are no crystallites interacting resulting in only an average particle size being obtained. The particle size and distance does influence the properties, in this study a wide range of samples with different crystallinities, blends and applications have been compared. For furthering investigation of the final comparison additional techniques to measure the particle sizes would need to be applied.

6. An MAS NMR and Diffraction Study of Cis/Trans Polymeric Materials.

6.1 Introduction

Elastomers are polymers, existing above their glass transition temperature, that exhibit high elasticity and reversible elongation up to 1500 %. The elasticity is derived from the ability of the long macromolecular chains to reconfigure themselves to distribute an applied stress. The chains elongate when stress is applied in a preferred direction. Covalent or physical cross-links prevent the macromolecular chains from slipping and undergoing permanent deformation. Additionally, elastomers are described as viscoelastic polymers and are characterized by very weak intermolecular forces, low Young's modulus and failure strain.

There are two types of cross-links that exist in elastomers, the first of these are covalent cross-links often formed by addition of sulphur at high temperatures forming sulphidic bridges between macromolecular chains. These cross-links result in an inability to reprocess or recycle the elastomers in dienes. The second type are physical cross-links, these are present in phase-separated block copolymers where a disperse phase is presented in a glassy crystalline matrix. Thermodynamics plays a role in this form of cross-linking, consequently these materials are referred to as thermoplastic elastomers and can be molded, extruded and reused while maintaining typical elastic properties.

There are 5 main structural conditions that must be met to allow an elastomer to have a rubbery behavior. The first of these is the presence of long, highly flexible chains, which allow for the rearrangement and extension of the chains as a response to stress. Unstrained elastomers exist as a random coil of the macromolecular chains, this structure is more thermodynamically stable than the fully extended chains as there are infinite arrangements of random coils whilst there is only one fully extended chain arrangement. Elastomers favourably exist of simple hydrocarbon chains with minimal stiff groups, bulky side chains and hydrogen bonding groups to allow for minimal steric hinderance during elongation. The network structure is highly important, this is controlled by cross-linking between macromolecular chains. The third condition is that there must be weak interchain interactions to allow the chains to move freely and reversibly past each other. Thus elastomers must exist above their glass transition temperature to allow for segmental motion. The final consideration is the amorphous structure, any crystalline domains present

cannot contribute to elastic properties; to prevent crystallinity irregularity is required in the molecular structure.[103]

Elastomers unique properties result in a multitude of uses depending on their physical properties. General purpose elastomers are comprised of hydrocarbon polymers, commonly polybutadiene and polyisopropene rubbers. The primary application of general purpose elastomers is as automotive and truck tyres, due to their high strength, abrasion resistance, low hysteresis and high resilience. Special purpose rubbers are made in smaller quantities and have tailored resistance to heat and solvent resistance. Neoprene is one such example of a special purpose rubber due to its resistance to weather and ozone, as a consequence it is used where fire resistance is required. Nitrile based rubbers are often used in engineering as oil seals, o-rings and fuel and oil hoses Finally fluorocarbon rubbers are used in aircraft, aerospace and automotive applications due to its superior oil and heat resistance.

There are two categories that rubbers can be broadly placed into, thermosets and thermoplastics. Thermosets are 3D molecular networks held together by chemical bonds. Thermoplastics are comprised of chains connected by physical aggregation of hard domains; thermoplastic elastomers (TPEs) will be focused upon here. TPEs can be modified to suit the needs of the application and are predominantly manufactured by extrusion and injection molding. TPEs are used for footwear, wire insulation and adhesives for polymer blending, their resistance to solvents and deformation at high temperatures restrict their uses.

The key characteristics of TPEs are similar to other elastomers, nominally that the must possess the ability to stretch and returned to their original shape, in addition to being processed as a melt at high temperatures and have the absence of significant creep, which is the tendency of a polymer to distort under external loads. A TPE is a two-phase material, each molecule must consist of a soft elastomeric part and are hard domain that forms the physical cross-links. A TPE can be classified as either a block copolymer or an elastomer blend. Block copolymers exist as hard/soft alternating domains within the same macromolecular chain, in the case of polyester/polyamide based TPEs a multiblock motif is seen of A-B-A-B… In an elastomer blend there is a mixing of hard and soft phases under intensive shear conditions, this method is simpler than the production of block copolymers.

In a phase separated system the characteristics of the individual polymers are seen, with each phase undergoing a separate glass transition temperature and melting temperature. The temperature at which a TPE undergoes transitions of its physical properties is dependent upon the thermal characteristics of both phases. To control the characteristics several

parameters can be controlled such as the molecular weight, proportion of each phase and the choice of the hard and soft phases.[103-104] The hard segments determine the degree of crystallinity and consequent mechanical strength of the TPE, whereas the soft segments control the elastomers chemical resistance, thermal oxidative stability, hydrolytic stability and low temperature flexibility.

The stereochemical orientation of double bonds in the elastomer backbone is also crucial to controlling the properties of elastomers; this is exemplified by natural elastomers, such as natural rubber and gutta percha, where the properties are enhanced by the superior chain packing of poly(*cis*-isopropene) over poly(*trans*-isopropene). Double bond stereochemical control is challenging in synthetic methods however careful consideration of catalyst and solvent in organobase-catalysed addition reactions combined with step-growth polymerisation and click chemistry can allow for control of double bond stereochemistry and molecular mass.[105-107] The 'click' chemistry method is used to synthesise the materials used in this chapter.

The term 'click' chemistry was coined by Sharpless to describe a stepwise Huisgen cycloaddition process however the concept was originally developed by Huisgen in 1950.[108] The term 'click' chemistry is applied to describe reactions that are high yielding, create only byproducts that can be removed without chromatography, are simple, sterospecific and conducted in solvents that are either benign or easily removable. The applications of click chemistry are ever increasing and recently have been used for thiol-yne reactions.[106, 109-110] [105, 111] Click reactions proceed without eliminating a small molecule, consequently creating no by-products and are classified as a polyaddition polymerisation. There are many benefits to click reactions; in addition to the lack of by-products there is high reactant specificity and tolerance of other functional groups. These reactions occur with high conversions in any solvent at relatively low temperatures, making this approach advantageous for the synthesis of polyesters. There are some disadvantages to click methodologies including poor solubility of the final product and difficulties in removing the metal catalysts, however the benefits outweigh these disadvantages.

A powerful technique for studying block copolymers is solid state NMR, one of the main areas of research both historically and recently has been on domain sizes and the implementation of spin diffusion techniques.[112-121] Spin diffusion is a selective technique that is affected by homonuclear dipolar couplings and is sensitive to the distances between nuclei and molecular mobilities, consequently it is useful for investigating the domains in block

copolymers. Molecular mobility can also be investigated using relaxation methods, many studies have involved the use of T_1,[116, 118, 120, 122] T_2[114, 123-125] and $T_{1\rho}$[118, 120, 122, 124] relaxation measurements for both ^{1}H and ^{13}C nuclei to probe the differences between the hard and soft domains. Solid state NMR has relevantly been implemented on polyamides and particularly nylon-6 especially with regards to the strength of hydrogen bonding between the intermolecular chains and structural configuration. [126-128 129]

In addition to Solid state NMR techniques, small angle X-ray scattering (SAXS) has been used to study block copolymers.[104, 116, 118, 130] Many studies have been undertaken on polyurethane (PU) elastomers to investigate the nature of polymers with hard-soft domains and how they relate to the morphology and properties of Pus.[131-134] SAXS measurements have also been used to investigate the mechanical properties of elastomers and how they are affected by crosslinking and fillers.[104, 135]

In this chapter a series of polyester and polyamide TPEs synthesized by 'click' chemistry and thiol-yne reactions are investigated by a multi technique approach. The effect of *cis*/*trans* ratio and molecular weight is investigated; the physical properties, in this case the Young's modulus, are then related to the crystallinity, molecular mobility and melting temperature of the TPEs.

6.2 Materials and Methods

6.2.1 Materials

All elastomers were synthesized at the University of Birmingham by Dr. Joshua Worch via the following procedures.

General procedure for thiol-yne step growth ester. 1,6-Hexanedithiol was added to a 20 mL scintillation vial. To this, propane-1,3-diyl dipropiolate was added by quantitative transfer with $CHCl_3$ (6 mL). The solution was then cooled to -15 °C with stirring for 5 min before a base was added, 1,8-Diazabicycloundec-7-ene (DBU) or NEt_3 for the high *cis* and high *trans* materials respectively, was added in one portion. The addition of the base produced an exotherm and after 2 min of stirring, the reaction was warmed to room temperature and stirred. After 1 hr the solution was then precipitated into diethyl ether and collected by decanting the supernatant. The esters were then dried *in vacuo* at room temperature for 24 hrs and the oligomers were then dried for an additional 2 hrs at 60 °C *in vacuo*. The molecular weight of the polyesters was controlled by the $CHCl_3$/DMF solvent ratio. Four polyesters of 15 %, 57 %, 67 % and 82 % *cis* content, four oligomers of 20 % *cis* and 80 % *cis* content and two dimers of 18 % and 80 % *cis* content have been synthesised by the above method,

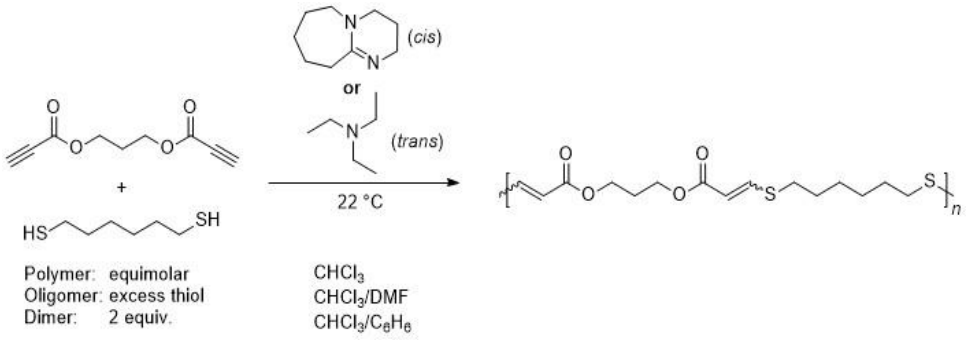

Scheme 1. The synthesis of the ester materials via thiol-yne step growth polymerisation.

Scheme 1 . All polyesters were provided in powder form, the oligomers and dimer of 80 % *cis* content were also in powder form, the two oligomers of 20 % *cis* content were provided in a rubbery form and the dimer was provided as a liquid.

General procedure for thiol-yne step growth polyamide. 1,6-Hexanedithiol was added to a 100 mL round bottom flask. To this, *N*,*N*'-(propane-1,3-diyl)dipropiolamide was added by quantitative transfer with DMSO/MeOH/$CHCl_3$, the solvent ratio was used to control the *cis:trans* ratio. The solution was temperature controlled in a 15 °C water bath before DBU (32.9 µL, 0.22 mmol, 0.01 equiv) was added in one portion.

The addition of DBU produced an exotherm which was mitigated by heat transfer to the water bath. After 2 min of stirring, the reaction flask was sealed, removed from the bath and stirred at 50 °C or 65 °C for the high *cis* and high *trans* polyamides respectively, in order to increase the solubility of the polymer product. After 2 h the reaction was quenched with 1-dodecanethiol to end-cap any alkyne chain-ends and stirred for 30 min. Then, the solution was diluted with DMSO and BHT was added in order to prevent crosslinking during the precipitation step. The polymer solution was then precipitated into methanol and collected by decanting the supernatant. The polymer was dried *in vacuo* at 100−110 °C overnight (*ca*. 16 h) in order to remove any residual DMSO. Four polyamides of 35 %, 46 %, 73 % and 82 %

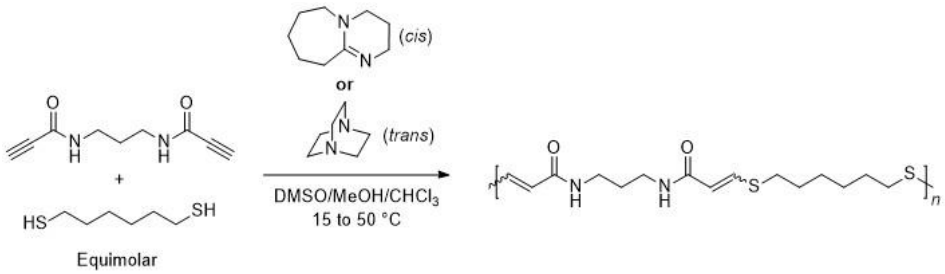

Scheme 2. Synthesis of the amide materials via thiol-yne step growth polymerisation.

cis content, have been synthesised by the above method, Scheme 2, the four polyamides were provided in a powder form.

The double bond stereochemistry was determined by integration of the resonances in the ^{1}H solution state NMR spectrum that are attributed to *cis* and *trans* double bond isomers respectively. These signals typically appeared at *ca*. δ = 5.9 and 7.1 ppm for the *cis* isomer and δ = 5.8 and 7.6 ppm for the *trans* isomer (in $CDCl_3$). Critically, they can be distinguished from their different coupling constants (*cis*: 3*J*H-H = 10.2 Hz, *trans*: 3*J*H-H = 15.2 Hz).

6.2.2 Methods

Gel Permeation Chromatography (GPC) measurements were performed on an Agilent 1260 Infinity II Multi-Detector GPC/SEC System fitted with RI and ultraviolet (UV) detectors (λ = 309 nm) and PLGel 3 µm (50 × 7.5 mm) guard column and two PLGel 5 µm (300 × 7.5 mm) mixed-C columns. For polyamides, DMF with 5 mM NH_4BF_4 was the eluent (flow rate 1 mL/min, 50 °C) and a 12-point calibration based on poly(methyl methacrylate) standards (PMMA, Easivial PM, Agilent) was applied for determination of molecular weights. For polyesters, $CHCl_3$ with 0.5% NEt_3 was the eluent (flow rate 1 mL/min, 40 °C) and a 12-point calibration based on poly(styrene) standards (PS, Easivial PS, Agilent) was applied for determination of molecular weights.

All ^{13}C Solid State Nuclear Magnetic Resonance measurements were performed at 9.4 T using a Bruker Avance 400 MHz spectrometer operating at ^{13}C Larmor frequency (ν_o) of 100.59 MHz. These experiments were performed using a Bruker 4 mm HX probe which enabled a MAS frequency of 12 KHz to be implemented. Pulse length calibration was performed on alanine$_{(s)}$ from which a π/2 pulse time of 2.5 μs was measured. All measurements were undertaken with a π/2 nutation angle along with a delay between subsequent pulses of 10 s. A cross polarisation contact time of 1500 ms was used with a 70-100 % ramp[73] for ^{13}C cross polarisation magic angle spinning (CPMAS) experiments. The $T_{1\rho}$ relaxation experiments used spin lock delays from 0.3 to 50 ms, the T_{CH} experiments used contact times of 0.1 to 10 ms. The $T_{1\rho}$ and T_{CH} values were obtained from the experimental data as described in chapter 4 section 4.2.1.

All ^{1}H MAS NMR measurements were performed at 11.7 T using a Bruker Avance 500 MHz spectrometer operating at ^{1}H Larmor frequency (ν_o) of 500 MHz. These experiments were performed using a Bruker 1.3 mm HXY probe which enabled a MAS spinning frequency of 60 kHz to be implemented. Flip angle calibration was performed on alanine$_{(s)}$ from which a π/2 pulse time of 2.5 μs was measured. All measurements were undertaken with a π/2 tip angle

along with a delay between subsequent pulses of 10 s. 2D ^{1}H single quantum (SQ) spin-diffusion (NOESY-type) and 2D ^{1}H double quantum (DQ) BaBa recoupling[136-138] experiments were performed they each employed a rotor synchronised t_1 increment of 20.27 μs. The spin diffusion spectrum was acquired with 4 coadded transients for each 164 t_1 FIDs using a recycle of 10 s and a spin-diffusion mixing time of 3 ms. The ^{1}H DQ spectrum was acquired with 4 coadded transients for each of 380 t_1 FIDs using a recycle delay of 10 s.

A 2D hCH HETCOR spectrum and a 2D frequency switched Lee-Goldburg (FSLG) HETCOR measurements were performed at 11.7 T using a Bruker Avance 500 MHz spectrometer operating at ^{1}H Larmor frequency (ν_o) of 500 MHz and a ^{13}C larmor frequency of 125.8 MHz, with 128 transients coadded for each of 73 t_1 FIDs and 137 t_1 FIDs respectively, using a recycle delay of 10 s. A t_1 increment of 29.45 µs and 2 CP contact times of 1000 µs with a 70-100 % ramp were used for the hCH HETCOR. A t_1 increment of 25.07 µs and a CP contact time of 200 µs with a 70-100 % ramp was used for the FSLG HETCOR. The FSLG HETCOR experiments were performed using a Bruker 4 mm HXY probe which enabled a MAS spinning frequency of 12 kHz to be implemented and the hCH HETCPR experiments were performed using a Bruker 1.3 mm HXY probe which enabled a MAS spinning frequency of 60 kHz to be implemented.

All ^{13}C chemical shifts were externally referenced against the IUPAC recommended primary reference of $Me_4Si_{(l)}$ (1 % in $CDCl_3$, δ_{iso} = 0.0 ppm), via the secondary $alanine_{(s)}$ reference (δ_{iso} = 20.5 ppm)[74]. All ^{1}H chemical shifts were externally referenced against the IUPAC recommended primary reference of $Me_4Si_{(l)}$ (1 % in $CDCl_3$, δ_{iso} = 0.0 ppm), via the secondary $alanine_{(s)}$ reference (δ_{iso} = 1.1 ppm)[74].

Small angle X-ray scattering (SAXS) measurements were performed on a Xeuss 2.0 Cu Kα (1.54) Å with a q range of 0.004 to 0.16 Å^{-1}. SAXS data was analysed using modelling II of Irena package[139]. Wide angle X-ray scattering (WAXS) was performed simultaneously with a q range of 1.31 to 3.26 Å^{-1}, q values were converted to 2θ angles using the equation $q = \left(\frac{4\pi}{\gamma}/\sin\theta\right)$ where λ is the wavelength of Cu, 1.54 Å. Particle size distribution was determined as described in chapter 3 section 3.5.

Powder X-ray diffraction was performed on a Panalytical X'Pert Pro MPD equipped with a curved Ge Johansson monochromator, giving pure Cu Kα1 radiation (1.54 Å) and a solid state PiXcel detector. The powder was mounted on a zero-background offcut-Si holder, spinning at 30 rpm with a step size of 0.013° and a time per step of ~ 100 s with a 2θ range from 2° to 40°.

Differential scanning calorimetry (DSC, Mettler Toledo) measurements were performed under nitrogen heating from -50 °C to 150 °C at a scanning rate of 10 °C/min.

Thin films of each polymer were fabricated using a vacuum compression machine (TMP, Technical Machine Products Corp.). The machine was preheated to 170 °C. Then polymer was added into the 50 × 50 × 0.5 mm mould and put into the compression machine with vacuum on. After 15 minutes of melting, the system was degassed three times. Next, 10 lbs*1000, 15 lbs*1000, 20 lbs*1000, 25 lbs*1000 of pressure were applied for 2 minutes respectively. After that, the mould was cooled down with 1000 psi of pressure to prevent the wrinkle on the film's surface. Dumbbell-shaped samples were cut using a custom ASTM Die D-638 Type V.

Tensile tests were carried out using Instron (Instron 5543 Universal Testing Machine) at room temperature (25 ± 1 °C). The gauge length was set as 7 mm and the crosshead speed was set as 10 mm/min. The dimensions of the neck of the specimens were 7.11 mm in length, 1.70 mm in width and 0.50 mm in thickness. The elastic moduli were calculated using the slope of linear fitting of the data from strain of 0 to 0.1 %. The reported results are average values from three individual measurements.

6.3 Results and Discussion

6.3.1 Structural determination

The assignment of the ^{1}H and ^{13}C resonance is important for understanding the structure of novel materials on which SSNMR measurements have not been previously performed, Figure 6-2. The confident assignment of the chemical shifts is achieved by combining 1D ^{1}H MAS and ^{13}C CPMAS and 2D ^{1}H-^{13}C HETCOR, ^{1}H-^{1}H NOESY and ^{1}H-^{1}H BABA experiments. Two ^{1}H-^{13}C HETCOR experiments have been used.

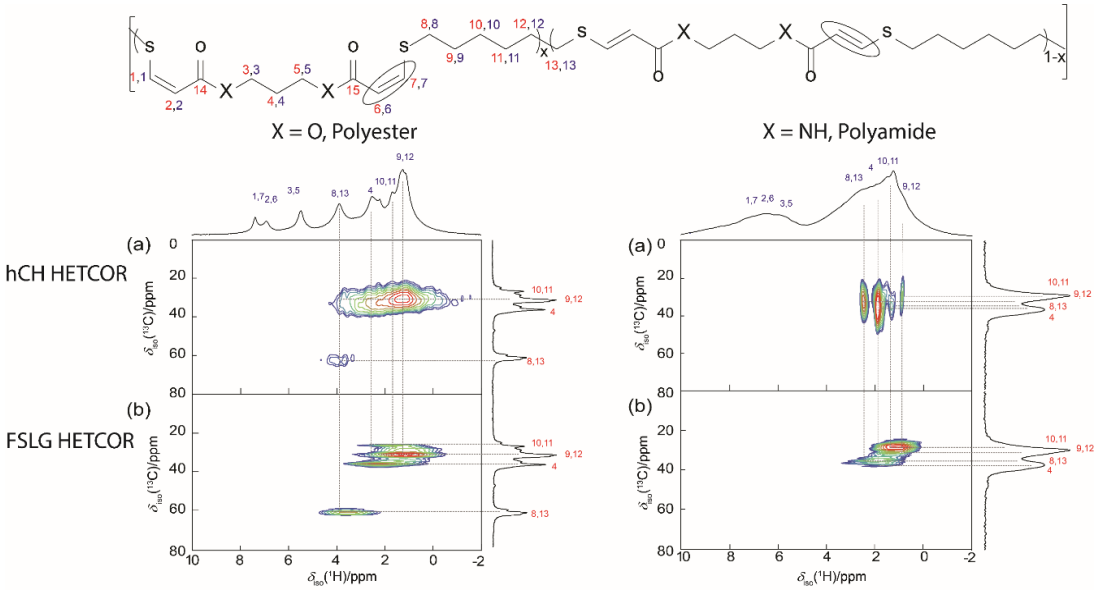

Figure 6-1. The (a) hCH HETCOR, B_0 = 11.7 T, ν_r = 60 kHz, (b) Frequency Switch Lee-Goldburg HETCOR, B_0 = 11.7 T, ν_r = 12 kHz for the polyester (left) and the polyamide (right).

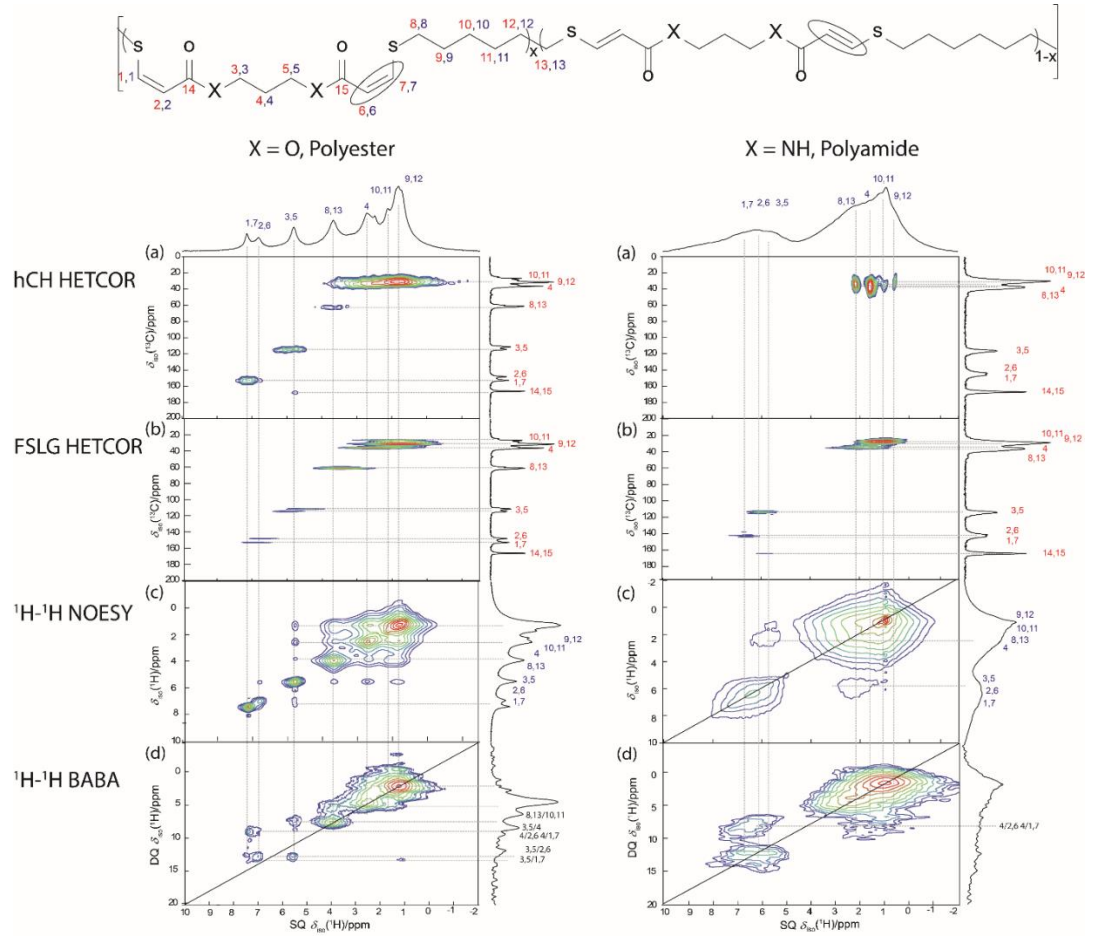

Figure 6-2. The 2D NMR spectra of 80% cis, 7.6 kDa ester, a) hCH HETCOR, B_0 = 11.7 T, ν_r = 60 kHz, b) FSLG HETCOR, B_0 = 9.4 T, ν_r = 12 kHz, c) ^{1}H-^{1}H NOESY, spin-diffusion mixing time = 3 ms and d) ^{1}H-^{1}H double quantum BABA for the 80 % polyester (left) and 82 % polyamide(right)

The hCH HETCOR for the polyester does show several correlations between the C and H species however the resolution in the CH_2 region of the spectrum is not great enough to be able to assign the individual CH_2 species in the aliphatic chain. The FSLG HETCOR provides greater resolution allowing for the assignment of each of the aliphatic CH_2's. The hCH spectrum for the polyamide shows four distinct H environments between 0 – 3 ppm correlating to the CH_2 region, between ~ 0 - 40 ppm, in the ^{13}C dimension, Figure 6-1

The corresponding region in the polyester contains three environments with the fourth appearing at ~ 60 ppm. The ^{13}C CPMAS spectra of both forms of nylon-6 shows that there is no resonance peak at 60 ppm[129], this helps to confirm the assignments here.

The FSLG HETCOR for the polyamide additionally shows that there are two environments at 150 ppm similarly to the polyester showing that there are still two environments under the broad resonance.

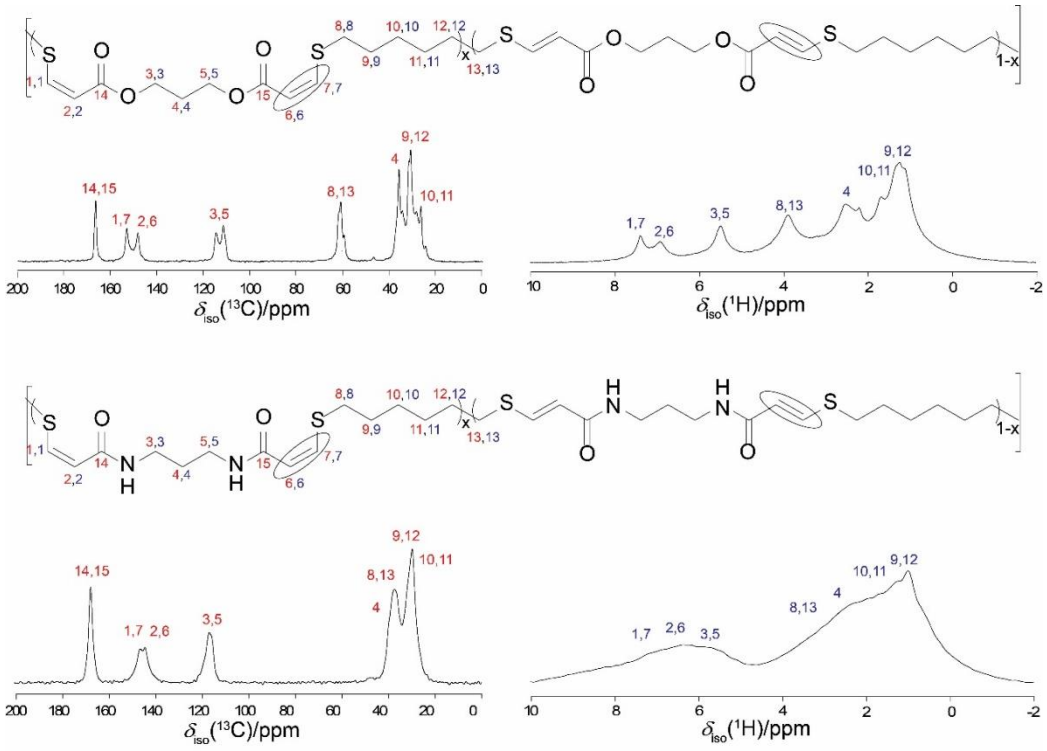

Figure 6-3. The assignment of the Carbon and Proton resonance peaks for the polyester (top) and polyamide (bottom). The Carbon atoms are assigned the numbers in red and the corresponding bonded protons are numbered in blue.

The ^{1}H-^{1}H NOESY for the polyester shows a greater number of correlations between the CH_2 group 3,5 and additional CH_2 groups, in particular those in the aliphatic chain. The ^{1}H-^{1}H BABA showed only correlations between the CH_2 3,5 and the neighbouring CH_2 4, and the double bond CH's. This potentially suggests, due to the different distances at which the NOESY and BABA experiments produce correlations at that the BABA is only seeing H species within the same repeat unit or in neighbouring chains and the NOESY is potentially seeing H species on folded chains where the aliphatic chain is aligned with the ester groups.

The ^{1}H-^{1}H NOESY for the polyamide shows a correlation between the aliphatic chain and amide region, the correlation is not as strong as the polyester suggesting the distance between the folded chains is greater and the material is more amorphous and less tightly held. The ^{1}H-^{1}H BABA for the polyamide additionally shows fewer correlations than the polyester. The final peak assignments are shown in Figure 6-3

6.3.2 Changing *cis* content

^{13}C cross polarisation magic angle spinning measurements have been performed on the four polyesters and four polyamides, Figure 6-4. A higher c*is* % results in greater splittings of the CH_2 resonance peak which shows greater crystallinity of the elastomeric materials. There is a very pronounced change in the ^{13}C CPMAS spectra at 57 % *cis* content which shows the change to a more amorphous material. The ^{1}H MAS NMR spectra also show an increase in crystallinity with increasing *cis* content as the resolution decreases with an increase in *cis* content. The ^{13}C CPMAS spectra of the polyamide, does not change with increasing *cis* content, this shows that the *cis*/*trans* ratio does not affect the crystallinity of these materials, this could be due to the hydrogen bonding present in the polyamides. The ^{1}H MAS NMR data for the polyamides does however shows a change in resolution and transition from a more amorphous material to crystalline material with increasing *cis* content.

The $T_{1\rho}$ relaxation times have been plotted as a function of c*is* content % for the polyesters, Figure 6-5 (left) and compared to the change in network Young's modulus. As the c*is* content increases so does the relaxation time. A longer relaxation time means that the polymer chains are less mobile and is another indication of increased crystallinity. The sharp increase in $T_{1\rho}$ relaxation times between 57 % and 67 % c*is* also shows the change to a more amorphous material. The trends in $T_{1\rho}$ relaxation times of the polyesters and polyamides confirm the differences already seen in the ^{13}C CPMAS data. There is no trend in the change in $T_{1\rho}$ relaxation of the polyamides, Figure 6-5 (right) which indicates there is no trend in mobility and consequently crystallinity. The correlation between the cross polarisation time

constant (T_{CH}) and dynamic moduli has been investigated previously on a series of polyurethane elastomers.[140-141] The work by Marcinko and Parker[140] showed that T_{CH} measurements and macroscopic moduli are influenced by similar distributions of molecular motions. The trend in the T_{CH} times have been investigated here, Figure 6-6, the resonance peaks at 31 ppm and 59.9 ppm show an inverse trend to the $T_{1\rho}$ times.

This shows an increase in intermolecular interaction strength and decrease in distance between the polymer chains as the *cis* content increases correlating with an increase in the Young's modulus and crystallinity of the polyesters. The C environments with fewer surrounding H's, *e.g.* 112 ppm, do not follow this inverse trend. As with the $T_{1\rho}$ times for the polyamides there is no trend in the T_{CH} times. The T_{CH} times for the polyamides are shorter than those of the polyester, indicating a greater cross polarisation efficiency, whereas replacement of the ester group with an amide group results in increased hydrogen bonding and improves cross polarisation.

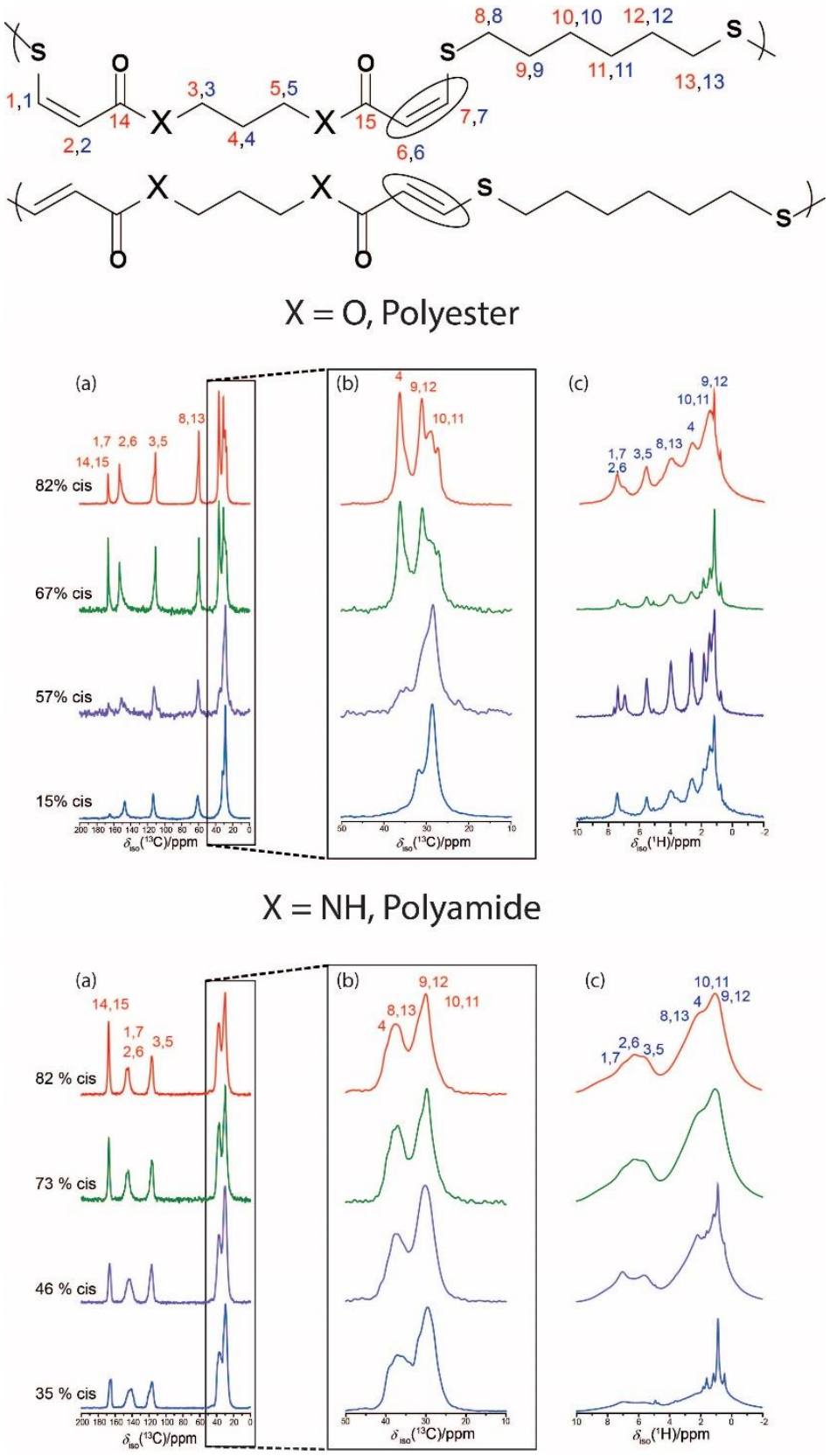

Figure 6-4. a) The ^{13}C CPMAS NMR spectra b) the ^{13}C CPMAS expanded CH_2 region c) the ^{1}H MAS NMR spectra for 82%, 67%, 57% and 15% Cis content polyesters, with C (red) and H (blue) assignments for the polyester (left) and polyamide (right).

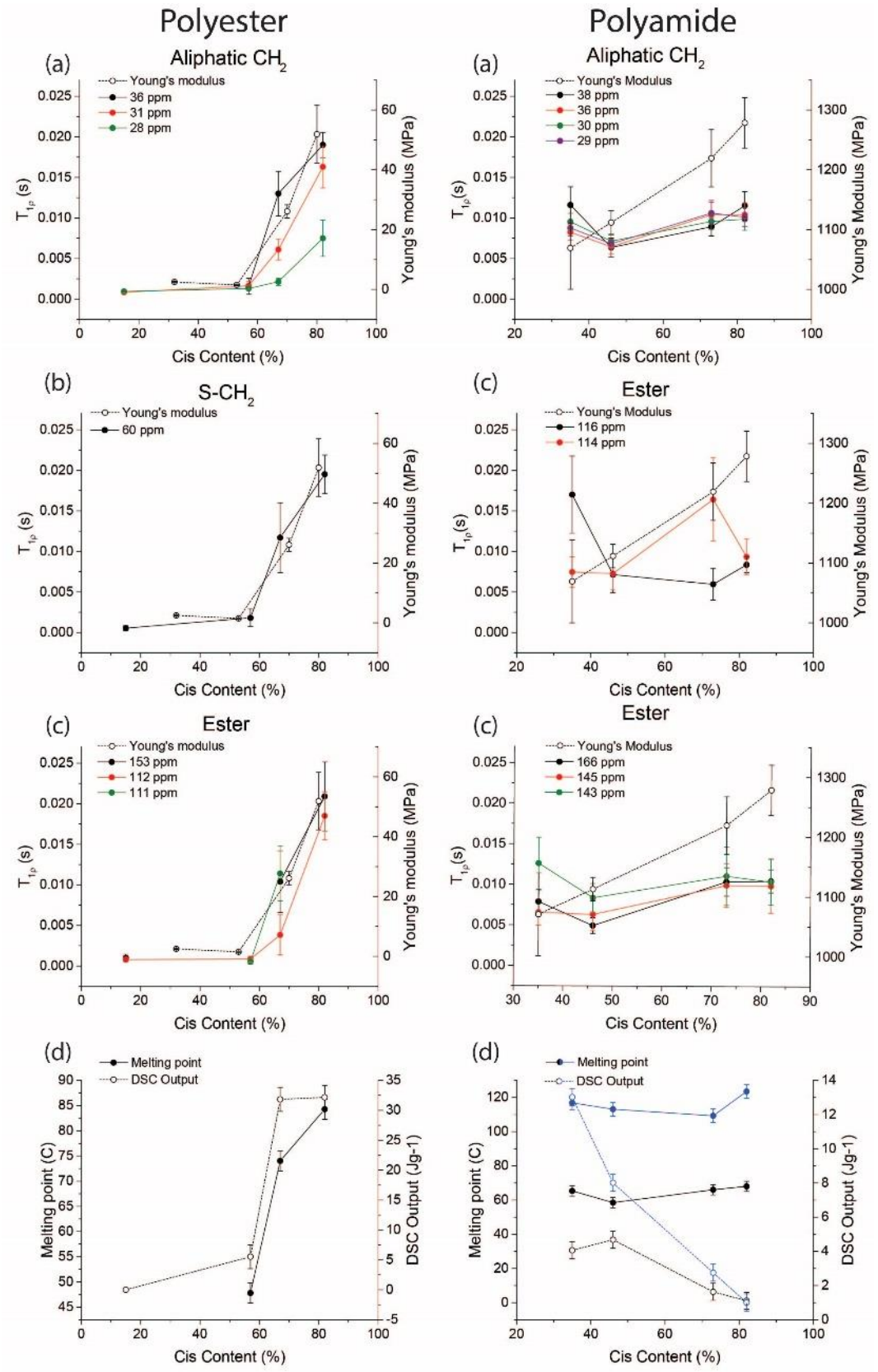

Figure 6-5. The $T_{1\rho}$ times as a function of cis content for a) the aliphatic CH_2 chain, b) the S-CH_2 and c) the ester C's and d) the melting point and DSC output as a function of cis content for the polyesters (left) and polyamides (right).

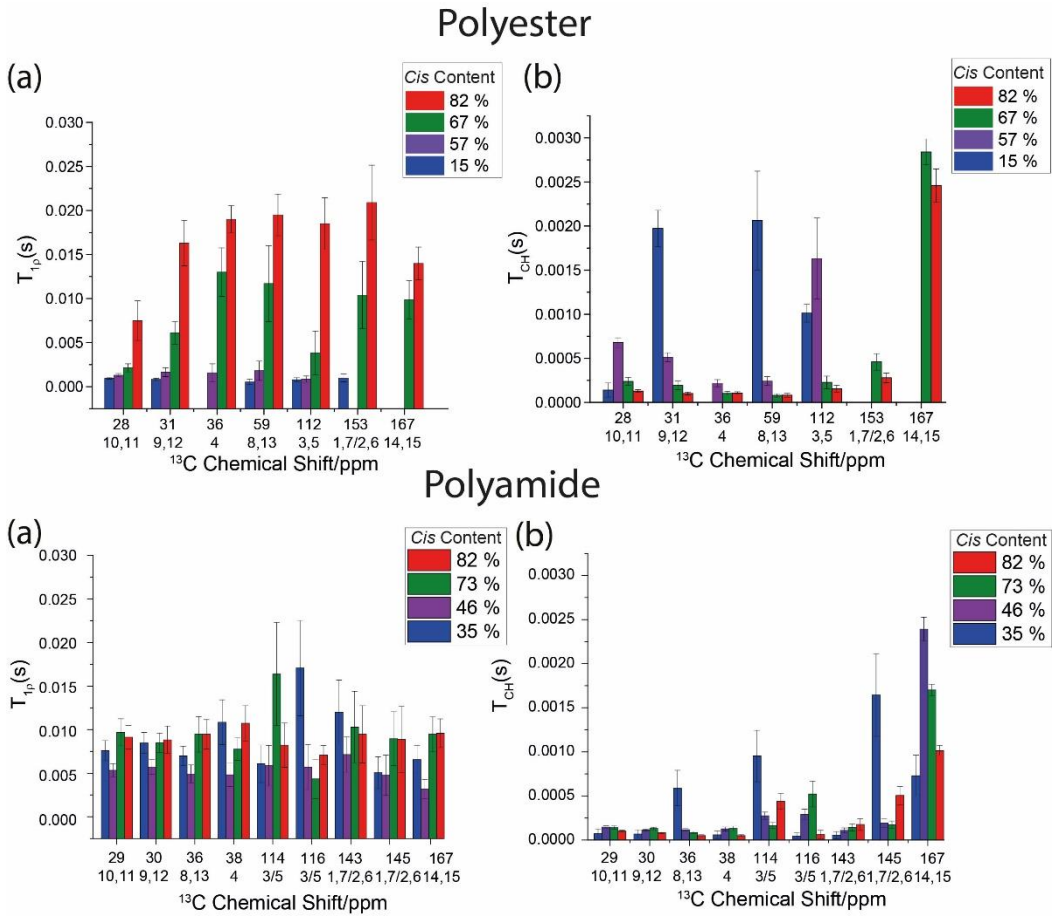

Figure 6-6. The a) $T_{1\rho}$ relaxation times and b) T_{CH} times for each of the carbon resonances for the polyester (top) and polyamide (bottom).

The change in $T_{1\rho}$ and T_{CH} times have been compared to the change in Young's modulus for the polyamides. There is an increase in Young's modulus with increasing *cis* content however this is only a 16.4 % increase compared to a 1976 % increase for the polyesters between the lowest and highest *cis* content. The increase for the polyamides is not large enough to affect the $T_{1\rho}$ times or T_{CH} times and show a change in molecular mobility or distance and interaction strength between polymer chains. The Young's modulus does increase sharply between 46 % and 73 % *cis* content, this is reflected in the ^{1}H MAS NMR data where the resolution of the spectra greatly changes between 46 % and 73 % *cis* content showing a transition from an amorphous material to a more crystalline material.

The $T_{1\rho}$ times of the ^{13}C environments within each sample can also be compared to distinguish between 'hard' and 'soft', Figure 6-6. The $T_{1\rho}$ relaxation times for the aliphatic CH_2 chain, especially C's 11, 12, 13 and 14 are much shorter than CH_2's 4, 5 and 6 next to the ester groups.

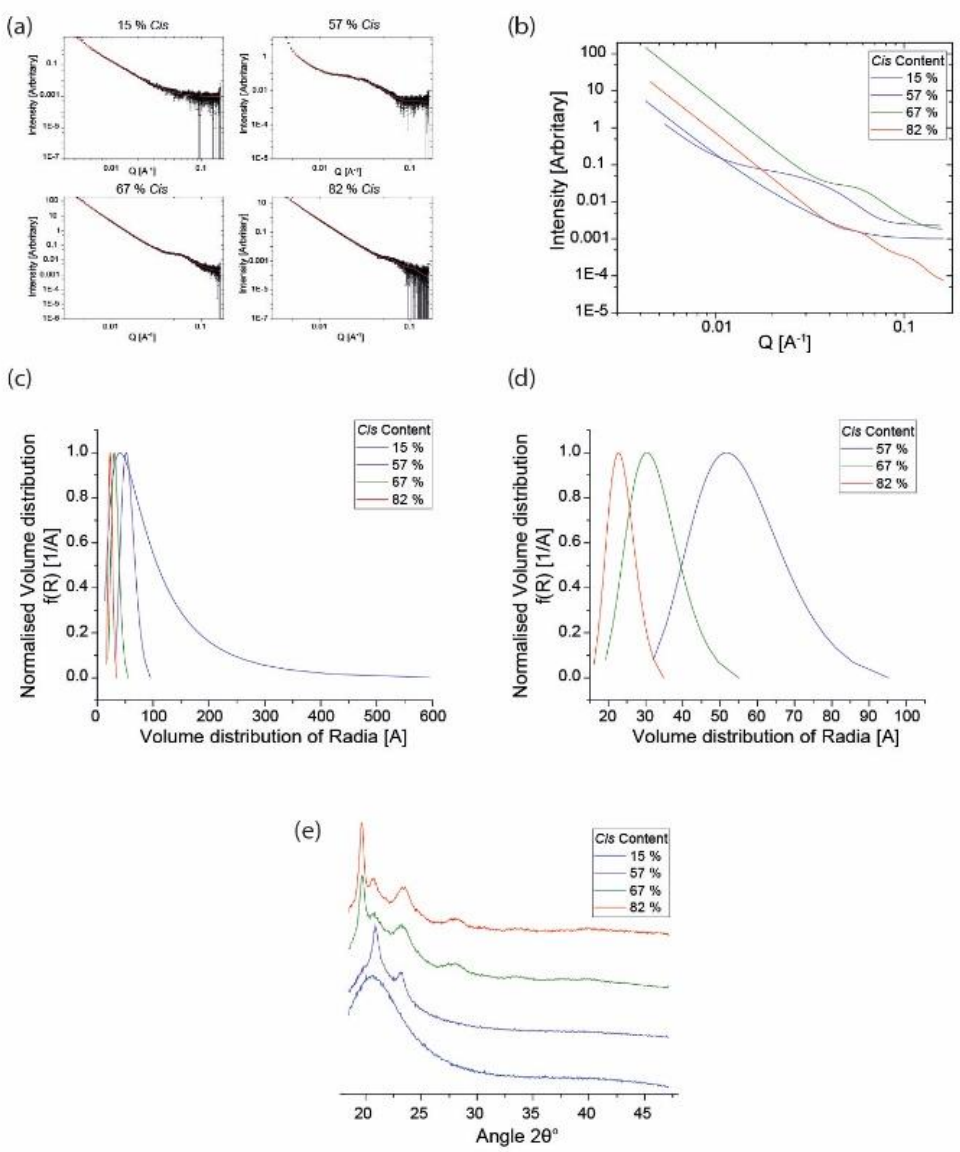

Figure 6-7. The SAXS and WAXS measurements for the 82 %, 67 %, 57 % and 15 % *cis* polyesters, a) the SAXS pattern, b) the hard spheres model of the SAXS pattern, c) the particle size distribution for the four polyesters, d) the particle size distribution for 82 %, 67 % and 57 % cis polyesters and e) WAXS patterns.

This, along with the longer $T_{1\rho}$ times of the ester and CH, suggests that there is a 'soft' more mobile domain of CH_2's alternating with a 'hard' more rigid domain containing the esters and double bond regions. This pattern is the case for all four of the c*is* content percentages for the polyesters however is more noticeable in 82 % and 67 % *cis* content which are more crystalline and less mobile across all C's. The other point of consideration in the $T_{1\rho}$ times is the much shorter relaxation time of the double bond C's in the 67 % *cis*, this could potentially be to do with the changing mobility from the more amorphous 57 % *cis* to the highly crystalline 82 % *cis*. The T_{CH} times have been determined for each of the c*is* contents however

there is no trend between them in the same way as the $T_{1\rho}$ times. The $T_{1\rho}$ and T_{CH} times for the polyamide do not show the same pattern as the polyesters indicating uniform mobility across the repeat unit. The $T_{1\rho}$ and T_{CH} times for the COO group, 167 ppm, polyesters cannot be compared with the trend as a relaxation time was unable to be obtained for 15 % and 57 % *cis* content. This is due to the motional nature of the samples resulting in an inability to efficiently cross polarisation the esters, therefore being unable to detect it during $T_{1\rho}$ experiments.

The SAXS and WAXS measurements for the polyesters, Figure 6-7, both show the difference in crystallinity of the four polyester c*is* percentages. The 15 % *cis* is clearly an amorphous material which is also seen in the solid state NMR ^{13}C CPMAS spectra and with the shorter $T_{1\rho}$ relaxation times. The SAXS and WAXS measurements for the polyamides, Figure 6-8, also show the similarity of the different *cis* percentages, however there is a single diffraction peak for 73 % and 82 % *cis* content in the WAXS pattern showing some crystallinity. The WAXS pattern for 35 % and 46 % *cis* content have a similar appearance to the α-form of nylon 6 whilst the 73 % and 82% *cis* polyamides have a diffraction peak characteristic of the γ-form

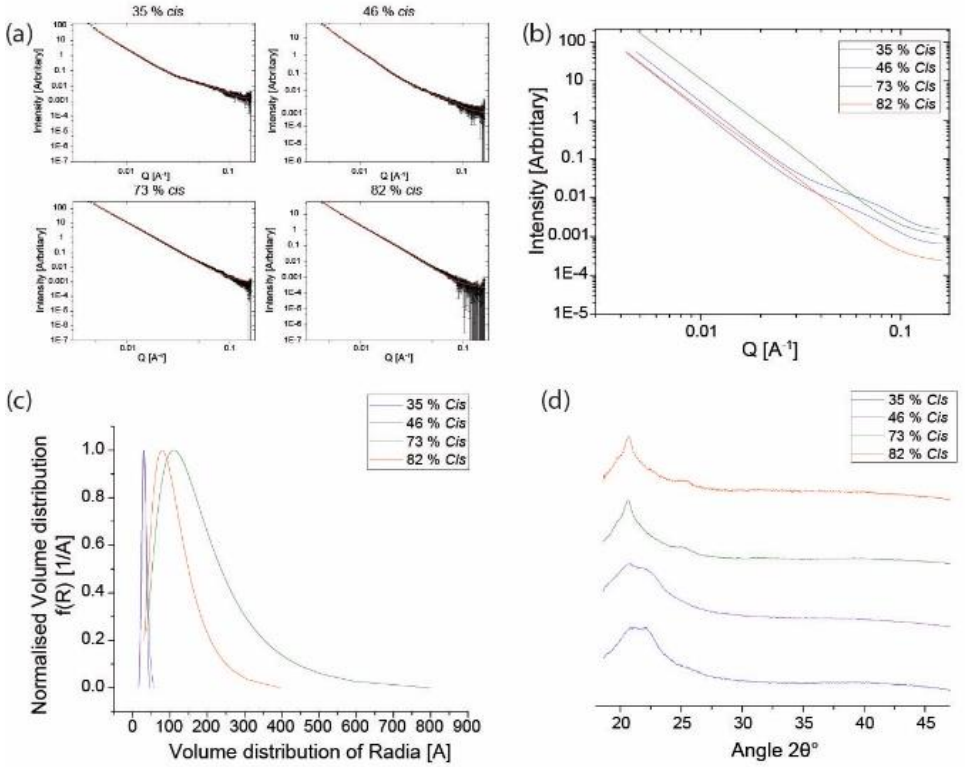

Figure 6-8. The SAXS, WAXS measurements for the 82 %, 73 %, 46 % and 35 % *cis* polyamides, (a) the SAXS pattern, (b) the hard spheres model of the SAXS pattern, (c) the particle size distribution and (d) the WAXS patterns.

of nylon 6.[129] Due to the weak scattering of the amorphous 15 % *cis* polyester sample the volume distribution was harder to obtain, it was possible however the distribution extends to much higher sizes. When comparing only 57 %, 67 % and 82 % there is a clear trend in volume distribution and therefore particle size, as the c*is* content increases the particle size decreases and the distribution also narrows. There is no trend in volume distribution and consequent particle size for the polyamides, there is a distinction between the higher two *cis* percentages 73 % and 82 %, which have larger average particle sizes and wider volume distribution, and the lower two *cis* percentages 35 % and 46 %, which have smaller sizes and a narrower distribution. As previously stated, 73 % and 82 % *cis* polyamide are potentially in the α form, this form has weaker hydrogen bonding and greater intermolecular distances.

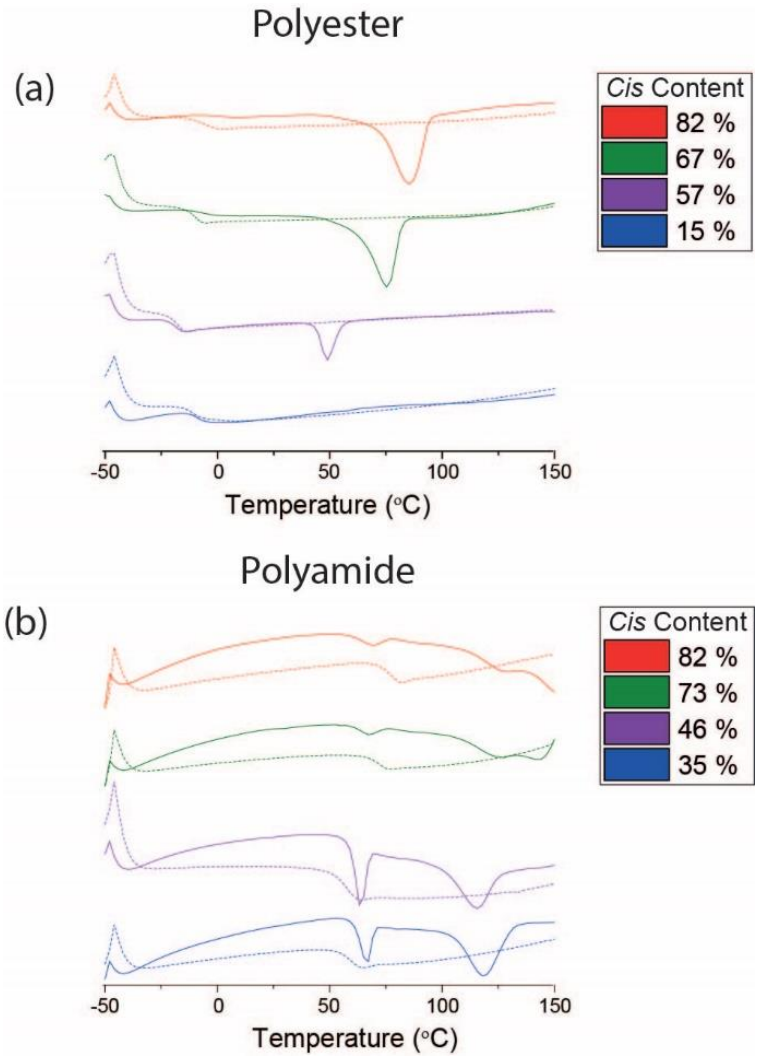

Figure 6-9. The DSC for the a) polyesters and b) polyamides (solid = first scan, dashed = second scan).

The wider distribution and larger average particle size would result in greater irregularity in the packing of the polyamide chains leading to weaker hydrogen bonding and larger intermolecular distances compared to 35 % and 46 % *cis* polyamide.

The DSC first heating scans show one exotherm for the polyesters and two for the polyamides, Figure 6-9. The higher exotherm, T_{III}, is attributable to the melting of crystalline regions, the lower exotherm, T_{II}, is attributed to the destruction of long range order and the onset of intersegmental mixing.[142] The polyester shows only one exotherm which increases with increasing *cis* content, the temperature at which this peak occurs would suggest that it is T_{II} and the T_m has not been reached. A higher *cis* content results in greater order, as is demonstrated by the SAXS and WAXS measurements, therefore a larger amount of energy will be required to destroy the long-range order resulting in a higher temperature and greater heat output. This trend matches that of the mechanical properties and $T_{1\rho}$ relaxation times. The 15 % *cis* polyester has no exotherms, the WAXS pattern demonstrates that it is amorphous and would therefore be in a disordered state at both low and high temperatures. The polyamides have two exotherms, both T_{II} and T_{III}, the heat output for 82 % and 73 % *cis* content is greater than 46 % and 35 % *cis*; the weaker hydrogen bonding in the α form polyamides would result in less energy being required to destroy the long range order and allow for intersegmental mixing as well as causing melting of crystalline regions.

6.3.3 Changing Molecular weight

Two ester oligomers of 80 % *cis* content with two molecular weights, 14.7 kDa and 7.6 kDa, with a dispersity of 2.49 and 1.99 respectively, have been compared to the corresponding polyester of 82 % *cis* content and a dimer of 82 % cis content. Two ester oligomers of 20 % *cis* content with molecular weights, 9.6 kDa and 12.6 kDa, with a dispersity of 2.42 and 2.89 respectively, have been compared to the corresponding polyester of 15 % *cis* content and a dimer of 20 % *cis* content.

The ^{13}C CPMAS spectra of all four 80 % *cis* materials, Figure 6-10 (top), are highly crystalline, the crystallinity increases with decreasing molecular weight. A comparison of the resonance peaks at 111 ppm and 150 ppm, C's 1,7/2,6 and 3,5 respectively show the difference in symmetry of the four materials. The dimer has a single resonance peak for each of the pairs of C's showing that they exist in the exact same environment and the dimer is therefore symmetrical. The same resonance peaks in both oligomers are split into two distinct peaks which shows that the C's are in two separate environments and therefore do not possess any symmetry. The resonance peak in the polymer has a shoulder to it which shows that the

environments are not completely equivalent. The ^{13}C CPMAS spectra of the four 20 % *cis* materials, Figure 6-10 (bottom), are more amorphous and the resolution between the polymer and two oligomers does not vary. The 20 % *cis* dimer is less comparable as it is a liquid consequently a single pulse experiment was implemented with no spinning; due to the liquid state of the material the resolution is increased. The ^{13}C spectra for both dimers have an additional resonance peak at 14 ppm attributable to the CH_3 end chain group. The $T_{1\rho}$ relaxation and T_{CH} times for the 80% *cis* materials have been measured, Figure 6-11 (top), the $T_{1\rho}$ relaxation times are a factor of 10 longer for the dimer than the other three materials. There is a direct correlation of the T_{CH} times with greater mw as they are affected by interaction strength and distance as well as mobility. The longer $T_{1\rho}$ relaxation times of the dimer contributes to the shorter T_{CH} time and greater cross polarisation efficiency however the T_{CH} times are not a factor of 10 shorter than the oligomer and polymers suggesting that in the case of the polymers interaction strength and distance have a greater role. The $T_{1\rho}$ and T_{CH} times for the 20 % *cis* materials have also been measured, Figure 6-11 (bottom), it was not possible to measure the dimer as it is a liquid and no Hartmann-Hahn condition is possible.

While the $T_{1\rho}$ relaxation times do not change as a function of molecular weight the T_{CH} times are shorter for the oligomers. This difference in trend suggests that the distance between the molecules is greater and results in a weaker interaction strength is weaker for the oligomers. The highly amorphous nature of the dimers and polymers resulted in inefficient cross polarisation, leading to greater noise in the spectra, and consequently larger errors in the $T_{1\rho}$ and T_{CH} measurements for the 20 % *cis* content despite an increase in scans. Interestingly the increase of T_{CH} with greater molecular weight is inverse for the 80 % *cis* materials.

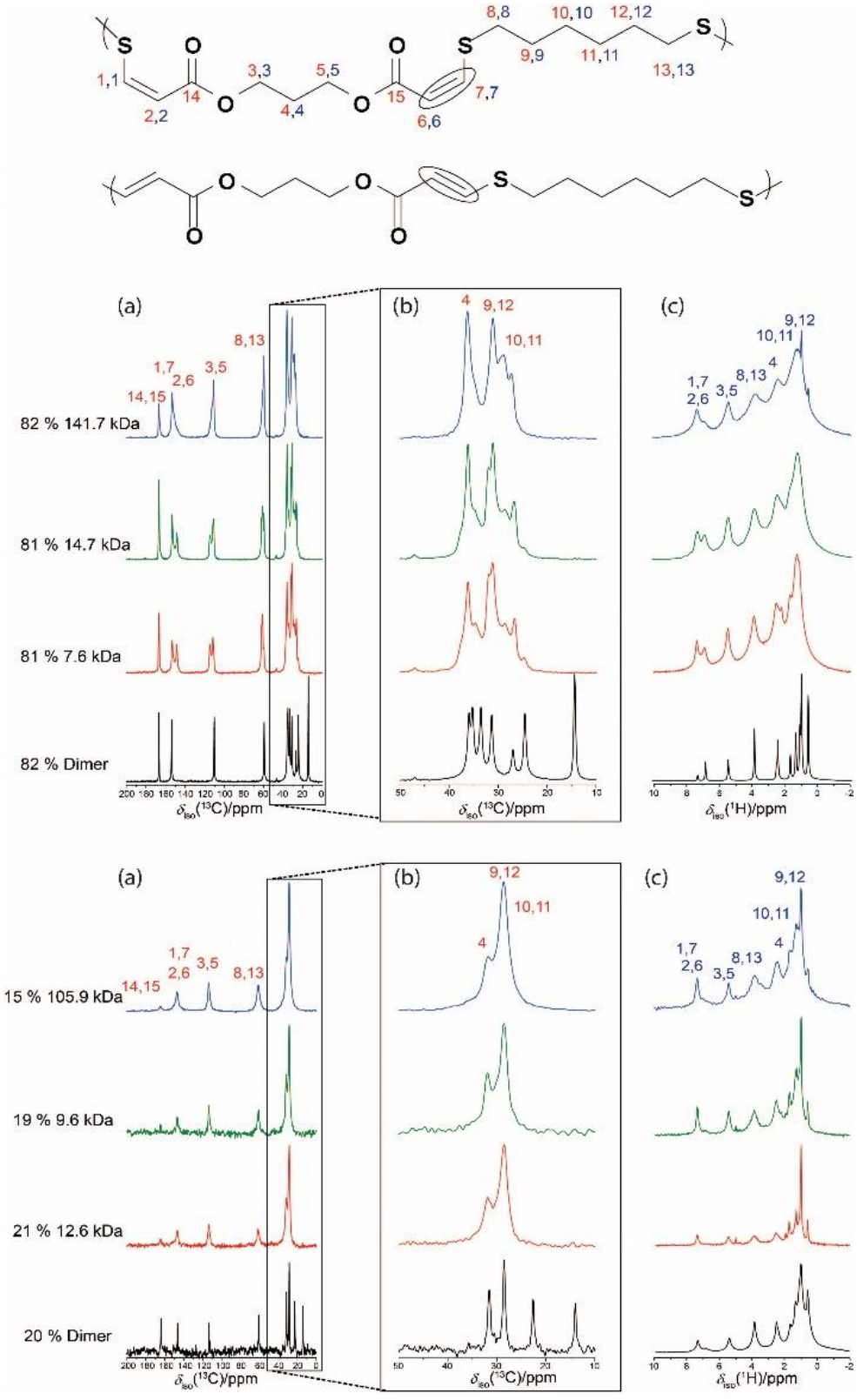

Figure 6-10. (a) The ^{13}C CPMAS NMR spectra (b) the ^{13}C CPMAS expanded CH_2 region (c) the ^{1}H MAS NMR spectra, with C (red) and H (blue) assignments, for the 80 % cis esters of molecular weight 141.7 kDa, 14.7 kDa 7.6 kDa and the dimer (top) and the 20 % cis esters of molecular weight 105.9 kDa, 9.6 kDa, 12.6 kDa and the dimer (bottom).

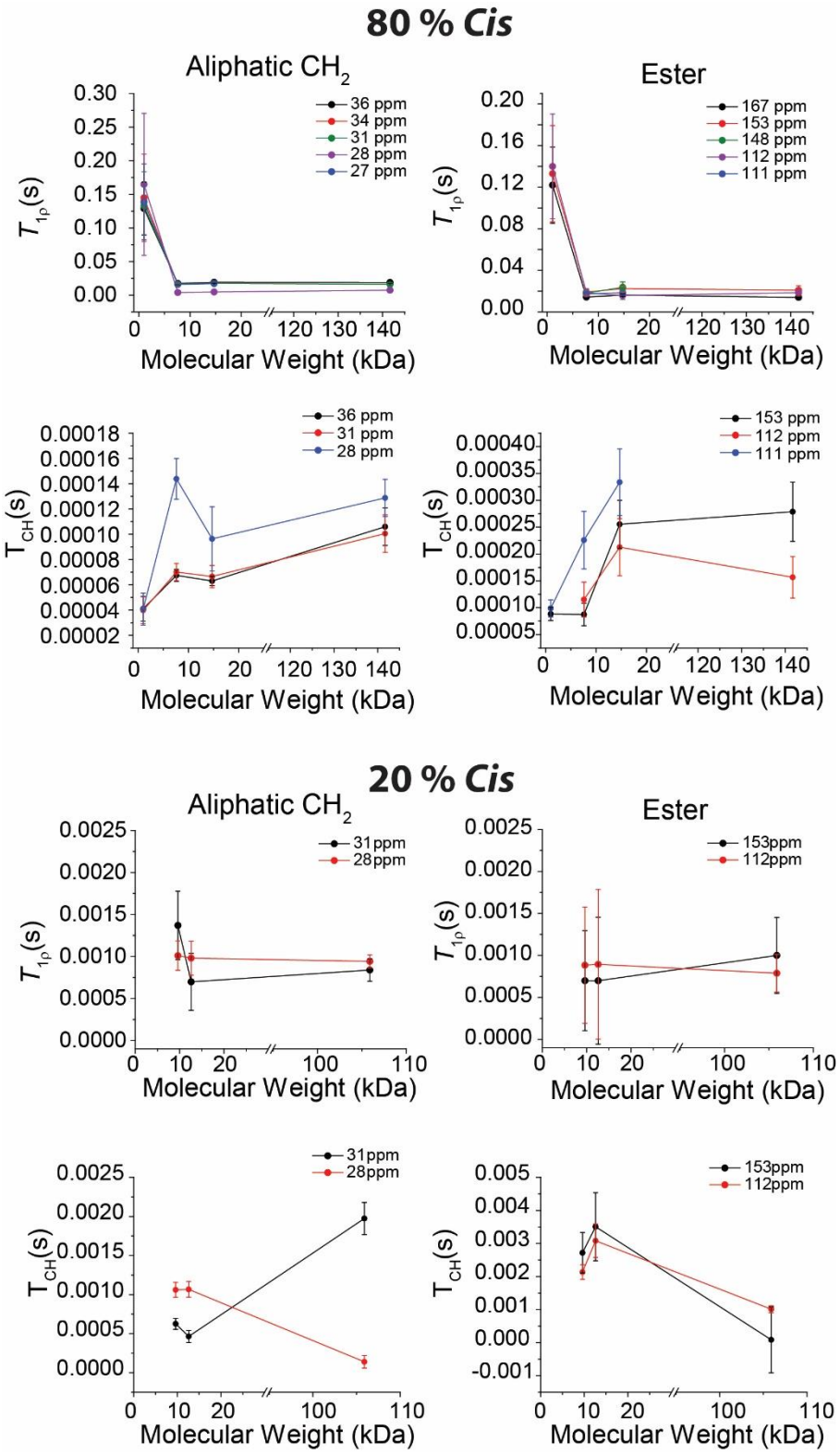

Figure 6-11. The $T_{1\rho}$ and T_{CH} times as a function of molecular weight for the 80 % *cis* (top) and 20 % *cis* (bottom)

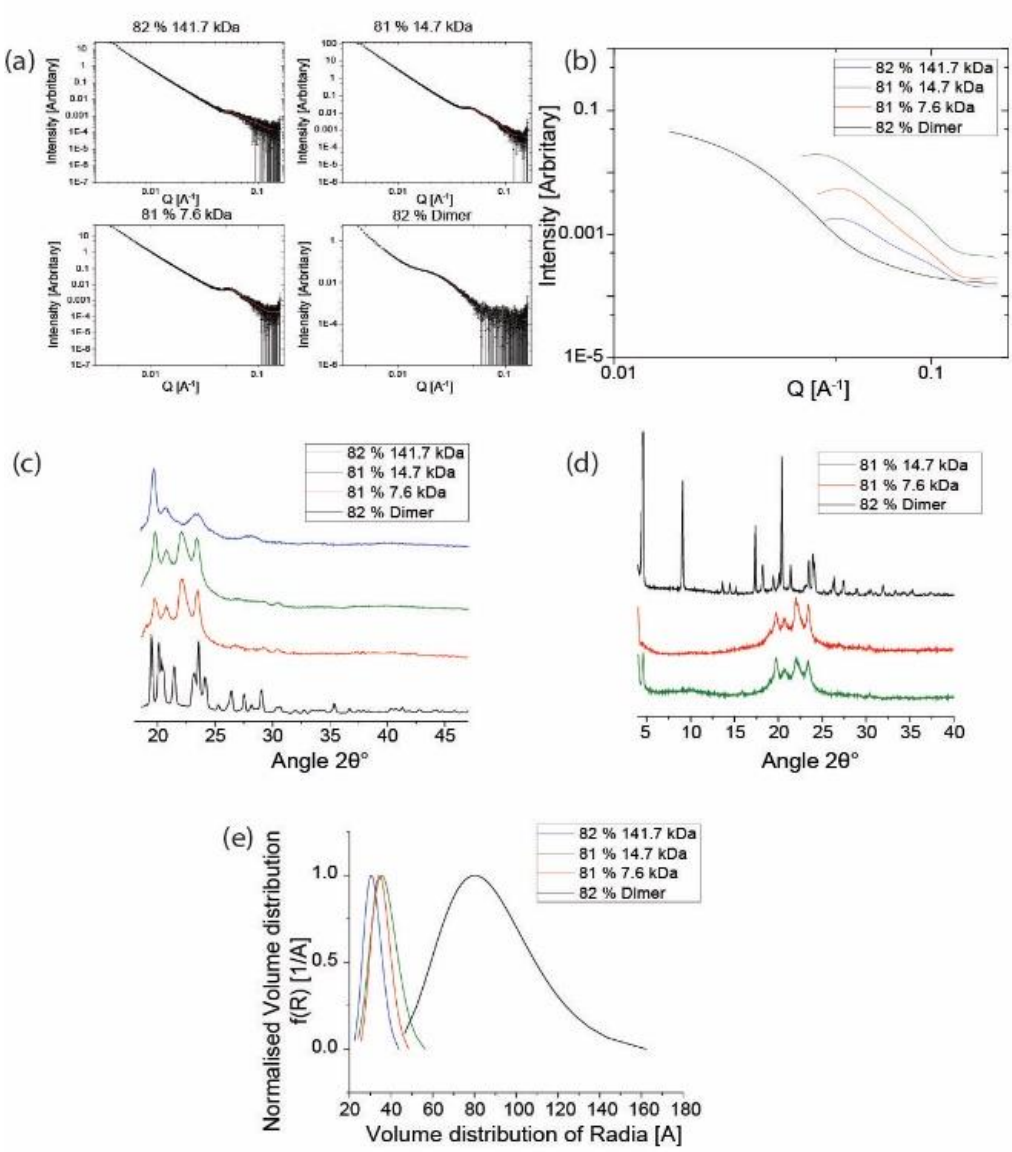

Figure 6-12. The SAXS and WAXS measurements for the 80 % *cis* esters, a) the SAXS pattern, b) the hard spheres model of the SAXS pattern, c) the WAXS patterns, d) powder XRD pattern and e) the particle size distribution.

SAXS/WAXS measurements have been performed on the 20 % *cis*, Figure 6-13, and 80 % *cis*, Figure 6-12, polyesters. The 20 % *cis* materials have SAXS/WAXS patterns characteristic of amorphous materials, as such it was not possible to fit the SAXS pattern and determine a volume distribution. The 80 % *cis* materials all have characteristically crystalline patterns with strong scattering allowing for a volume distribution to be determined. The average particle radius is larger for the dimer than the polymer and oligomers and has a wider distribution. Full powder patterns have been acquired for the two oligomers and the dimer, the dimer has a greater number of diffraction peaks in the WAXS and powder patterns.

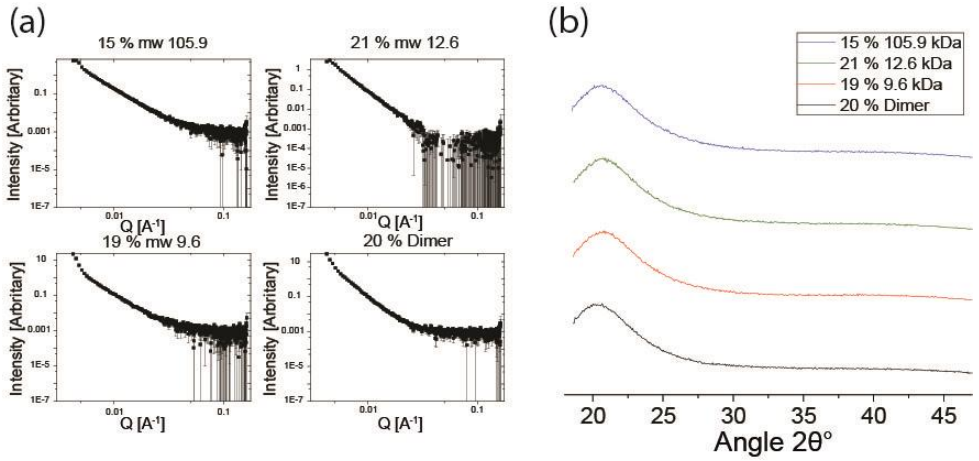

Figure 6-13. a) The SAXS and b) WAXS measurements for the 20 % *cis* esters

The dimer has a shorter chain length and can therefore have a larger number of orientations which leads to a different unit cell to the oligomers, the dimer also appears to be more crystalline and ordered.

The DSC first heating scans of the 80 % and 20 % *cis* content polyesters confirm that the 20 % *cis* polyesters are amorphous, and the 80 % *cis* polyesters are crystalline,

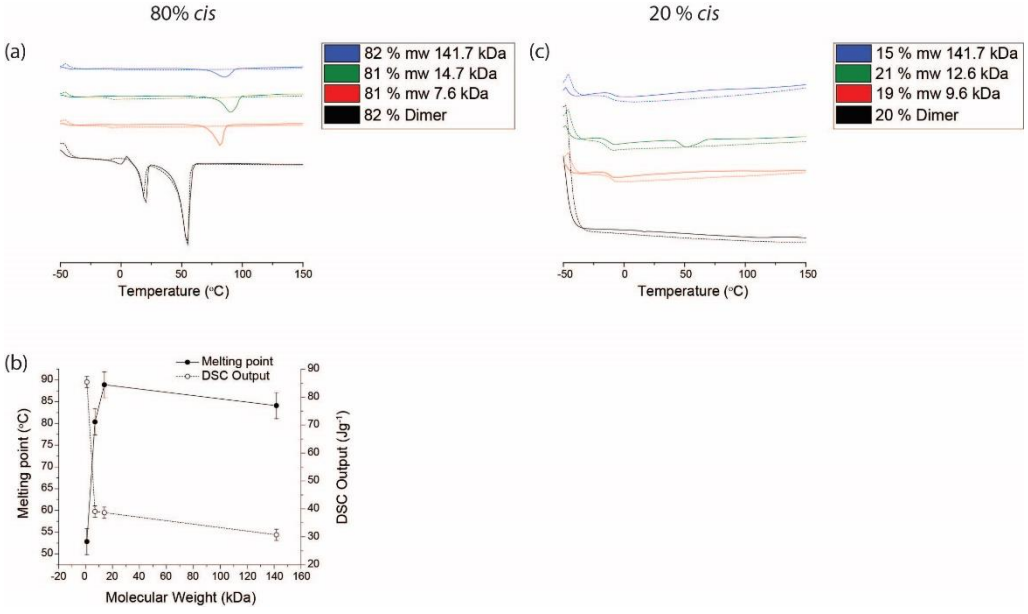

Figure 6-14. The decrease in the endotherm output at the melting point follows the change in mobility shown by the $T_{1\rho}$ measurements, showing the higher crystallinity of the dimer. The trend in melting point mirrors the change in T_{CH} with an increase in melting temperature; additionally, the dimer has a second melting point, indicating a second crystalline phase which is observed in the PXRD. This secondary crystalline phase

contributes to the significant reduction of mobility of the chains in the dimer and leads to increased long- and short-range order.

6.4. Conclusion

The stress-strain measurements on the four polyesters showed that a lower c*is* content resulted in a more amorphous material, this was confirmed by the SSNMR measurements which showed that a lower *cis* content had greater mobility and a ^{13}C CPMAS spectra characteristic of amorphous materials. The SAXS and WAXS measurements also showed that the lower *cis* content polymers are more amorphous, the particle size distribution also suggested that the higher *cis* content materials were capable of tighter packing due to the smaller average particle size and narrower distribution of the high c*is* content materials. The polyamides showed that replacing the dialkyne with an amide results in a material with stable crystallinity and mobility with a change in *cis* content, likely due to the increased hydrogen bonding present.

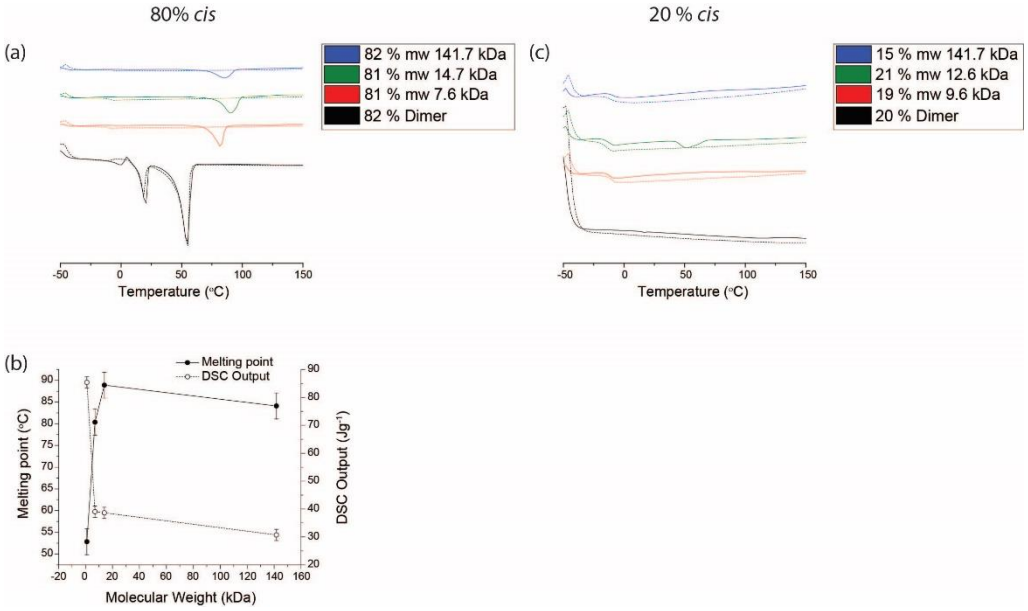

Figure 6-14. The differential scanning calorimetry for the 80 % and 20 % cis esters, a) the DSC scans (solid = first scan, dashed = second scan) for the 80 % cis esters, b) the melting temperature (black) and heat output (red) as a function of molecular weight for the esters, c) the DSC scans (solid = first scan, dashed = second scan) for the 20 % cis esters.

SSNMR, SAXS and WAXS has also been used to compare the crystallinity and molecular mobility of high and low c*is* content polyesters and ester oligomers. The 80% *cis* materials showed how SSNMR can be used to determine levels of symmetry in dimers, oligomers and

polymers demonstrated by the different splittings of the resonance peaks in the ^{13}C CPMAS spectra. There is a greater difference between the materials with 80 % *cis* content than the 20 % *cis* content. The 80 % *cis* dimer had longer relaxation times than the oligomers and polymers, there is little difference between the two different molecular weight oligomers. The powder XRD pattern showed that the dimer has a larger number of orientations and is more ordered this correlates with the reduced mobility as shown by the $T_{1\rho}$ relaxation times.

A combined approach of SSNMR, SAXS/WAXS and DSC allows for a greater understanding of how crystallinity and mobility affect the mechanical properties of polymeric materials and how it relates to the *cis* content and molecular weight of the polymers.

7. A Study on the Effect of Copper Doping on Calcium Phosphate Bioactive Glasses

7.1 Introduction

Bioactive glasses have a wide range of applications and compositions.[143] The first bioactive glass was developed by Hench *et al.* in 1969 using a Na_2O-CaO-SiO_2-P_2O_5 system.[144] The development of early compositions such as Bioglass 45S5® were found to form strong bonds with bones that could only be removed by breaking the bone.[145] This research stimulated the formation of many other bioactive materials, such as bioactive glasses with alternative and tuned compositions,[143] glass-ceramics[146] and synthetic hydroxyapatites.[147] Bioactive glass research has diversified greatly and now assumes many compositions silicate-based systems (analogous to the Bioglass® 45S5 family),[148-149] borate-based systems,[150] and phosphate-based glasses.[151] Many studies have demonstrated that phosphate-based glasses exhibit superior properties over silicate and borate-based analogues as they have lower glass transition temperatures and higher thermal expansion, in addition to the fact that they contain elements that are natural constituent of the human body that are easily resorbed under physiological pH conditions.[152] [153] The enhanced properties of phosphate-based bioactive glasses lead to many potential applications focussing on disc,[154-155] microtube,[156] microsphere[157-159] and fibrous shaped devices.[160-162] Phosphate glass fibres are used for cell transportation devices,[157] as nerve conduits[153] and as scaffolds for muscle regeneration.[163] The scaffolds can be improved when the fibres used for microtubes are combined with various polymers which aid in diffusion of nutrients and ingrowth of vascularisation.[164] Phosphate glasses microspheres have fewer uses than fibres but can most importantly be used for radiotherapy[165] by preventing tissue damage by providing a stable surface for cells to attach and proliferate.[159]

In addition to the morphological diversity that phosphate glass structures can offer, they also are able to chemically accommodate many different metal ions, such as Ti^{4+},[155, 159, 166] Ga^{3+},[167-168] Ag^{+},[169-170] and $Cu^{+/2+}$,[151, 171-172] into the network to improve mechanical strength and antibacterial and anti-inflammatory response. In particular, Cu has been recognised throughout history to have effective antimicrobial and antibacterial properties.[173] Several studies have demonstrated that Cu ions are beneficial to endothelial cells,[173-174] with its presence promoting angiogenesis and blood vessel maturation.[175-176] Other specific applications include the incorporation of Cu ions into phosphate glass fibre networks used for wound dressing meshes in the treatment of leg ulcers and severe burns.[177] In particular,

Cu^{2+} ions have been shown to help with bone remodelling due to inhibiting osteoclast activity.[178] The stable addition of copper into biomaterials, such as phosphate bioactive glasses and hydroxyapatites has been well established.[151, 171, 177, 179]

From a structural perspective, many studies have demonstrated that the phosphate group speciation comprising bioactive glass systems assumes several different arrangements depending on the number and type of directly bonded O atoms on the immediate coordination environment (see Figure 7-1 below). The Q^n terminology has been introduced to describe polymeric phosphate systems and denote the degree of condensation of each phosphate species based on the number of bridging O atoms linking each unit. Hence, Q^n represents the number of directly bonded bridging O species only leading to a polymeric glass network.[180-181] Furthermore, Cu^+ and Cu^{2+} ions can be introduced into the bioactive phosphate glass network with the method of incorporation determining the final distribution between these oxidation state(s) and different material properties.[151, 171, 177, 182-184] The structural moieties needed to accommodate the different oxidation states are an important consideration when proposing the method of incorporation into the structure. As depicted in Figure 2(a), the Cu^+ cation can be incorporated through bonding to bridging O (BO) and chain end OH species, resulting in termination of the phosphate chain. Alternatively, Cu cations can also bond to two BOs as shown in *Figure 7-2*(b), or two Cu cations can bond to two BOs attached to the same P positions as shown in *Figure 7-2*(c); these representations yield quasi-linear arrangements thus restricting the oxidation state of the Cu metal centre to be Cu^{2+}.[185] In addition, Cu cations can bond to BOs that bridge or crosslink across multiple polymeric chain to form tetrahedral and tetragonally distorted octahedral arrangements around the Cu cations (see Figure 7-2(d) and (e)). These scenarios promotes both Cu^+ and Cu^{2+} oxidation states, however the Cu^{2+} cation characterised by a smaller ionic radius is preferred as the shorter Cu-O bond lengths accommodates more sterically crowded arrangements with variable structural distortion around the immediate octahedrally coordinated environment.[185] It is well-established that Cu^+ and Cu^{2+} cations have different stabilities depending on the geometry of the coordination environment.[186-187]

Cu^+ and Cu^{2+} cations will exhibit different preferential arrangements depending on the respective d_9 or d_{10} electronic structures of these systems and their crystal field degeneracies. The stabilities of the ions will be different; Cu^{2+} ions are more stable than Cu^+ ions as they have a greater charge density than Cu^+ consequently forming stronger bonds. Additionally, the full outer shell of Cu^{2+} results in greater stability than Cu^+ ions which have one less electron, this is the difference between the d_{10} and d_9 electronic structure.

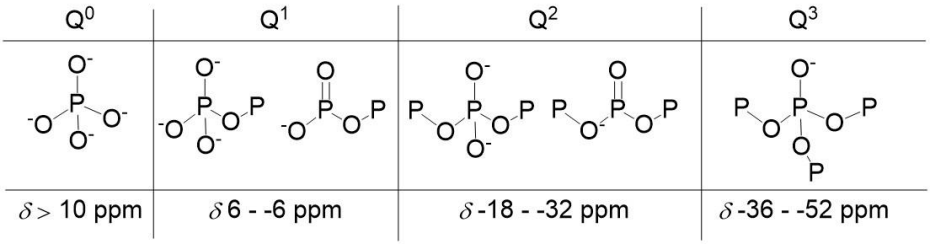

Figure 7-1. The established ^{31}P chemical shifts ranges corresponding to Q^n species, where n is the number of directly bonded bridging oxygen atoms.

The Jahn-Teller effect, which is a measure of the geometric distortion of non-linear transition metal systems that simultaneously reduces the symmetry and total energy, is a prominent interaction that governs the final structural arrangements of the Cu cations in bioactive glasses[188-189]. The d_9/d_{10} electronic structures result in very different coordination environments; the Cu^+ systems are characterised by higher energies for the $3d_{xy}$, $3d_{xz}$ and $3d_{yz}$ orbitals over their $3d_{x^2-y^2}$ and $3d_{z^2}$ counterparts, while the converse occurs for Cu^{2+} systems. A tetrahedral arrangement is preferred for Cu^+ systems possessing four negatively charged ligands (i.e. such as O), as depicted in *Figure 7-2*(d) below.[187] In contrast, the d_9 electronic structure of the Cu^{2+} is dominated by octahedral geometries,[190] however square planar and tetrahedrally coordinated systems can occur.[187] Octahedrally coordinated Cu^{2+} systems are often tetragonally distorted (i.e. a lengthening of two bonds, see *Figure 7-2*(e)) as a consequence of the Jahn-Teller effect,[188] and these arrangements clearly dominate the Cu^{2+} speciation in bioactive calcium phosphate glasses as demonstrated by previous EPR studies.[172, 182]

Techniques such as X-ray diffraction (XRD),[127, 151, 191] differential scanning calorimetry (DSC),[184, 191-193] solid state NMR (SSNMR),[151-152, 194] electron paramagnetic resonance (EPR),[183, 195] and Raman spectroscopy,[151, 171, 196] have all been used to investigate the incorporation of Cu into the calcium phosphate network. Despite the use of many techniques, there is little consistency in the outcomes and descriptions of how Cu is introduced into these biomaterials. It is widely accepted that Cu^{2+} ions are incorporated into the glass structure, however the structural descriptions vary from its simplistic function as a crosslinker[151, 171, 183] to more in-depth postulates involving the formation of octahedrally coordinated Cu^{2+} cations (with tetragonal distortions) bridging the phosphate chains.[172, 182, 191] EPR studies directly interrogate the paramagnetic Cu^{2+} centres; based on the measurement of g factors, a $g_{\parallel} > g_{\perp}$ scenario indicates the occurrence of Cu^{2+} cations assuming tetragonally distorted octahedral geometries between the phosphate chains.[183, 195, 197-198] However, the EPR technique is

insensitive to diamagnetic Cu^{+} species that can also adopt octahedrally coordinated environments at high levels of Cu incorporation, greater than 60 weight % CuO, as reported by Bae *et al.,*[182] Koo *et al*.,[36] and Debnath *et al.*[199] using ICP and complexometric titrations, Raman spectroscopy and UV absorption and emission, respectively.

A precise structural characterisation of Cu incorporation into calcium phosphate biomaterials has been reported for hydroxyapatite (HA) systems.[179, 200-201] These studies demonstrated that the Cu oxidation state was dominated by the Cu^{+} species which adopts a linear coordination environment within the HA channels. However, a much greater structural diversity exists for positioning of Cu^{+} and Cu^{2+} cations within the disordered calcium phosphate bioactive glass network; in addition, the incorporation of Cu can also induce other significant effects upon the network such as the depolymerisation of the phosphate chains. In many studies, only the method of incorporation has been considered, and the overall effect on the network structure is overlooked,[172, 182-183] however, early work reported by Koo *et al.* demonstrated that depolymerisation was observed to occur with increasing Cu incorporation, suggesting that Cu^{+} chain ends are formed which thus inhibit chain formation.[171]

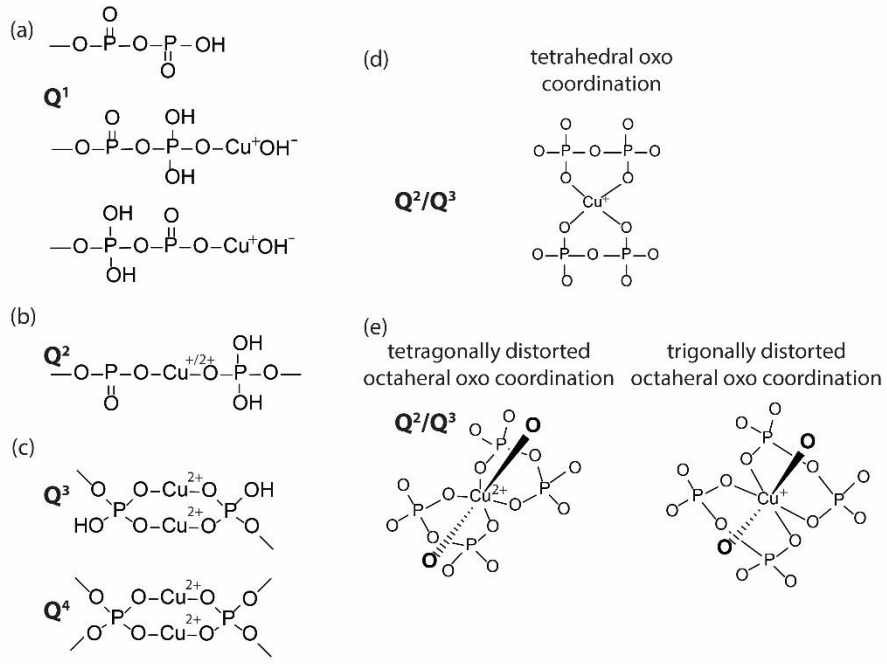

Figure 7-2. The potential arrangements of Cu^{+} and Cu^{2+} cations incorporated into calcium phosphate bioactive glass systems as represented by (a) chain end Cu^{+} species, (b) and (c) quasi-linear oxo coordinated arrangements, (d) tetrahedral oxo coordination Cu^{+} arrangements, and (e) tetragonally distorted octahedral Cu^{2+} and trigonally distorted octahedral Cu^{+} arrangements.

In order to fully rationalise the methods of Cu incorporation and the effect on the network structure a fully comprehensive study comprising of multiple techniques is required. Furthermore, the quantities of Cu added into the bioactive glass system causes alterations to the materials properties and thermal characteristics of the system. The effect of Cu on the glass transition temperature has been studied on many bioactive glass systems, and the T_g is shown to decrease with an increase in Cu content with several different explanations given.[184, 192-193]

The high resolution ^{31}P and ^{1}H solid state NMR (SSNMR) techniques can probe the immediate short-range environments and chemical speciation comprising highly disordered systems, and quantitatively measure the presence of the Q^n speciation of the system under different degrees of perturbation and chemical change.[151, 194] Crucially, chemical shifts of the Q^n species schematically represented in Figure 1 are influenced by the identity of the nearest neighbour atoms such as Ca and Cu.[202-203] The addition of Cu into a bioactive glass system can potentially influence the ^{31}P (and ^{1}H) MAS NMR data in several ways. Initially, intensity changes in the resonances assigned to Q^n species can emerge as increased depolymerisation of the phosphate chains and chain-end species develop. Secondly, additional line broadenings will become apparent as the addition of diamagnetic Cu^+ cations introduce increased structural disorder and chemical shift dispersion as Cu-O-P linkages develop, while the presence of Cu^{2+} cations can induce very large paramagnetic shifts and broadenings.

The therapeutic effect of Cu^{2+} is greater than Cu^+, especially when incorporated in an arrangement which is less tightly bound allowing for greater deposition of Cu. The therapeutic effect of Cu^+ is highlighted in hydroxyapatites where Cu exists as predominantly Cu^+.[179, 204] In bioactive glasses Cu exists in both states however Cu^{2+} is desired in order to enhance the properties. It has been shown many times that larger amounts of Cu^{2+} result in a greater therapeutic effect.[151, 205-207] In order to enhance and control the therapeutic effect of copper doped bioactive glasses a thorough understanding of how Cu^{2+} ions are incorporated is required. It is especially important to be able to differentiate between the potential methods of incorporation as they will have different amounts of enhancement of the therapeutic effect.

This study will investigate the incorporation of Cu^+ and Cu^{2+} cations into a series of calcium phosphate bioactive glasses ranging from 0 - 25 weight % total Cu content using a comprehensive range of analytical techniques including SSNMR, EPR, DSC, Raman, XRF and SAXS/WAXS to elucidate the structural consequences of the glass network modification. In

particular, this work is underpinned by a variable B_0 field and variable temperature SSNMR approaches. Very low field (2.35 T) ^{31}P MAS NMR focuses on the detection of species influenced by strong paramagnetic broadenings, with analogous measurements at higher field strengths (11.7 T) emphasizing higher resolution data from regions of the glass network exhibiting reduced (or no) paramagnetic influence.[208] These measurements are implemented in conjunction with variable temperature ^{31}P MAS NMR studies to exploit the Curie-Weiss relationship in order to probe the existence of paramagnetic influences on specific P and H species.[209]

7.2 Materials and Methods

7.2.1 Materials

The phosphate glasses were provided by Song-Yi Baek (UCL), who had prepared them as follows. Copper containing phosphate based glasses were prepared by combining sodium dihydrogen phosphate (NaH_2PO_4), calcium carbonate ($CaCO_3$), phosphorous pentoxide (P_2O_5) and copper sulphate ($CuSO_4$) in a Pt/10 % Rh crucible. The glasses were placed in a pre-heated furnace at 700 °C for half an hour and further heated at 1100 °C for 1 h. The molten glass was poured into 15 mm diameter graphite moulds that were preheated to 400 °C. These moulds were maintained at 400 °C for 1 hour for annealing, and then slowly cooled to room temperature. The resulting glass rods were sectioned with a diamond saw into 2 mm thick glass discs using water as the cutting fluid.

7.2.2 Experimental Methods

All of the experimental measurements were undertaken on powdered samples heated for 12 hours at 200 °C to remove water in the samples. The samples were stored under nitrogen in a glove box.

The solid state ^{31}P single pulse, magic-angle-spinning (MAS) NMR and cross-polarisation, magic-angle-spinning (CPMAS) NMR measurements were performed at 11.7 T using a Bruker Avance III-500 spectrometer operating at a ^{31}P Larmor frequency (ν_o) of 202.4 MHz. These experiments were performed using a Bruker 3.2 mm HX probe which enabled a MAS frequency of 20 kHz to be implemented. Pulse length calibration was performed on solid ammonium dihydrogen phosphate ($(NH_4)H_2PO_4$) from which a π/2 pulse time of 3 μs was measured. All single pulse measurements were undertaken using a π/4 nutation angle together with a recycle delay of 40 s. For the analogous ^{31}P CPMAS measurements, a MAS frequency of 12 kHz was implemented with an initial ^{1}H π/2 pulse length of 3 μs, a ^{1}H-^{31}P contact time of 1.5 ms, a CP ramp from 50 - 100 % and a recycle delay of 10 s were

implemented. For both the ^{31}P single MAS pulse and CPMAS experiments strong heteronuclear ^{1}H decoupling (100 kHz in strength) was applied during the acquisition of all FIDs. Variable temperature ^{31}P single pulse MAS NMR measurements were performed from 258.1 K to 298.1 K.

The corresponding low field ^{31}P Hahn-Echo MAS NMR measurements were performed at 2.35 T using a Bruker Avance III HD-100 spectrometer operating at a ^{31}P Larmor frequency (ν_0) of 40.5 MHz. These experiments were undertaken using a Bruker 1.3 mm HX probe that enabled MAS frequencies of 60 kHz to be achieved. Pulse length calibration was performed on solid ammonium dihydrogen phosphate ($(NH_4)H_2PO_4$) from which a $\pi/2$ pulse time of 1 µs was measured. All measurements were undertaken using a rotor-synchronised Hahn-echo MAS ($\pi/2$ - τ - π - acquire) experiment with a recycle delay of 40 s to match the quantitative studied undertaken at higher field. Variable temperature ^{31}P Hahn-echo MAS NMR measurements were performed over a 258 - 298 K range. All ^{31}P chemical shifts measured at 11.7 and 2.35 T were externally referenced against the IUPAC recommended primary reference of 85% $H_3PO_{4(aq)}$ (δ_{iso} = 0.0 ppm) via the secondary solid $(NH_4)H_2PO_4$ reference (δ_{iso} = 0.99 ppm).

All ^{1}H MAS NMR measurements were performed at 11.7 T using a Bruker Avance III-500 spectrometer operating at a Larmor frequency (ν_0) of 500.13 MHz. These experiments were performed using a Bruker 1.3 mm HXY probe which enabled a MAS frequency of 50 kHz to be implemented. Pulse calibration was performed on solid alanine from which a $\pi/2$ pulse time of 2 µs was measured. All measurements were undertaken with a $\pi/2$ nutation angle together with a recycle delay of 35 s. All ^{1}H chemical shifts were externally referenced against the IUPAC recommended primary reference $Me_4Si_{(aq)}$ (1% in $CDCl_3$) via the secondary solid alanine (δ_{iso} = 1.1 ppm).[74] Data collection and processing was performed using TopSpin® software (Bruker). All deconvolutions were performed in Origin(Pro)[210] using a Gaussian/Lorentzian fit.

Continuous wave EPR measurements were performed on a Bruker E580 X-band spectrometer operating nominally at 9.4 GHz with a Bruker HS cylindrical cavity. Non-saturating microwave power was used along with field modulated lock-in detection. An Oxford Instruments ESR-900 cryostat and 503 intelligent temperature controller were used which enabled temperatures of ~5 K to be approached and maintained using liquid helium flow. All samples were flame sealed and evacuated in 20 mm EPR tubes. Simulations of the

EPR patterns were performed using EasySpin[211] in MatLab R2017b, a two component fit was used from which the g and A values were extracted.

Small angle X-ray scattering (SAXS) measurements were performed using a Xenocs Xeuss 2.0 equipped with a micro-focus Cu Kα (1.54) Å source under vacuum. Scattering was measured by a Pilatus 300k hybrid photon counting detector with a pixel size of 0.172 mm x 0.172 mm. The distance between the detector and the sample was calibrated by using silver behenate ($AgC_{22}H_{43}O_2$). Measurements were taken over a q range of 0.004 to 0.16 $Å^{-1}$. Wide angle X-ray scattering (WAXS) was performed simultaneously with a q range of 1.31 to 3.26 $Å^{-1}$, q values were converted to 2θ angles using the equation $q = 4\pi\sin(\theta)/2$, where λ is the wavelength of Cu, 1.54 Å. SAXS and WAXS data was acquired and processed using Foxtrot 3.3.4 software.

All DSC measurements were undertaken using a Discovery DSC-25 manufactured by TA Instruments which monitored the modulated heat flow under continuous heating rates of 10 °C /min up to 550 °C. The thermal scanning process used helium gas at 50 ml/min with a nitrogen base purge of 300 ml/min, and the glass transition temperatures (T_g) were calculated directly from the measured data.

The corresponding Raman data were acquired using a Renishaw inVia Raman microscope using a 514 nm DPSS laser operating over a 500 - 1500 cm^{-1} wavenumber range, a Renishaw CCD detector and a grating of 2400 lines/mm. A ×20 Olympus objective lens was employed to focus the beam into the sample. Calibration was performed on diamond and 3 static scans of 3 s each at 50 % laser power were used for all measurements.

X-ray fluorescence measurements were performed on a Rigaku Primus IV WD-XRF spectrometer using a helium seal under vacuum. A 20 mm sample holder was used with a polypropylene film to prevent sample loss in the vacuum. A 30 µm rhodium tube was used allowing for detection of elements from sodium through to uranium, with the rhodium tube lines present at 15 - 20 °. AEZ analysis software was used for collection and processing of the data.

7.3 Results and Discussion

7.3.1 Glass Characterisation

X-ray fluorescence measurements have been performed to determine the mass percentage of each heavy element weighted to oxygen content, Figure 7-3 (a), *Table 7-1*. The mass % is different to the nominal composition, however the mass% of copper relative to Cu 1 does

Table 7-1. The nominal composition and shorthand notation, the mass % of phosphorous, calcium, sodium and copper weighted to oxygen, the actual composition of the bioactive glasses and, the peak and onset of the glass transition temperature.

Nominal composition (Shorthand notation)	P	Ca	Na	Cu	Measured composition	T_g Peak °C	T_g Onset °C
P50Ca40Na10 (Cu 0)	59.5	28.1	12.4	0	P60Ca28Na12	449	436
P50Ca39Na10Cu1 (Cu 1)	59.6	26.7	12.4	1.4	P60Ca27Na12 Cu1	435	419
P50Ca35Na10Cu5 (Cu 5)	56.8	24.0	12.3	6.9	P57Ca24Na12 Cu7	425	409
P50Ca30Na10Cu10 (Cu 10)	54.2	20.9	12.1	12.8	P54Ca21Na12 Cu13	416	401
P50Ca20Na10Cu20 (Cu 20)	50.5	13.4	11.1	25.0	P51Ca13Na11 Cu25	415	399

approximately follow the desired Cu proportions of 0:1:5:10:20, Figure 7-3 (b). In the nominal compositions the copper is predicted to be incorporated at the expense of Ca. The XRF measurements show that whilst the Ca content is reduced it is not as great as predicted, the P content is additionally reduced to facilitate the incorporation of Cu. The reduction in P suggests that Cu is causing some depolymerisation rather than solely reducing the amount of network forming Ca. The SAXS/WAXS measurements of Figure 7-3 (c) and (d) are characteristic of bioactive glass systems demonstrating that the systems are fully amorphous, and that no crystalline component(s) have emerged with increasing Cu incorporation; i.e. the full Cu inventory of each preparation has been assimilated into the glass network.

The DSC first heating scans, show a single transition between 414 °C and 450 °C, this is assigned to the glass transition temperature, T_g, Figure 7-4 (a), as the level of Cu doping increases the T_g decreases, Figure 7-4 (b). The trend in T_g with Cu content has been compared to those found in the literature, Figure 7-4 (c). Where there is a decrease in Ca content there will also be a decrease in T_g, Cu^{2+} ions can replace Ca^{2+} ions which causes a reduction in thermal resistance, additionally a decrease in Ca will decrease the internal strain of the glass structure.[184, 193] A decrease in T_g is also observed when CuO bonds are formed at the expense

of POP. CuO bonds are more ionic and weaker than the covalent POP consequently the T_g decreases as more CuO bonds are formed.[192]

The effect of CuO formation has also been shown to cause an increase in the T_g when CuO replaces Na_2O rather than POP and strengthening the POP bonds.[212] Compared to the samples in the literature the change in T_g is relatively smaller however does follow the trends where Ca content decreases and Na content remains the same. This shows that in the samples studied here there is little overall change to the network, there will be depolymerisation due to the formation of CuO end chain species and the formation of linear Q^2-Cu species causing repolymerisation, consequently there will be no net depolymerisation. The plateau in T_g at Cu content above 10% is reflected in the literature.[184]

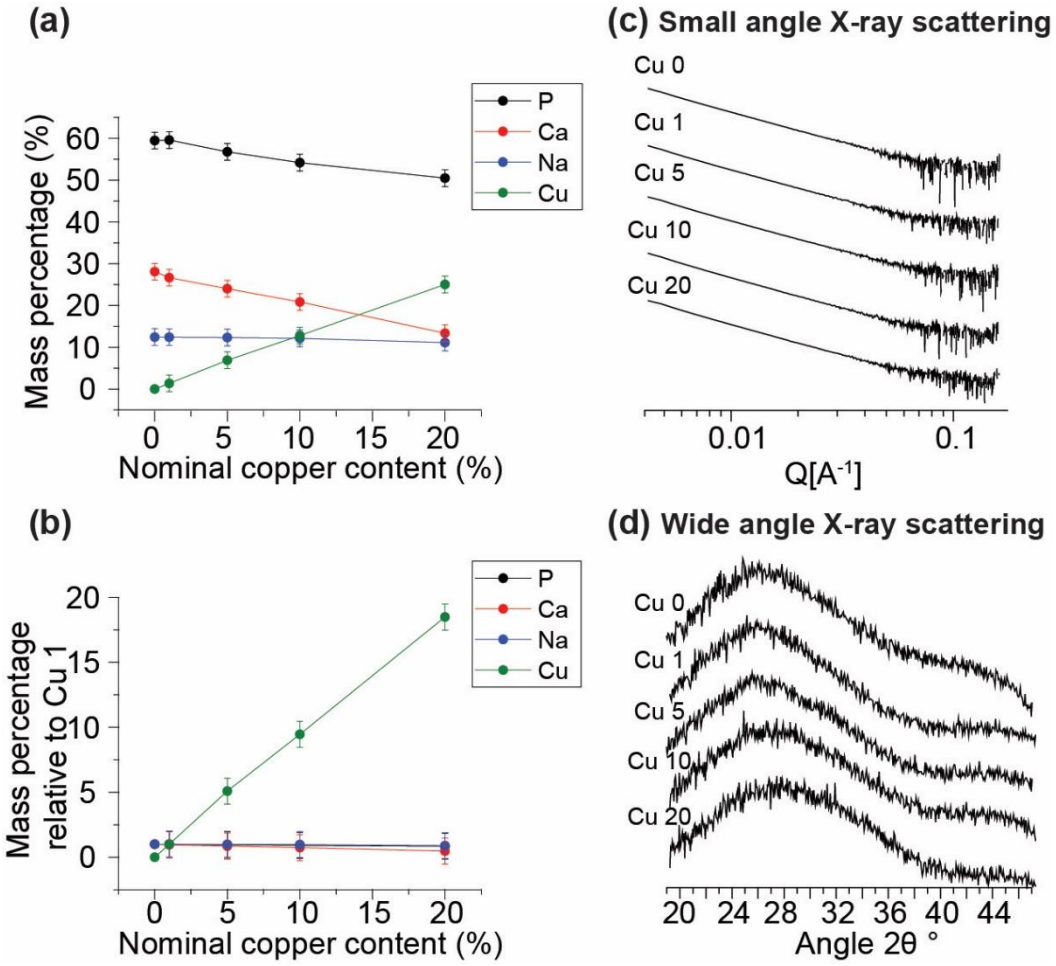

Figure 7-3. (a) The mass percentage of each element weighted to oxygen content and (b) the ratio of each element with respect to P50Ca40Na10 for P, Ca and Na and to P50Ca39Na10Cu1 for Cu, (c) the small angle X-ray scattering patterns and (d) the wide angle X-ray scattering patterns

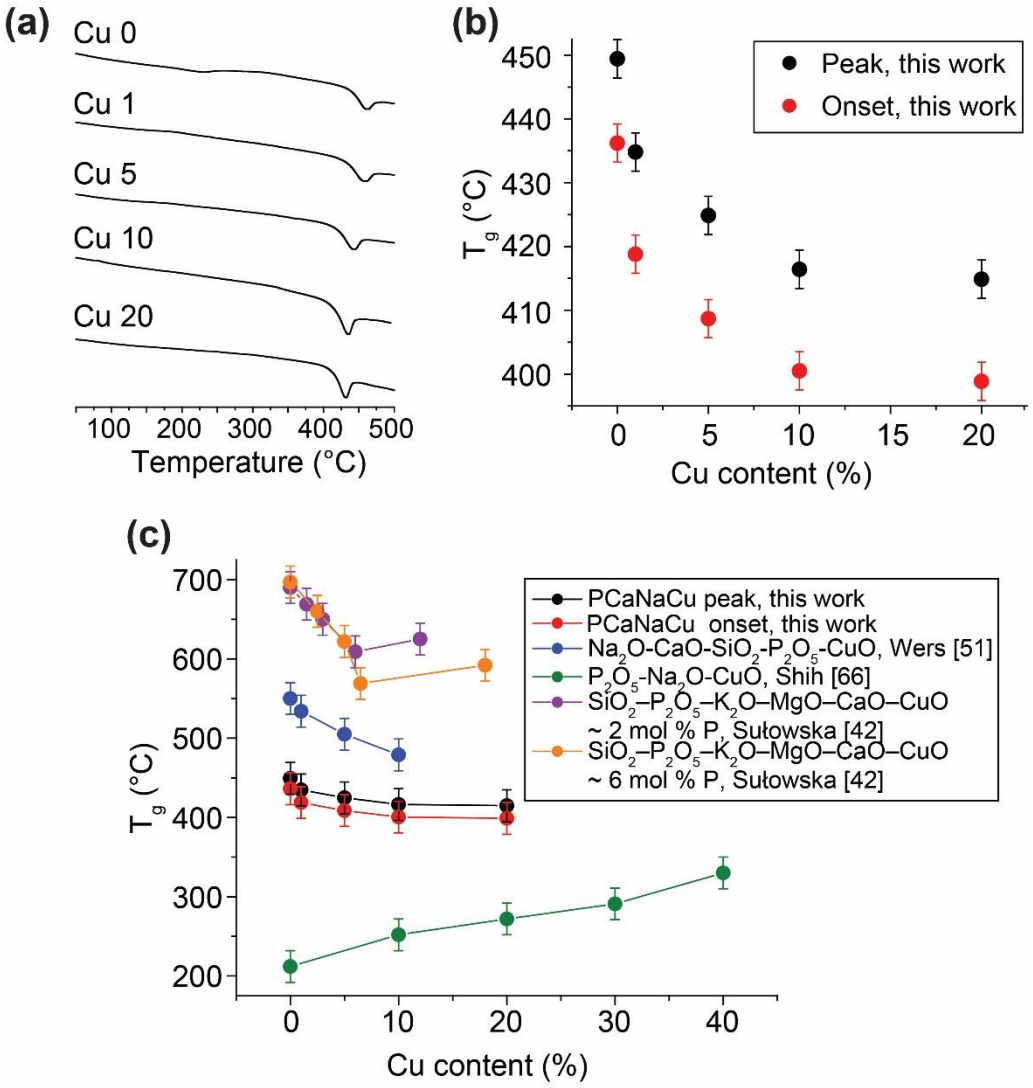

Figure 7-4. The (a) DSC first heating scans for the Cu doped calcium phosphate bioactive glasses, (b) the T_g minima and onset as a function of Cu content, and (c) a comparison of the measured T_g (peak and onset) values relative to literature values for similar bioactive glass compositions.

7.3.2 Copper Incorporation

Combining solid state NMR, EPR and Raman measurements, the incorporation of Cu^{+} ions, Cu^{2+} ions and the effect on the phosphate chains can be determined. Solid state NMR measurements allow for quantitative determination of the Q species comprising the phosphate network. The network is initially comprised of long phosphate chains of Q^1 and Q^2 species with some Q^0 species at low doping levels, the absence of Q^3 species shows that there are no branching chains, Figure 7-5 (a). The incorporation of Cu into the systems resulted in the presence of a third species in the MAS spectra in the range of ~ –35 - –43

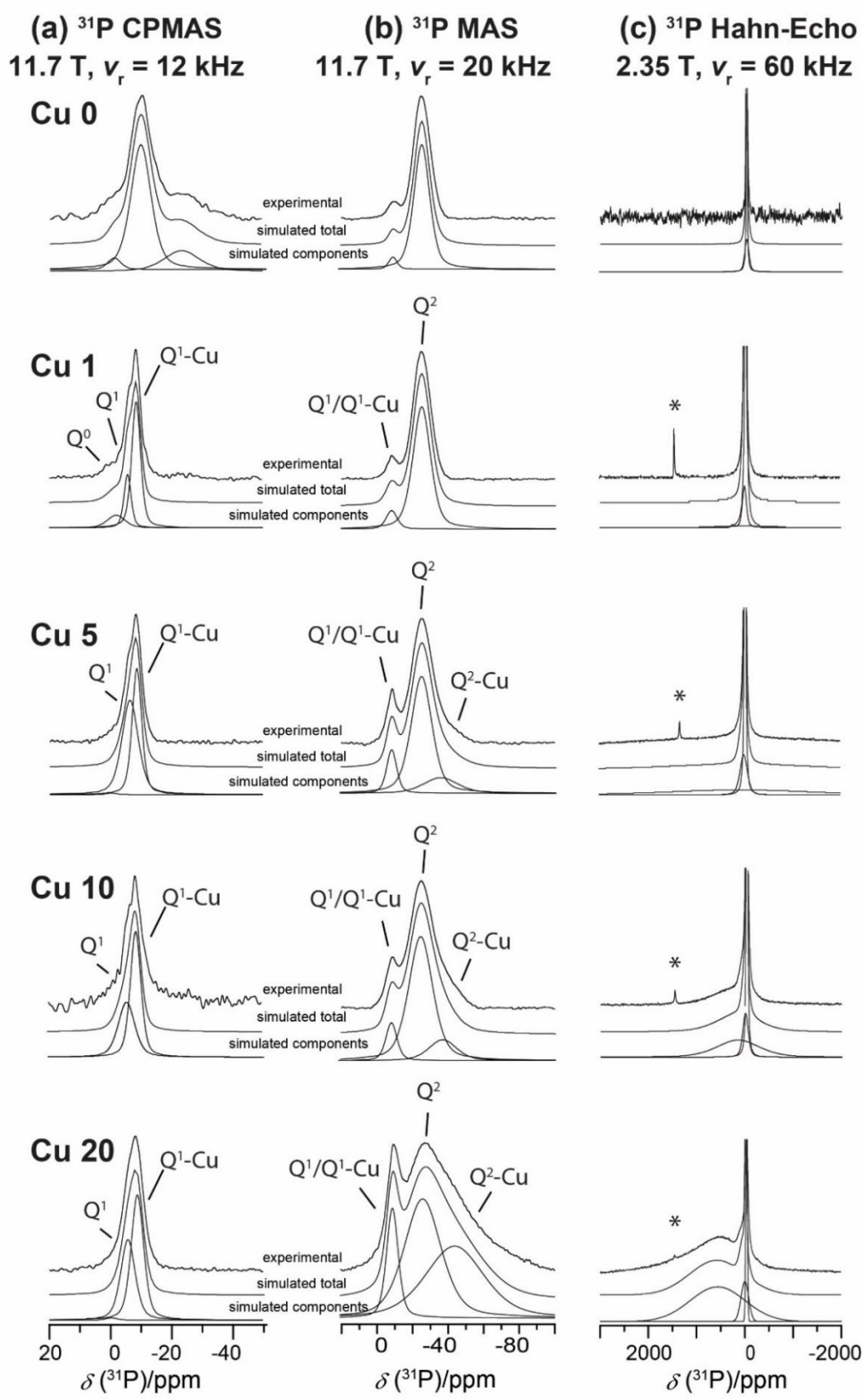

Figure 7-5.The (a) ^{31}P CPMAS NMR data (B_0 = 11.7 T, ν_r = 20 kHz), (b) ^{31}P MAS NMR data (B_0 = 11.7 T, ν_r = 20 kHz), and (c) the ^{31}P Hahn-Echo MAS NMR spectra (B_0 = 2.35 T, ν_r = 60 kHz) for Cu doped calcium phosphate bioactive glasses.

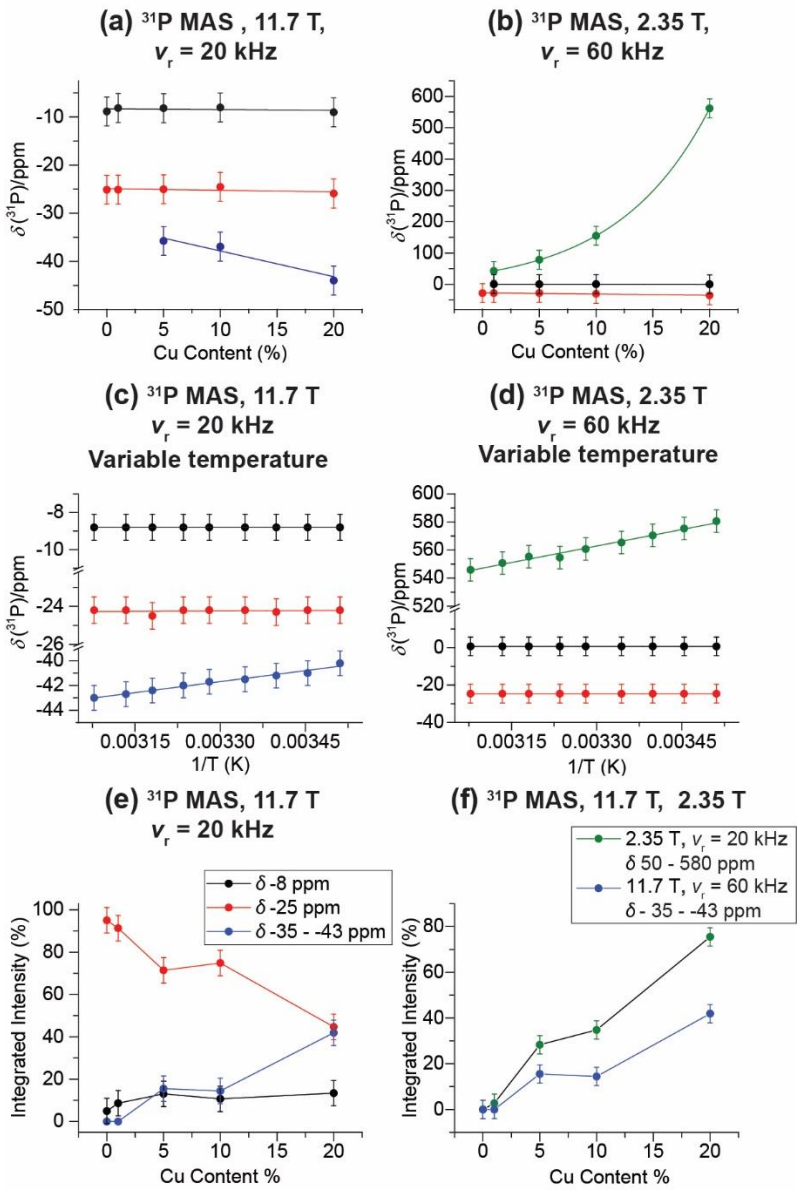

Figure 7-6. Analyses of the ^{31}P MAS NMR data showing, (a) the change in chemical shift with increasing Cu content (B_0 = 11.7 T, ν_r = 20 kHz) (the next nearest neighbour P (Cu-O-P-O-P) is observed at ~ –35 - –43 ppm), (b) the change in ^{31}P chemical shift with increasing Cu content (B_0 = 2.35 T, ν_r = 60 kHz) (the nearest neighbour (Cu-O-P)) is observed, (c) the change in ^{31}P chemical shift with increasing temperature for Cu 20 sample (B_0 = 11.7 T, ν_r = 20 kHz), (d) the change in ^{31}P chemical shift with increasing temperature for Cu 20 sample (B_0 = 2.35 T, ν_r = 60 kHz), (e) the change in ^{31}P integrated intensity with increasing Cu content (B_0 = 11.7 T, ν_r = 20 kHz), and (f) the change in integrated intensity with increasing Cu content for the nearest neighbour (Cu-O-P) species (2.35 T) and the next nearest neighbour (Cu-O-P-O-P) species (11.7 T).

Table 7-2. The chemical shift and percentage of each of the simulated resonances in the ^{31}P MAS NMR data (B_0 = 11.7 T, ν_r = 20 kHz) and (B_0 = 2.35 T, ν_r = 60 kHz).

Sample	B_0 = 11.7 T, ν_r = 20 kHz					
	δ_{iso} [ppm]	*I* [%]	δ_{iso} [ppm]	*I* [%]	δ_{iso} [ppm]	*I* [%]
Cu 0	-8.86	5.0	-25.1	95.0		
Cu 1	-8.15	8.7	-25.1	91.3		
Cu 5	-8.18	13.0	-25.0	71.4	-35.8	15.5
Cu 10	-8.04	10.7	-24.5	74.8	-36.9	14.4
Cu 20	-8.87	13.4	-25.9	44.7	-43.5	41.9
	B_0 = 2.35 T, ν_r = 60 kHz					
Cu 0			-30.6	18.8	-28.1	81.2
Cu 1	42.6	2.7	0.40	4.9	-28.2	92.4
Cu 5	78.4	28.3	0.40	12.3	-27.7	59.4
Cu 10	155	34.8	0.50	11.9	-30.4	53.3
Cu 20	562	75.5	0.20	12.2	-35.3	12.3

ppm, which increases in intensity with an increase in Cu content, indicating that it is associated with Cu next to Q^2 species. Upon incorporation of copper there are two Q^1 species observed in the CPMAS data, the new resonance at ~ –5 ppm is attributable to Cu^+ next to Q^1 species, caused by the formation of Cu-O end chain species, Figure 7-5 (b). The presence of Cu^+ ions is confirmed in the NMR data as if only Cu^{2+} ions were present then there would be no observable NMR signal as their paramagnetic nature would cause the spectra to be extensively broadened. The change in intensity of the Q^1 and Q^2 species has been investigated as a function of Cu content, Figure 7-6 (e). Greater incorporation of copper results in a direct exchange of Q^2 and Q^2-Cu with minimal change in the Q^1 species. There is no plateau in the increase in Q^2-Cu species showing that Cu is continually incorporated into the system and has not become fully saturated. Quantitation of the Q^1 species shows that there is no net depolymerisation of the phosphate chains as the increase in Q^1 is minimal especially compared to the exchange of Q^2 species. The incorporation of Cu results in a change in chemical shift for Q^2-Cu from ~ –35 - 45 ppm, this helps to confirm the identity of this resonance, Figure 7-6 (a).

The ^{31}P MAS NMR measurements have been repeated at a lower field, allowing for the paramagnetic effect of Cu^{2+} to be fully observed. In addition to the species observed at 11.7 T, an additional broad component is detected that shifts from ~40 ppm to ~560 ppm with increasing copper, Figure 7-5(a) and Figure 7-6 (b). This additional component also does not reach a saturation point as with the high field measurements Figure 7-6 (f). At a lower field the 1st coordination sphere, Cu-O-P, P species can be detected, whereas at a higher field only the 2nd coordination sphere, Cu-O-P-O-P, P species can be detected. The final evidence of paramagnetic Cu^{2+} is from the variable temperature measurements, Figure 7-6 (c), (d), at both fields there is a linear relationship between 1/T and chemical shift for the Cu induced species which is the characteristic Curie-Weiss relationship.

The ^{1}H NMR spectra have 5 components, Figure 7-7 (a) and *Table 7-3*, three of the components, δ ~ 0.9, attributable to OH end chain species, ~4 and ~6.5 ppm, attributed to water residing between and adsorbed to phosphate chains respectively, are characterised in other calcium phosphate systems[213-214]. The additional two components at δ ~ –0.15 - 1 and 10 - 12 ppm, could be attributable to secondary regions of OH chain species and adsorbed water respectively which are affected by Cu. These two components also shift on incorporation of greater amounts of copper confirming that they reside near to copper, Figure 7-7 (b). These components also broaden with increased copper indicative of increased disorder in these regions.

The intensity of ~9 - 12 ppm changes with incorporation of copper, Figure 7-7 (c), there is an initial increase until 5 % Cu which indicates greater adsorption of water into the network. Copper residing between the phosphate chains cause a dilation and allows for water adsorption.

Table 7-3. The chemical shift and percentage of each of the fitted components in the ^{1}H MAS NMR data (B_0 = 11.7 T, v_r=50 kHz).

Sample	δ_{iso} [ppm]	*I* [%]	δ_{iso} [ppm]	*I* [%]	δ_{iso} [ppm]	*I* [%]	δ_{iso} [ppm]	*I* [%]	δ_{iso} [ppm]	*I* [%]
Cu 0	0.45	22.3	0.90	5.4	3.60	11.2	6.59	38.5	8.72	22.7
Cu 1	0.25	19.1	0.83	4.7	3.60	9.1	6.59	33.7	9.68	33.4
Cu 5	-0.12	20.9	0.81	4.2	3.60	13.6	6.66	30.3	11.1	31.0
Cu 10	-0.32	27.4	0.81	3.7	3.57	11.7	6.66	36.5	10.5	20.7
Cu 20	-0.10	30.4	0.91	5.2	3.68	8.6	6.66	30.2	10.6	25.6

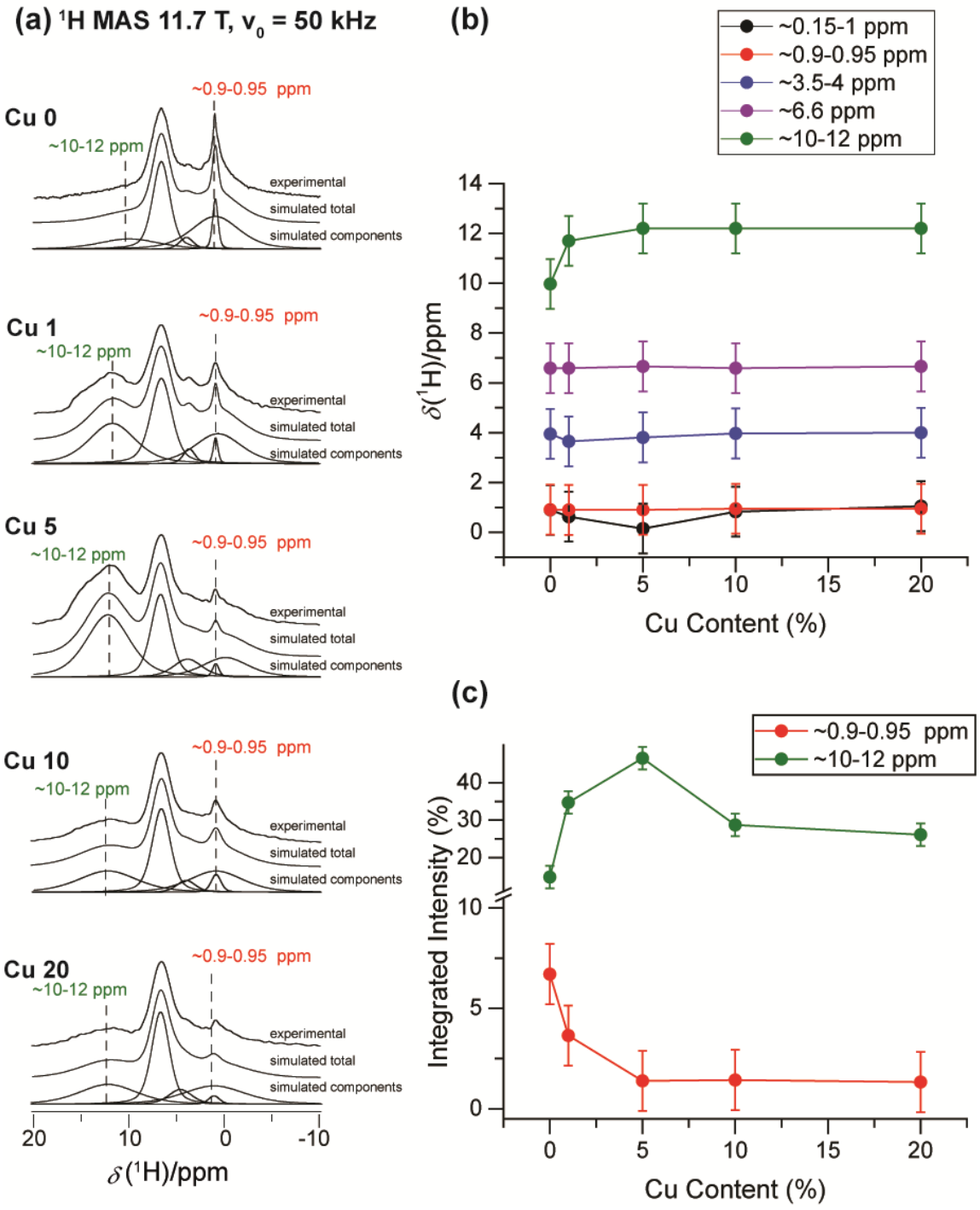

Figure 7-7. The (a) ^{1}H MAS NMR data (B_0= 11.7 T, ν_r = 60 kHz), (b) the change in ^{1}H chemical shift with increasing Cu content, and (c) the change in integrated intensity with Cu content for ~0.9-0.95 and ~10-12 ppm resonances, as measured from the Cu doped calcium phosphate bioactive glasses.

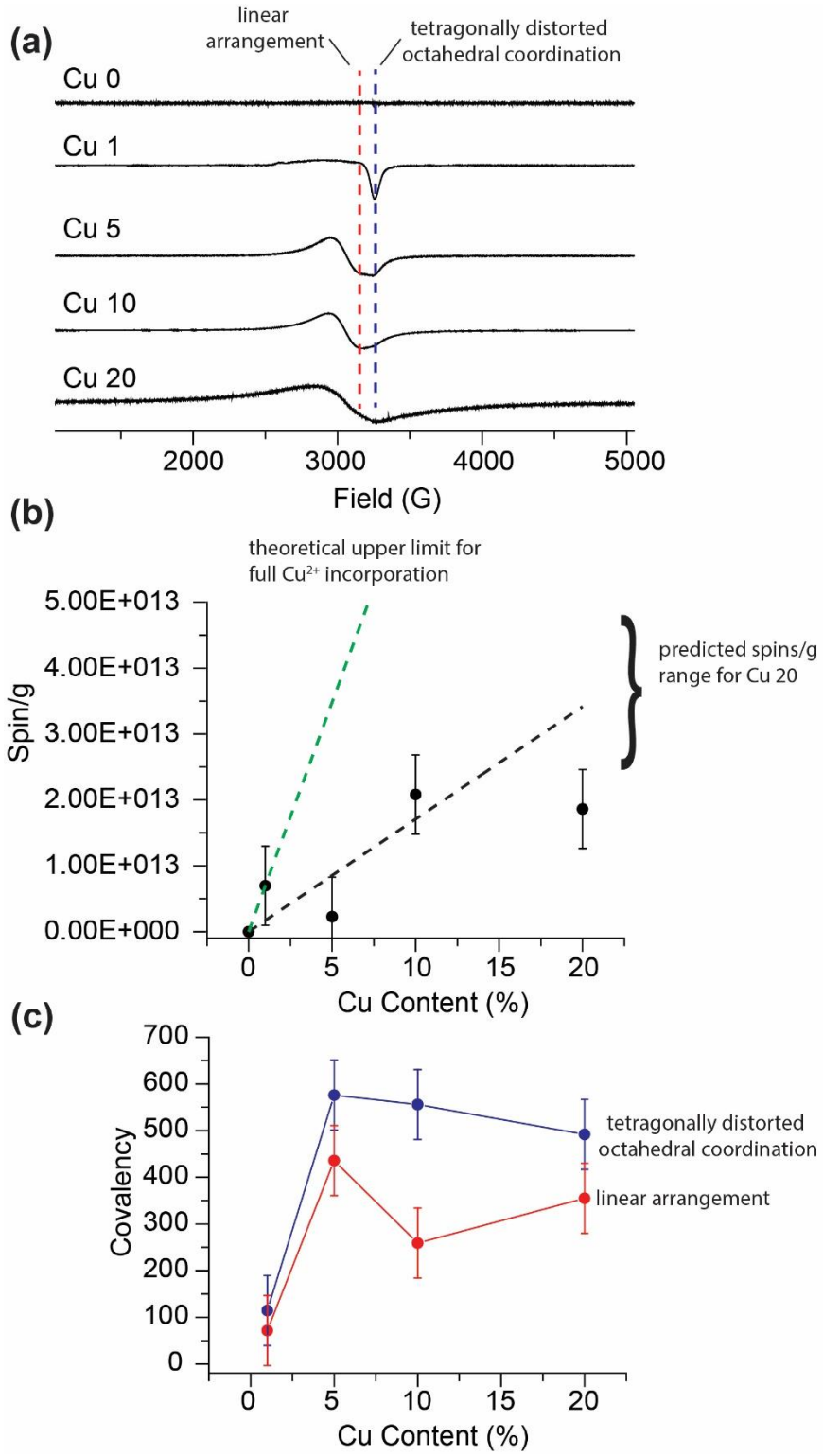

Figure 7-8. (a) The EPR spectra for the copper doped phosphate glasses. (b) The number of spins per gram as a function of copper content and the predicted range of spins/g for Cu 20 by extrapolation if the whole signal was collected and (c) the covalency parameters for the tetragonally distorted octahedral coordination and the linear arrangements of Cu^{2+}.

The intensity then decreases in 10% and 20% Cu, as the ^{31}P NMR measurements show that Cu is continuously incorporated this decrease is most likely caused by broadening of this resonance due to the high amounts of copper. There is a decrease in the intensity of ~0.9 - 0.95 ppm which shows that there is a reduction in the number of OH^- chain ends, these are replaced by Cu-O chain end species and linear Q^2-Cu. Solid state NMR measurements confirm the presence of Cu^{2+} ions however they cannot differentiate between the different arrangements that can Cu^{2+} can take. EPR measurements have been performed first to further confirm the presence of paramagnetic Cu^{2+}, second to quantify the amount of Cu^{2+} spins and finally to identify different forms of Cu^{2+} arrangements.

The EPR data acquired from the entire range of Cu-doped bioactive glass samples is shown in *Figure 7-8*(a). These measurements were undertaken at 5 K to reduce the motional effect of Cu^{2+} and reduce broadening of the signal. The EPR signal is significantly broadened as the Cu doping increases; this is attributed to the shortening of the electronic T_2 time with the increasing content of the paramagnetic Cu^{2+} species. A two-component fit was performed on the EPR data for all samples, with the two components assigned to the commonly observed tetragonally distorted octahedral coordination and to quasi-linear Cu^{2+} arrangements.[195, 198, 215-218] Furthermore, these data are accompanied by a quantitative estimate of the increasing Cu^{2+} paramagnetic content (measured as spins/g) as depicted in *Figure 7-8*(b). As summarised in *Table 7-4*, the EPR measurements have shown that Cu^{2+} ions induce a distortion of the *g* tensor as observed from the two discrete $g_\perp$ values, thus indicating a departure from axial symmetry.[183] To confirm the difference between the two structural realisations accommodating the Cu^{2+} species, the covalency parameters (α) for each sample have been determined from the g and A values, and the electron g factor g_e (= 2.0024), using the following equation:[172]

$$\propto^2 = (A_\parallel/0.36) + (g_\parallel - g_e) + (\frac{3}{7} \times (g_\perp - g_e)) + 0.04 \qquad (8.1)$$

The covalency parameter is a measure of the strength of the Cu-O covalent character forming the immediate nearest-neighbour environment comprising each coordination arrangement, and *Figure 7-8*(c) and *Table 7-4* illustrate the change α with increasing Cu concentration for the two proposed Cu^{2+} coordination arrangements.[197] *Figure 7-8*(c) clearly demonstrates that one component is unambiguously of lower covalency than the other, subsequently allowing for a clear discrimination between these Cu^{2+} coordination environments. Covalency parameters will exhibit higher values when there is a greater coordination number; in these particular cases the tetragonally distorted octahedral coordination (coordination no. = 6) will

have an increased covalency in comparison to its quasi-linear counterpart (coordination no. = 2).[218-220] The assignment of the two data sets in *Figure 7-8*(c) underpins this rationale, and these assignments are also corroborated by the assignments of the coordination arrangements in *Figure 7-8*(a) based solely on *g* values.

Figure 7-8(b) shows a diagrammatic representation of the Cu^{2+} spin counting (in spins/g) extracted from the EPR data in *Figure 7-8*(a). While there is a general increase in the spins/g trend, the increase falls well below the line or proportionality delineating the occurrence that all Cu is introduced as the Cu^{2+} oxidation state. There are two main reasons for this discrepancy. Firstly, this simply confirms that not all Cu will be present as Cu^{2+} since the Cu^{+} oxidation state will also be represented. This is clearly demonstrated in the high resolution ^{31}P MAS NMR data acquired at 11.7 T which exhibits the tendency for Cu^{+} species to participate in the depolymerisation/repolymerisation process leading to no net change in phosphate chain length. Secondly, the Cu 20 data point (in spins/g) on *Figure 7-8*(b) falls well below the line of best fit for that series of data, and additionally the signal/noise of the Cu 20 EPR signal is reduced in comparison to those signals observed from the lower Cu concentration samples. These observations suggest that the entire Cu^{2+} EPR signal is not captured due to very large paramagnetic line broadening effects. This contrasts with the low field ^{31}P MAS NMR data acquired at 2.35 T (see *Figure 7-5*(c) and *Figure 7-6*(f)) indicating continuously increasing contributions from the presence of Cu^{2+} species.

Table 7-4. The $g_{\parallel}$, $g_{\perp}$, A and covalency parameters determined from the EPR data from the suite of Cu-containing bioactive glasses.

Sample	$g_{\parallel}$	$g_{\perp}$	$g_{\perp}$	$A_{\parallel}$	$A_{\perp}$	Covalency,α
Tetragonally distorted octahedral coordination						
Cu 1	2.10	2.16	2.48	99.5	200	115
Cu 5	2.24	2.04	2.40	207	433	576
Cu 10	2.07	2.63	2.63	200	335	555
Cu 20	1.19	1.89	2.37	177	347	491
Quasi-linear coordination						
Cu 1	2.08	2.08	2.46	0.023	400	71.6
Cu 5	2.15	2.11	2.28	156	212	436
Cu 10	2.22	2.26	2.26	93.1	479	259
Cu 20	2.02	2.20	2.85	128	598	355

These apparent contradictions are rationalised by distance considerations to the paramagnetic centre. The nearest P species to the Cu^{2+} species are two bond lengths away from the paramagnetic centre; hence, the low field ^{31}P MAS NMR data will reflect an attenuated broadening due to the $1/r^6$ dependence of both the Fermi contact and electron-nuclear dipolar contributions. In contrast, the EPR measurements of each Cu^{2+} centre represent the full strength of the paramagnetic interaction that can evade the bandwidth and detection limits of the technique, thus resulting in signal loss and inaccurate quantitation (see the artificial plateau effect formed after the Cu 10 sample in *Figure 7-8*(b)). In *Figure 7-8*(b), a range of spins/g values has been estimated for the Cu 20 sample via extrapolation.

Solid state NMR have been used to observe Q^1 and Q^2 species near to Cu and EPR measurements directly observe Cu^{2+}. The Raman measurements observe phosphorous and oxygen species and the effect of copper can be observed through changes to the POP and PO_2 species especially changes to symmetrical POP species. Raman spectroscopy measurements have been performed on all the samples, Figure 7-9 (b), there are five bands present in all samples at 693 and 725 cm^{-1} for symmetric POP, 1140 cm^{-1} which is tentatively assigned to POP species near Cu, 1172 cm^{-1} for symmetric PO_2 and 1258 cm^{-1} for asymmetric PO_2.[171, 196, 221]

The ratio of $\nu_s(POP)/\nu_s(PO_2)$,[222] Figure 7-9(c) and Table 7-5, have been calculated to investigate how the amount of POP and PO_2 groups changes with copper incorporation. The incorporation of copper results in a decrease in $\nu_s(POP)$ groups relative to $\nu_s(PO_2)$ groups. There are two explanations for this change the first is the formation of tetrahedrally distorted octahedral coordination's with Cu^{2+} which causes distortion of the phosphate chains and therefore a decrease in symmetrical POP species. This is also shown by an increase in the $\nu_s(POP)$ position which is caused by a decrease in bond angle, Figure 7-9(c).

The second reason is the increase in tentative $\nu_{s/as}(POP)Cu$, Figure 7-9(c), which increases consistently with greater Cu incorporation. The formation of Cu-O chain end species as Cu^+ and linear Q^2-Cu as well as tetrahedrally distorted octahedral coordination's with Cu^{2+} contribute to the intensity change and also change in wavenumber.

Each of the individual techniques provides information on the presence and arrangement of Cu^+ and Cu^{2+}, and how this effects the phosphate chains. As previously mentioned, the initial system is comprised of long and short phosphate chains, with terminal hydroxyl species. Cu is incorporated as both Cu^+ and Cu^{2+}, as confirmed by the EPR. Cu^+ ions terminate the

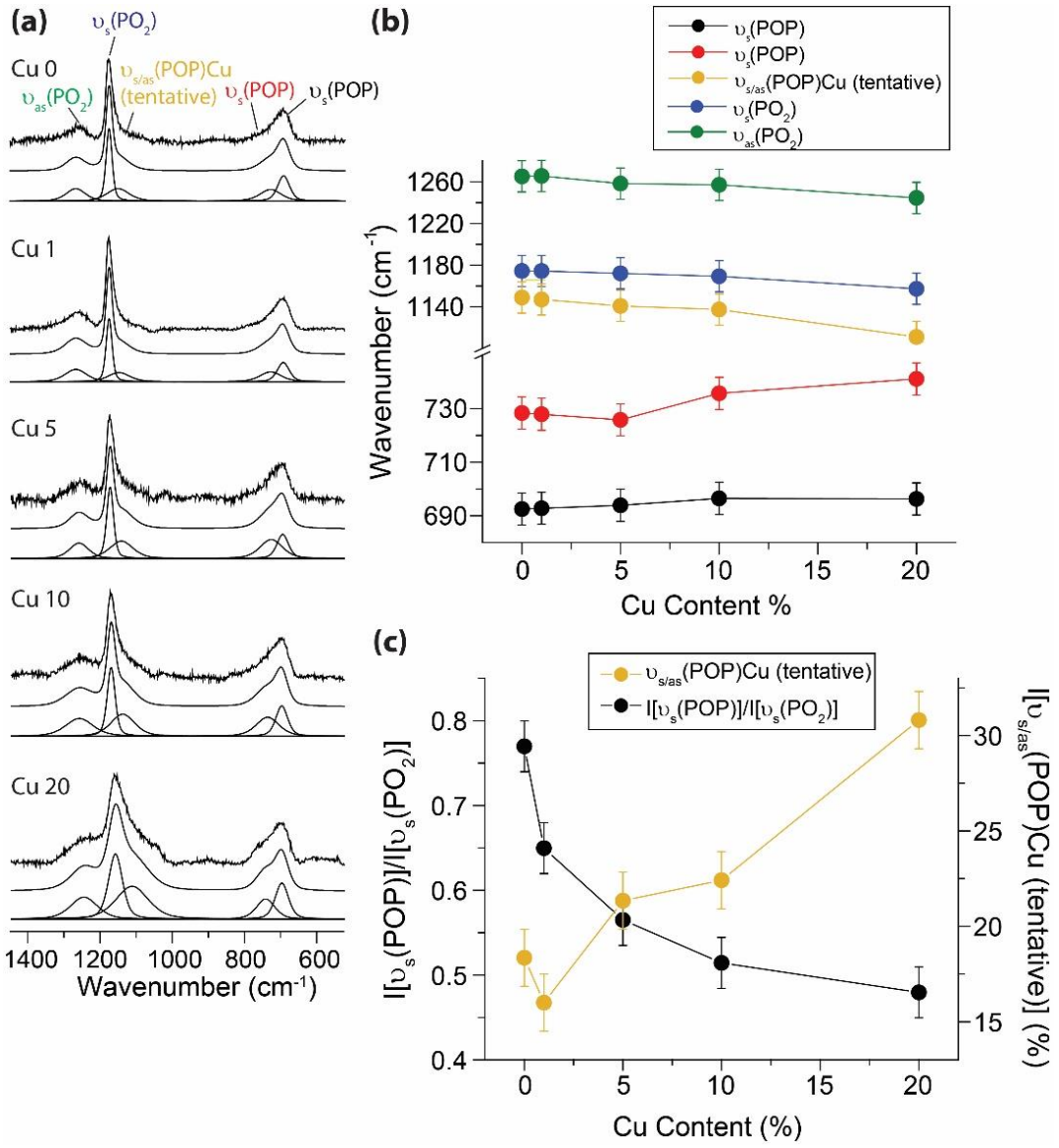

Figure 7-9. (a) The Raman spectra for the bioactive glasses, (b) the change in wavenumber for the ν_s,(POP), tentative $\nu_{s/as}$(POP)Cu, $\nu_s(PO_2)$ and $\nu_{as(}PO_2)$ stretches and (c) the ratio of ν_s(POP)/$\nu_s(PO_2)$ species and intensity of tentative $\nu_{s/as}$(POP)Cu.

phosphate chains forming Q^1-Cu end species seen in the ^{31}P CPMAS NMR data. This is also confirmed by the reduction in OH species elucidated for the ^{1}H MAS NMR data. Whilst these would cause depolymerisation there is an opposing repolymerisation of linear Q^2-Cu species, state I', resulting in no net depolymerisation. In addition to the linear arrangement, Cu^{2+} is incorporated as tetragonally distorted octahedral coordination. The incorporation of Cu causes distortion of the phosphate chains shown by the decrease in ν_s(POP) and increase in tentative $\nu_{s/as}$(POP)Cu. The addition also causes a dilation of the network, which results in the adsorption of water between the phosphate chains, observed

Table 7-5. The Raman wavenumber for the ν_s,(POP), $\nu_{s/as}$(POP)Cu (tentative), $\nu_s(PO_2)$ and $\nu_{as}(PO_2)$ stretches, and the ratio of I[ν_s(POP)]/I[$\nu_s(PO_2)$].

Sample	ν_s(POP) (cm^{-1}) ± 2	ν_s(POP) (cm^{-1}) ± 2	$\nu_{s/as}$(POP)Cu (cm^{-1}) ± 2	$\nu_s(PO_2)$ (cm^{-1}) ± 2	$\nu_{as}(PO_2)$ (cm^{-1}) ± 2	I[ν_s(POP)]/ I[$\nu_s(PO_2)$] ± 0.05
Cu 0	695	728	1149	1172	1265	0.77
Cu 1	701	727	1147	1173	1265	0.65
Cu 5	704	725	1141	1170	1258	0.56
Cu 10	706	735	1137	1166	1257	0.51
Cu 20	706	741	1111	1155	1244	0.48

in the ^{1}H MAS NMR data by the increase in intensity for δ ~10 - 12 ppm. The dilation of the network structure is beneficial as it allows for a greater amount of Cu^{2+} species to be incorporated which increases the therapeutic effect of the bioactive glasses. The incorporation of Cu does not reach a saturation point, which was shown by the continuous increase in Q^2-Cu species from the MAS NMR data and tentative $\nu_{s/as}$(POP)Cu stretch from the Raman data.

7.4 Conclusions

Through the combination of multiple techniques, the incorporation of Cu into the phosphate bioactive glasses has been comprehensively investigated. The initial solid state NMR data showed that Cu is incorporated as Cu^+ and Cu^{2+} ions due to the observation of paramagnetic broadening from Cu^{2+} and still having acquisition of the spectra due to the Cu^+ ions. There was a direct exchange of Q^2 and Q^2-Cu species which showed that there was no net depolymerisation. The Cu^{2+} ions have been shown to have two incorporation methods, in addition to the formation of a tetragonally distorted octahedral Cu^{2+} coordination there is a secondary incorporation resulting in quasi linear arrangements causing repolymerisation. Due to the absence of net depolymerisation there was a minimal change in the T_g comparatively to other studies. It was also shown that Raman spectroscopy can show how copper incorporation causes distortion in the phosphate chains and increase in the stretch at ~ 1100 cm^{-1} which can now be tentatively assigned to both symmetric and asymmetric POP species next to Cu. The greater understanding of how Cu ions are incorporated into the bioactive glass systems, especially Cu^{2+}, and how the overall network is affected will help to improve incorporation of Cu^{2+} ions to produce bioactive glasses with superior therapeutic effects.

8. Summary and Outlook

Across all of the studies presented in this thesis the theme of using a multi analytical technique to comprehensively understand material systems and processes is present throughout. Despite the actual systems being fairly disparate all of them benefit from this same approach. It has been successfully demonstrated in this thesis that using many analytical techniques is superior to using only one or two for the understanding of how materials behave. There is however a point where too much information can be collected and either the important details become overlooked or the picture as a whole is missed among the minutia. The choice of techniques to combine is also important to make sure that no information is missed but there is not unnecessary repetition which adds to both the financial and time costs.

8.1 Understanding the physical ageing of high-heat polylactide

The first thing this study showed was how combining NMR and SAXS/WAXS allows for the elucidation of long and short range order of PLA powders and about the molecular mobility and interaction strength between PLA chains in three different regions, amorphous, stereocomplex and homocrystalline sites. The change in molecular mobility and interaction strength has been tracked over a year to study how degradation occurs with respect to the mobility of the function groups within PLA.

The study was performed on four different PLA samples MG PLLA, IG PLLA and scPLA under three different storage conditions, room temperature, glove box and freezer; there was found to be no significant difference between the storage conditions and all four samples were stable over the course of a year with no change to the molecular mobility and SAXS/WAXS, the only change was the rearrangement of the PLA helix. There are many other techniques that can be incorporated into future studies on degradation including Raman spectroscopy to investigate the PLA back bone as a whole, gravimetric measurements and also looking at the effect high temperatures play on degradation.

8.2 Injection Moulding of polylactide

No matter what the form of a material is the same techniques can be applied, this has been demonstrated in this chapter where the same analytical techniques with the addition of Raman spectroscopy were used to determine the cause for the differences in the mechanical properties of injection moulded PLA materials with different mould temperatures, grades and additives.

The mix of NMR $T_{1\rho}$ measurements and Raman spectroscopy data, in particular relating to the C=O stretch and backbone, showed that combining the two is useful to understand both the individual function groups and their mobility (NMR) but also the backbone as a whole unit (Raman). The stress, strain, impact resistance and thermal characteristics can all be correlated to the crystallinity or amorphicity of the material and how the molecular mobility results from this.

8.3 An MAS NMR and Diffraction Study of Cis/Trans Polymeric Materials.

In addition to PLA in this chapter the multi technique was applied to two different novel elastomers, one polyester and one polyamide to investigate the correlation between *cis/trans* ratio, Young's modulus, molecular mobility, and crystallinity. The NMR measurements showed that an increase in *cis* content for PE resulted in an increase in crystallinity which was not observed in the PA's. The molecular mobility directly correlated to the change in Young's modulus showing that it is intrinsically linked to crystallinity. The PA's had a much reduced difference in Young's modulus which also showed in the $T_{1\rho}$ measurements. For the PA the only difference between *cis* content was shown in the WAXS data where two different forms, α and γ, where observed.

The molecular weight was also investigated in relation to the crystallinity and molecular mobility of the polyesters. Molecular weight was found to have no effect on the crystallinity or molecular mobility for both high and low molecular weight PE. In addition to the observations about the correlation between Young's modulus and molecular mobility, the $T_{1\rho}$ relaxation times were also able to demonstrate that the elastomers are comprised of alternating hard and soft domains.

8.4 A Study on the Effect of Copper Doping on Calcium Phosphate Bioactive Glasses

In this chapter it has been shown that the same multi technique approach can be utilised for the analysis of materials other than polymers, in this case copper doped bioactive glasses. Due to the addition of copper paramagnetic effects will be felt by the system, adding EPR to the suite of techniques allowed for the direct probing of paramagnetic Cu^{2+} ions.

The incorporation of copper into these BG's has been proven to be as both Cu^{2+} and Cu^{+}, depending on the oxidation state the site in which copper resides is different. There was found to be no net depolymerisation as Cu^{2+} ions form quasi linear arrangements as well as tetragonally distorted octahedral coordination's which offset the depolymerisation effect of

terminal Cu^{+} species. The main aim for incorporating copper is to enhance the therapeutic effects of the bioactive glasses consequently it would be useful in the future to undertake biological studies to probe the efficacy of the copper doped bioactive glasses.

References

1. Levitt, M. H., *Spin Dynamics: Basics of Nuclear Magnetic Resonance*. second edition ed.; Wiley: 2008.
2. MacKenzie, K. J. D.; Smith, M. E., *Multinuclear Sild-state NMR of Inorganic Materials*. Elsevier Science Limited: 2002.
3. Duer, M. J., *Introduction to Solid-State NMR Spectroscopy*. Wiley: 2005.
4. Wasylishen, R. E.; Ashbrook, S. E.; Wimperis, S., *NMR of Quadrupolar Nuclei in Solid Materials*. Wiley: 2012.
5. Bertmer, M., Paramagnetic solid-state NMR of materials. *Solid State Nuclear Magnetic Resonance* **2017,** *81*, 1-7.
6. Pintacuda, G.; Kervern, G., Paramagnetic Solid-State Magic-Angle Spinning NMR Spectroscopy. In *Modern NMR Methodology*, Heise, H.; Matthews, S., Eds. Springer Berlin Heidelberg: Berlin, Heidelberg, 2013; pp 157-200.
7. Man, P. P., *NMR of Quadrupolar Nuclei in Solid Materials*. Wiley: Chichester, 2012.
8. Andrew, E. R.; Bradbury, A.; Eades, R. G., Nuclear Magnetic Resonance Spectra from a Crystal rotated at High Speed. *Nature* **1958,** *182* (4650), 1659-1659.
9. Lowe, I. J., Free Induction Decays of Rotating Solids. *Physical Review Letters* **1959,** *2* (7), 285-287.
10. Wilkening, M.; Heitjans, P., Li jump process in $h\text{\ensuremath{-}}{\mathrm{Li}}_{0.7}\mathrm{Ti}{\mathrm{S}}_{2}$ studied by two-time $^{7}\mathrm{Li}$ spin-alignment echo NMR and comparison with results on two-dimensional diffusion from nuclear magnetic relaxation. *Physical Review B* **2008,** *77* (2), 024311.
11. Fung, B. M.; Khitrin, A. K.; Ermolaev, K., An Improved Broadband Decoupling Sequence for Liquid Crystals and Solids. *Journal of Magnetic Resonance* **2000,** *142* (1), 97-101.
12. Bennett, A. E.; Rienstra, C. M.; Auger, M.; Lakshmi, K. V.; Griffin, R. G., Heteronuclear decoupling in rotating solids. *The Journal of Chemical Physics* **1995,** *103* (16), 6951-6958.
13. Hahn, E. L., Spin Echoes. *Physical Review* **1950,** *80* (4), 580-594.
14. Carr, H. Y.; Purcell, E. M., Effects of Diffusion on Free Precession in Nuclear Magnetic Resonance Experiments. *Physical Review* **1954,** *94* (3), 630-638.
15. Skoog, D. A.; Holler, F. J.; Crouch, S. R., *Principles of Instrumental Analysis*. 6th ed.; Brooks/Cole: CA, USA, 2007.
16. Skoog, D. A.; West, D. M.; Holler, F. J.; Crouch, S. R., *Fundamentals of Analytical Chemistry*. 8th ed.; Brooks/Cole: CA, USA, 2004.
17. Schnablegger, H.; Singh, Y., *The SAXS Guide*. 3rd ed.; Anton Paar: Austria, 2013.
18. Toledo, M., Interpreting DSC curves. In *Information for users of METTLER TOLEDO thermal analysis systems*, 2000.
19. Ouchi, T.; Saito, T.; Kontani, T.; Ohya, Y., Encapsulation and/or Release Behavior of Bovine Serum Albumin within and from Polylactide-Grafted Dextran Microspheres. *Macromolecular Bioscience* **2004,** *4* (4), 458-463.
20. Hu, Y.; Jiang, X.; Ding, Y.; Zhang, L.; Yang, C.; Zhang, J.; Chen, J.; Yang, Y., Preparation and drug release behaviors of nimodipine-loaded poly(caprolactone)–poly(ethylene oxide)–polylactide amphiphilic copolymer nanoparticles. *Biomaterials* **2003,** *24* (13), 2395-2404.
21. Chandy, T.; Das, G. S.; Wilson, R. F.; Rao, G. H. R., Development of polylactide microspheres for protein encapsulation and delivery. *Journal of Applied Polymer Science* **2002,** *86* (5), 1285-1295.

22. Park, T. G.; Alonso, M. J.; Langer, R., Controlled release of proteins from poly(L-lactic acid) coated polyisobutylcyanoacrylate microcapsules. *Journal of Applied Polymer Science* **1994,** *52* (12), 1797-1807.
23. Kesenci, K.; Fambri, L.; Migliaresi, C.; Piskin, E., Preparation and properties of poly(L-lactide)/hydroxyapatite composites. *Journal of Biomaterials Science, Polymer Edition* **2000,** *11* (6), 617-632.
24. Chien-Chung Chen, J.-Y. C., How Tseng, Haw-Ming huang, Sheng-Yang Lee, Preparation and Characterisation of biodegradable PLA polymeric blends. *Biomaterials* **2003,** *24*, 1167-1173.
25. Benninga, H., *A History of Lactic Acid Making*. Springer: New York, 1990.
26. Masanobu, A.; Katashi, E.; Kazuhiko, S.; Akihiro, Y., Basic Properties of Polylactic Acid Produced by the Direct Condensation Polymerization of Lactic Acid. *Bulletin of the Chemical Society of Japan* **1995,** *68* (8), 2125-2131.
27. Moon, S. I.; Lee, C. W.; Miyamoto, M.; Kimura, Y., Melt polycondensation of L-lactic acid with Sn(II) catalysts activated by various proton acids: A direct manufacturing route to high molecular weight Poly(L-lactic acid). *Journal of Polymer Science Part A: Polymer Chemistry* **2000,** *38* (9), 1673-1679.
28. Maharana, T.; Mohanty, B.; Negi, Y. S., Melt–solid polycondensation of lactic acid and its biodegradability. *Progress in Polymer Science* **2009,** *34* (1), 99-124.
29. Hyon, S.-H.; Jamshidi, K.; Ikada, Y., Synthesis of polylactides with different molecular weights. *Biomaterials* **1997,** *18* (22), 1503-1508.
30. Kowalski, A.; Libiszowski, J.; Duda, A.; Penczek, S., Polymerization of l,l-Dilactide Initiated by Tin(II) Butoxide. *Macromolecules* **2000,** *33* (6), 1964-1971.
31. de Boer, J. P.; de Mattos Teixeira, M. J.; Neijssel, O. M., d(−)lactic acid production by suspended and aggregated continuous cultures of Bacillus laevolacticus. *Applied Microbiology and Biotechnology* **1990,** *34* (2), 149-153.
32. Fukushima, K.; Sogo, K.; Miura, S.; Kimura, Y., Production of D-Lactic Acid by Bacterial Fermentation of Rice Starch. *Macromolecular Bioscience* **2004,** *4* (11), 1021-1027.
33. Fukushima, K.; Kimura, Y., An efficient solid-state polycondensation method for synthesizing stereocomplexed poly(lactic acid)s with high molecular weight. *Journal of Polymer Science Part A: Polymer Chemistry* **2008,** *46* (11), 3714-3722.
34. Hirata, M.; Kimura, Y., Thermomechanical properties of stereoblock poly(lactic acid)s with different PLLA/PDLA block compositions. *Polymer* **2008,** *49* (11), 2656-2661.
35. Hirata, M.; Kobayashi, K.; Kimura, Y., Synthesis and properties of high-molecular-weight stereo di-block polylactides with nonequivalent D/L ratios. *Journal of Polymer Science Part A: Polymer Chemistry* **2010,** *48* (4), 794-801.
36. Keles, H.; Naylor, A.; Clegg, F.; Sammon, C., Investigation of factors influencing the hydrolytic degradation of single PLGA microparticles. *Polymer Degradation and Stability* **2015,** *119*, 228-241.
37. Lü, J.-M.; Wang, X.; Marin-Muller, C.; Wang, H.; Lin, P. H.; Yao, Q.; Chen, C., Current advances in research and clinical applications of PLGA-based nanotechnology. *Expert Review of Molecular Diagnostics* **2009,** *9* (4), 325-341.
38. Sun, X.; Xu, C.; Wu, G.; Ye, Q.; Wang, C., Poly(Lactic-co-Glycolic Acid): Applications and Future Prospects for Periodontal Tissue Regeneration. *Polymers* **2017,** *9* (6), 189.
39. Swider, E.; Koshkina, O.; Tel, J.; Cruz, L. J.; de Vries, I. J. M.; Srinivas, M., Customizing poly(lactic-co-glycolic acid) particles for biomedical applications. *Acta Biomaterialia* **2018,** *73*, 38-51.
40. Vaidya, A. N.; Pandey, R. A.; Mudliar, S.; Kumar, M. S.; Chakrabarti, T.; Devotta, S., Production and Recovery of Lactic Acid for Polylactide—An Overview. *Critical Reviews in Environmental Science and Technology* **2005,** *35* (5), 429-467.
41. Doelle, H. W., *Bacterial Metabolism*. Academic Press: New York, 1969.

42. Filachione, E. M.; Costello, E. J., Lactic Esters by Reaction of Ammonium Lactate with Alcohols. *Industrial & Engineering Chemistry* **1952,** *44* (9), 2189-2191.
43. Nishida, H.; Mori, T.; Hoshihara, S.; Fan, Y.; Shirai, Y.; Endo, T., Effect of tin on poly(l-lactic acid) pyrolysis. *Polymer Degradation and Stability* **2003,** *81* (3), 515-523.
44. Tsuji, H., Poly(lactide) Stereocomplexes: Formation, Structure, properties, Degradation, and Applications. *Macromol. Biosci.* **2005,** *5*, 569-597.
45. Li, S.; Hu, Y., Chapter 2 Polylactide Stereo-complex: From Principles to Applications. In *Poly(lactic acid) Science and Technology: Processing, Properties, Additives and Applications*, The Royal Society of Chemistry: 2015; pp 37-65.
46. Ana Rita Brás, M. T. V., Yaming Wang, Madalena Dionísio and João F. Mano, Crystallization of Poly(L-lactic acid) Probed with Dielectric Relaxation Spectroscopy. *Macromolecules* **2006,** *39*, 6513-6520.
47. Elsawy, M. A.; Kim, K.-H.; Park, J.-W.; Deep, A., Hydrolytic degradation of polylactic acid (PLA) and its composites. *Renewable and Sustainable Energy Reviews* **2017,** *79*, 1346-1352.
48. Drumright, R. E.; Gruber, P. R.; Henton, D. E., Polylactic Acid Technology. *Advanced Materials* **2000,** *12* (23), 1841-1846.
49. Gan, Z.; Yu, D.; Zhong, Z.; Liang, Q.; Jing, X., Enzymatic degradation of poly(ε-caprolactone)/poly(dl-lactide) blends in phosphate buffer solution. *Polymer* **1999,** *40* (10), 2859-2862.
50. Grizzi, I.; Garreau, H.; Li, S.; Vert, M., Hydrolytic degradation of devices based on poly(dl-lactic acid) size-dependence. *Biomaterials* **1995,** *16* (4), 305-311.
51. Tsuji, H.; Miyauchi, S., Poly(l-lactide): VI Effects of crystallinity on enzymatic hydrolysis of poly(l-lactide) without free amorphous region. *Polymer Degradation and Stability* **2001,** *71* (3), 415-424.
52. Tsuji, H.; Ishida, T., Poly(L-lactide). X. Enhanced surface hydrophilicity and chain-scission mechanisms of poly(L-lactide) film in enzymatic, alkaline, and phosphate-buffered solutions. *Journal of Applied Polymer Science* **2003,** *87* (10), 1628-1633.
53. Iwata, T.; Doi, Y., Morphology and Enzymatic Degradation of Poly(l-lactic acid) Single Crystals. *Macromolecules* **1998,** *31* (8), 2461-2467.
54. Signori, F.; Coltelli, M.-B.; Bronco, S., Thermal degradation of poly(lactic acid) (PLA) and poly(butylene adipate-co-terephthalate) (PBAT) and their blends upon melt processing. *Polymer Degradation and Stability* **2009,** *94* (1), 74-82.
55. Najafi, N.; Heuzey, M. C.; Carreau, P. J.; Wood-Adams, P. M., Control of thermal degradation of polylactide (PLA)-clay nanocomposites using chain extenders. *Polymer Degradation and Stability* **2012,** *97* (4), 554-565.
56. Speranza, V.; De Meo, A.; Pantani, R., Thermal and hydrolytic degradation kinetics of PLA in the molten state. *Polymer Degradation and Stability* **2014,** *100*, 37-41.
57. Meng, Q.; Heuzey, M.-C.; Carreau, P. J., Control of thermal degradation of polylactide/clay nanocomposites during melt processing by chain extension reaction. *Polymer Degradation and Stability* **2012,** *97* (10), 2010-2020.
58. Norrish, R. G. W.; Bamford, C. H., Photo-decomposition of Aldehydes and Ketones. *Nature* **1937,** *140* (3535), 195-196.
59. Santonja-Blasco, L.; Ribes-Greus, A.; Alamo, R. G., Comparative thermal, biological and photodegradation kinetics of polylactide and effect on crystallization rates. *Polymer Degradation and Stability* **2013,** *98* (3), 771-784.
60. Belbachir, S.; Zaïri, F.; Ayoub, G.; Maschke, U.; Naït-Abdelaziz, M.; Gloaguen, J. M.; Benguediab, M.; Lefebvre, J. M., Modelling of photodegradation effect on elastic–viscoplastic behaviour of amorphous polylactic acid films. *Journal of the Mechanics and Physics of Solids* **2010,** *58* (2), 241-255.

61. Ikada, E., Photo- and Bio-degradable Polyesters. Photodegradation Behaviors of Aliphatic Polyesters. *Journal of Photopolymer Science and Technology* **1997,** *10* (2), 265-270.
62. Wasanasuk, K.; Tashiro, K.; Hanesaka, M.; Ohhara, T.; Kurihara, K.; Kuroki, R.; Tamada, T.; Ozeki, T.; Kanamoto, T., Crystal Structure Analysis of Poly(l-lactic Acid) α Form On the basis of the 2-Dimensional Wide-Angle Synchrotron X-ray and Neutron Diffraction Measurements. *Macromolecules* **2011,** *44* (16), 6441-6452.
63. Wu, Y.; Li, L.; Chen, S.; Qin, J.; Chen, X.; Zhou, D.; Wu, H., Synthesis, characterization, and crystallization behaviors of poly(D-lactic acid)-based triblock copolymer. *Scientific Reports* **2020,** *10* (1), 3627.
64. Tashiro, K.; Kouno, N.; Wang, H.; Tsuji, H., Crystal Structure of Poly(lactic acid) Stereocomplex: Random Packing Model of PDLA and PLLA Chains As Studied by X-ray Diffraction Analysis. *Macromolecules* **2017,** *50* (20), 8048-8065.
65. Battegazzore, D.; Bocchini, S.; Frache, A., Crystallization kinetics of poly(lactic acid)-talc composites. *eXPRESS Polymer Letters* **2011,** *5*, 849-858.
66. Day, M.; Nawaby, A. V.; Liao, X., ADSC study of the crystallization behaviour of polylactic acid and its nanocomposites. *Journal of Thermal Analysis and Calorimetry* **2006,** *86* (3), 623-629.
67. Thakur, K. A. M.; Kean, R. T.; Zupfer, J. M.; Buehler, N. U.; Doscotch, M. A.; Munson, E. J., Solid State 13C CP-MAS NMR Studies of the Crystallinity and Morphology of Poly(l-lactide). *Macromolecules* **1996,** *29* (27), 8844-8851.
68. Pan, P.; Yang, J.; Shan, G.; Bao, Y.; Weng, Z.; Cao, A.; Yazawa, K.; Inoue, Y., Temperature-Variable FTIR and Solid-State 13C NMR Investigations on Crystalline Structure and Molecular Dynamics of Polymorphic Poly(l-lactide) and Poly(l-lactide)/Poly(d-lactide) Stereocomplex. *Macromolecules* **2012,** *45* (1), 189-197.
69. Chen, W.; Reichert, D.; Miyoshi, T., Helical Jump Motions of Poly(l-Lactic Acid) Chains in the α Phase As Revealed by Solid-State NMR. *The Journal of Physical Chemistry B* **2015,** *119* (12), 4552-4563.
70. Chen, W.; Zhou, W.; Makita, Y.; Wang, S.; Yuan, S.; Konishi, T.; Miyoshi, T., Characterization of the Slow Molecular Dynamics of Poly(l-Lactic Acid) in α and α′ Phases, in a Glassy State, and in a Complex with Poly(d-Lactic Acid) by Solid-State NMR. *Macromolecular Chemistry and Physics* **2018,** *219* (3), 1700451.
71. Olčák, D.; Hronský, V.; Kovaľaková, M.; Vrábel, P.; Chodák, I.; Alexy, P., High-Resolution Solid-State NMR Characterization of Morphology in Annealed Polylactic Acid. *International Journal of Polymer Analysis and Characterization* **2015,** *20* (5), 396-405.
72. Baran, A.; Vrábel, P.; Olčák, D.; Chodák, I., Solid state 13C-NMR study of a plasticized PLA/PHB polymer blend. *Journal of Applied Polymer Science* **2018,** *135* (21), 46296.
73. Metz, G.; Wu, X. L.; Smith, S. O., Ramped-Amplitude Cross Polarization in Magic-Angle-Spinning NMR. *J. Magn. Reson., Ser A* **1994,** *110* (2), 219-227.
74. Harris, R. K.; Becker, E. D.; Menezes, S. M. C. d.; Goodfellow, R.; Granger, P., Nomenclature: Nuclear Spin Properties and Conventions for Chemical Shifts: IUPAC Recommendations 2001. *Solid State Nucl.* **2002,** *22* (4), 458-483.
75. Pengju, P., Lili, Han., Guorong, Shan. and Yongzhong, Bao., Heating and Annealing Induced Structural Reorganization and Embrittlemnt of Solution-Crystallized Poly(L-lactic acid). *Macromolecules* **2014,** *47*, 8126-8130.
76. Ruihua Lv, n. p., Tianxiang Jin, Bing Na, Jie Wang and Hesheng Liu, Stereocomplex mesophase and its phase transition in enantiomeric polylactides. *Poymer* **2017,** *116*, 324-330.
77. Hideto Tsuji, F. H., Masaru Nakagawa, Yoshito Ikada, Hisashi Odani and Ryozo Kitamaru, Stereocomplex formation between enantiomeric poly(lactic acid)s. 7. Phase

structure of the stereocomplex crystallized from a dilute acetonitrile solution as studied by high-resolution solid-state carbon-13 NMR spectroscopy. *Macromolecules* **1992,** *25* (16), 4114-4118.
78. Jianming Zhang, H. S., Hideto Tsuji, Isao Noda and Yukihiro Ozaki, Infrared Spectroscopic Study of CH3···OC Interaction during Poly(l-lactide)/Poly(d-lactide) Stereocomplex Formation. *Macromolecules* **2005,** *38* (5), 1822-1828.
79. Jianming Zhang, H. S., Hideto Tsuji, Isao Noda and Yukihiro Ozaki, Differences in the CH3···OC interactions among poly(l-lactide), poly(l-lactide)/poly(d-lactide) stereocomplex, and poly(3-hydroxybutyrate) studied by infrared spectroscopy. *J. Molstruc.* **2005,** *735*, 249-257.
80. Yuan-ying Liang, H. T., Gan-ji Zong and Zhong-ming Li, Formation of Poly(L-lactide) mesophase and It's Chain Mobility Dependent Kinetics. *Chinese J Polym Sci* **2014,** *32* (9), 1176 - 1187.
81. Borisova, G. P. M. a. T. I., Molecular motion in polymers. *Sov. Phys. Uspekhi* **1964,** *7* (3), 375-384.
82. Vibeke K. Holm, S. N., and Jens Risbo, The Stabilit of Poly(lactic acid) Packaging Films as Influenced by Humidity and Temperature. *J. Food. Sci* **2006,** *71* (2), 40-44.
83. Goodship, V., *Practical guide to injection moulding*. Rapra Technology Ltd.

Arburg Ltd.: Shrewsbury, 2004.
84. Harper, C. A., *Handbook of plastics technologies: the complete guide to properties and performance*. McGraw-Hill: New York, USA, 2006.
85. Bart, J. C. J., *Additives in polymers: industrial analysis and applications*. John Wiley & Sons: 2006.
86. Mouldings, A. What is injection moulding? https://www.avplastics.co.uk/what-is-injection-moulding (accessed 29/03/2021).
87. Harris, A. M.; Lee, E. C., Improving mechanical performance of injection molded PLA by controlling crystallinity. *Journal of Applied Polymer Science* **2008,** *107* (4), 2246-2255.
88. Fu, S.-Y.; Feng, X.-Q.; Lauke, B.; Mai, Y.-W., Effects of particle size, particle/matrix interface adhesion and particle loading on mechanical properties of particulate–polymer composites. *Composites Part B: Engineering* **2008,** *39* (6), 933-961.
89. Cho, J.; Joshi, M. S.; Sun, C. T., Effect of inclusion size on mechanical properties of polymeric composites with micro and nano particles. *Composites Science and Technology* **2006,** *66*, 1941-1952.
90. Bai, H.; Bai, D.; Xiu, H.; Liu, H.; Zhang, Q.; Wang, K.; Deng, H.; Chen, F.; Fu, Q.; Chiu, F.-C., Towards high-performance poly(l-lactide)/elastomer blends with tunable interfacial adhesion and matrix crystallization via constructing stereocomplex crystallites at the interface. *RSC Advances* **2014,** *4* (90), 49374-49385.
91. Chandra, M.; Roy, S. K., *Plastic technology handbook*. 4th ed.; CRC Press: Roca Raton, FL, 2007.
92. Štěpek, J.; Daoust, H., *Additives for plastics*. Springer Science & Business Media: Berlin, Germany, 1983.
93. Fillon, B.; Thierry, A.; Lotz, B.; Wittmann, J. C., Efficiency scale for polymer nucleating agents. *Journal of thermal analysis* **1994,** *42* (4), 721-731.
94. Yachigo, S. i.; Sasaki, M.; Takahashi, Y.; Kojima, F.; Takada, T.; Okita, T., Studies on polymer stabilisers: Part I—A novel thermal stabiliser for butadiene polymers. *Polymer Degradation and Stability* **1988,** *22* (1), 63-77.
95. Pospíšil, J.; Horák, Z.; Pilař, J.; Billingham, N. C.; Zweifel, H.; Nešpůrek, S., Influence of testing conditions on the performance and durability of polymer stabilisers in thermal oxidation. *Polymer Degradation and Stability* **2003,** *82* (2), 145-162.

96. Suksut, B.; Deeprasertkul, C., Effect of Nucleating Agents on Physical Properties of Poly(lactic acid) and Its Blend with Natural Rubber. *Journal of Polymers and the Environment* **2011,** *19* (1), 288-296.
97. Shakoor, A.; Thomas, N. L., Talc as a nucleating agent and reinforcing filler in poly(lactic acid) composites. *Polymer Engineering & Science* **2014,** *54* (1), 64-70.
98. Ferrage, E.; Martin, F.; Boudet, A.; Petit, S.; Fourty, G.; Jouffret, F.; Micoud, P.; De Parseval, P.; Salvi, S.; Bourgerette, C.; Ferret, J.; Saint-Gerard, Y.; Buratto, S.; Fortune, J. P., Talc as nucleating agent of polypropylene: morphology induced by lamellar particles addition and interface mineral-matrix modelization. *Journal of Materials Science* **2002,** *37* (8), 1561-1573.
99. Maiti, S. N.; Sharma, K. K., Studies on polypropylene composites filled with talc particles. *Journal of Materials Science* **1992,** *27* (17), 4605-4613.
100. Arias, V.; Odelius, K.; Höglund, A.; Albertsson, A.-C., Homocomposites of Polylactide (PLA) with Induced Interfacial Stereocomplex Crystallites. *ACS Sustain Chem Eng* **2015,** *3* (9), 2220-2231.
101. Rosato, D. V.; Rosato, M. G., *Injection Molding Handbook*. Springer US: 2000.
102. Kogure, T.; Kameda, J.; Matsui, T.; Miyawaki, R., Stacking structure in disordered talc: Interpretation of its X-ray diffraction pattern by using pattern simulation and high-resolution transmission electron microscopy. *American Mineralogist* **2006,** *91* (8-9), 1363-1370.
103. Drobny, J. G., Thermoplastic Elastomers. In *Handbook of Thermoplastic Elastomers*, 2nd ed.; Ebnesajjad, S., Ed. Elsevier Inc: 2014.
104. Jignesh P Sheth, J. X., Garth L Wilkes, Solid state structure–property behavior of semicrystalline poly(ether-block-amide) PEBAX® thermoplastic elastomers. *Polymer* **2003,** *44* (3), 743-756.
105. Bell, C. A.; Yu, J.; Barker, I. A.; Truong, V. X.; Cao, Z.; Dobrinyin, A. V.; Becker, M. L.; Dove, A. P., Independent Control of Elastomer Properties through Stereocontrolled Synthesis. *Angew. Chem. Int. Ed* **2016,** *55*, 13076-13080.
106. Truong, V. X.; Dove, A. P., Organocatalytic, Regioselective Nucleophilic "Click" Addition of Thiols to Propiolic Acid Esters for Polymer–Polymer Coupling. *Angew. Chem. Int. Ed* **2013,** *52*, 4132-4136.
107. Jim, C. K. W.; Qin, A.; lam, J. W. Y.; Mahtab, F.; Yu, Y.; Tang, B. Z., Metal-Free Alkyne Polyhydrothiolation: Synthesis of Functional Poly(vinylenesulfide)s with High Stereoregularity by Regioselective Thioclick Polymerization. *Adv. Funct. Mater.* **2010,** *20*, 1319-1328.
108. Kolb, H. C.; Finn, M. G.; Sharpless, K. B., Click Chemistry: Diverse Chemical Function from a Few Good Reactions. *Angew. Chem. Int. Ed* **2001,** *40* (11), 2004-2021.
109. Hawker, C. J.; Wooley, K. L., The Convergence of Synthetic Organic and Polymer Chemistries. *Science* **2005,** *309* (15), 1200-1205.
110. Tang, W.; Becker, M. L., "Click" Reactions: a Versatile Toolbox for the Synthesis of Peptide-Conjugates. *Chem. Soc. Rev.* **2014,** *43*, 7013-7039.
111. Yu, B.; Chan, J. W.; Hoyle, C. E.; Lowe, A. B., Sequential Thiol-Ene/Thiol-Ene and Thiol-Ene/Thiol-YneReactions as a Route to Well-Defined Mono and BisEnd-Functionalized Poly(N-isopropylacrylamide). *J. Polym. Sci., Part A: Polym. Chem* **2009,** *47*, 3544-3557.
112. Buda, A.; Demco, D. E.; Bertmer, M.; Blümich, B.; Reining, B.; Keul, H.; Höcker, H., Domain sizes in heterogeneous polymers by spin diffusion using single-quantum and double-quantum dipolarfilters. *Solid State Nuclear Magnetic Resonance* **2004,** *24*, 39-67.
113. Hou, S. S.; Bonagamba, T. J.; Beyer, F. L.; Madison, P. H.; Schmidt-Rohr, K., Clay Intercalation of Poly(styrene-ethylene oxide) Block Copolymers Studied by Two-Dimensional Solid-State NMR. *Macromolecules* **2003,** *36*, 2769-2776.

114. Kretschmer, A.; Drake, R.; Neidhoefer, M.; Wilhelm, M., Quantification of Composition and Domain Sizes of Industrial Poly(phthalamide)/Poly(dimethylsiloxane) Block Copolymers Using Di¡erent 1H Solid State NMR Methods. *Solid State Nucl. Magn. Reson.* **2002,** *22*, 204-217.
115. Paul, S. M. D.; Zwanziger, J. W.; Ulrich, R.; Wiesner, U.; Spiess, H. W., Structure, Mobility, and Interface Characterization of Self-Organized Organic-Inorganic Hybrid Materials by Solid-State NMR. *J. Am. Chem. Soc.* **1999,** *121*, 5727-5736.
116. Yu, H.; Natansohn, A.; Singh, M. A.; Torriani, I., Solid-State NMR and Small-Angle X-ray Scattering Study of Microphase Structure of Amorphous and Semicrystalline Poly(styrene-ethylene oxide) Diblock Copolymers. *Macromolecules* **2001,** *34*, 1258-1266.
117. Clauss, J.; Schmidt-Rohr, K.; Spiess, H. W., Determination of Domain Sizes in Heterogeneous Polymers by Solid-State NMR. *Acta Polym.* **1993,** *44* (1), 1-17.
118. Neagu, C.; Puskas, J. E.; Singh, M. A.; Natansohn, A., Domain Sizes Determination for Styrene−Isobutylene Block Copolymer Systems Using Solid-State NMR Spectroscopy. *Macromolecules* **2000,** *33* (16), 5976-5981.
119. Weigand, F.; E.Demco, D.; Blümich, B.; Spiess, H. W., Spatially Resolved NMR Spin Diffusion in Solid Polymers. *J. Magn. Reson., Ser A* **1996,** *120* (2), 190-200.
120. Colquhoun, I. J.; Packer, K. J., Nuclear Magnetic Resonance in Solid Ethylene/α-Olefin Copolymers: Relaxation, Spin-Diffusion and Lamellar Widths. *Br. Polym. J.* **1987,** *19* (2), 151-163.
121. Assink, R. A., Nuclear Spin Diffusion Between Polyurethane Microphases. *Macromolecules* **1978,** *11* (6), 1233-1237.
122. Gandhi, S.; Melian, C.; Demco, D. E.; Brar, A. S.; Blümich, B., Morphology and Motional Heterogeneity in PS/PMMA Diblock Copolymers Studied by 1H and 13C Solid-State NMR Spectroscopy. *Macromol. Chem. Phys.* **2008,** *209*, 156-1585.
123. Litvinov, V. M.; Bertmer, M.; Gasper, L.; Demco, D. E.; Blümich, B., Phase Composition of Block Copoly(ether ester) Thermoplastic Elastomers Studied by Solid-State NMR Techniques. *Macromolecules* **2003,** *36*, 7598-7606.
124. Hucher, C.; Eustache, R.-P.; Beaume, F.; Tekely, P., Motional Heterogeneity in Poly(ether-block-amide) Copolymers As Revealed by Solid-State NMR. *Macromolecules* **2005,** *38*, 9200-9209.
125. Oh, S. J.; Koenig, J. L., Solid-State NMR Studies of cis-1,4-polyisoprene Crosslinked with Dicumyl Peroxide in the Presence of Triallyl Cyanurate. *J. Polym. Sci. Pol. Phys.* **2000,** *38*, 1417-1423.
126. El-Nahhal, I. M., Synthesis and Solid-State NMR Structural Characterization of Polysiloxane-immobilized Thiol-Amine Metal(II) Complexes. *Phosphorus Sulfur and Silicon and the Related Elements* **2000,** *1*, 245-258.
127. Jahromi, S.; Gabrielse, W.; Braam, A., Effect of melamine polyphosphate on thermal degradation of polyamides: a combined X-ray diffraction and solid-state NMR study. *Polymer* **2003,** *44*, 25-37.
128. McElheny, D.; Frydman, V.; Frydman, L., A solid-state 13C NMR analysis of molecular dynamics in aramide polymers. *Solid State Nuclear Magnetic Resonance* **2006,** *29*, 132-141.
129. Okada, A.; Kawasumi, M.; Tajima, I.; Kurauchi, T.; Kamigaito, O., A Solid State NMR Study on Crystalline Forms of Nylon 6. *Journal of Applied Polymer Science* **1989,** *37*, 1363-1371.
130. Murthy, N. S.; Wang, W.; Kohn, J., Microphase Separation in Copolymers of Hydrophilic PEG Blocks and Hydrophobic Tyrosine-Derived Segments Using Simultaneous SAXS/WAXS/DSC. *Polymer* **2010,** *51*, 3978-3988.

131. Bonart, R.; Morbitzer, L.; Müller, E. H., X-Ray Investigations Concerning the Physical Structure of Crosslinking in Urethane Elastomers. III. Common Structure Principles for Extensions with Aliphatic Diamines and Diols. *J. Macromol. Sci. Part B* **1974,** *9* (3), 447-461.
132. Martin, D. J.; Meijs, G. F.; Gunatillake, P. A.; McCarthy, S. J.; Renwick, G. M., The Effect of Average Soft Segment Length on Morphology and Properties of a Series of Polyurethane Elastomers. II. SAXS-DSC Annealing Study. *J. Appl. Polym. Sci.* **1997,** *64* (4), 803-817.
133. Leung, L. M.; Koberstein, J. T., Small-Angle Scattering Analysis of Hard-Microdomain Structure and Microphase Mixing in Polyurethane Elastomers. *J. Polym. Sci.* **1985,** *23*, 1883-1913.
134. Krol, P., Synthesis Methods, Chemical Structures and Phase Structures of Linear Polyurethanes. Properties and Applications of Linear Polyurethanes in Polyurethane Elastomers, Copolymers and Ionomers. *Prog. Mater. Sci.* **2007,** *52*, 915-1015.
135. Ehrburger-Dolle, F.; Bley, F.; Geissler, E.; Livet, F.; Morfin, I.; Rochas, C., Filler Networks in Elastomers. *Macromol. Symp.* **2003,** *200*, 157-167.
136. M.Feike; D.E.Demco; R.Graf; J.Gottwald; S.Hafner; H.W.Spiess, Broadband Multiple-Quantum NMR Spectroscopy. *Journal of Magnetic Resonance Series A* **1996,** *122* (2), 214-221.
137. Sommer, W.; Gottwald, J.; Demco, D. E.; Spiess, H. W., Dipolar Heteronuclear Multiple-Quantum NMR Spectroscopy in Rotating Solids. *J. Magn. Reson., Ser A* **1995,** *113* (1), 131-134.
138. Schnell, I.; Lupulescu, A.; Hafner, S.; Demco, D. E.; Spiess, H. W., Resolution Enhancement in Multiple-Quantum MAS NMR Spectroscopy. *J. Magn. Reson.* **1998,** *133* (1), 61-69.
139. Jemian, J. I. a. P. R., Irena: tool suite for modeling and analysis of small-angle scattering. *J. Appl. Cryst.* **2009,** *42* (2), 347-353.
140. Marcinko, J. J.; Parker, A. A., An Overview of the Correlation Between NMR Cross Polarization Time Constants and Dynamic Moduli. *Macromol. Symp.* **1994,** *86*, 251-257.
141. Parker, A. A.; Marcinko, J. J.; Rinaldi, P.; Hedrick, D. P.; Ritchey, W. M., A relationship between NMR Cross-Polarization Rates and dynamic Storage Modulae of Polymers. *J App. Poly. Sci.* **1993,** *48*, 677-681.
142. Koberstein, J. T.; Russell, T. P., Simultaneous SAXS-DSC Study of Multiple Endothermic Behavior in Polyether-Based Polyurethane Block Copolymers. *Macromolecules* **1986,** *19*, 714-720.
143. Jones, J. R., Review of bioactive glass: From Hench to hybrids. *Acta Biomaterialia* **2013,** *9* (1), 4457-4486.
144. Hench, L. L., The story of Bioglass. *J. Mater. Sci. Mater. Med.* **2006,** *17* (11), 967-978.
145. Hench, L. L.; Splinter, R. J.; Allen, W. C.; Greenlee, T. K., Bonding Mechanisms at the Interface of Ceramic Prosthetic Materials. *J. Biomed. Mater. Res. A* **1971,** *5* (6), 117-141.
146. Kokubo, T., Bioactive Glass Ceramics: Properties and Applications. *Biomaterials* **1991,** *12*, 155-163.
147. LeGeros, R. Z., Properties of Osteoconductive Biomaterials: Calcium Phosphates. *Clin. Orthop. Relat. Res.* **2002,** *395*, 81-98.
148. Elgayar, I.; Aliev, A. E.; Boccaccini, A. R.; Hill, R. G., Structural Analysis of Bioactive Glasses. *J. Non-Cryst. Solids* **2005,** *351* (2), 173-183.
149. Hench, L. L.; Xynos, I. D.; Polak, J. M., Bioactive Glasses for in Situ Tissue Regeneration. *J . Biomater. Sci. Polym. Ed.* **2004,** *15* (4), 543-562.
150. Yao, A.; Wang, D.; Huang, W.; Fu, Q.; Rahaman, M. N.; Day, D. E., In Vitro Bioactive Characteristics of Borate-Based Glasses with Controllable Degredation Behaviour. *J. Am. Ceram. Soc* **2007,** *90* (1), 303-306.

151. Foroutan, F.; McGuire, J.; Gupta, P.; Nikolaou, A.; Kyffin, B. A.; Kelly, N. L.; Hanna, J. V.; Gutierrez-Merino, J.; Knowles, J. C.; Baek, S.-Y.; Velliou, E.; Carta, D., Antibacterial Copper-Doped Calcium Phosphate Glasses for Bone Tissue Regeneration. *ACS Biomater. Sci. Eng* **2019,** *5* (11), 6054-6062.
152. Brow, R. K.; Kirkpatrick, R. J.; L.Turner, G., The short Range Structure of Sodium Phosphate Glasses 1.MAS NMR Studies. *J. Non-Cryst. Solids* **1990,** *116*, 39-45.
153. Abou Neel, E. A.; Pickup, D. M.; Valappil, S. P.; Newport, R. J.; Knowles, J. C., Bioactive functional materials: a perspective on phosphate-based glasses. *Journal of Materials Chemistry* **2009,** *19* (6), 690-701.
154. Abou Neel, E. A.; Mizoguchi, T.; Ito, M.; Bitar, M.; Salih, V.; Knowles, J. C., In vitro bioactivity and gene expression by cells cultured on titanium dioxide doped phosphate-based glasses. *Biomaterials* **2007,** *28* (19), 2967-2977.
155. Abou Neel, E. A.; Knowles, J. C., Physical and biocompatibility studies of novel titanium dioxide doped phosphate-based glasses for bone tissue engineering applications. *Journal of Materials Science: Materials in Medicine* **2008,** *19* (1), 377-386.
156. Neel, E. A. A.; Young, A. M.; Nazhat, S. N.; Knowles, J. C., A Facile Synthesis Route to Prepare Microtubes from Phosphate Glass Fibres. *Advanced Materials* **2007,** *19* (19), 2856-2862.
157. Guedes, J. C.; Park, J.-H.; Lakhkar, N. J.; Kim, H.-W.; Knowles, J. C.; Wall, I. B., TiO2-doped phosphate glass microcarriers: A stable bioactive substrate for expansion of adherent mammalian cells. *Journal of Biomaterials Applications* **2012,** *28* (1), 3-11.
158. Nunzi Conti, G.; Chiasera, A.; Ghisa, L.; Berneschi, S.; Brenci, M.; Dumeige, Y.; Pelli, S.; Sebastiani, S.; Feron, P.; Ferrari, M.; Righini, G. C., Spectroscopic and lasing properties of Er3+-doped glass microspheres. *Journal of Non-Crystalline Solids* **2006,** *352* (23), 2360-2363.
159. Lakhkar, N. J.; Park, J.-H.; Mordan, N. J.; Salih, V.; Wall, I. B.; Kim, H.-W.; King, S. P.; Hanna, J. V.; Martin, R. A.; Addison, O.; Mosselmans, J. F. W.; Knowles, J. C., Titanium phosphate glass microspheres for bone tissue engineering. *Acta Biomaterialia* **2012,** *8* (11), 4181-4190.
160. Ahmed, I.; Collins, C. A.; Lewis, M. P.; Olsen, I.; Knowles, J. C., Processing, characterisation and biocompatibility of iron-phosphate glass fibres for tissue engineering. *Biomaterials* **2004,** *25* (16), 3223-3232.
161. Bitar, M.; Salih, V.; Knowles, J. C.; Lewis, M. P., Iron-phosphate glass fiber scaffolds for the hard–soft interface regeneration: The effect of fiber diameter and flow culture condition on cell survival and differentiation. *Journal of Biomedical Materials Research Part A* **2008,** *87A* (4), 1017-1026.
162. Vitale-Brovarone, C.; Novajra, G.; Lousteau, J.; Milanese, D.; Raimondo, S.; Fornaro, M., Phosphate glass fibres and their role in neuronal polarization and axonal growth direction. *Acta Biomaterialia* **2012,** *8* (3), 1125-1136.
163. Shah, R.; Sinanan, A. C. M.; Knowles, J. C.; Hunt, N. P.; Lewis, M. P., Craniofacial muscle engineering using a 3-dimensional phosphate glass fibre construct. *Biomaterials* **2005,** *26* (13), 1497-1505.
164. Nazhat, S. N.; Abou Neel, E. A.; Kidane, A.; Ahmed, I.; Hope, C.; Kershaw, M.; Lee, P. D.; Stride, E.; Saffari, N.; Knowles, J. C.; Brown, R. A., Controlled Microchannelling in Dense Collagen Scaffolds by Soluble Phosphate Glass Fibers. *Biomacromolecules* **2007,** *8* (2), 543-551.
165. Sene, F. F.; Martinelli, J. R.; Okuno, E., Synthesis and characterization of phosphate glass microspheres for radiotherapy applications. *Journal of Non-Crystalline Solids* **2008,** *354* (42), 4887-4893.
166. Martin, R. A.; Moss, R. M.; Lakhkar, N. J.; Knowles, J. C.; Cuello, G. J.; Smith, M. E.; Hanna, J. V.; Newport, R. J., Structural characterization of titanium-doped Bioglass using

isotopic substitution neutron diffraction. *Physical Chemistry Chemical Physics* **2012,** *14* (45), 15807-15815.
167. Rana, K. S.; Souza, L. P. d.; Isaacs, M. A.; Raja, F. N. S.; Morrell, A. P.; Martin, R. A., Development and Characterization of Gallium-Doped Bioactive Glasses for Potential Bone Cancer Applications. *ACS Biomaterials Science & Engineering* **2017,** *3* (12), 3425-3432.
168. Valappil, S. P.; Ready, D.; Neel, E. A. A.; Pickup, D. M.; Chrzanowski, W.; O'Dell, L. A.; Newport, R. J.; Smith, M. E.; Wilson, M.; Knowles, J. C., Antimicrobial Gallium-Doped Phosphate-Based Glasses. *Advanced Functional Materials* **2008,** *18* (5), 732-741.
169. Ahmed, A. A.; Ali, A. A.; Mahmoud, D. A. R.; El-Fiqi, A. M., Study on the preparation and properties of silver-doped phosphate antibacterial glasses (Part I). *Solid State Sciences* **2011,** *13* (5), 981-992.
170. Kyffin, B. A.; Foroutan, F.; Raja, F. N. S.; Martin, R. A.; Pickup, D. M.; Taylor, S. E.; Carta, D., Antibacterial silver-doped phosphate-based glasses prepared by coacervation. *Journal of Materials Chemistry B* **2019,** *7* (48), 7744-7755.
171. Koo, J.; Bae, B.-S.; Na, H.-K., Raman Spectroscopy of Copper Phosphate Glass. *J. Non-Cryst. Solids* **1997,** *212*, 173-179.
172. Ravikumar, R. V. S. S. N.; Reddy, V. R.; Chandrasekhar, A. V.; Reddy, B. J.; Reddy, Y. P.; Rao, P. S., Tetragonal Site of Transition Metal Ions Doped Sodium Phosphate Glasses. *J. Alloys Compd.* **2002,** *337*, 272-276.
173. Uauy, R.; Olivares, M.; Gonzalez, M., Essentiality of copper in humans. *The American journal of clinical nutrition* **1998,** *67* (5 Suppl), 952s-959s.
174. Hu, G.-f., Copper stimulates proliferation of human endothelial cells under culture. *Journal of Cellular Biochemistry* **1998,** *69* (3), 326-335.
175. Finney, L.; Vogt, S.; Fukai, T.; Glesne, D., Copper and angiogenesis: unravelling a relationship key to cancer progression. *Clinical and experimental pharmacology & physiology* **2009,** *36* (1), 88-94.
176. Gérard, C.; Bordeleau, L. J.; Barralet, J.; Doillon, C. J., The stimulation of angiogenesis and collagen deposition by copper. *Biomaterials* **2010,** *31* (5), 824-31.
177. Neel, E. A.; Ahmed, I.; Pratten, J.; Narzhat, S. N.; Knowles, J. C., Characterisation of Antibacterial Copper Releasing Degradable Phosphate Glass Fibres. *Biomaterials* **2005,** *26* (15), 2247-2254.
178. Chen, Q.; Zhu, C.; Thouas, G. A. Progress and challenges in biomaterials used for bone tissue engineering: bioactive glasses and elastomeric composites *Prog Biomater* [Online], 2012, p. 2. PubMed.
179. Bhattacharje, A.; Fang, Y.; Hooper, T. J. N.; Kelly, N. L.; Gupta, D.; Abalani, K.; Manna, I.; Baikie, T.; Bishop, P. T.; White, T. J.; Hanna, J. V., Crystal Chemistry and Antibacterial Properties of Cupriferous Hydroxyapatite. *Materials* **2019,** *12* (11), 1814.
180. Gibbs, G. V.; Meagher, E. P.; Newton, M. D.; Swanson, D. K., A Comparison of Experimental and Theoretical Bond Length and Angle Variations for Minerals, Inorganic Solids, and Molecules. In *Structure and Bonding in Crystals*, Nsvrotsky, A., Ed. Academic Press: 1981.
181. Zachariasen, W. H., The Atomic Arrangement in Glass. *J. Am. Chem. Soc.* **1932,** *54*, 3841-3851.
182. Bae, B.-S.; Weingberg, M. C., Oxidation-Reduction Equilibrium in Copper Phosphate Glass Melted in Air. *J. Am. Ceram. Soc* **1991,** *74* (12), 3039-2045.
183. Bogomolova, L. D.; Jachkin, V. A.; Lazukin, V. N.; Pavlushkina, T. K.; Shmuckler, V. A., The Electron Paramagnetic Resonance and Optical Spectra of Copper and Vanadium in Phosphate Glasses. *J. Non-Cryst. Solids* **1978,** *28*, 375-389.
184. Sułowska, J.; Waclawska, I.; Szumera, M., Effect of copper addition on glass transition of silicate–phosphate glasses. *J. Therm. Anal. Calorim.* **2012,** *109*, 705-710.

185. Jiang, X.; Zhang, J.; Zhou, B.; Hu, X.; Zhu, Z.; Tan, Y.; Chang, C.; Lu, J.; Song, B., Anomalous Behavior of Membrane Fluidity Caused by Copper-Copper Bond Coupled Phospholipids. *Sci. Rep.* **2018,** *8*, 14093 - 14100.
186. Ambundo, E. A.; Deydier, M.-V.; Grall, A. J.; Aguera-Vega, N.; Dressel, L. T.; Cooper, T. H.; Heeg, M. J.; Ochrymowycz, L. A.; Rorabacher, D. B., Influence of Coordination Geometry upon Copper(II/I) Redox Potentials. Physical Parameters for Twelve Copper Tripodal Ligand Complexes. *Inorganic Chemistry* **1999,** *38* (19), 4233-4242.
187. Conry, R. R., Copper: Inorganic & Coordination Chemistry. In *Encyclopedia of Inorganic Chemistry*, King, R. B.; Crabtree, R. H.; Lukehart, C. M.; Atwood, D. A.; Scott, R. A., Eds. 2005.
188. Veidis, M. V.; Schreiber, G. H.; Gough, T. E.; Palenik, G. J., Jahn-Teller distortions in octahedral copper(II) complexes. *Journal of the American Chemical Society* **1969,** *91* (7), 1859-1860.
189. Magini, M., Coordination of copper(II). Evidence of the Jahn-Teller effect in aqueous perchlorate solutions. *Inorganic Chemistry* **1982,** *21* (4), 1535-1538.
190. Aly, M. M., The Isolation and Characterization of Square Planar, Square Pyramidal, and Octahedral Copper(II) Complexes with Mixed Ligands. *Zeitschrift für Naturforschung B* **1978,** *33* (8), 906-910.
191. Hoppe, A.; Meszaros, R.; Stähli, C.; Romeis, S.; Schmidt, J.; Peukert, W.; Marelli, B.; Nazhat, S. N.; Wondraczek, L.; Lao, J.; Jallot, E.; Boccaccini, A. R., In vitro reactivity of Cu doped 45S5 Bioglass® derived scaffolds for bone tissue engineering. *Journal of Materials Chemistry B* **2013,** *1* (41), 5659-5674.
192. Wers, E.; Oudadesse, H.; Lefeuvre, B.; Lucas-Girot, A.; Rocherullé, J.; Lebullenger, R., Excess entopy and thermal behaviour of Cu- and Ti- doped bioactive glasses. *J. Therm. Anal. Calorim.* **2014,** *117*, 579-588.
193. Sitarz, M.; Bulat, K.; Szumercca, M., Influence of modifiers and glass-forming ions on the crystallization of glasses of the NaCaPO4_SiO2 system. *J. Therm. Anal. Calorim.* **2012,** *109*, 577-584.
194. Kirkpatrick, R. J.; Brow, R. K., Nuclear magnetic resonance investigation of the structures of phosphate and phosphate-containing glasses: a review. *Solid State Nucl.* **1995,** *5* (1), 9-21.
195. Yadav, A.; Seth, V. P., Electron Paramagnetic Resonance of Cu^{2+} and VO^{2+} Ions in Phosphate Glasses. *J. Mater. Sci.* **1987,** *22*, 239-243.
196. Pemberton, J. E.; Laifzadeh, L., Raman Spectroscopy of Calcium Phosphate Glasses with Varying CaO Modifier Concentrations. *Chem. mater* **1991,** *3*, 195-200.
197. Campbell, M. J. M.; Collis, A. J.; Grzeskowiak, R., Electron Paramagnetic Resonance Spectrum and Covalency Parameters of Copper-63(KTS). *Bioinorg. Chem.* **1976,** *6*, 305-311.
198. Rao, A. S.; Rao, J. L.; Lakshman, S. V. J., Electron Paramagnetic Resonance and Optical Absorption Spectra of Cu^{2+} Ions in Alkali Cadmium Borosulphate Glasses. *J. Phys. Chem. Solids* **1992,** *51* (9), 1221-1226.
199. Debnath, R.; Chaudhury, J.; Bera, S. C., Optical Properties and Nature of Coordination of Cu+ Ions in Calcium Metaphosphate Glass. *physica status solidi (b)* **1990,** *157* (2), 723-733.
200. Yu, W.; Sun, T.-W.; Ding, Z.; Qi, C.; Zhao, H.; Chen, F.; Shi, Z.; Zhu, Y.-J.; Chen, D.; He, Y., Copper-doped mesoporous hydroxyapatite microspheres synthesized by a microwave-hydrothermal method using creatine phosphate as an organic phosphorus source: application in drug delivery and enhanced bone regeneration. *Journal of Materials Chemistry B* **2017,** *5* (5), 1039-1052.
201. Imrie, F.; Skakle, J., Preparation of Copper-Doped Hydroxyapatite with Varying x in the Composition Ca10(PO4)6CuxOyHz. *Bioceramics Development and Applications* **2013,** *3*.

202. Edathazhe, A. B.; Shashikala, H. D., Dissolution Studies of Na_2O-BaO-CaO-P_2O_5 Glasses in Deionized Water Under Semi-Dynamic Conditions for Bioactive Applications *Mater. Today: Proceedings* **2018,** *5*, 21241-21247.
203. Ainsworth, R. I.; Tommaso, D. D.; Christie, J. K.; Leeuw, N. H. d., Polarizable Force Field Development and Molecular Dynamics Study of Phosphate-based Glasses. *J. Chem. Phys* **2012,** *137*, 234502.
204. Chi, W.; Zou, J.; Lin, Y.; Li, W.; Cao, C.; Yang, K.; Zhou, K., Research of Cu-Doped Hydroxyapatite Microbeads Fabricated by Pneumatic Extrusion Printing. *Materials* **2019,** *12*, 1769.
205. Moreno, L. I.; McCord, B. R., Understanding metal inhibition: The effect of copper (Cu2+) on DNA containing samples. *Forensic Chemistry* **2017,** *4*, 89-95.
206. Mulligan, A. M.; Wilson, M.; Knowles, J. C., The effect of increasing copper content in phosphate-based glasses on biofilms of Streptococcus sanguis. *Biomaterials* **2003,** *24* (10), 1797-1807.
207. Milkovic, L.; Hoppe, A.; Detsch, R.; Boccaccini, A. R.; Zarkovic, N., Effects of Cu-doped 45S5 bioactive glass on the lipid peroxidation-associated growth of human osteoblast-like cells in vitro. *Journal of Biomedical Materials Research Part A* **2014,** *102* (10), 3556-3561.
208. Stobridge, F. C.; Middlemiss, D. S.; Pell, A. J.; leskes, M.; Clement, R. J.; Pourpoint, F.; Lu, Z.; Hanna, J. V.; Pintacuda, G.; Emsley, L.; Samoson, A.; Grey, C. P., Characterising Local Environments in High Energy Density Li-ion Battery Cathodes: a Combined NMR and First Principles Study of $LiFe_xCo_{1-x}PO_4$. *J. Mater. Chem. A* **2014,** *2*, 11948-11957.
209. Gaj, J. A., 2.04 - Semimagnetic Semiconductors. In *Comprehensive Semiconductor Science and Technology*, Bhattacharya, P.; Fornari, R.; Kamimura, H., Eds. Elsevier: Amsterdam, 2011; pp 95-124.
210. *Origin(Pro)*, Version 2016; OriginLab Corporation: Northampton, MA, USA.
211. Stoll, S.; Schweiger, A., EasySpin, a comprehensive software package for spectral simulation and analysis in EPR. *J. Magn. Reson.* **2006,** *178* (1), 42-55.
212. Shih, P. Y.; Yung, S. W.; Chin, T. S., FTIR and XPS Studies of P_2O_5-Na_2O-CuO Glasses. *J. Non-Cryst. Solids* **1999,** *244*, 211-222.
213. Ben Osman, M.; Diallo-Garcia, S.; Herledan, V.; Brouri, D.; Yoshioka, T.; Kubo, J.; Millot, Y.; Costentin, G., Discrimination of Surface and Bulk Structure of Crystalline Hydroxyapatite Nanoparticles by NMR. *The Journal of Physical Chemistry C* **2015,** *119* (40), 23008-23020.
214. Jarlbring, M.; Sandström, D. E.; Antzutkin, O. N.; Forsling, W., Characterization of Active Phosphorus Surface Sites at Synthetic Carbonate-Free Fluorapatite Using Single-Pulse 1H, 31P, and 31P CP MAS NMR. *Langmuir* **2006,** *22* (10), 4787-4792.
215. Sundar, H. G. K.; Rao, K. J., ESR of Cu^{2+} and Mn^{2+} in K_2SO_4-$ZnSO_4$ Glasses. *J. Non-Cryst. Solids* **1982,** *50* (1), 137-138.
216. Rao, J. L.; Sreedhar, B.; Reddy, M. R.; Lakshman, S. V. J., Electron Spin Resonance and Optical Absorption Spectra of Cr^{3+} and Cu^{2+} Ions in K_2SO_4-$ZnSO_4$ Glasses. *J. Non-Cryst. Solids* **1989,** *111*, 228-237.
217. Narendra, G. L.; Sreedhar, B.; Rao, J. L.; lakshman, S. V. J., Electron Spin Resonance and Optical Absorption Spectra of Cu^{2+} Ions in Na_2SO_4-$ZnSO_4$ Glasses. *J. Mater. Sci.* **1991,** *26*, 5342-5346.
218. Cereghetti, G. M.; Schweiger, A.; Glockshuber, R.; Van Doorslaer, S., Electron Paramagnetic Resonance Evidence for Binding of Cu2+ to the C-terminal Domain of the Murine Prion Protein. *Biophysical Journal* **2001,** *81* (1), 516-525.
219. Peisach, J.; Blumberg, W. E., Structural implications derived from the analysis of electron paramagnetic resonance spectra of natural and artificial copper proteins. *Archives of Biochemistry and Biophysics* **1974,** *165* (2), 691-708.

220. Messerschmidt, A., Metal sites in small blue copper proteins, blue copper oxidases and vanadium-containing enzymes. In *Metal Sites in Proteins and Models Redox Centres*, Hill, H. A. O.; Sadler, P. J.; Thomson, A. J., Eds. Springer Berlin Heidelberg: Berlin, Heidelberg, 1998; pp 37-68.
221. Stammeier, J. A.; Purgstaller, B.; Hippler, D.; Mavromatis, V.; Dietzel, M., In-situ Raman Spectroscopy of Amorphous Calcium Phosphate to Crystalline Hydroxyapatite Transformation. *MethodsX* **2018,** *5*, 1241-1250.
222. Brow, R. K., Review: The Structure of Simple Phosphate Glasses. *J. Non-Cryst. Solids* **2000,** *263*, 1-28.

A. Appendix Understanding the Physical Ageing of High-heat Polylactide

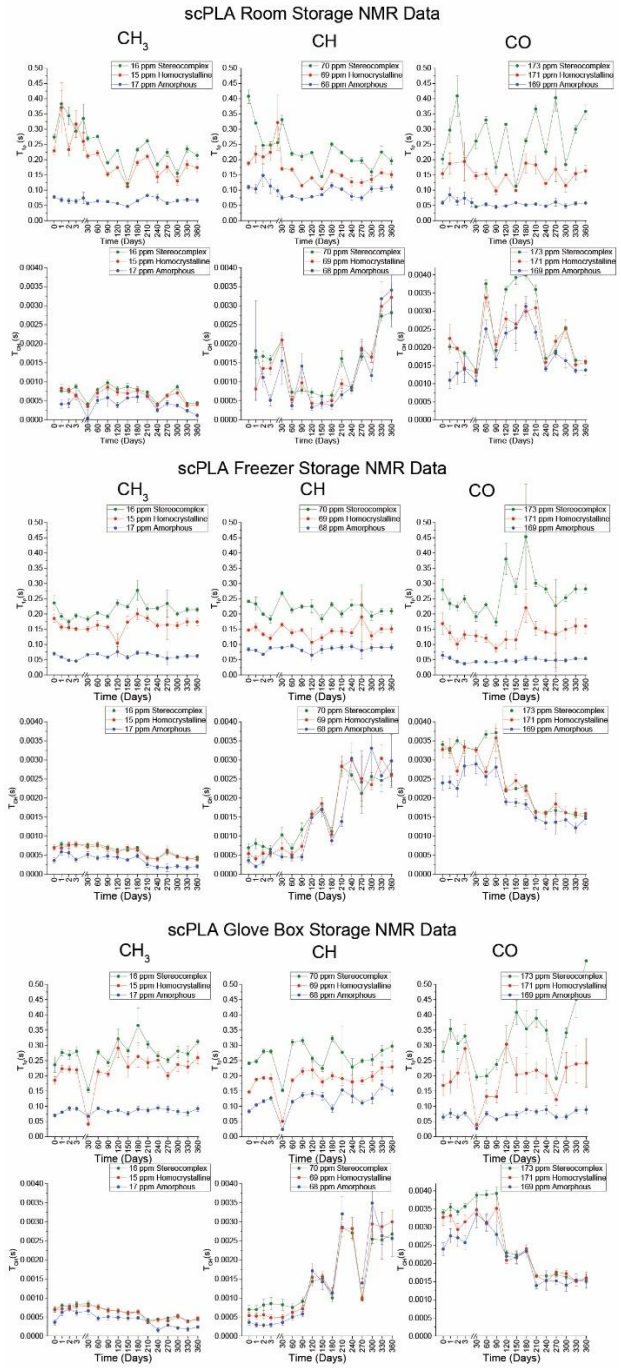

Figure A-1. The change in $T_{1\rho}$ (top) and T_{CH} (bottom) times for scPLA PLA stored in room conditions for the two crystalline and one amorphous region for CH_3 (left), CH (middle)and COO (right), under room conditions (top) , stored in a freezer (middle) ands tored in a glovebox (bottom).

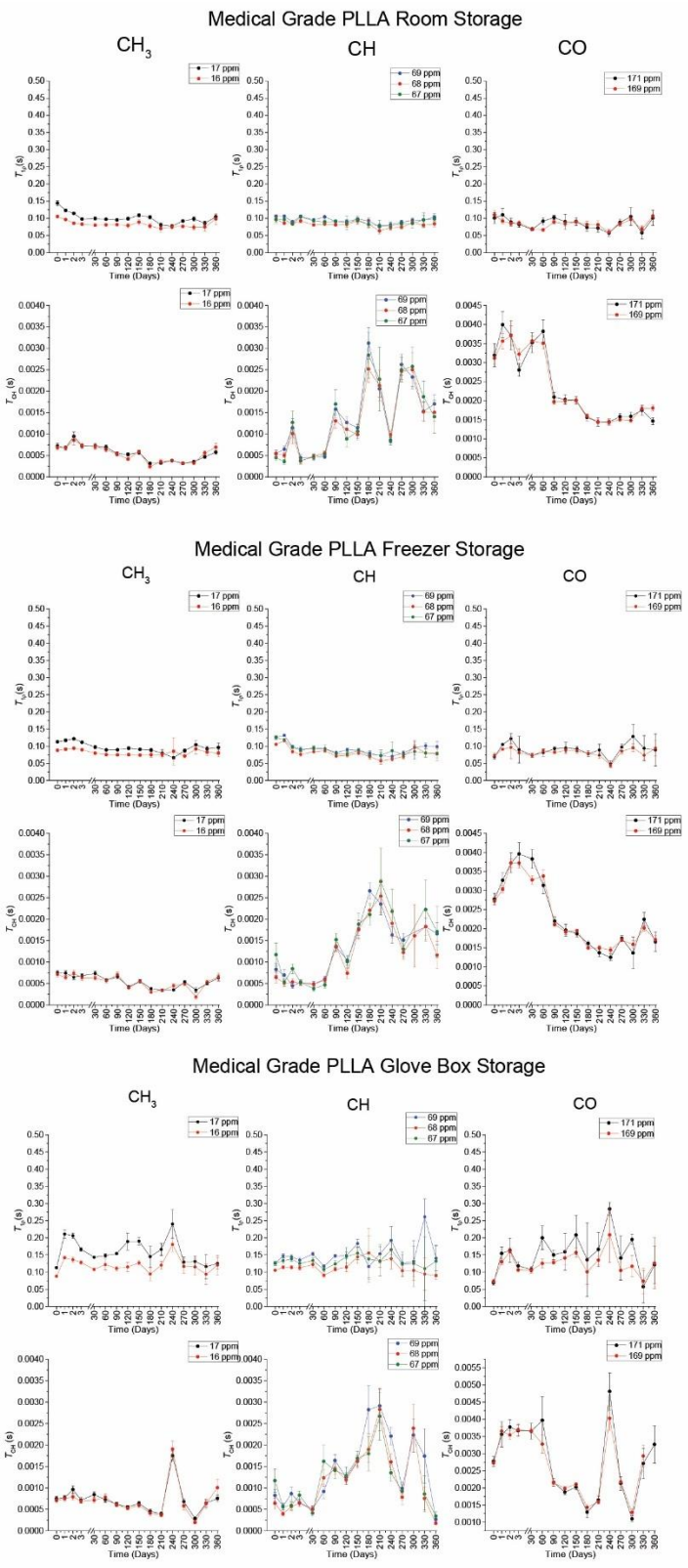

Figure A-2. The change in $T_{1\rho}$ (top) and T_{CH} (bottom) times for medical grade PLA for CH_3 (left), CH (middle)and COO (right), under room conditions (top) , stored in a freezer (middle) and stored in a glovebox (bottom).

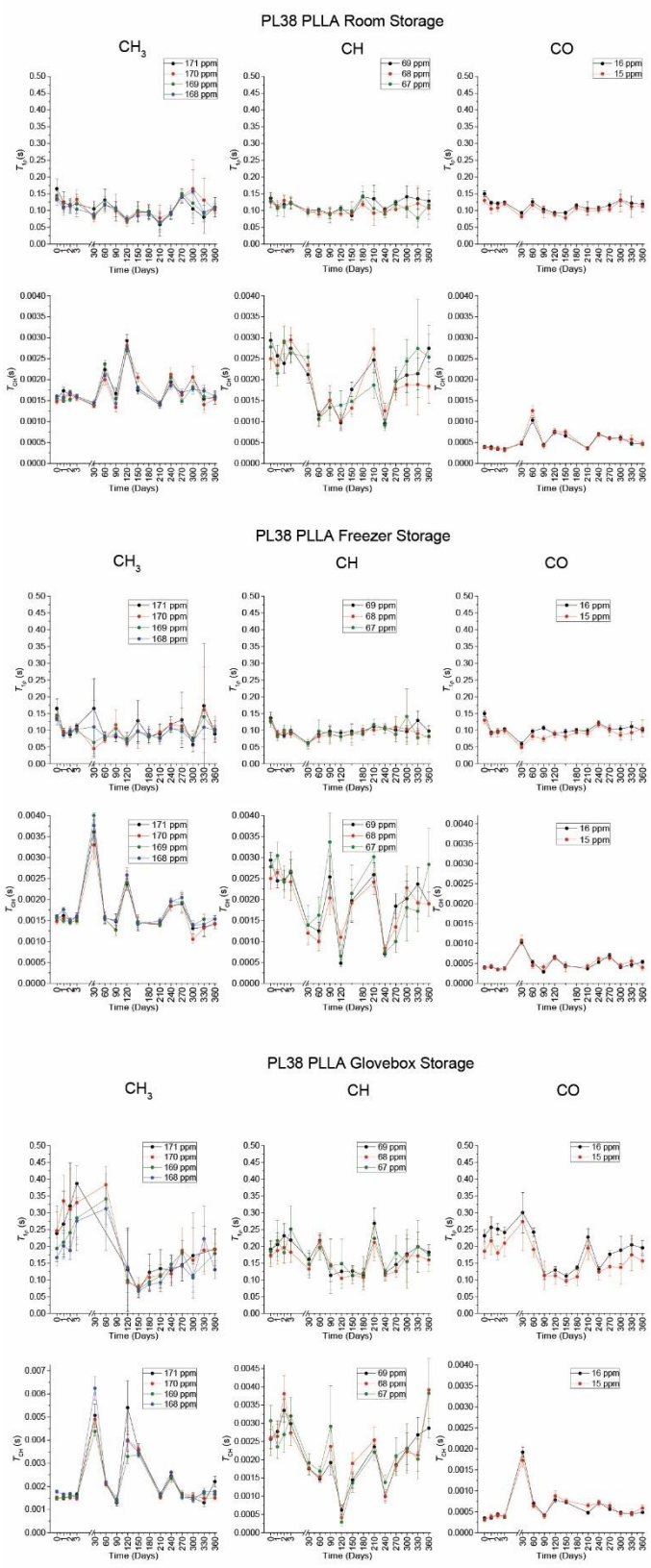

Figure A-3. The change in $T_{1\rho}$ (top) and T_{CH} (bottom) times for industrial grade PLLA for CH_3 (left), CH (middle)and COO (right), under room conditions (top) , stored in a freezer (middle) and stored in a glovebox (bottom).

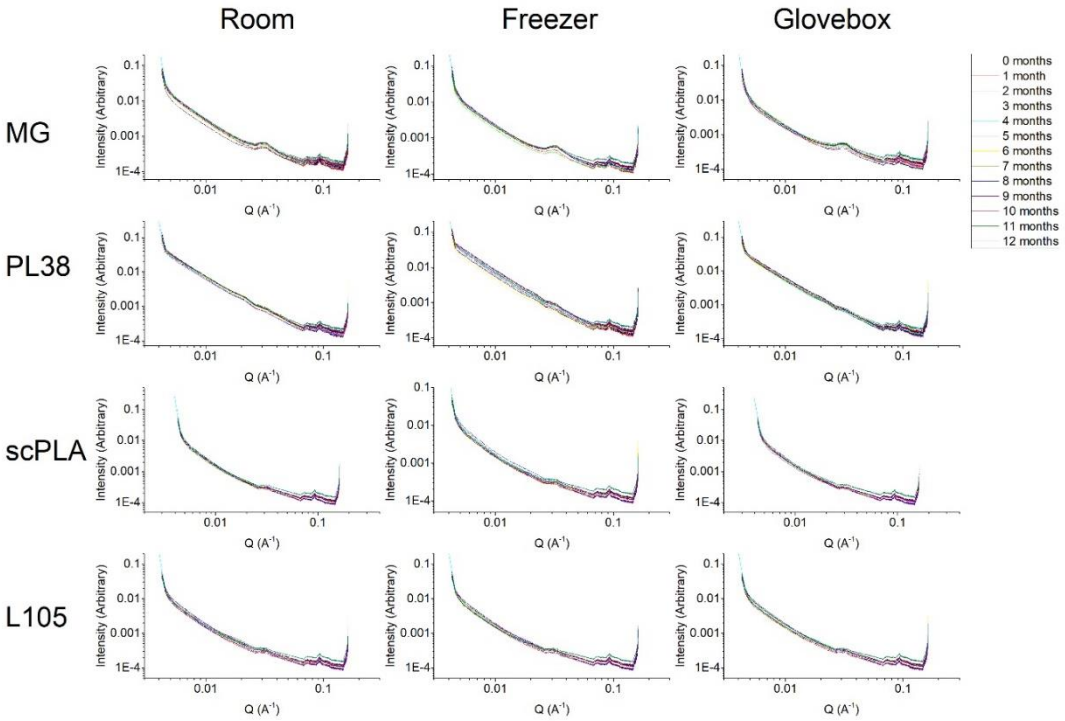

Figure A-4. The small-angle X-ray scattering patterns for the four PLA samples over a year, stored in room conditions (left), in a freezer (middle) and in a glove box (right).

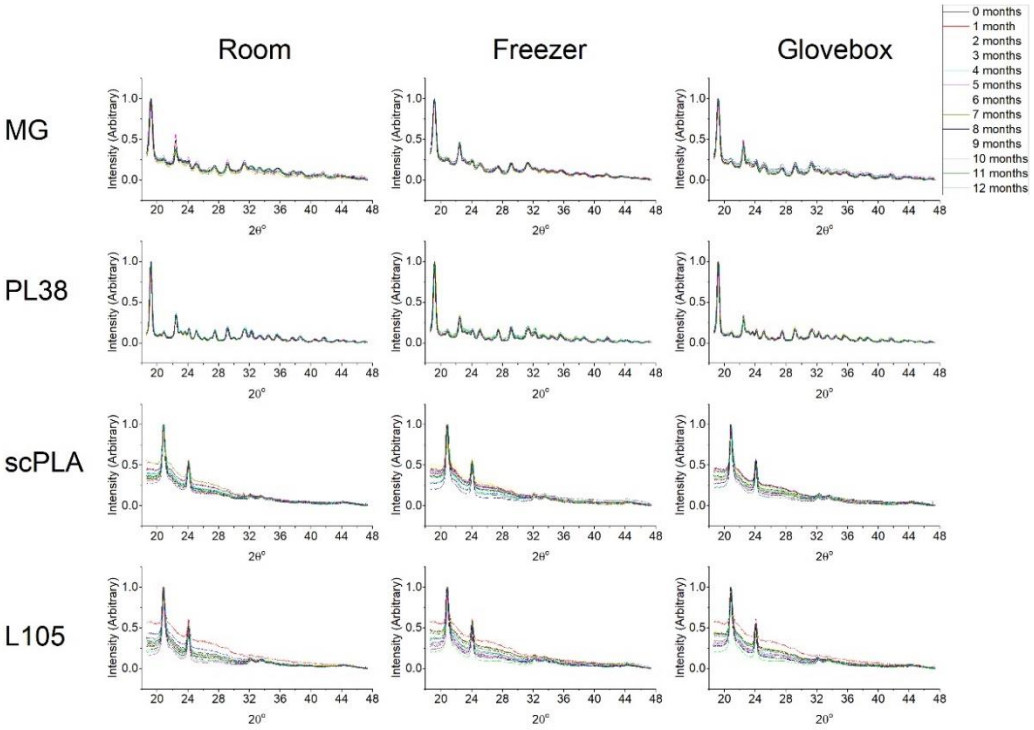

Figure A-5. The wide-angle X-ray scattering patterns for the four PLA samples over a year, stored in room conditions (left), in a freezer (middle) and in a glove box (right).

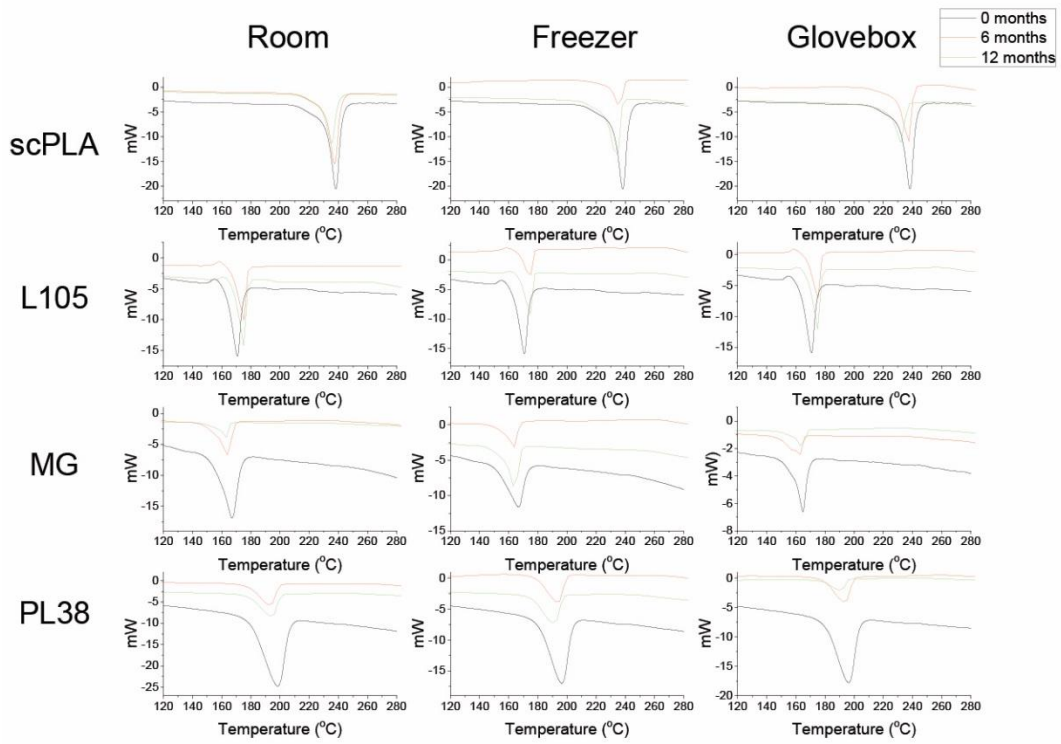

Figure A-6. The DSC scans at 0, 6 and 12 months for the four PLA samples over a year, stored in room conditions (left), in a freezer (middle) and in a glove box (right).